Transcriptomic and Functional Characterization of Adeno-associated Virus Induced Dorsal Root Ganglia Toxicity in the C57BL/6J Mouse Model

Sam Hana

PSL UNIVERSITÉ PARIS

THÈSE DE DOCTORAT
DE L'UNIVERSITÉ PSL

Préparée à l'École Pratique des Hautes Études

Transcriptomic and Functional Characterization of Adeno-associated Virus Induced Dorsal Root Ganglia Toxicity in the C57BL/6J Mouse Model

Soutenue par
Sam HANA
Le 3 octobre 2024

École doctorale n° 472
École doctorale de l'École Pratique des Hautes Études

Spécialité
Neurosciences

Composition du jury:

Giovanni STEVANIN Directeur de recherche INSERM EPHE/PSL Univ Bordeaux	*Président*
Ana BUJ BELLO Directrice de recherche INSERM Genethon, Université Paris Saclay	*Rapporteur*
Hélène PUCCIO Directrice de recherche INSERM Université Lyon 1	*Rapporteur*
Shih-Ching (Joyce) LO Directrice scientifique associée BIOGEN	*Examinateur*
Maria ZAVODSZKY Directrice scientifique associée BIOGEN	*Examinateur*
Christelle LASBLEIZ Maitre de conférences EPHE/PSL	*co encadrante*
Nadine MESTRE FRANCES Directrice d'Etudes EPHE/PSL	*Directrice de thèse*

École Pratique des Hautes Études | PSL

Acknowledgements

First and foremost, I want to express my deepest gratitude to my supervisors: Dr. Joyce Lo, Professor Nadine Mestre Frances, Dr. Fergal Casey, Dr. Christelle Lasbleiz and Dr. Maria I. Zavodszky, for their incredible and invaluable support and guidance throughout this PhD journey. Dr. Joyce Lo has played an instrumental role in my success and completion of this work, and I am profoundly grateful for her efforts and encouragement over the years.

Though the journey has been challenging at times with many sudden changes, all of you have reassured me and provided me with confidence. I feel incredibly fortunate to be surrounded by great minds that have pushed me to my limits and beyond.

I would like to extend my sincere thanks to the members of my committee, Dr. Puccio Hélène and Dr. Buj Bello Ana, for their helpful feedback and suggestions on this dissertation. Their input is crucial in refining and polishing my ideas. Thank you to Giovanni Stevanin for serving as the president of the jury. Additionally, I am grateful to Biogen and PSL University for providing this incredible opportunity for young scientists in the industry. I want to also thank Dr. Patrick Carroll and Dr. Thomas Moore-Morris for their advice, suggestions and feedback during all the committee meetings during this PhD.

To my close Biogen collaborators, thank you immensely for supporting these studies. Your contribution was key to the success of these endeavors. Special mentions go to Zachary Hawley for sharing ownership of the AAV DRG toxicity project, Dan Ferretti for animal support and operations, Gerald Ferreras for animal support, Patrick Cullen for snRNA sequencing, Adam Sheehy for behavior testing, Kevin Ghaemi for gait testing, Dora Bodnar for muscle dual lever, Taras Tuczkewycz for CMAP, and Brian Harvey for action potential testing. Also, Ben Doyle and David Koske for joining me and offering their incredible fine microdissection support. Special thanks to Biogen's Gene Therapy Accelerator Unit members for providing AAV test articles. I also want to express my gratitude to my colleagues within Joyce Lo's subgroup and many scientists across various research units for their comments and advice on this research project.

Lastly, I would like to acknowledge my friends and family for their love and unwavering belief in me over the years. Your unwavering support and motivational words have empowered me to persevere through difficult times and give my utmost effort. Glory be to the Father, and to the Son, and to the Holy Spirit. Amen.

Manuscript Summary (French)

1. INTRODUCTION GENERALE

La thérapie géniquea

Le concept de thérapie génique est apparu dans les années 1960, lorsque la recherche s'est lancée dans le développement de lignées cellulaires génétiquement modifiées par l'introduction de gènes exogènes. Une nouvelle approche thérapeutique est apparue en l'espace de quelques décennies, la première thérapie clinique ayant été approuvée au début des années 1990 (Blaese et al., 1995). La thérapie génique consiste à introduire un gène thérapeutique exogène dans les cellules. Les gènes introduits peuvent remplacer des gènes non fonctionnels, réduire des gènes au silence, éditer des gènes et modifier l'expression des gènes. Cela a permis de traiter et de prévenir des troubles monogéniques, des maladies rares, des cancers, des maladies oculaires et d'autres maladies difficiles à traiter auparavant (Nobrega et al., 2020). La thérapie génique permet une approche précise et ciblée avec un potentiel de correction permanente ou de longue durée. Cette approche ciblée permet de réduire les effets secondaires et offre la possibilité d'une médecine personnalisée. Deux stratégies d'administration différentes sont utilisées en fonction de la maladie concernée. La thérapie génique *in vivo* implique l'introduction de gènes directement dans le corps du patient. La thérapie génique *ex vivo* implique le prélèvement de cellules du patient qui sont par la suite modifiées par l'introduction d'un gène thérapeutique, et réintroduites dans le corps du patient. Il existe actuellement 36 thérapies géniques approuvées par la FDA, les thérapies *in vitro* représentant la majeure partie des approbations, et des centaines d'essais cliniques sont en cours (Approved Cellular and Gene Therapy products 2024)

Voies d'administration

L'un des défis rencontrés par les chercheurs et les concepteurs de médicaments réside dans la méthode d'introduction du gène thérapeutique chez l'hôte. Différentes stratégies

d'administration peuvent être nécessaires pour des maladies spécifiques, mais de manière générale, la stratégie d'administration dépend des cellules et des tissus cibles. Deux principales stratégies sont utilisées : les vecteurs non viraux et les vecteurs viraux.

Vecteurs non viraux

Les vecteurs non viraux utilisent des moyens chimiques ou physiques pour introduire les gènes dans l'hôte par divers moyens tels que la micro-injection, l'électroporation, la magnétoporation, la sonoporation, le canon balistique et d'autres méthodes (Nóbrega et al., 2020). Il existe de nombreuses méthodes chimiques, les plus connues étant les liposomes, diverses nanoparticules et les polymères. Les nanoparticules lipidiques constituent l'une des méthodes non virales les plus utilisées. Les nanoparticules lipidiques sont stables et capables de protéger les acides nucléiques et de maintenir la biocompatibilité. Les vaccins Moderna et Pfizer COVID-19 utilisent tous deux des nanoparticules lipidiques pour introduire l'ARNm dans les cellules. Les méthodes non virales offrent une sécurité accrue avec une immunogénicité réduite, une cytotoxicité moindre et une meilleure spécificité cellulaire par rapport aux vecteurs viraux. Les vecteurs non viraux offrent également une certaine souplesse de conception, la taille de l'ADN n'étant pas limitée. Cependant, les vecteurs non viraux sont moins efficaces queles vecteurs viraux.

Vecteurs viraux

Les virus sont les vecteurs les plus utilisés en thérapie génique, car ils permettent une transduction efficace des cellules/tissus cibles. De nombreux vecteurs ont été utilisés, tels que le virus adéno-associé (AAV), le lentivirus, l'adénovirus et le virus de l'herpès simplex et d'autres encore. Les vecteurs viraux sont composés d’une capside protéique qui encapsule le gène thérapeutique transporté avec les éléments d'expression (c'est-à-dire les activateurs, les promoteurs) et de régulation (c'est-à-dire les éléments post-transcriptionnels et le signal de

polyadénylation) (Bulcha et al., 2021). Les virus peuvent être enveloppés, comme les lentivirus, ou nus, comme les AAV. Les virus présentent un profil de sécurité plus faible, avec un risque accru d'immunogénicité et des limitations liées à la capacité d'empaquetage. Les stratégies actuelles d'ingénierie vectorielle tirent parti de tous les composants viraux pour améliorer l'efficacité, éviter les réponses immunitaires, réduire la cytotoxicité et permettre une spécificité tissulaire.

Environ la moitié des essais cliniques impliquant des vecteurs viraux utilisent des virus adéno-associés (AAV). (Bulcha et al., 2021). Les AAV sont les vecteurs de choix en raison de leur faible immunogénicité, de leur intégration limitée dans le génome de l'hôte, qui élimine la possibilité de mutagenèse insertionnelle, et de leur polyvalence, qui leur permet de transduire un large éventail de types de cellules. Les AAV ont été testés et se sont révélés efficaces et sûrs.

Les virus adéno-associés sont de petits virus non enveloppés (26 nm de diamètre) composés de sous-unités protéiques de capside icosaédriques. La capacité génomique est de 4,7 kb pour l'ADN simple brin, y compris les séquences répétitives terminales inversées (ITR) en forme de T de 145 bp à chaque extrémité. Les séquences ITR sont vitales pour l'encapsulation, ce qui signifie que la longueur utilisable n'est que de 4,4 kb. La capside est composée des protéines virales VP1, VP2 et VP3 dans un rapport 1:1:10. Les protéines virales et les ITR déterminent le sérotype de l'AAV, lequel détermine des caractéristiques essentielles telles que le tropisme, la liaison aux récepteurs et l'immunogénicité (Wang et al., 2024). Le génome de l'AAV de type sauvage comporte deux cadres de lecture ouverts codant pour les gènes Cap et Rep. Le gène Cap code pour 3 protéines de capside, Assembly-Activating Protein (AAP) et Membrane Associated Accessory Protein (MAAP). Le gène Rep code pour 4 protéines de réplication qui font partie intégrante de la réplication et de l'empaquetage. L'AAV sauvage est un dependo-parvovirus, ce qui signifie qu'il a besoin d'un adénovirus ou d'un virus de l'herpès simplex pour

se répliquer (Fig. 1). Il existe 12 sérotypes d'AAV connus et de nombreuses variantes identifiées dans de nombreuses espèces (Wang et al., 2024). Le sérotype définit le tropisme de l'AAV pour un tissu spécifique. Les variations distinctes de neuf régions du gène cap entre les sérotypes d'AAV contribuent aux préférences spécifiques des tissus et des types de cellules, les parties variables du VP3 étant considérées comme les plus critiques pour le tropisme (Wang et al., 2024). L'AAV2 a été le premier à être identifié et est basé sur l'AAV de type sauvage. En termes de tropisme pour le SNC, l'AAV9 est l'un des AAV les plus utilisés, pour sa transduction neuronale efficace par rapport à d'autres AAV..

Les recherches actuelles en thérapie génique se concentrent sur la découverte de capsides innovantes capables d'assurer une transduction spécifique, efficace et à haut rendement. Pour cela, l'ingénierie des capsides repose sur trois approches principales :

- **Isolement de nouveaux variants naturels** : Identifier des sérotypes issus de différentes espèces peut aider à contourner les anticorps neutralisants observés chez de nombreux patients contre les sérotypes AAV sauvages courants. Par exemple, le variant AAVv66, présentant une homologie de 98 % avec l'AAV2, a démontré une meilleure transduction dans le système nerveux central (Hsu et al., 2020).
- **Conception rationnelle** : Cette méthode consiste à modifier les capsides existantes en introduisant des mutations génétiques ou des domaines de liaison spécifiques. Par exemple, la capside BI-hTFR1, dotée d'un domaine optimisé pour le récepteur 1 de la transferrine humaine, s'est avérée plus performante que l'AAV9 pour la transduction cérébrale (Huang et al., 2024).
- **Évolution dirigée et outils in silico** : En générant des bibliothèques de capsides mutées (via PCR ou insertion de peptides) et en sélectionnant les plus efficaces, il est possible d'améliorer les performances. L'intégration de l'intelligence artificielle

et de l’apprentissage automatique facilite également la création de capsides optimisées à partir de données sur les génomes ancestraux (Bryant et al., 2021).

En résumé, le développement de capsides sûres, spécifiques et performantes reste un pilier essentiel pour renforcer l’efficacité et la pérennité de la thérapie génique.

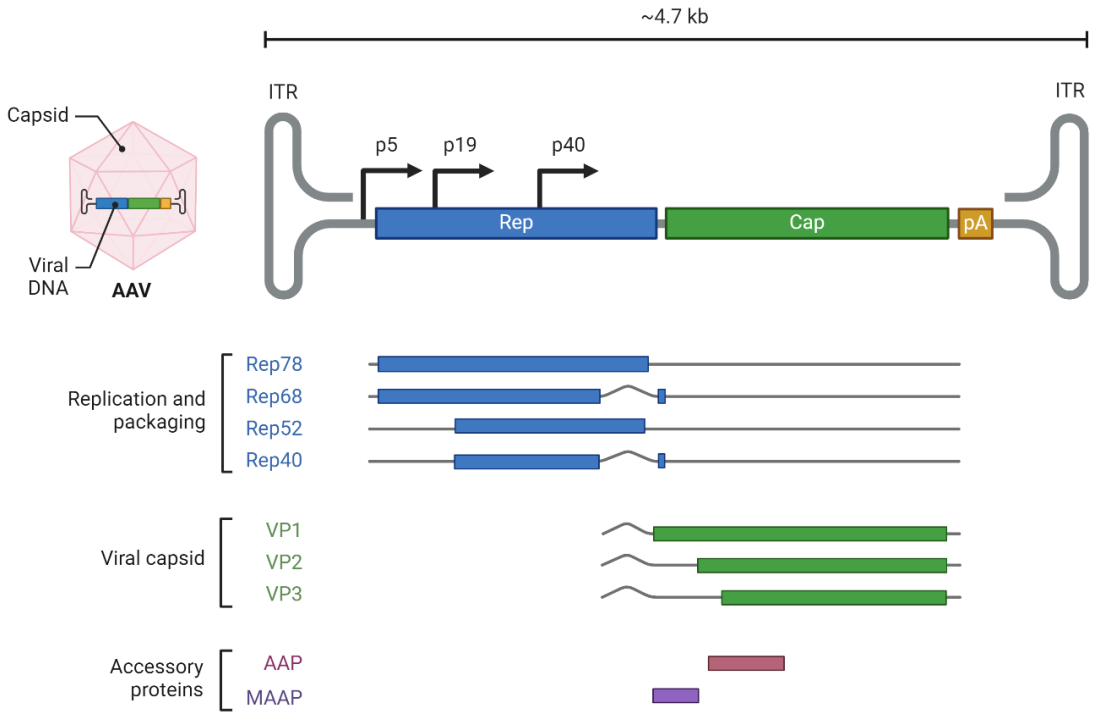

Figure 1 : La biologie des vecteurs AAV implique l'arrangement génomique de l'AAV2 de type sauvage, illustrant son génome d'ADN simple brin d'environ 4,7 kb et l'expression de sept ARN viraux et de deux protéines accessoires par l'intermédiaire des gènes Rep et Cap. Les régions promotrices p5, p19 ou p40 sont indiquées dans le gène Rep. Créé par Biorender.com

Transduction des AAV

On pense que les AAV se fixent à la surface des cellules en se liant à des récepteurs primaires tels que les glycanes, les glycoconjugués et l'acide sialique. Par la suite, les interactions avec les corécepteurs sont essentielles pour l'endocytose (Wang et al., 2024). Chez l'homme, l'AAV9 se lie au galactose en tant que récepteur primaire et au récepteur de la laminine et à l'intégrine en tant que corécepteurs (Shen et al., 2011, p. 9 ; Wang et al., 2024). L'AAV est ensuite internalisé et l'altération du pH dans les endosomes entraîne un changement de confirmation de l'AAV. L'AAV s'échappe de l'endosome et peut entrer dans le noyau via le pore nucléaire. L'AAV peut également être dégradé dans le cytoplasme par le protéasome, ce qui pourrait déclencher des réponses immunitaires par la présentation des composants de l'AAV à la surface de la cellule. Dans le noyau, l'AAV est désenrobé et la synthèse des brins secondaires se produit pour générer de l'ADNdb, un processus vital pour l'expression du gène exogène. L'ADNdb viral subit ensuite une concaténérisation entraînée par les événements de recombinaison des ITR pour produire un épisome circularisé qui persiste dans le noyau.

Voies d'administration des thérapies géniques

Les thérapies géniques peuvent être administrées par différentes méthodes, selon la maladie et les cellules ou tissus ciblés. Chaque stratégie est adaptée pour maximiser l’efficacité et la sécurité du patient.

Pour les thérapies géniques *ex vivo*, les cellules du patient sont extraites, modifiées pour intégrer un gène thérapeutique, puis réintroduites généralement par injection intraveineuse. Plusieurs traitements ont été approuvés : **Yescarta** pour le lymphome à grandes cellules B (Locke et al., 2022), **Zynteglo** pour la bêta-thalassémie (Locatelli et al., 2022), **Libmeldy** pour la leucodystrophie métachromatique (Fumagalli et al., 2024). La thérapie par cellules T à

récepteur d'antigène chimérique (CAR-T), qui consiste à modifier les cellules T, connaît un essor depuis une décennie, avec de nombreux essais cliniques en oncologie (Dabas & Danda, 2023).

Les thérapies géniques *in vivo* sont utilisées pour administrer directement le traitement aux tissus ciblés via diverses voies. La voie intraveineuse est appropriée pour des maladies nécessitant une distribution étendue à tous les tissus affectés : par exemple, **Elevidys**, est approuvé pour la dystrophie musculaire de Duchenne (Zaidman et al., 2023). La voie intramusculaire directe a été testée pour des pathologies localisées comme la dystrophie musculaire oculopharyngée (OPMD), dans le cadre de l'essai clinique BB-301 (Strings-Ufombah et al., 2021). Enfin récemment une nouvelle voie, la voie topique adaptée aux maladies de la peau, comme **Vyjuvek**,a été approuvée pour l'épidermolyse bulleuse dystrophique (Guide et al., 2022).

Les efforts en thérapie génique se concentrent largement sur le traitement des maladies neurodégénératives et du système nerveux central (SNC). Toutefois, la barrière hémato-encéphalique représente un obstacle majeur pour une administration efficace. Actuellement, des vecteurs viraux, tels que les AAV (adeno-associated virus), sont développés pour franchir cette barrière. Les AAV peuvent être administrés par injection intraveineuse pour une distribution systémique dans le SNC, mais cela nécessite souvent des doses élevées de vecteur, augmentant le risque de toxicité.

Une alternative consiste à administrer le traitement directement dans le liquide céphalorachidien (LCR), ce qui permet une distribution plus ciblée et à des doses plus faibles. Cette administration peut se faire par voie intrathécale (ponction lombaire), intracisternale ou intracérébroventriculaire, avec l'avantage d'une délivrance plus précise dans le SNC (Perera et al., 2024). L'injection intraparenchymateuse, ciblant des régions spécifiques du cerveau (par

exemple, le noyau sous-thalamique ou le putamen dans la maladie de Parkinson), permet également une transduction élevée, bien que cette méthode soit invasive et technique (Hwu et al., 2021).

Chacune de ces voies présente des avantages et des inconvénients : l'administration systémique par voie intraveineuse peut entraîner des effets indésirables dus à un manque de ciblage précis, des réactions immunitaires, des cytotoxicités ou des problèmes liés aux anticorps neutralisants (L. Xu et al., 2024). En revanche, les injections intraparenchymateuses offrent une forte efficacité locale, mais elles sont plus invasives et techniquement complexes (Hudry & Vandenberghe, 2019).

Les maladies oculaires représentent également une cible idéale pour les thérapies géniques en raison de la petite taille de l'œil et de son environnement immunitaire privilégié (Hudry & Vandenberghe, 2019). Différentes injections permettent de cibler efficacement toutes les régions de l'œil, comme le vitré, la rétine et la choroïde. Des approches similaires sont également en cours de développement pour traiter des maladies de l'oreille (Morgan et al., 2020 ; Sahu et al., 2021).

Pour les troubles métaboliques, qui affectent souvent le cerveau, la rétine et les muscles squelettiques, des stratégies d'administration variées, adaptées aux tissus concernés, sont utilisées. Les défis liés à l'administration, notamment la transduction insuffisante de certains tissus ou la toxicité pour des organes sensibles comme le foie, sont progressivement surmontés grâce à la conception de nouvelles capsides AAV capables de cibler avec précision les tissus affectés tout en réduisant l'impact sur les organes non visés.

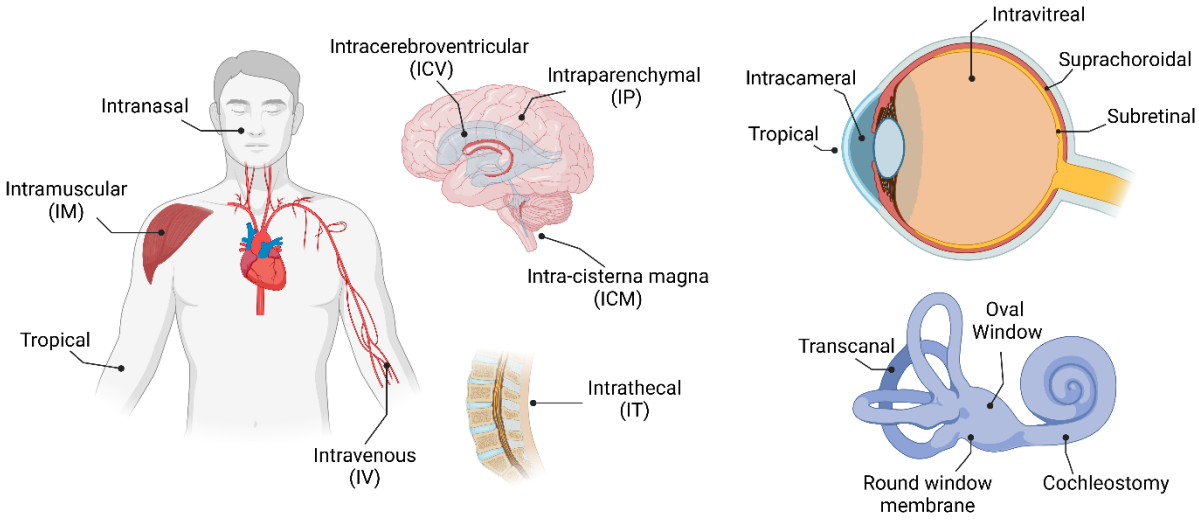

Figure 2 : Les voies d'administration des thérapies géniques in vivo dans le SNC et les organes spécialisés. Créé par BioRender.com.

Cassette d'expression génique AAV

La cassette d'expression génique, contenant le transgène ou "cargo" thérapeutique, est l'élément clé de toute thérapie génique, qu'elle soit véhiculée par des vecteurs viraux ou non. Elle comprend des régions ITR (Inverted Terminal Repeats), un promoteur, des amplificateurs, des introns, le gène exogène, ainsi que des éléments post-transcriptionnels et de régulation en aval. Cette cassette est rigoureusement testée lors des études précliniques pour évaluer son efficacité et son profil de sécurité.

Il existe plusieurs stratégies d'ingénierie pour la cassette d'expression génique, chacune étant adaptée à l'étiologie spécifique de la maladie. La stratégie la plus simple, l'augmentation génique, consiste à introduire un gène thérapeutique pour remplacer un gène mutant non fonctionnel, sans altérer le génome de l'organisme (Fig. 3). Par exemple, **Zolgensma**, utilise l'AAV9 pour transporter le gène SMN1, afin de traiter l'amyotrophie spinale (Pane et al., 2023). Cette méthode est particulièrement répandue pour les maladies neurologiques (Gao et al., 2024)., La deuxième stratégie, **le s**ilencing et modulation génique, vise à cibler et dégrader des ARN toxiques dans les maladies à gain de fonction ARN, grâce à des molécules comme les petits ARN interférents (siRNA), les petits ARN en épingle à cheveux (shRNA) ou les microARN. Des outils récents, comme les endonucléases ciblant l'ARN, telles que Cas13d et Cas9, permettent une dégradation efficace des ARN mutants (Burmistrz et al., 2020). La dernière stratégie utilise l'édition génomique. Un essai clinique sur la dégénérescence maculaire liée à l'âge utilise le système CRISPR-Cas13Y encapsulé dans un AAV (Luk et al., 2024). Les technologies CRISPR-Cas permettent de corriger des mutations précises dans le génome. Les éditeurs de base permettent de modifier une paire de bases unique. Les éditeurs de cytosine convertissent une paire cytosine-guanine en thymine-adénine, tandis que les éditeurs d'adénine effectuent l'inverse (Porto et al., 2020). Cette approche est utilisée pour

l’hypercholestérolémie familiale et la drépanocytose (Horie & Ono, 2024). Cependant, de nombreuses maladies sont causées par des gènes présentant des mutations étendues sur plusieurs loci. Par conséquent, il est nécessaire de corriger une partie importante du gène mutant, ce qui peut être réalisé par l'édition primaire. Cette technique permet de modifier avec précision la séquence d'ADN en utilisant une matrice de correction génétique et une Cas9 modifiée. Cette stratégie est testée pour des maladies comme la granulomatose chronique (Chen & Liu, 2023).

Le rôle du promoteur, situé en amont du transgène est crucial dans l’expression génique. La région promotrice peut comprendre des activateurs, une région promotrice centrale et des introns. Les **promoteurs ubiquitaires** (ex. : CAG, CMV), actifs dans toutes les cellules transduites, offrent une expression forte mais non spécifique (Au et al., 2022). Les **promoteurs spécifiques à un type cellulaire** par exemple CBA, PGK, UBC (Qin et al., 2010) entraînent une expression à un niveau modéré à faible mais réduisent les effets secondaires liés à l'expression non ciblée. Divers promoteurs cellulaires spécifiques ont été utilisés, tels que la synapsine I (Syn 1) pour les neurones, la créatine kinase musculaire (CK8) pour les muscles, la transthyrétine (TTR) pour le foie et d'autres encore (Chuah et al., 2014 ; Hart et al., 2024 ; McLean et al., 2014). Les recherches actuelles en thérapie génique se concentrent sur l’identification de nouveaux promoteurs et le développement de promoteurs synthétiques. Ces derniers offrent une régulation précise de l'expression des gènes et permettent de dépasser les limites des promoteurs naturels. En complément de la région promotrice, les éléments de régulation post-transcriptionnelle sont essentiels pour stabiliser, exporter et traduire l’ARNm en protéines thérapeutiques. Parmi ces éléments, l’élément WPRE (Woodchuck Hepatitis Virus Post-Transcriptional Regulatory Element), inséré après le codon d’arrêt, agit comme une région 3' non traduite (UTR) avec un signal de polyadénylation. Il améliore la stabilité de l’ARNm, l’exportation nucléaire et l’efficacité de l'expression génique (Mouzannar et al., 2024 ; Patrício

et al., 2017). Les signaux de polyadénylation, présents dans la plupart des cassettes, sont cruciaux pour la terminaison de la transcription, la stabilité et la traduction de l'ARNm. Enfin les sites de liaison pour microARN, permettent un silencing génique supplémentaire et un contrôle supplémentaire de l'expression (Hordeaux et al., 2020). Ainsi, chaque composant de la cassette d'expression contribue à garantir une expression efficace et stable du gène thérapeutique.

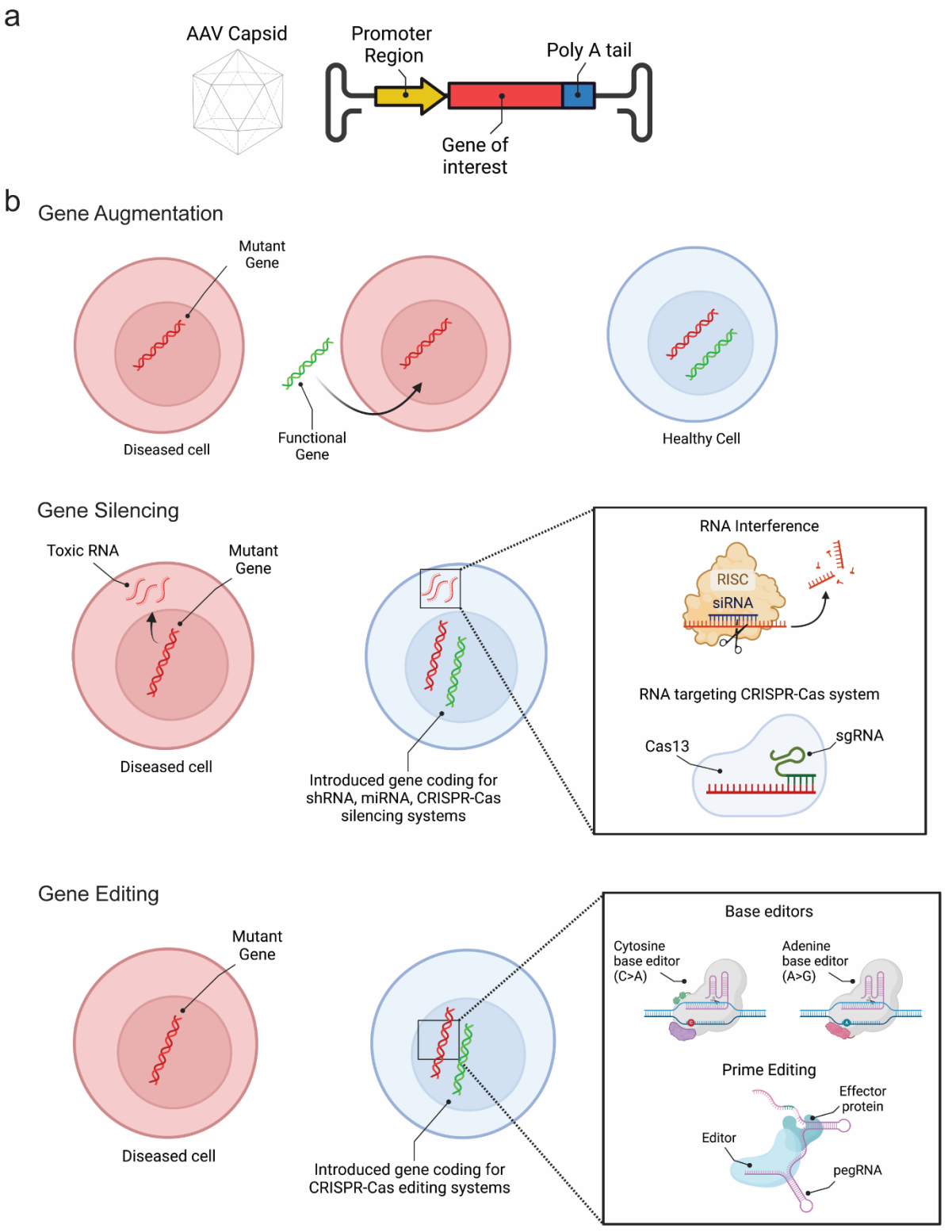
a
AAV Capsid
Promoter Region
Poly A tail
Gene of interest
b
Gene Augmentation
Mutant Gene
Diseased cell
Functional Gene
Healthy Cell
Gene Silencing
Toxic RNA
Mutant Gene
Diseased cell
Introduced gene coding for shRNA, miRNA, CRISPR-Cas silencing systems
RNA Interference
RISC
siRNA
RNA targeting CRISPR-Cas system
Cas13
sgRNA
Gene Editing
Mutant Gene
Diseased cell
Introduced gene coding for CRISPR-Cas editing systems
Base editors
Cytosine base editor (C>A)
Adenine base editor (A>G)
Prime Editing
Effector protein
Editor
pegRNA

Figure 3 : Stratégies de thérapie génique axées sur les thérapies géniques à base d'AAV. a. Composants de la cassette d'expression génique recombinante AAV. b. L'augmentation génique implique l'introduction d'un gène thérapeutique qui rétablit la fonction des cellules malades. Les stratégies d'extinction des gènes consistent à cibler les espèces d'ARNm toxiques dans le cytoplasme par divers mécanismes tels que la voie de l'interférence ARN par le complexe RISC guidé par l'ARNsi. En outre, les endonucléases Cas ciblant l'ARN, telles que Cas13d, peuvent cibler et dégrader efficacement l'ARN toxique. Les technologies d'édition directe de l'ADN se concentrent sur l'utilisation d'éditeurs de base pour modifier une seule base et corriger les mutations dans les gènes. Les technologies d'édition primaire sont capables de modifier de grandes séquences d'ADN. Ces technologies d'édition modifient l'ADN sans rupture de double brin, contrairement aux systèmes CRISPR-Cas9 traditionnels. Il convient de noter que les éditeurs actuels ne s'adaptent pas aux AAV. L'éditeur peut être délivré dans les cellules malades via des nanoparticules lipidiques ou directement sous forme de ribonucléoprotéine. Créé par BioRender.com.

Modalité basée sur l'AAV pour le traitement des maladies neurodégénératives

Selon l'OMS, 50 millions de personnes dans le monde souffrent de troubles neurodégénératifs, (Lamptey et al., 2022 ; Neurological Disorders Affect Millions Globally, n.d.) notamment la maladie d'Alzheimer, de Parkinson, de Huntington, la sclérose latérale amyotrophique (SLA) et la sclérose en plaques Ces maladies, caractérisées par la perte progressive de neurones, se développent lentement avec l'âge et sont souvent associées à l'accumulation de protéines dysfonctionnelles, entraînant des dommages cellulaires et la mort neuronale (Disorders et al., 2013). Les mutations génétiques jouent un rôle central dans leur apparition, aggravées par des réponses inflammatoires chroniques impliquant la microglie et les astrocytes (Kwon & Koh, 2020). Bien que l'inflammation soit initialement protectrice, elle contribue avec le temps à accélérer la progression de la maladie. Avec le vieillissement de la population, le nombre de cas devrait augmenter dans les décennies à venir. En l'absence de thérapies capables de modifier les causes sous-jacentes de ces pathologies, le besoin de nouvelles approches thérapeutiques est crucial.

Les avancées en thérapie génique ont révolutionné le traitement des maladies neurodégénératives, notamment celles dont la base génétique est identifiée (J. Gao et al., 2024). Cette approche permet de corriger les mécanismes pathologiques, de protéger les neurones contre la dégénérescence, de réguler l'inflammation chronique, et de favoriser la régénération et la neuromodulation par l'expression de gènes clés impliqués dans la neurogenèse. Les vecteurs AAV sont privilégiés pour administrer des transgènes thérapeutiques, particulièrement efficaces dans les maladies dues à une perte de fonction. Des stratégies d'extinction génique et d'édition génomique utilisant des AAV sont également mises en œuvre. Les sérotypes couramment employés incluent AAV2, AAV9, AAVrh10, AAV5 et AAV1. L'administration intrathécale dans le liquide céphalorachidien (LCR) est la voie la plus utilisée en essais

cliniques, généralement sous un schéma de dose unique. Cela minimise les risques liés aux anticorps neutralisants, bien que l'immunosuppression soit souvent nécessaire pour limiter les réponses immunitaires.

Les thérapies géniques basées sur les AAV montrent un potentiel prometteur, résumé dans le tableau 1 des thérapies pour les maladies neurodégénératives.

Disease	Gene Therapy#	Strategy	Route of Administration	Dosing Frequency	Study Phase	Trial Identifier
Alzheimer's Disease	AAV2-BDNF	Gene augmentation	MRI guided stereotaxic delivery to entorhinal cortex	Single Dose	I	NCT05040217
Alzheimer's Disease	AAVrh10- APOE2	Gene augmentation	IT	Single Dose	I/II	NCT03634007
Huntington's Disease	AAVrh10 - CYP46A1	Gene augmentation	ICV	N/A	I/II	NCT05541627
Huntington's Disease	rAAV5-miHTT	Gene silencing	MRI guided stereotaxic brain delivery	Single Dose	I/II	NCT04120493
Huntington's Disease	rAAV5-miHTT	Gene silencing	MRI guided stereotaxic bilateral delivery to striatum	Single Dose	I/II	NCT05243017
Parkinson's Disease	AAV9-GBA1	Gene augmentation	IC	Single Dose	I/II a	NCT04127578
Parkinson's Disease	AAV –GAD	Gene augmentation	Bilateral infusion to subthalamic nuclei	Single Dose	I/II	NCT05603312
Parkinson's Disease	AAV2-GDNF	Gene augmentation	Bilateral infusion into putamen	Single Dose	I	NCT04167540
Parkinson's Disease	AAV2- AADC	Gene augmentation	Bilateral infusion into putamen	Single Dose	II	NCT03562494
Amyotrophic Lateral Sclerosis (ALS)	AAVrh10- miRNA- SOD1	Gene silencing	IT	Single Dose	I/II	NCT06100276
Frontotemporal Dementia (FTD)	AAV9- GRN	Gene augmentation	MRI guided intrathalamic delivery	Single Dose	I/II	NCT06064890
Frontotemporal Dementia (FTD)	AAV1-GRN	Gene augmentation	IC	Single Dose	I/II	NCT04747431
Frontotemporal Dementia (FTD)	AAV9-GRN	Gene augmentation	IC	Single Dose	I/II	NCT04408625
Spinal Muscular Atrophy (SMA) Type 1	AAV9-SMN	Gene augmentation	IT	Single Dose	I/II	NCT05824169
SMA Type 2	AAV9-SMN	Gene augmentation	IT	Single Dose	I/II	NCT05901987
SMA Type 2	AAV9-SMN	Gene augmentation	IT	Single Dose	III	NCT05089656
SMA	AAV9-SMN	Gene augmentation	IT	Single Dose	IIIb	NCT05386680
Unilateral Refractory Mesial Temporal Lobe Epilepsy (MTLE)	AAV9-miRNA- GRIK2	Gene silencing	MRI-Guided Convection- enhanced Delivery (CED)	Single Dose	I//IIa	NCT06063850

Hereditary Spastic Paraplegia	AAV9-AP4M1	Gene augmentation	IT	Single Dose	I/II	NCT05518188
Giant Axonal Neuropathy	scAAV9-Gigaxonin	Gene augmentation	IT	Single Dose	I	NCT02362438
Metachromatic Leukodystrophy (MLD)	AAVrh10-ARSA	Gene augmentation	Bilateral intracerebral injections to white matter	Single Dose	I/II	NCT01801709
Adrenomyeloneuropat hy	AAV9-ABCD1	Gene augmentation	IT	Single Dose	I/II	NCT05394064
GM1 Gangliosidosis	AAV9-GLB1	Gene augmentation	IV	Single Dose	I/II	NCT03952637
GM2 Gangliosidosis	AAV9-Hexokinase A	Gene augmentation	IT	Single Dose	I/II	NCT04798235
Krabbe Disease	AAVrh10-GALC-Hematopoietic stem cells	Gene augmentation	IV	N/A	I/II	NCT04693598
Krabbe Disease	AAVrh10-GALC	Gene augmentation	IV	Single Dose	I/II	NCT05739643
Canavan Disease	AAV9-ASPA	Gene augmentation	IV	Single Dose	I/II	NCT04998396
Canavan Disease	rAAV-ASPA	Gene augmentation	Intracranial	Single Dose	I/II	NCT04833907
Batten Disease	scAAV9-CLN3	Gene augmentation	IT	Single Dose	I/II	NCT03770572
Batten Disease	AAV9-TPP	Gene augmentation	Subretinal	Single Dose	I/II	NCT05791864
Batten Disease	AAV9-CLN5	Gene augmentation	ICV, ICT	Single dose per administration route	I/II	NCT05228145
Batten Disease	AAV9-MFSD8	Gene augmentation	IT	Single Dose	I	NCT04737460
Fabry Disease	AAV-C102 - GLA	Gene augmentation	IV	Single Dose	I/II	NCT04519749
Fabry Disease	AAV2/6- GLA	Gene augmentation	IV	Single Dose	I/II	NCT04046224
Fabry Disease	AAVS3- GLA	Gene augmentation	IV	Single Dose	I/II	NCT04455230
Mucopolysaccharidosi s Type I (Hurler Syndrome)	rAAV9- IDUA	Gene augmentation	IC	Single Dose	I/II	NCT03580083
Mucopolysaccharidosi s Type II (Hunter Syndrome)	rAAV9-IDS	Gene augmentation	IC or ICV	Single and Multiple Doses	II/III	NCT03566043
Mucopolysaccharidosi s Type III (Sanfilippo Syndrome)	scAAV9- SGSH	Gene augmentation	IV	Single Dose	II/III	NCT02716246
Dravet Syndrome	rAAV9-reGABA and eTFSCN1A	Gene augmentation	ICV	Single Dose	I/II	NCT05419492
Rett Syndrome	AAV9- Mini- MECP2	Gene augmentation	IT	Single Dose	I/II	NCT05606614
Rett Syndrome	AAV9-MECP2	Gene augmentation	ICV	Single Dose	I/II	NCT05898620

Tableau 1 : Essais cliniques en cours basés sur les AAV pour les maladies neurodégénératives en 2024. Le tableau est adapté de Gao et al, 2024. Intracérébroventriculaire (ICV), intrathécal (IT), intraveineux (IV), intracisternal (IC), intravitréen (ICT)

Défis actuels en matière de sécurité de la thérapie génique *in vivo* à base d'AAV

Les thérapies géniques recombinantes *in vivo* à base d'AAV posent des problèmes beaucoup plus importants que les thérapies géniques *ex vivo* (Shirley et al., 2020). La thérapie génique *ex vivo* contourne les réponses immunitaires, ce qui réduit considérablement les toxicités potentielles. L'introduction d'AAV dans l'organisme pose de nombreuses difficultés et de nombreux aspects doivent être pris en compte. La voie d'administration dépend de la maladie et de la zone cible. L'administration intraveineuse peut cibler plusieurs organes, tandis que l'administration intramusculaire ou intraparenchymateuse est localisée. Le sérotype AAV et les promoteurs utilisés sont essentiels pour le tissu cible et la spécificité. L'atténuation de la réponse immunitaire par l'utilisation d'immunosuppresseurs est généralement employée pour contourner les anticorps préexistants. Certaines toxicités ont été observées dans les essais cliniques et les modèles animaux précliniques :

- Génotoxicité : la mutagenèse insertionnelle associée à l'AAV recombinant et à l'AAV sauvage est similaire (Martins et al., 2023). Des insertions pourraient se produire à des doses élevées, en particulier dans les organes fortement transduits tels que le foie. Une étude récente de séquençage de nouvelle génération a montré que d'autres types de tissus tels que le rein, le cœur, le poumon et la rate peuvent être affectés (Martins et al., 2023).
- Hépatotoxicité : l'administration systémique de fortes doses de vecteur entraîne des lésions hépatiques. Une élévation des enzymes hépatiques telles que l'aminotransférase a été observée dans des modèles animaux précliniques et chez des patients lors d'essais cliniques (Chand et al., 2021). L'administration de corticostéroïdes et de produits prophylactiques atténue cette toxicité.

- Microangiopathie thrombotique : formation de caillots sanguins dans les vaisseaux sanguins en raison de l'agrégation des plaquettes. On pense que le système immunitaire inné contribue à cette lésion qui peut évoluer vers l'ischémie (Salabarria et al., 2024).
- Immunogénicité : la capside de l'AAV et les composants du vecteur peuvent activer des réponses immunitaires innées et adaptatives entraînant une inflammation et des dommages aux tissus, ce qui pourrait aggraver l'état des patients (T. Yang et al., 2022). En outre, les réponses immunitaires peuvent éliminer les cellules transduites, réduisant ainsi l'efficacité.
- Neurotoxicité : des titres élevés d'AAV administrés dans le liquide céphalorachidien (LCR), par voie intracrânienne, intraparenchymateuse ou intraveineuse peuvent rompre la barrière hémato-encéphalique, ce qui peut entraîner une infiltration de cellules immunitaires et une inflammation. L'AAV peut également entraîner une toxicité neuronale, qui a été observée dans le cerveau, la moelle épinière, le trijumeau et les ganglions de la racine dorsale (Guo et al., 2023 ; Hinderer et al., 2018).

Toxicité des ganglions de la racine dorsale (DRG) après administration d'AAV

Des cas de neurotoxicité touchant le système nerveux central et périphérique ont été signalés dans des essais cliniques utilisant des doses élevées d'AAV. L'administration intrathécale, courante dans ces études, augmente le risque de toxicité des DRG, bien que celle-ci soit généralement asymptomatique.

Dans une étude clinique expérimentale visant à mesurer la sécurité, un AAV9 codant un microARN ciblant le gène SOD1 humain a été administré par voie intrathécale à deux patients atteints de SLA SOD1 (Mueller et al., 2020). Un patient a ressenti des picotements dans les

mains après trois semaines et des décharges électriques douloureuses au pied droit après quatre semaines. Dix semaines après l'administration, il présentait une absence de potentiels sensitifs dans certains nerfs, une réduction de l'amplitude et des vitesses de conduction nerveuse, et une aggravation progressive des symptômes. Ce patient est décédé de la SLA 15,6 mois après le traitement. L'autopsie a révélé une perte neuronale dans les DRG bilatéraux, des infiltrations de cellules T dans les racines nerveuses et une perte de motoneurones dans la moelle épinière. Le second patient, sous immunosuppresseurs, n'a pas développé de toxicité liée aux DRG. Ce cas souligne l'importance de l'immunomodulation dans la gestion des effets secondaires des thérapies géniques basées sur l'AAV. La toxicité des DRG a été également signalée dans un essai clinique utilisant le scAAV9 pour délivrer le gène *GAN* chez des patients atteints de neuropathie axonale géante, via une injection intrathécale combinée à un traitement immunosuppresseur (Farrar et al., 2022 ; Mullard, 2021). Un patient est décédé huit mois après l'administration, avec une perte neuronale sévère dans les DRG, mais sans signe d'inflammation. Il reste incertain d'attribuer ce décès au traitement ou à la maladie elle-même, qui provoque également une neuropathie sensorielle. Globalement, les cas de toxicité des DRG liés aux thérapies géniques sont rares. Cependant, les essais cliniques en cours surveillent étroitement les patients pour détecter d'éventuelles altérations des neurones sensoriels ou des neuropathies associées au traitement.

Vue d'ensemble des ganglions de la racine dorsale

Les ganglions de la racine dorsale (DRG) sont situés à l'intérieur ou à proximité des foramens intervertébraux de la colonne vertébrale (Haberberger et al., 2019). Chaque nerf rachidien possède une paire de DRG qui est latérale à la moelle épinière et se connecte via la racine nerveuse dorsale. Les souris possèdent 30 à 31 paires de DRG, dont 8 cervicaux, 13 thoraciques, 5 ou 6 lombaires et 4 sacrés. Les DRG font partie du système nerveux

somatosensoriel périphérique et abritent les corps neuronaux sensoriels des nerfs périphériques. Le DRG conduit les signaux neuronaux sensoriels du système nerveux périphérique au système nerveux central. Les neurones du DRG ont une morphologie unipolaire qui se divise en deux prolongements, l'un se projetant dans la moelle épinière et l'autre dans la périphérie (Crawford & Caterina, 2019). Le soma neuronal occupe les régions périphériques du DRG tandis que les régions centrales sont composées de faisceaux de fibres nerveuses. Les neurones sensoriels du DRG sont entourés de cellules gliales satellites qui forment une unité étroite permettant de moduler le microenvironnement et de soutenir les neurones par l'expression de récepteurs et de canaux ioniques spécifiques (Hanani & Verkhratsky, 2021). Le DRG est constitué pour une part importante de fibroblastes et de cellules de Schwann mais aussi de cellules endothéliales, des péricytes et de cellules immunitaires résidentes (macrophages, cellules T et cellules B) (Haberberger et al., 2019). Les vaisseaux sanguins forment un vaste réseau d'artérioles et de capillaires à l'intérieur du DRG, ce qui facilite la pénétration des petites et grandes molécules (Fig. 2).

Les neurones sensoriels se distinguent par leur morphologie, leur physiologie, leurs facteurs de transcription, les récepteurs couplés aux protéines G qu'ils expriment, leur myélinisation, leurs neurotransmetteurs et leurs canaux ioniques (Jung et al., 2023 ; Meltzer et al., 2021, 2021 ;Renthal et al., 2020 ; Sharma et al., 2020).

Historiquement, les neurones sensoriels étaient classés selon la taille de leur soma, leur degré de myélinisation, et leur vitesse de conduction nerveuse (Bhuiyan et al., 2024). Les neurones des fibres A, de grand diamètre, présentent une vitesse de conduction rapide, tandis que ceux des fibres C, non myélinisés, ont une conduction lente. Aujourd'hui, les avancées en séquençage de l'ARN à cellule et noyau uniques permettent une classification plus précise basée sur l'expression génétique. Cependant, les variations techniques entre études compliquent

l'harmonisation des données, entraînant des incohérences dans le nombre de sous-types neuronaux identifiés et leur nomenclature, particulièrement entre espèces (Bhuiyan et al., 2024). Pour résoudre ces divergences, Bhuiyan et ses collaborateurs ont créé un atlas harmonisé des ganglions de la racine dorsale et des ganglions trigéminaux chez six espèces. Cet atlas regroupe 18 sous-types neuronaux distincts définis uniquement par des marqueurs génétiques moléculaires, indépendamment de leur physiologie cutanée. La nomenclature associe les gènes marqueurs aux espèces, aux types de fibres et, lorsqu'elle est connue, à leur fonction sensorielle. À ce jour, une fonction est attribuée à 15 sous-types neuronaux grâce à des modèles murins *knock-in* exprimant la recombinase Cre.

Les principaux groupes de neurones sensoriels sont les mécanorécepteurs à bas seuil (LTMR), les nocicepteurs peptidergiques (PEP), les nocicepteurs non peptidergiques (NP), les propriocepteurs et les thermorécepteurs. Les neurones des fibres A incluent divers sous-types définis par leur profil moléculaire et leur fonction : des propriocepteurs : exprimant *Pvalb* et *des m*écanorécepteurs Aβ à faible seuil (LTMR) , des mécanorécepteurs Aδ-LTMR des mécanorécepteurs à haut seuil (HTMR). Les neurones des fibres C incluent des nocicepteurs :, des thermorécepteurs au froid :, des mécanorécepteurs C-LTMRs :, des pruricepteurs : et des nocicepteurs spécifiques aux blessures. Ces classifications sont dynamiques et devraient s'affiner avec l'émergence de nouvelles technologies de séquençage et d'analyses.

Dans cette thèse, les annotations neuronales adoptent la nomenclature de Jung et al. (2023), établie via une stratégie de séquençage monocellulaire utilisant la plateforme *10x Genomics*. Leur étude a identifié 11 groupes transcriptionnellement distincts de neurones sensoriels chez la souris :

- Propriocepteurs.
- Aβ LTMRs : RA-LTMRs et SA-LTMRs.
- Aδ-LTMRs.
- C-LTMRs.
- Thermorécepteurs du froid.
- Nocicepteurs non peptidergiques : NP1, NP2, NP3.
- Nocicepteurs peptidergiques : PEP1, PEP2, PEP2.3.

Cette classification a été étendue à d'autres espèces, dont le cochon d'Inde, le singe *Cynomolgus* et l'homme, pour construire un atlas inter-espèces des neurones sensoriels.

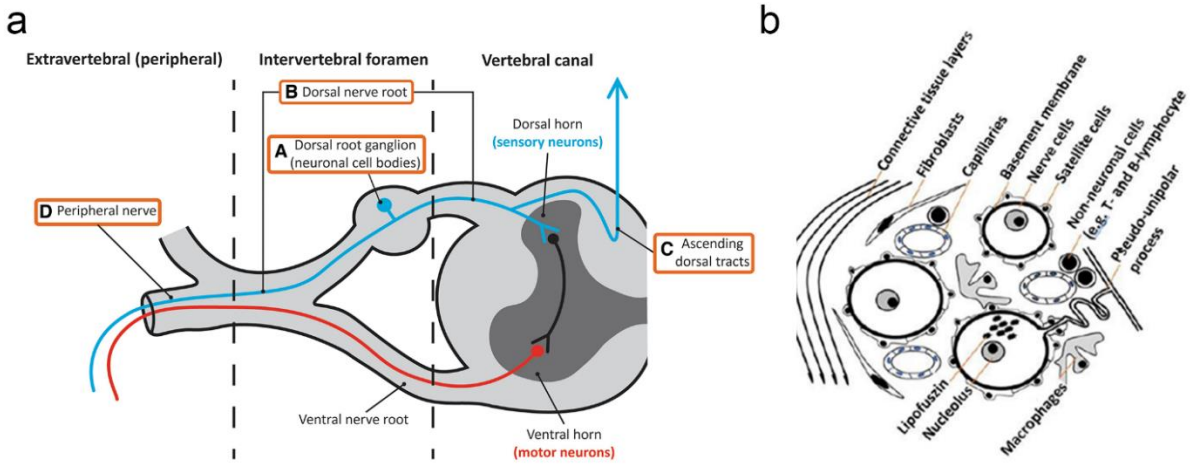

Figure 4 : Neuroanatomie des ganglions de la racine dorsale et des composants connexes du système nerveux. a. Les prolongements des neurones sensoriels s'étendent dans le système nerveux central, dans la corne dorsale et vers la périphérie. Figure adaptée de Hordeaux et al, 2020 b. Types de cellules présentes dans les ganglions de la racine dorsale. La figure est adaptée de Haberberger et al. 2019.

Le DRG et le système sensorimoteur

Le système sensorimoteur est constitué de neurones moteurs et sensoriels situés dans le cerveau, la moelle épinière, et les DRG. Ils jouent un rôle crucial dans la locomotion. Les informations sensorielles telles que la pression, la chaleur, la proprioception et la nociception, provenant de la périphérie, sont transportées vers la moelle épinière, puis remontent vers le cerveau où elles sont intégrées et traitées dans le cortex somatosensoriel et le cortex moteur (Kaas, 2012). La réponse motrice est alors générée dans le cerveau ou la moelle épinière, conduisant à la contraction des muscles via les nerfs efférents (Flanders, 2011). Les muscles sont contrôlés par des unités motrices, qui comprennent un neurone moteur et le faisceau de fibres musculaires qu'il innerve. Les fuseaux neuromusculaires et les organes tendineux de Golgi, présents dans les muscles, fournissent des informations proprioceptives (Tuthill & Azim, 2018). Les fuseaux neuromusculaires détectent l'étirement du muscle, tandis que les organes tendineux de Golgi détectent la tension musculaire. Ces organes spécialisés induisent des potentiels d'action sensoriels dans les nerfs afférents, qui activent ou inhibent les motoneurones pour contrer une extension ou une flexion excessive du muscle. Les muscles sont organisés en groupes et fonctionnent par paires agonistes et antagonistes, permettant ainsi une coordination efficace de la contraction et de la relaxation musculaires. Une lésion des neurones sensoriels et moteurs, ainsi que de leurs fibres, perturbe la régulation de la contraction musculaire, ce qui peut entraîner une atrophie, une faiblesse ou une paralysie musculaire, comme observées dans de nombreuses maladies neurodégénératives. Ces altérations affectent à leur tour la locomotion et le comportement de marche.

Toxicité dans le DRG induite par l'AAV dans les modèles animaux.

La toxicité dans le DRG après l'administration d'AAV a bien été documentée chez les primates non-humains (PNH) (Hordeaux, Buza, Dyer, et al., 2020 ; Johnson et al., 2023 ; Tukov et al.,

2022) (Hawley et al., 2024). Les PNH sont souvent considérés comme le modèle le plus sensible pour l'étude de cette toxicité. Toutefois, des cas de toxicité dans les DRG ont également été observés chez d'autres espèces animales, notamment les porcs (Hinderer et al., 2018), les lapins (Tien et al., 2024), et les rongeurs (Fader et al., 2022 ; Tyszkiewicz et al., 2024). La pathologie observée varie généralement de minime (moins de 10 % des neurones et axones affectés) à modérée (25-50 %), et est caractérisée comme transitoire ou aiguë, se résolvant avec le temps. Cette toxicité est souvent associée à des titres élevés d'AAV neurotropes, tels que l'AAV9, et se manifeste lorsque l'AAV est administré soit par voie systémique, soit dans le LCR. L'administration intrathécale (dans le LCR) est entraine une gravité plus élevée et une incidence accrue des lésions des DRG. Les neurones sensoriels sont fortement transduits. Les résultats histopathologiques suivants ont été observés dans les modèles animaux :

1. Dégénérescence des corps cellulaires neuronaux : diminution de la taille du soma et morphologie irrégulière, formation de corps de Nissl dans les neurones.

2. Infiltration de cellules mononucléaires : observée chez les PNH, les porcelets et les lapins. Cependant, les rongeurs présentent une cellularité accrue sans infiltration de cellules mononucléaires.

3. Dégénérescence axonale dans la racine dorsale du nerf : axonopathie caractérisée par une dilatation de la gaine de myéline avec ou sans myélomacrophages.

4. Dégénérescence axonale centrale dans le funicule dorsal de la moelle épinière : axonopathie bilatérale et dilatation de la myéline dans les voies nerveuses sensitives de la substance blanche de la moelle épinière.

5. Une prolifération gliale réactive se produit sur le site de la dégénérescence neuronale. Augmentation de la population et du nombre de cellules gliales.

6. Dégénérescence axonale des nerfs périphériques : axonopathie du nerf sciatique et du nerf saphène caractérisée par une dilatation de la gaine de myéline.

Outre la dose d'AAV et la voie d'administration, le vecteur lui-même avec ses composants (promoteurs, produit génique thérapeutique, éléments transcriptionnels) peut jouer un rôle crucial dans la toxicité au niveau des DRG. L'âge des animaux peut également avoir un impact sur la toxicité, les jeunes primates non-humains montrant une sévérité moindre des lésions.

Les lésions des DRG ne sont pas uniformes et peuvent être unilatérales ou bilatérales. Tous les niveaux des DRG sont concernés par cette toxicité (Hordeaux, Buza, Dyer et al., 2020). Bien que les mécanismes sous-jacents restent mal compris, une hypothèse dominante suggère qu'une transduction excessive des neurones sensoriels provoque des lésions cellulaires dues à la surexpression du transgène (Hordeaux, Buza, Jeffrey et al., 2020). Ces lésions semblent déclencher un processus de dégénérescence, comme l'indiquent les observations histopathologiques. Les dommages neuronaux résultants pourraient alors induire des réponses immunitaires pro-inflammatoires, aggravant ainsi la pathologie.

Lors d'une lésion axonale ou d'une dégénérescence neuronale les neurofilaments sont libérés, potentiellement en quantités importantes. La chaîne légère des neurofilaments (NfL) (ou Nf-Light) est une protéine de filament intermédiaire du cytosquelette de 68 kDa exprimée dans les axones. La NfL s'associe au Neurofilament moyen (NfM) de 125 kDa et au Neurofilament lourd (NfH) de 200 kDa pour former les neurofilaments. Ce sont des composants majeurs du cytosquelette neuronal et on pense qu'ils ont pour fonction principale de fournir un soutien structurel à l'axone et de réguler le diamètre de l'axone. Une élévation des NfL dans le LCR et le sérum est détectée dans de nombreux modèles animaux précliniques de neurodégénérescence, ce qui est essentiel pour suivre la progression de la maladie (Loeffler et al., 2020).. Bien que NfL soit un biomarqueur de toxicité non spécifique du DRG, les niveaux

de neurofilaments sériques sont en corrélation avec la gravité des résultats histopathologiques (Fader et al., 2022 ; Johnson et al., 2023, 2023 ; Tyszkiewicz et al., 2024). Cela permet d'utiliser le taux de NfL sérique comme indicateur de la toxicité dans le DRG dans les modèles animaux.

Réponses immunitaires aux AAV

La toxicité dans les DRG, notamment la dégénérescence neuronale, a été associée aux réponses immunitaires contre les vecteurs adéno-associés (AAV). La capside des AAV, les composants du vecteur, le transgène et les impuretés peuvent tous contribuer au risque d'immunogénicité des AAV. Les réponses immunitaires innées constituent la première ligne de défense et jouent un rôle crucial dans l'amorçage des réponses immunitaires adaptatives (Arjomandnejad et al., 2021 ; Muhuri et al., 2021 ; Shirley et al., 2020 ; T. Yang et al., 2022).

Dans les heures suivant l'administration d'AAV, des réponses immunitaires innées sont détectées en réponse aux vecteurs viraux. Il a été démontré que les AAV activent le système du complément et la signalisation des récepteurs Toll-Like, ce qui peut déclencher des cascades de réponses interféron conduisant à la libération de cytokines et de chimiokines.

À des doses élevées, les anticorps neutralisants préexistants (NAb) peuvent se lier aux AAV circulants et former des complexes NAb-AAV. Ces complexes NAb-AAV peuvent être détectés par le complexe C1, qui fait partie de la voie classique du complément, déclenchant ainsi les cascades en aval. Le clivage du complément C3 en C3a et C3b par la C3 convertase est essentiel pour les processus en aval qui conduisent à l'activation du complexe d'attaque membranaire (MAC). Le MAC crée des pores dans la membrane plasmique des agents pathogènes ou des cellules cibles, entraînant leur lyse osmotique. À faible dose, l'AAV peut également se lier directement au C3, ce qui entraîne l'activation du MAC. L'AAV lié au C3 peut directement

activer les macrophages et les cellules dendritiques déclenchant ainsi une réponse immunitaire humorale. Les macrophages, les cellules dendritiques et les neutrophiles peuvent également absorber le complexe NAb-AAV et augmenter la réponse inflammatoire en libérant des cytokines et des chimiokines pro-inflammatoires.

Le système immunitaire inné peut détecter les motifs moléculaires associés aux pathogènes (PAMP) dans les AAV par le récepteur Toll-like 2 (TLR2) à la surface des cellules et la reconnaissance par le TLR9 du transgène avec des dinucléotides CpG dans l'endosome. Les deux récepteurs activent l'adaptateur TLR Myd88, ce qui entraîne des cascades en aval qui déclenchent le NFkB et induisent des gènes de réponse à l'interféron de type 1 (IFN). Ces processus entraînent la libération de cytokines et de chimiokines pro-inflammatoires telles que le TNF, l'IL-1β et l'IFN α/β. L'IFN α/β se lie à l'IFNAR-1 dans les cellules de présentation de l'antigène (CPA), telles que les cellules dendritiques ou les macrophages, qui sont alors activées. Les CPA activées activent à leur tour les cellules T CD8+ cytotoxiques par présentation antigénique de peptides AAV sur le complexe majeur d'histocompatibilité de classe 1 (MHCI). Les CPA peuvent stimuler les cellules T CD4+ auxiliaires par la présentation d'antigènes de peptides AAV sur le MHCII. Les cellules T CD8+ cytotoxiques activées identifient et éliminent les cellules transduites par l'AAV en libérant des cytokines telles que l'IFNγ et le TNFα. L'immunité adaptative à long terme est assurée par les cellules T CD4+ auxiliaires qui amorcent les cellules B, ce qui favorise la formation d'anticorps contre l'AAV. Les réponses immunitaires adaptatives se produisent dans les jours/semaines suivant l'administration de l'AAV. Les cellules T régulatrices (Treg) peuvent moduler les réponses adaptatives à l'AAV par la libération de cytokines anti-inflammatoires. Les Tregs peuvent également promouvoir la tolérance au transgène exprimé, ce qui contribue à contrôler les réponses neuroinflammatoires résultant d'une expression à long terme. Des stratégies de

suppression immunitaire ont été employées dans des essais cliniques pour éviter et réduire les réponses immunitaires et prévenir les effets indésirables graves chez les patients.

Vecteurs AAV pour modéliser la toxicité dans le DRG chez la souris

Dans un rapport récent de Hawley et collègues (2024), les vecteurs AAV-miR-SOD1 et AAV-mCherry ont démontré une toxicité au niveau des DRG chez des souris C57BL/6J. Six semaines après l'injection intrathécale de ces vecteurs, des lésions histopathologiques sont apparues : une légère dégénérescence neuronale, une cellularité accrue et une chromatolyse dans les DRG lombaires. Les souris ayant reçu une injection d'AAV-mCherry présentaient des granules intracytoplasmiques éosinophiles, qui n'étaient pas observés chez les souris traitées par AAV-miR-SOD1. En outre, une dégénérescence axonale a été notée dans les nerfs sciatique et saphène, de manière plus marquée que dans les DRG. Des lésions du funicule dorsal, incluant une dilatation et une dégénérescence axonale, ont également été observées. Ces lésions étaient associées à une augmentation des taux de neurofilaments dans le sérum, 6 et 13 semaines après l'administration des vecteurs. La toxicité dans les DRG était aiguë, mais la gravité et l'incidence des lésions diminuaient généralement entre 6 et 9 mois après l'injection. L'analyse transcriptionnelle a révélé une proportion importante de gènes différentiellement exprimés à 6 et 13 semaines après l'injection. Parmi les gènes surexprimés, on trouve des gènes associés à la réponse immunitaire innée, en particulier le complément, ainsi que des gènes des cellules T à médiation cellulaire, De plus, plusieurs cytokines et chimiokines pro-inflammatoires étaient élevées dans les DRG, indiquant une réponse inflammatoire significative.

Ces résultats soulignent la nécessité de surveiller attentivement la toxicité des vecteurs AAV dans les études précliniques, en particulier en ce qui concerne les effets neurologiques et immunitaires.

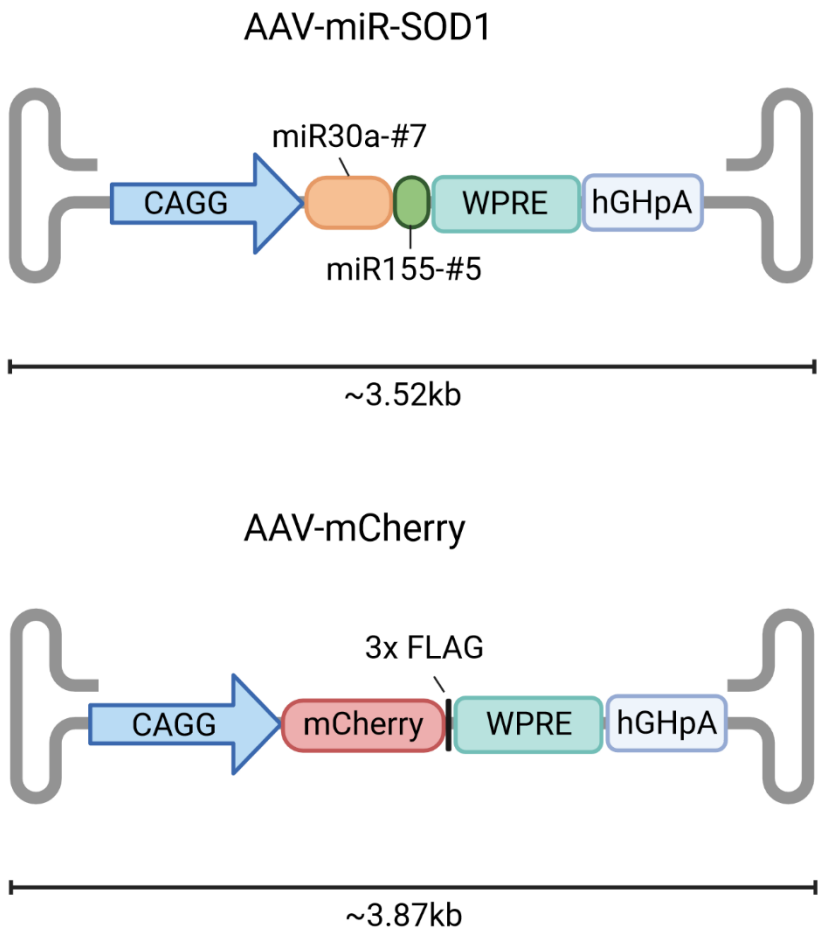

Figure 5 : Cartes vectorielles des vecteurs testés. Les transgènes ont été conditionnés dans l'AAV9. CAGG - élément enhancer du CMV, promoteur de la bêta-actine de poulet et gène intron. miR30a-#7 - microARN artificiel avec la séquence d'amorçage #7. miR155-#5 - microARN artificiel avec la séquence d'amorçage #5. WPRE - élément de régulation post-transcriptionnelle du virus de l'hépatite de la marmotte. hGHpA - queue poly A de l'hormone de croissance humaine. Les cartes vectorielles sont à l'échelle. Créé par Biorender.com

Objectifs et questions de recherche

De nombreuses études s'appuient sur l'histopathologie pour caractériser la toxicité dans les DRG après l'administration d'AAV. L'analyse histopathologique est descriptive et nécessite des pathologistes expérimentés pour détecter des changements minimes dans les DRG. Les coupes de tissus ne sont pas entièrement représentatives du DRG, d'où un risque de sous-estimation de la gravité de la toxicité. De plus, les cellules non abondantes et de petite taille ne sont pas faciles à analyser en histopathologie. Par conséquent, les méthodes quantitatives telles que les analyses transcriptomiques et protéomiques sont essentielles pour fournir une vue d'ensemble englobant tous les types cellulaires. Le séquençage de l'ARN a récemment été utilisé pour découvrir les profils d'expression de l'ARN dans le DRG. En outre, les phénotypes fonctionnels ont été rarement observés chez les patients et dans les études animales. Cette thèse a pour objectif de déterminer si des doses élevées d'AAV peuvent induire un phénotype physiologique et/ou comportemental cohérent chez la souris. Des doses comparables à celles utilisées dans les études sur des modèles animaux et en clinique (X. Chen et al., 2022 ; Fader et al., 2022 ; Johnson et al., 2023 ; Tukov et al., 2022 ; Tyszkiewicz et al., 2024) ont été administrées à des souris âgées de 6 semaines.

Deux objectifs clés

- Explorer les modifications transcriptionnelles spécifiques aux cellules dans le DRG dues à la toxicité induite par l'AAV. Identifier les principales signatures d'expression génique dans les neurones, la glie satellite, les cellules immunitaires et les voies enrichies pertinentes.

  Cet objectif a été atteint au chapitre 2. Dosage intrathécal de l'AAV et prélèvement de DRG lombaires pour l'isolement des noyaux et le séquençage de l'ARN d'un seul noyau.

- Examiner si les souris présentent des déficits fonctionnels, en particulier des altérations physiologiques et comportementales en réponse à la toxicité des DRG induite par l'AAV.

  Cet objectif a été atteint au chapitre 3-5. Des souris ont reçu par voie intrathécale des titres élevés d'AAV pour induire une toxicité DRG et ont été soumises à divers tests physiologiques et comportementaux.

La thèse est structurée comme suit : elle commence par une introduction générale au chapitre 1, suivie des chapitres autonomes 2, 3, 4 et 5. Chaque chapitre comprend des sections complètes, notamment l'introduction, les méthodes, les résultats et la discussion. Le chapitre 6 est centré sur une discussion générale, qui relie les principaux résultats de tous les chapitres et les développe davantage.

2. RESUME DES RESULTATS

2.1 Caractérisation transcriptomique de la toxicité induite par l'AAV dans le ganglion de la racine dorsale chez la souris (voir chapter 2)

Le séquençage de l'ARN est un outil précieux pour examiner les altérations du profil génétique dans les tissus; néanmoins, le profil transcriptomique représente une moyenne de tous les types cellulaires. L'objectif était d'explorer comment un vecteur AAV induit des changements transcriptomiques dans le DRG et d'élucider les interactions entre les différents types de cellules en réponse aux neurones lésés ou en dégénérescence. Le séquençage de l'ARN à noyau unique a permis d'étudier les changements spécifiques aux cellules dans le DRG et les principales voies modifiées dans chaque type cellulaire, ce qui a permis d'étudier la complexité biologique de cette toxicité. Des souris C57BL/6J de type sauvage (12 à 14 par groupe) ont reçu par voie intrathécale, à l'âge de 6 semaines, des doses d'AAV-miR-SOD1 à 5E11, 1,0E12 et 1,5E12 GC (Fig.1). Six semaines post-injection les DRG lombaires de chaque souris ont été prélevées pour l'isolement des noyaux et le séquençage. Le taux de neurofilament sérique (NfL) a été mesuré -1, 3-, et 6- semaines après l'injection pour suivre les lésions des DRG et des nerfs. Le taux de neurofilament sérique (NfL) a été utilisé comme indicateur de la toxicité dans le DRG malgré l'écart-type important des mesures de NfL sérique en fonction de la dose de vecteur AAV injecté. Pour éliminer la dispersion et la perte du signal d'expression génique, les souris ont été regroupées par quartiles de NfL (Q1 à Q4 allant du taux NfL faible au taux NfL élevé) par opposition à l'analyse basée sur la dose d'AAV.

Le nombre de noyaux après les filtrations était de 219 442 dans 11 groupes distincts représentés dans le graphique UMAP (Fig. 1). Les fibroblastes et la glie satellite représentaient ~50% de tous les noyaux suivis par les cellules de Schwann et les neurones. L'AAV a transduit les

neurones le plus efficacement à tous les niveaux de dose, avec ~65% des neurones transduits à la dose la plus élevée, 1,5E12 GC.

Sous-groupes et détermination des sous-types de neurones

Il existe différents types de neurones sensoriels dans le DRG, différenciés par leur physiologie (stimuli détectés), leur anatomie (degré de myélinisation et projections axonales) et les gènes marqueurs moléculaires (neurotransmetteurs, canaux ioniques, récepteurs couplés aux protéines G et facteurs de transcription) (Meltzer et al., 2021). Les noyaux neuronaux isolés ont été regroupés en 11 groupes distincts (Fig. 2). Les neurones sensoriels annotés correspondaient à trois types de mécanorécepteurs à bas seuil (AβRA-LTMR, Aδ-LTMR et C-LTMR), des thermorécepteurs au froid, trois types de nocicepteurs non peptidergiques (NP1 NP2, NP3), trois types de nocicepteurs peptidergiques (PEP1, PEP2.1, PEP2.2) et un groupe inconnu. Les populations de neurones sensoriels les plus importantes étaient Aβ RA-LTMR et NP1 dans toutes les répétitions biologiques.

Gènes activés différemment en réponse au traitement par AAV

La méthode informatique, NEBULA, a été utilisée pour effectuer l'analyse de l'expression différentielle pour chaque type de cellule par quartiles de NfL (Q2, Q3 et Q4) par rapport à Q1. Les souris du quartile 1 ne présentaient aucune toxicité pour le DRG, tandis que le quartile 4 représentait les animaux présentant une toxicité sévère pour le DRG (Fig.3)

Les nombres les plus élevés de gènes différentiellement exprimés ont été trouvés dans la glie satellite activée (1047), les macrophages (107) et les cellules T (98) dans la comparaison de NfL Q4 par rapport à Q1 (log2 fold change cutoff of 1.2 v FDR < 0,05) (Fig. 4a, Tableau S5). On a constaté que le nombre de gènes différentiellement exprimés augmentait par quartile. Il est intéressant de noter que les gènes différentiellement exprimés dans les neurones étaient minimes. De nombreux gènes différentiellement exprimés se chevauchent entre les quartiles,

comme dans le cas de la glie satellite activée, où 400 gènes ont été trouvés dans toutes les comparaisons (Fig. 4b). De plus, la glie satellite activée est probablement sensible aux lésions neuronales, car des altérations transcriptomiques importantes ont été observées dans le quartile 2 par rapport au quartile 1. De même, de nombreux gènes ont été trouvés altérés dans les macrophages et cependant moins dans les cellules T (Fig. 4c, d).

Les neurones subissent une mort cellulaire dans le DRG lésé

Un déclin brutal et spectaculaire a été observé dans les neurones : la médiane diminue de 14,39 % au NfL Q1 à 5,91 % au NfL Q4 (Fig. 4h). En se concentrant sur les gènes différentiellement exprimés, 41 gènes ont été identifiés. Un grand nombre de ces gènes sont associés aux processus de développement et de neurogenèse : Lrrc4c, Mir6236 ,Resf1 , Capsn1 , Gprasp2 ,Trpv1, Ncl et Tcp1 (Fig. 5a). Certains gènes sous-exprimés sont associés à la morphologie cellulaire et à l'organisation du cytosquelette - Cnn3, à l'intégrité axonale - Zfp36l2 , à la myélinisation - Gap1 et à la régulation de la baisse du canal potassique - Kcng2 (Fig. 5a). L'augmentation constante de l'expression des gènes de mort cellulaire dans les neurones (associée au terme biologique GO « Processus apoptotique des neurones ») était particulièrement évidente dans le NfL Q4, (voir Fig. 5b, c). Certains de ces gènes surexprimés , comme Bax, Cdk5 et Diablo, et des gènes down-régulés, comme Adnp, ont été observés (Fig. 5c). Après avoir identifié et quantifié dix sous-types neuronaux différents dans ces échantillons de DRG, il est devenu évident que tous les sous-types neuronaux déclinaient du NfL Q1 à Q4 (Fig. 5d). La population la plus importante, AβRA-LTMR, est passée d'une moyenne de 5,54 ± 2,10 % à 3,03 ± 1,89 % et la deuxième, NP1, est passée de 3,90 ± 1,03 % à 1,77 ± 0,97 % (Fig. 5d).

La glie satellite activée atténue les lésions des DRG induites par l'AAV

La glie satellite activée est apparue comme un nouveau groupe en réponse à la toxicité induite par l'AAV (Fig. 3h). Il s'agit du groupe qui présente le plus grand nombre de gènes différentiellement exprimés, en particulier lors de la comparaison Q4 vs. Q1, avec plus de gènes sous exprimés (697) que de gènes surexprimés (350) (Fig. 4a, Tableau S5). Pour approfondir l'étude de ces gènes, l'analyse d'enrichissement de l'ensemble des gènes a été utilisée pour déterminer les voies et les processus biologiques modifiés. Un enrichissement robuste du processus « neurogenèse » ainsi que d'autres processus tels que la « migration cellulaire » ont été observés (Fig. 6a). L'analyse pseudo-bulk des gènes du processus de neurogenèse a montré une augmentation constante d'un sous-ensemble de gènes chez les souris NfL Q2, Q3 et Q4 et une diminution importante d'un autre sous-ensemble (Fig. 6b). Il est intéressant de noter que les gènes surexprimés présentaient des niveaux d'expression similaires entre les souris NfL Q2 et Q4. Une tendance similaire a été observée pour le processus de migration cellulaire. L'étude d'un sous-ensemble de ces gènes dans la glie satellite activée a révélé une forte expression de Dok4, Gdnf et Wnt10b, des gènes importants pour la croissance des neurites et le développement neuronal (Fig. 5d). La cytokine du système nerveux central, Tafa2, qui joue un rôle essentiel dans la survie des neurones, était également fortement exprimée dans les cellules gliales satellites et les neurones activés (Fig. 5d). D'autres exemples de gènes fortement régulés dans la glie satellite activée sont connus pour être essentiels à la prolifération, à la différenciation et au guidage axonal : Nrcam, Epha5, Tgfbi, Ngfr et Runx2 (Fig. 6e). D'autre part, certains exemples de gènes sous exprimés comme Adam23, Nrp2, Sema6d, Plce1 et Ntrk2 sont essentiels au guidage axonal, à la prolifération et à la différenciation, ainsi qu'à la migration cellulaire. En résumé, la proportion de glie satellite activée augmente et les processus associés au neurodéveloppement, au guidage axonal et à la différenciation sont significativement affectés après une lésion neuronale et une dégénérescence axonale.

Dans le DRG de la souris, dans le groupe des macrophages trois marqueurs cellulaires ont été identifiés Cx3cr1 des monocytes, Mrc1 des macrophages anti-inflammatoires (M2) et Cd86 des macrophages pro-inflammatoires (M1) (Fig.7a). Un changement dans l'expression des gènes spécifiques des monocytes et des macrophages a été observé entre les NFL Q1 et Q4. Un sous-ensemble de gènes spécifiques aux monocytes est sous exprimé entre les NFL Q1 et Q4, tels que Csf1r et Ccr2 (Fig. 7b). Il est intéressant de noter que les marqueurs anti-inflammatoires des macrophages (M2), tels que Cd163 et Irf4, étaient également sous exprimés, ce qui coïncidait avec la surexpression des signatures génétiques des macrophages pro-inflammatoires (M1), Cd80 et Cd38 (Fig. 7c, d). Il y a eu une diminution de l'expression de Tlr4, ce qui indique que tous les marqueurs n'ont pas été uniformes ou n'ont pas évolué dans la même direction. Un sous-ensemble de gènes de la cascade des récepteurs Toll like (TLR) a été sous exprimé dans les macrophages, indiquant la détection de l'AAV et l'activation des acteurs de la signalisation en aval. En ce qui concerne le système d'activation du complément, seul un sous-ensemble de gènes présentait une tendance à l'augmentation, notamment C4b, C6, Itgax, C1qc, C1qb, qui sont des composants du système classique du complément (Fig. 7f). Collectivement, ces changements dans les processus immunitaires innés ont activé le facteur nucléaire Kappa B (NF-kB) qui a conduit à l'augmentation de plusieurs chimiokines (Ccl5, Ccl22, Cxcl13) et cytokines (Il1a et Osm) (Fig. 7g). Ces chimiokines et cytokines libérées peuvent alors influencer le microenvironnement et activer/recruter d'autres cellules immunitaires telles que les cellules T pour initier la réponse immunitaire adaptative.

Des réponses immunitaires innées ont été observées dans les fibroblastes où un sous-ensemble de gènes de signalisation des récepteurs Toll-Like (TLR) a été surexprimé, comme Traf3, Tlr12, Tlr4, Tlr7, Ripk2 et Tnf (Fig. S3). Les composants des voies classiques du complément ont été notés de façon similaire aux macrophages, à l'exception du C3 qui n'était régulé que dans les fibroblastes (Fig. S4). Un large sous-ensemble de gènes de réponse à l'interféron (IFN) a été

surexprimé chez les souris NfL Q4, parmi lesquels Ifngr2, Myd88, Infnar2, Stat2, Stat1 et Jak1 (Fig. S5). Il est intéressant de noter que Myd88, qui est une protéine adaptatrice de la plupart des récepteurs TLR, n'était surexprimée que dans les fibroblastes et non dans les macrophages. De nombreuses cytokines et chimiokines ont été surexprimées dans les fibroblastes, ce qui renforce la réponse inflammatoire et contribue à l'activation de la réponse adaptative (Fig. S6).

Les cellules T induisent la réponse immunitaire à médiation cellulaire

Les cellules T jouent un rôle essentiel dans la réponse immunitaire adaptative et se coordonnent avec les macrophages pour remplir leurs fonctions. Dans cet ensemble de données, trois populations de cellules T devraient être présentes dans le groupe de cellules T : les cellules T CD8+ cytotoxiques (Cd8a), les cellules T CD4+ auxiliaires (Cd4) et les cellules T régulatrices (Foxp3) (Fig. 8a). L'expression de ces marqueurs a augmenté entre la NfL Q1 et Q4, ce qui coïncide avec l'augmentation de la population de cellules T entre Q1 (médiane de 0,81 %) et Q4 (médiane de 8,08 %) (Fig. 8b, Fig. 3h). Les gènes différentiellement exprimés détectés dans les cellules T dans la comparaison NfL Q4 vs. Q1 montrent une augmentation de l'activation lymphocytaire (Fig. 8c, d), avec un certain nombre de cytokines et de chimiokines telles que Ccl3, Cxcl9, Il21, Il10, Ifng et Ccl5 surexprimées chez les souris NfL Q4 (Fig. 8e).

En résumé, la réponse immunitaire des macrophages, des fibroblastes et des cellules T était évidente avec l'expression d'une multitude de cytokines et de chimiokines contribuant à l'inflammation dans le microenvironnement du DRG et jouant probablement un rôle dans la réponse aux neurones lésés et en dégénérescence.

2.2 EXPLORATION DES POTENTIELS D'ACTION DU NERF SCIATIQUE EN RÉPONSE À LA TOXICITÉ INDUITE PAR L'AAV DANS LE DRG (VOIR CHAPTER 3)

L'objectif de cette étude est d'évaluer si les lésions du nerf sciatique induites par l'AAV affectent les propriétés de conduction du nerf sciatique. Des études antérieures ont indiqué que les lésions du nerf sciatique entraînent un ralentissement de la vitesse de conduction, qui se manifeste par une augmentation de la latence des potentiels d'action (Büttner et al., 2018). Afin de mesurer l'effet de la toxicité sur le nerf sciatique, des souris (n = 12 à 14) ont reçu une injection intrathécale d'une dose élevée de 1,5E12 GC d'AAV-miR-SOD1. Des enregistrements extracellulaires des potentiels d'action du nerf sciatique ont été effectués sur une période prolongée. Les latences des minima et maxima des ondes biphasiques ont été analysées. Pour suivre longitudinalement le potentiel d'action du nerf sciatique de manière non invasive et minimiser l'impact sur les animaux étudiés, les électrodes ont été placées sous la peau avec une pénétration limitée dans le muscle. Pour obtenir des enregistrements cohérents, les électrodes de stimulation et d'enregistrement ont été ajustées afin de générer des formes d'ondes comparables chez toutes les souris (Fig. 2a).

La réponse biphasique du potentiel d'action enregistrée représente la somme des potentiels d'action des axones individuels. La latence moyenne aux minima pour toutes les souris , se situe entre 1,0 et 1,5 millisecondes sans tendance claire observée quel que soit le groupe expérimental (Fig. 2c). La latence moyenne aux maxima est d'environ 1,5 à 2,0 millisecondes (Fig. 2d) dans tous les groupes de traitement. Trois semaines après l'injection, les latences aux minima et maxima augmentent par rapport au groupe témoin, mais cette augmentation n'est plus observée six semaines après l'injection (Fig. 2c, d).

L'amplitude du potentiel d'action, mesurée entre les minima et les maxima de l'onde biphasique, varie et présente un écart-type important. Trois semaines après l'injection, l'amplitude moyenne du potentiel d'action était de 2,39 ± 1,46 mV pour les souris traitées avec l'AAV, contre 1,07 ± 0,23 mV pour les souris traitées avec le véhicule (Fig. 2e). Cependant, cette augmentation de l'amplitude n'était pas observée six semaines après l'injection, bien que les valeurs de base pour les souris traitées avec l'AAV soient plus élevées que celles du véhicule

La toxicité dans le nerf sciatique peut être variable et incohérente, c'est pourquoi les données ont été regroupées par sexe et par côté anatomique (Hawley et al. 2024).

Chez les mâles, la latence aux minima est similaire pour les souris traitées avec l'AAV et celles traitées avec le véhicule, variant de 1,0 à 1,5 millisecondes (Fig. 3a). Bien qu'un changement de latence aux maxima puisse être observé à 3 et 6 semaines après l'injection, ce n'est pas significatif (Fig. 3b). L'amplitude présente un écart-type important et on n'observe pas de différence entre les souris traitées avec l'AAV et celles traitées avec le véhicule (Fig. 3c).

Chez les femelles, les latences aux minima et aux maxima sont similaires entre les souris traitées avec l'AAV et celles traitées avec le véhicule (Fig. 3d, e). L'amplitude est plus élevée chez deux souris femelles traitées avec l'AAV, ce qui augmente la moyenne pour ce groupe (Fig. 3f).

Pour le nerf sciatique droit, les latences aux minima et aux maxima sont similaires entre les souris traitées avec l'AAV et celles traitées avec le véhicule (Fig. 4a, b). Cette tendance est également observée pour le nerf sciatique gauche (Fig. 4d, e). Les amplitudes des nerfs sciatiques droit et gauche sont plus élevées chez les souris traitées avec l'AAV comparé à celles traitées avec le véhicule, avec un écart-type important (Fig. 4c, e). Cependant, les nerfs sciatiques droit et gauche ne montrent pas de tendance caractéristique en réponse à

l'administration de l'AAV. Pour l'analyse en fonction du sexe et du côté enregistré, le nombre d'animaux est insuffisant pour des résultats significatifs.

2.3. EVALUATION DE LA CAPACITÉ MUSCULAIRE DES MEMBRES POSTÉRIEURS APRÈS ADMINISTRATION INTRATHÉCALE D'AAV (VOIR CHAPTER 4)

L'objectif de ce rapport est d'étudier les effets des AAV sur les contractions musculaires et la conduction du signal dans les membres postérieurs. Pour cela, des AAV ont été administrés par voie intrathécale à des souris. Nous avons mesuré le potentiel d'action musculaire et la force musculaire générée par le pied afin d'examiner en détail le couplage excitation-contraction et la fonction neuromusculaire (Zhao et al., 2017).. Diverses analyses de corrélation ont été effectuées pour étudier la relation entre le taux de NfL sérique, le potentiel d'action musculaire composé (CMAP) et la faiblesse musculaire des membres postérieurs.

L'AAV-miR-SOD1 augmente le taux de neurofilament sérique

Dans cette étude, des souris (N=8 par groupe) ont été injectées par voie intrathécale à l'âge de six semaines avec deux doses différentes, 8E11 et 1,6E12 GC, d'AAV-miR-SOD1, ainsi qu'une dose de 1,6E12 GC d'AAV-mCherry. Les souris ont été soumises à deux évaluations physiologiques à différents moments, accompagnées de prélèvements sanguins (Fig.1a) pour mesurer le degré de lésion des DRG et des nerfs périphériques. Les taux de NfL ont augmenté quatre semaines après l'injection, atteignant 1900 ± 800 pg/mL chez les souris traitées avec 8E11 GC et 2197 ± 1324 pg/mL chez celles traitées avec 1,6E12 GC d'AAV-miR-SOD1 (Fig. 1b, c). Les taux de NfLt étaient plus bas chez les souris traitées avec 1,6E12 GC d'AAV-

mCherry (Fig. 1b, c). Comme démontré précédemment, les taux de NfL diminuent au cours des 12 semaines suivant l'injection.

L'AAV-miR-SOD1 réduit la force musculaire dans les membres postérieurs.

Deux enregistrements physiologiques principaux ont été réalisés pour évaluer la santé des nerfs et des muscles chez les souris traitées par l'AAV (Fig. 1a). Le potentiel d'action musculaire composé (CMAP) a été utilisé pour évaluer la fonction des axones moteurs du nerf sciatique et des jonctions neuromusculaires. Une réduction de l'amplitude du CMAP indique une neurodégénérescence (McCampbell et al., 2018 ; Weng et al., 2021).

Le nerf sciatique a été stimulé et des électromyogrammes ont été enregistrés à partir du muscle tibial antérieur. L'activité CMAP moyenne se situait entre ~60-80 mV pour toutes les souris, avec une réduction significative observée chez les souris traitées avec 8E11 GC d'AAV-miR-SOD1 à 11 semaines post-injection (p.i.) par rapport aux souris traitées avec le véhicule (Fig. 2a-c). Les valeurs CMAP corrigées par rapport à la ligne de base ont également montré cette relation, les souris traitées avec 8E11 GC d'AAV-miR-SOD1 se situant en dessous de la ligne de base (Fig. 2d).

Le nerf tibial a été stimulé pour générer une force de flexion plantaire, principalement due à la force du muscle gastrocnémien. Toutes les souris ont montré une augmentation de la force musculaire normalisée tout au long de l'étude, ce qui était attendu en raison de l’avancée en âge des souris. Cependant, les souris traitées par AAV présentaient une force plus faible à 12 semaines post-injection par rapport aux souris traitées avec le véhicule, bien que cette différence ne soit pas significative (Fig. 2e-g).

2.4. EVALUATION DU COMPORTEMENT MOTEUR (VOIR CHAPTER 5)

L'AAV-miR-SOD1 entraîne une réduction dose-dépendante de la survie.

Les souris (N=12 par groupe) ont reçu par voie intrathécale, en bolus, l'AAV-miR-SOD1 à des doses de 8E11 GC, 1,2E12 GC et 1,6E12 GC à l'âge de 6 semaines. Les souris ont ensuite été soumises à une batterie de tests comportementaux, comprenant l'open field, le test de crispation des membres postérieurs (clasping), le test de préhension et l'analyse de la marche. Ces tests ont été effectués à des moments distincts pour minimiser le stress et permettre un temps de récupération adéquat (Fig. 1a).

Les niveaux sériques de (NfL ont atteint environ 2000 pg/mL chez les souris traitées par AAV-miR-SOD1 comparativement au groupe véhicule, 3 semaines après l'injection (p.i.) (Fig. 1b). Le pic de NfL a été observé à 3 semaines p.i. pour la majorité des souris, indiquant une relation transitoire et une réduction substantielle de la survie après 7 semaines p.i. (Fig. 1c). Le poids corporel moyen des souris traitées par 1,2E12 GC et 1,6E12 GC d'AAV-miR-SOD1 était inférieur à celui des souris traitées au véhicule, malgré une supplémentation en gel alimentaire pendant toute la durée de l'étude (Fig. 1d). La survie médiane des souris traitées par 1,6E12 GC et 1,2E12 GC d'AAV-miR-SOD1 était respectivement de 105 et 170 jours (Fig. 1e). Ces résultats ont montré une réduction significative et dose-dépendante de la survie des souris (test de Long-rank, **P<0,01, ***P<0,001) (Fig. 1e). L'injection d'AAV-miR-SOD1 a induit des lésions neuronales et nerveuses, entraînant une diminution du poids corporel et de la survie.

L'AAV-miR-SOD1 modifie les mesures clés de l'open field chez les souris traitées

Le test en openfield est couramment utilisé pour évaluer le comportement exploratoire, la locomotion et les comportements de type anxieux chez les souris. Il permet également d'évaluer la tolérance et la sécurité de nouveaux médicaments chez la souris (Hutter-Saunders et al.,

2012). Dans cette étude les souris ont été placées dans l'arène pour explorer librement pendant 30 minutes. Les mesures de la distance parcourue, du temps passé au centre, du temps de toilettage et du temps de redressements ont été recueillies.

On observe une diminution de la distance parcourue chez toutes les souris traitées par AAV-miR-SOD1 3 semaines p.i. (Fig. 2a). À 13 semaines p.i., les souris traitées avec 1,2E12 GC AAV-miR-SOD1 ont parcouru une distance significativement plus courte que les contrôles, 512,2 ± 281,8 cm contre 1017,4 ± 212,2 cm (analyse des effets mixtes suivie du test de comparaisons multiples de Bonferroni ; **P<0,01) (Fig. 2a). La tendance est la même pour les souris traitées par 1,6E12 GC AAV-miR-SOD1, mais ce n'est pas significatif car le nombre de souris est restreint (n=3). Pour le temps passé au centre de l'arène, on observe une différence non significative en fonction de la dose reçue entre les contrôles et les traitées à 13 semaines p.i (Fig. 2b).

L'activité de toilettage chez les souris traitées aux doses 1,2E12 GC et 1,6E12 GC a augmenté par rapport aux contrôles à 13 semaines p.i. (Fig. 2c). Le temps moyen de toilettage pour la dose de 1,2E12 GC (535,9 ± 450,7 sec) et pour la dose de 1,6E12 GC (528,8 ± 702,3 sec) était significativement plus long que pour les témoins (94,5 ± 702,3 sec) (analyse des effets mixtes suivie du test de comparaisons multiples de Bonferroni ; **P<0,01, ***P<0,001).

La durée des redressements était également significativement réduite chez toutes les souris traitées par AAV-miR-SOD1 à 13 semaines p.i. (analyse des effets mixtes suivie du test de comparaisons multiples de Bonferroni ; *P<0,05, **P<0,01, ***P<0,001) (Fig. 2d). Les souris traitées avec 1,2E12 GC d'AAV-miR-SOD1 ont montré un temps moyen de redressement de 99,2 ± 45,9 secondes, contre 192,8 ± 83,4 secondes pour les témoins (analyse des effets mixtes suivie du test de comparaisons multiples de Bonferroni ; ***P<0,001).

En conclusion, l'administration d'AAV-miR-SOD1 modifie significativement les comportements observés en open field, avec des souris parcourant des distances plus courtes et présentant une réduction du comportement de redressement.

Les souris présentent des déficits de la force musculaire et de la crispation des membres postérieurs

Des études antérieures ont révélé que les souris traitées par AAV-miR-SOD1 présentent une faiblesse caractéristique, particulièrement marquée au niveau des membres postérieurs. Pour évaluer ce phénomène, le test de préhension a été utilisé pour mesurer la force musculaire des membres. Les souris ont été placées de manière à saisir une maille reliée à un capteur de force, puis tirées par la queue pour enregistrer la force exercée. Les résultats montrent une réduction significative de la force de préhension normalisée par rapport au poids corporel à tous les niveaux de dose d'AAV-miR-SOD1 (analyse des effets mixtes suivie du test de comparaisons multiples de Bonferroni ; **P<0,01, ***P<0,001) (Fig. 3a,b).

À 9 semaines post-injection (p.i.), les souris traitées avec le véhicule ont conservé un score moyen normalisé de force de préhension de 6,65 ± 0,46 gForce/poids corporel, contre 4,99 ± 1,40 gForce/poids corporel pour celles traitées avec la dose 8E11 GC, 5,82 ± 0,69 gForce/poids corporel pour la dose 1,2E12 GC, et 4,68 ± 0,93 gForce/poids corporel pour la dose1,6E12 GC (Fig. 3a,b). La faiblesse musculaire observée était indépendante de la dose administrée mais la faiblesse était progressive au sein de chaque groupe

Ces résultats indiquent que l'administration d'AAV-miR-SOD1 induit une faiblesse musculaire notable, affectant particulièrement la force de préhension des membres postérieurs.

Les souris traitées par l'AAV-miR-SOD1 ont développé un comportement de crispation, un déficit neurologique qui est généralement observé dans les modèles de souris neurodégénératifs

(Lalonde & Strazielle, 2011). Ce comportement de rétraction des membres postérieurs s'est aggravé de manière dose-dépendante entre les semaines 3 et 15 post-injection (p.i.) (Fig. 3c-f). Pour les souris traitées avec la dose 8E11 GC d'AAV-miR-SOD1, le score médian de crispation est resté à ≤2 entre les semaines 3 et 11 p.i. (Fig. 3d). En revanche, pour les souris traitées avec la dose 1,6E12 GC, le score médian de crispation à augmenter rapidement, passant de 2 (3 semaines p.i.) à un score de 4 (9 semaines p.i). (Fig. 3f, Fig. S1). Toutes les souris traitées avec la dose la plus élevée (1,6E12 GC) ont maintenu un score de crispation de 4 entre les semaines 9 et 15 (Fig. 3f, Fig. S1).

Pour explorer la relation entre ces déficits fonctionnels et le marqueur NfL, une analyse de corrélation de Pearson a été réalisée. Le score de force musculaire à 5 semaines p.i. était modérément corrélé avec le score de crispation à 9 semaines p.i. (Pearson, R = -0,644), bien que la corrélation négative soit due à une relation bimodale, les souris étant réparties aux extrêmes opposés (Fig. 3g).

Le marqueur NfL était modérément corrélé à la force de préhension (Pearson, R = -0,609) (Fig. 3h). En revanche, on observe un lien entre des niveaux élevés de NfL et la crispation des membres postérieurs (Pearson, R = 0,799) (Fig. 3i). Toutefois, l'interprétation de cette corrélation doit rester prudente, car les groupes contrôle et traité à la dose 1,6E12 GC d'AAV-miR-SOD1 se situaient aux extrémités de la courbe (Fig. 3i).

Un résumé complet de toutes les corrélations de Pearson concernant la force musculaire, la crispation et NfL est présenté dans la figure S2 de ce rapport. En résumé, une forte diminution de la force musculaire et une détérioration progressive du comportement de crispation ont été observées en réponse à l'administration de l'AAV-miR-SOD1.

Les souris ne présentent aucun signe d'anomalie de la démarche

Le Catwalk XT est un outil complet capable de détecter des altérations subtiles des schémas de locomotion et est largement utilisé dans la recherche (Timotius et al., 2023). Les souris ont été placées individuellement sur une plaque de verre dans un couloir et leur déplacement vers leur point d'origine a été enregistré. Les souris ont été suivies pour diverses mesures de locomotion : temps d'attente debout, temps de balancement, vitesse de balancement, longueur de la foulée pour chaque patte, largeur de la foulée et position de la patte pour les membres antérieurs et postérieurs (Fig. 4a) (Pitzer et al., 2021). Les souris traitées par AAV-miR-SOD1 n'ont pas présenté de déficits caractéristiques dans le temps de station debout, le temps de balancement, la vitesse de balancement et la longueur de la foulée (Fig. 4b-e). En ce qui concerne la largeur de la foulée, certaines souris traitées par AAV-miR-SOD1 présentaient une foulée globalement plus large à 6 et 10 semaines p.i., mais ces résultats étaient mineurs et variables (Fig. 4f). Aucune tendance claire n'a été observée concernant la position de l'empreinte, bien que certaines souris traitées par l'AAV-miR-SOD1 aient présenté une position moyenne de l'empreinte droite supérieure à celle des contrôles (Fig. 4g). L'analyse de la démarche dépendait de la capacité des souris à accomplir la tâche. Le nombre de souris ayant échoué à la tâche a été noté (Fig. S3a). Un certain nombre de souris des groupes 8E11 GC et 1,6E12 GC n'ont pas réussi la tâche à 6, 10 et 18 semaines p.i. (Fig. S3a). Il est intéressant de noter que ces souris présentaient des niveaux de NfL supérieurs à la moyenne, ainsi qu'un clasping sévère (score = 4) à 9 semaines p.i.. Un résumé des paramètres clés pour ces souris est noté dans la figure S3b.

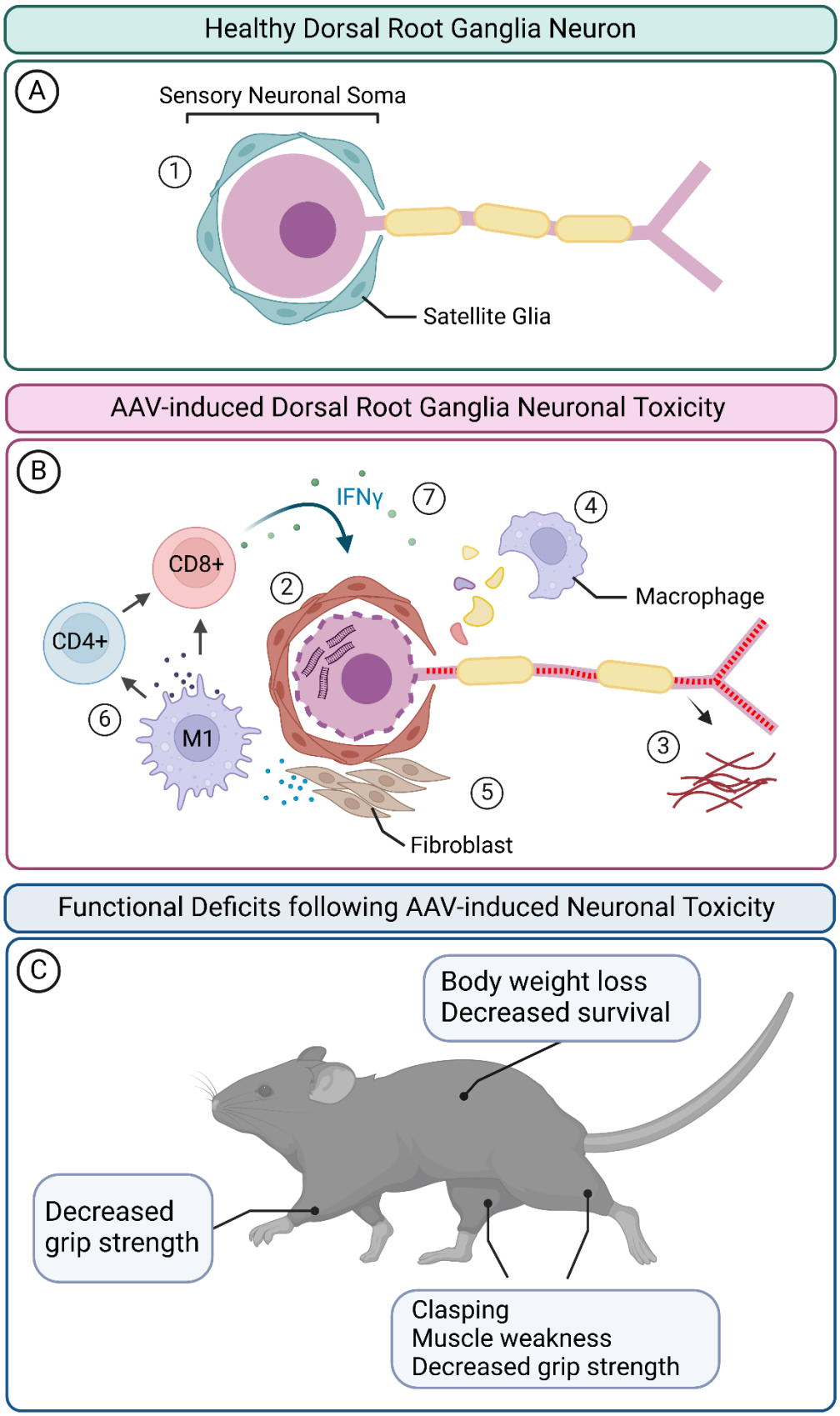
Healthy Dorsal Root Ganglia Neuron
A
Sensory Neuronal Soma
1
Satellite Glia
AAV-induced Dorsal Root Ganglia Neuronal Toxicity
B
IFNγ
7
CD8+
2
4
Macrophage
CD4+
6
M1
3
5
Fibroblast
Functional Deficits following AAV-induced Neuronal Toxicity
C
Body weight loss
Decreased survival
Decreased
grip strength
Clasping
Muscle weakness
Decreased grip strength

Figure 1 : *Résumé des résultats moléculaires et phénotypiques de la toxicité des ganglions de la racine dorsale induite par l'AAV chez les souris C57BL/6J. A. Neurone sain. [Chaque neurone sensoriel est enveloppé par des cellules gliales satellites]. B. Dégénérescence neuronale induite par l'AAV. [2] Neurone fortement transduit et dégénérant avec accumulation du produit du transgène. Prolifération et activation des cellules gliales satellites en réponse à la lésion et à la dégénérescence neuronales [3]. [Dégénérescence axonale et libération de lumière de neurofilament dans le LCR et le sérum. [Macrophage engloutissant les débris cellulaires et la myéline en réponse à la perte de cellules de Schwann]. [5] Prolifération des fibroblastes et libération de cytokines et de chimiokines. [6] Prolifération de macrophages pro-inflammatoires (M1), libération de cytokines et de chimiokines et induction de la réponse immunitaire adaptative. [Destruction potentielle à médiation cellulaire des neurones infectés]. C. Altérations comportementales et physiologiques consécutives à la dégénérescence des neurones sensoriels*

Déficits phénotypiques et fonctionnels

La toxicité d DRG induite par l'AAV a entraîné des modifications constantes de plusieurs mesures effectuées au cours de la vie des souris. Toutes les souris traitées à l'AAV ont reçu une supplémentation en gel alimentaire pour éviter une perte de poids et une euthanasie précoce. Des doses élevées d'AAV ont réduit de manière significative la survie dans les études de comportement et d'évaluation de la capacité musculaire. La faiblesse musculaire initialement observée dans les cages s'est traduite par une perte de force de flexion plantaire (chapitre 4) et par une diminution constante de la force musculaire (chapitre 5). La mesure de la force musculaire a été plus sensible que la force de flexion plantaire. En effet une réduction significative de la force musculaire a été observée 5 semaines après l'injection contre 12 semaines après l'injection pour la force de flexion. Enfin, le comportement de crispation est le phénotype le plus marquant chez toutes les souris traitées par AAV. Ce phénotype neurologique s'est manifesté très tôt et a progressé avec le temps. Il a été observé chez toutes les souris traitées 3 semaines après l'injection. Le comportement de crispation semblait dépendre de la dose, contrairement à d'autres mesures fonctionnelles. Ces déficits fonctionnels correspondent à certains phénotypes observés chez la souris (Alstyne et al., 2021) et d'autres espèces. Chez le lapin, une réduction du poids corporel, un manque d'activité, une faiblesse des membres postérieurs, une réduction du tonus musculaire, une incoordination ainsi que d'autres phénotypes ont été observés (Tien et al., 2024). L'administration d'AAV a entraîné une ataxie des membres postérieurs et l'euthanasie précoce des porcelets (Hinderer et al., 2018). En revanche toutes les études portant sur des rats et des primates non humains n'ont pas révélé de déficits fonctionnels (Fader et al., 2022 ; Johnson et al., 2023 ; Tukov et al., 2022).

Altérations moléculaires et dysfonctionnement sensorimoteur

Le séquençage de l'ARN à noyau unique a révélé une forte diminution de la population de neurones sensoriels et de cellules de Schwann dans le DRG. La perte de neurones sensoriels et de myélinisation contribue aux déficits physiologiques et comportementaux observés chez les souris. Les mécanorécepteurs jouent un rôle essentiel dans la proprioception, le toucher et la sensation de pression . Tous les types de mécanorécepteurs à bas seuil ont diminué en même temps que le reste des neurones sensoriels annotés dans le DRG dans l'étude snRNAseq (chapitre 2). La perte de neurones mécanorécepteurs réduit l'amplitude de l'entrée sensorielle requise pour une intégration correcte, processus nécessaire à une fonction motrice efficace. En outre, la dégénérescence axonale est également évidente dans les nerfs sensoriels, comme le montre la perte de myélinisation dans le DRG. Les études histopathologiques ont montré des dommages constants aux axones sensoriels dans la périphérie et au niveau central, ce qui a un impact négatif sur l'entrée sensorielle dans le SNC. Ces modifications anatomiques des neurones et des axones contribuent à la diminution de la force musculaire, des mesures de force de flexion et de la crispation dans les membres postérieurs des souris traitées par AAV. De nombreuses régions du cerveau, comme le cervelet, sont impliquées dans le comportement de crispation des membres postérieurs (Lalonde & Strazielle, 2011) mais le DRG est aussi impliqué. La perte de neurones proprioceptifs dans le DRG suite à l'administration d'AAV9 (codant pour le gène du motoneurone de survie) serait à l'origine du phénotype de crispation observé chez les souris (Alstyne et al., 2021). Chez une souris knock-out Hoxb8, la dégénérescence neuronale dans le DRG a entraîné une crispation des membres antérieurs et postérieurs (van den Akker et al., 1999). Chez la souris, une dégénérescence des fibres nerveuses du nerf sensitif saphène due à la toxicité du DRG a été récemment rapportée (Hawley et al., 2024).

Il est peu probable que les déficits fonctionnels observés dans cette thèse soient dus à la fonction motrice. En général, aucune altération anatomique ou morphologique n'a été rapportée dans les motoneurones à la suite de la toxicité induite par l'AAV dans le DRG. Les résultats histopathologiques dans toutes les espèces ont révélé une dégénérescence axonale du funicule dorsal sans aucun autre résultat dans les motoneurones ventraux (Fader et al., 2022 ; Hordeaux et al., 2018 ; Hordeaux, Buza, Dyer, et al., 2020 ; Tien et al., 2024). Une seule étude chez la souris a rapporté une réduction tardive de la taille et du nombre des motoneurones à l'âge de 10 mois dans la moelle épinière, phénomène lié à la surexpression du transgène (Alstyne et al., 2021). Dans le chapitre 3 de cette thèse, les mesures du potentiel d'action musculaire composé, connu pour sonder la fonction motrice, n'ont généralement pas été modifiées chez les souris traitées par AAV, ce qui suggère que les déficits fonctionnels sont probablement dus à une déficience sensorielle.

Mécanisme de fonctionnement chez la souris

Les résultats de la toxicité dans les DRG chez la souris sont probablement dus à la forte transduction des neurones sensoriels combinée à l'expression d'un produit transgénique nuisible. Un puissant promoteur constitutif entraîne l'expression du microARN duplex qui cible la SOD1 de la souris et de l'homme. Ces effets ne sont pas dus à la désactivation de la SOD1, car d'autres miR ciblant la SOD1 ont réduit efficacement la SOD1 chez les souris sans résultats phénotypiques. Des réponses immunitaires ont été détectées chez les souris et leur contribution à l'aggravation de la toxicité n'est pas connue. Dans des études antérieures sur les PNH, l'utilisation d'immunosuppresseurs n'a pas permis d'atténuer la toxicité dans les DRG et les auteurs ont conclu que la toxicité était due aux transgènes (Hordeaux, Buza, Jeffrey, et al., 2020 ; Hordeaux et al., 2018 ; Tukov et al., 2022). La réduction ciblée de l'expression du transgène dans le DRG réduit la gravité de la toxicité (Hordeaux, Buza, Jeffrey, et al., 2020). La perte de

corps cellulaires neuronaux entraîne la prolifération et l'activation de cellules gliales satellites, une dégénérescence axonale secondaire, la libération de neurofilaments dans le LCR et le sérum, une activation immunitaire et une fibrose. La perte d'une grande proportion de neurones, comme nous l'avons vu dans ce travail, provoque des déficits sensoriels qui affectent le système sensorimoteur, provoquant des déficits physiologiques et comportementaux.

Importance de la thèse

Cette thèse a caractérisé les profils d'expression génique de différentes populations de cellules dans le DRG et a révélé des altérations physiologiques et comportementales clés à la suite d'une lésion induite par l'AAV chez la souris. Il a été démontré qu'un changement significatif de la population cellulaire se produit après une toxicité induite par l'AAV et que des types de cellules clés jouent un rôle vital en réponse à une lésion du DRG induite par l'AAV. Malgré les résultats limités concernant les neurones, la glie satellite activée présente un profil d'expression génétique fort, caractérisé par des processus de régénération et de réparation. Les souris ont également montré une expression de gènes liés à l'immunité qui était comparable à celle d'études antérieures. Contrairement à d'autres animaux, les souris ont montré des changements fonctionnels cohérents, un outil précieux pour la détection phénotypique précoce de la toxicité dans les DRG. L'utilisation de souris a permis la polyvalence et la capacité d'effectuer des études statistiquement fiables sans nécessiter de ressources importantes.

Orientations futures

La prochaine étape de cette recherche vise à élucider quels sont les composants qui jouent un rôle critique dans l'apparition des lésions du DRG. L'utilisation de l'AAV9 permet une transduction efficace des neurones sensoriels, mais des études antérieures ont montré que la toxicité est induite par le transgène. Des éléments clés tels que la séquence promotrice jouent un rôle essentiel dans l'activation de la toxicité. L'utilisation de promoteurs ubiquitaires forts,

comme dans l'AAV-miR-SOD1 CAGG permet, , une expression élevée qui s'est révélée toxique dans une étude antérieure chez la souris (Alstyne et al., 2021). Il serait utile de déterminer si des promoteurs plus faibles ou modérés, tels que UBC et PGK, permettraient d'éviter la surexpression et la pathologie moléculaire. En outre, l'utilisation de différents modèles de cassettes d'expression (c.-à-d. cassette à transcription nulle, cassette à codage non protéique et cassette à codage protéique) permettrait d'obtenir un modèle d'étude plus complet. Il est certain que la conception pourrait également bénéficier d'un point temporel à plus long terme, tel que 12 ou 18 semaines après l'injection. Une autre stratégie consiste à utiliser des capsides neurotropes récemment découverts dans le DRG pour voir s'ils suffisent à réduire/éliminer la toxicité dans le DRG (Stanton et al., 2023). En outre, l'administration intrathécale dans toutes les études de cette thèse était une injection unique en bolus, ce qui pourrait contribuer à un écart-type important dans la sévérité de la toxicité chez les souris. Une perfusion lente de AAV pourrait potentiellement éliminer/réduire cette observation et également diminuer la sévérité de la toxicité (Rahman et al., 2023).

Table of Contents

List of Figures

List of Tables

List of Abbreviations

AAP	Assembly-activating protein
AAV	Adeno-associated virus
aCSF	Artificial cerebrospinal fluid
APC	Antigen presenting cell
C	Complement component
CAG/CAGG	Cytomegalovirus(CMV) early enhancer element, Chicken beta actin promoter and intron
CD	Cluster of differentiation
CMAP	Compound muscle action potential
CNS	Central nervous system
ddPCR	Droplet digital polymerase chain reaction
DEGs	Differentially expressed genes
DRG	Dorsal root ganglia
FC	Fold change
FDR	False discovery rate
FLAG	DYKDDDDK peptide protein tag
GC	Genomic copy
GSEA	Gene set enrichment analysis
hGHpA	Human growth hormone poly A tail
IFN	Interferon
IQR	Interquartile range
ITR	Inverted terminal repeat
LTMR	Low threshold mechanoreceptors
LNP	Lipid nanoparticle
M1	Pro-inflammatory macrophage
M2	Anti-inflammatory macrophage
MAAP	Membrane associated accessory protein
MAC	Membrane attack complex
mCherry	Reporter protein
MHC	Major histocompatibility complex
miR	Artificial microRNA
NfL/NFL	Neurofilament light chain
NfLq	Neurofilament light chain quartile
NP	Non-Peptidergic nociceptors
p.i.	Post-injection
PEP	Peptidergic nociceptors
Q	Quartile
ROA	Route of administration
SD	Standard deviation
snRNA-seq	Single nucleus RNA sequencing
SOD1	Superoxide dismutase 1 gene
TEM	Transmission electron microscopy
TLR	Tool like receptor
TPM	Transcripts per million

Treg	Regulatory T cell
UMI	Unique molecular identifier
VP	Major capsid protein
WPRE	Woodchuck Hepatitis Virus Posttranscriptional Regulatory Element

Chapter 1

General Introduction

Gene therapy

The idea of gene therapy originated in the 1960s, when scientists began developing genetically modified cell lines by introducing external genes. A novel approach in tackling disease emerged in a few decades with the first approved clinical study in the early 1990s (Blaese et al., 1995). Gene therapy is the delivery of an exogenous therapeutic gene into cells. Introduced genes could replace non-functional genes, silence genes, edit genes, and alter the expression of genes. This has enabled the possibly to treat challenging monogenic disorders, rare diseases, cancers, eye diseases, and others (Nóbrega et al., 2020). Unlike other modalities, gene therapy allows for precision and targeted approach with a potential for permanent or long-lasting correction. This focused strategy proves advantageous in minimizing side effects while presenting the potential for tailored medical treatments. Generally, gene therapy is divided into in-vivo and ex-vivo approaches. In-vivo gene therapy involves the introduction of genes directly into the patient's body. Ex-vivo gene therapy involves the removal of cells from a patient, these cells are then modified by the introduction of a therapeutic gene. The modified cells are then introduced into the patient. There are currently 36 FDA approved gene therapies with *in vitro* therapies making the bulk of all approvals. (*Approved Cellular and Gene Therapy Products*, 2024).

Vehicles of gene therapy

A primary challenge in gene therapy revolves around the vehicle in which a gene is introduced into a host. Varied administration strategies may be necessary for specific diseases. The overall approach relies on targeting specific cells and tissues. Two main delivery strategies are used: non-viral and viral vectors.

Non-viral vectors

Non-viral vectors use chemical or physical methods to introduce a gene into a host. Physical methods such as microinjection, electroporation, magnetoporation, sonoporation, ballistic gun

and others are used (Nóbrega et al., 2020). Chemical-based methods include liposomes, various nanoparticles and polymers. One of the most commonly used non-viral vehicle is lipid nanoparticles (LNP). Lipid nano particles are biocompatible, stable and capable of protecting nucleic acids. Both, the Moderna and Pfizer COVID-19 vaccines make use of LNPs to deliver mRNA cargo into cell. Non-viral methods offer improved safety with reduced immunogenicity, reduced cytotoxicity and potential for enhanced cell specificity. Non-viral vectors also offer flexibility in design with no cargo limitation relative to viral vectors. However, non-viral vectors suffer from reduced efficiency relative to viral vectors.

Viral vectors

Viruses serve as the primary vectors for gene therapy, enabling efficient transduction of target cells and tissues. Numerous vectors have been utilized, including Adeno-associated virus (AAV), lentivirus, adenovirus, herpes simplex virus, among others. Viral vectors are composed of the protein capsid that encapsulates the genetic cargo, the therapeutic gene carried along with the expression (i.e. enhancers, promoters), and regulatory elements (i.e. post-transcriptional elements and polyadenylation signal) (Bulcha et al., 2021). Viruses can be enveloped, i.e. lentivirus or naked such as AAV. Viruses suffer from a lower safety profile with increased risk for immunogenicity and cargo size limitation. Current vector engineering strategies take advantage of viral components to enhance efficiency, evade immune responses, reduce cytotoxicity and allow tissue specificity. About half of all clinical trials involving viral vectors utilize adeno-associated viruses (AAVs) (Bulcha et al., 2021). AAVs are the preferred due to their lower immunogenicity relative to other viral vectors. Also, AAVs exhibit minimal integration into the host genome thereby reducing the likelihood of insertional mutagenesis.

AAV vector biology

Adeno-associated viruses are small, with a diameter of 26 nm, and are non-enveloped viruses composed of icosahedral capsid protein subunits. The genomic capacity is 4.7kb for single-

stranded DNA, including the 145 bp T-shaped inverted terminal repeat (ITR) sequences at each end. These ITR sequences are vital for packaging, meaning only 4.4kb is usable space. The capsid is composed of viral proteins VP1, VP2, and VP3 in a 1:1:10 ratio. These viral proteins and ITRs determine the AAV serotype, which dictates key characteristics such as tropism, receptor binding, and immunogenicity (Wang et al., 2024). The genome of a wild-type AAV has two open reading frames encoding for the *Cap* and *Rep* genes. The *Cap* gene encodes for three capsid proteins, the Assembly-Activating Protein (AAP), and the Membrane Associated Accessory Protein (MAAP). The *Rep* gene encodes four replication proteins integral for replication and packaging. Wild-type AAV is a *Dependoparvovirus*, meaning that it requires an adenovirus or herpes simplex virus for replication (Fig. 1).

There are 12 known AAV serotypes and many variants identified in various species (Wang et al., 2024). The serotype defines the tropism of the AAV to specific tissues. The distinct variations in nine regions of the *cap* gene across AAV serotypes contribute to the specific tissue and cell type preferences. The variable portions of VP3 are thought to be most critical for tropism (Wang et al., 2024). AAV2 was the first to be identified and is based on wild type AAV. In terms of CNS tropism, AAV9 is one of the most used AAVs as it has been shown to achieve efficient neuronal transduction relative to other AAVs.

Current research fronts are intensively focused on discovering novel capsids that are cell specific and achieve high transduction efficiency. This is accomplished via capsid engineering which involves the following approaches: isolation of novel naturally occurring capsid variants, rational design, directed evolution, and in silico and machine learning methods. The majority of patients have neutralizing antibodies against the wild type AAV serotypes isolated in NHP and human. Discovering novel serotypes in other species might be a good strategy to evade neutralizing antibodies. Also, identification of novel AAV variants in humans such as AAVv66 which shared 98% homology with AAV2 with enhanced CNS transduction (Hsu et

al., 2020). Rational design relies on generating novel capsids by structural modification in key sites in the AAV capsid. This involves insertion of binding domains and genetic mutation. A novel AAV capsid, BI-hTFR1, expressed an optimized binding domain of the human transferrin receptor 1 on its surface was found to be significantly more efficient than AAV9 in transducing the brain (Huang et al., 2024). Directed evolution involves generation of random AAV libraries by inducing random mutation using error-prone PCR or peptide insertion methods in the *cap* gene. The most efficient variant is then assessed against the parental AAV for their transduction efficiency. In silico/machine learning approach makes use of computational methods to design and optimize AAVs. Highly diverse AAV capsids can be generated by deep learning which exceed the diversity of naturally occurring AAV serotype sequences (Bryant et al., 2021). In summary, the development of effective, safe, and cell/tissue-specific capsids is crucial for advancing and ensuring the success of gene therapy.

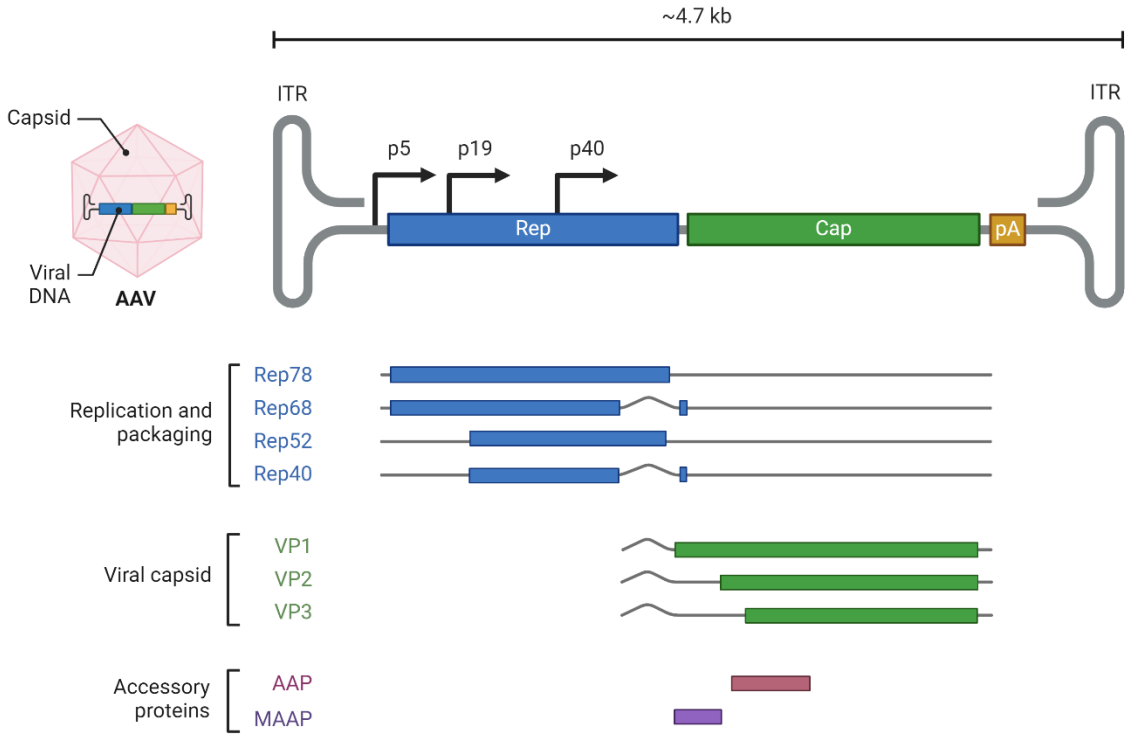

Figure 1: The biology of AAV vectors involves the genomic arrangement of wild-type AAV2, illustrating its ~4.7kb single-stranded DNA genome and the expression of seven viral RNAs and 2 accessory proteins through the *Rep* and *Cap* genes. The promoter regions p5, p19, or p40 are indicated in the *Rep* gene. The illustration was created by BioRender.com.

AAV transduction

AAVs are believed to attach to the cell surface by binding to primary receptors such as glycans, glycoconjugates, and sialic acid. Subsequently, interactions with co-receptors are critical for endocytosis (Wang et al., 2024). In humans, AAV9 binds to galactose as the primary receptor, laminin receptor and integrin as the co-receptors (Shen et al., 2011, p. 9; Wang et al., 2024). The AAV is then internalized, and changes in the pH in the endosome causes a confirmational alteration. The AAV escapes the endosome and enters the nucleus via the nuclear pore. In the nucleus, single stranded AAV undergoes uncoating and secondary strand synthesis occurs to generate double-stranded DNA (dsDNA). Secondary strand synthesis is rate-limiting and vital for the expression of the exogenous gene. The viral dsDNA undergoes concatamerization, driven by the recombination events of the ITRs, to yield a circularized episome which persists in the nucleus. Prior to entry to the nucleus, the AAV can also be degraded in the cytoplasm by the proteasome. This process could trigger immune responses via the presentation of AAV components and peptides on the cell surface.

Route of Administration

There are many ways in which gene therapies are introduced into patients. This is dictated by the target cells/tissue and the disease. The strategy for every disease varies and is optimized to achieve high efficacy and safety profile in patients. For ex-vivo gene therapies, cells are extracted from patients and are then modified by the introduction of a therapeutic gene. These cells are typically introduced into patients via intravenously. Some approved notable ex-vivo gene therapies include: Yescarta for large B-cell lymphoma (Locke et al., 2022), Zynteglo for beta-thalassemia (Locatelli et al., 2022) and Libmeldy for metachromatic leukodystrophy (Fumagalli et al., 2024). Chimeric Antigen Receptor T cell therapy which involved the extraction and modification of T cells has exploded in the last decade or so with many ongoing clinical trials for oncology indications (Dabas & Danda, 2023). On the other hand, in vivo gene

therapies require various routes to achieve their goal. Intravenous delivery is usually utilized for diseases requiring widespread distribution to all affected tissues. For muscle diseases, intravenous injections are common to ensure coverage of skeletal muscle as with many ongoing clinical trials, i.e. Elevidys is an FDA approved intravenous for Duchenne muscular dystrophy (Zaidman et al., 2023). Direct intramuscular injection is currently being investigated in the ongoing BB-301 clinical trial for Oculopharyngeal muscular dystrophy (OPMD) which effects the eyes and the throat (Strings-Ufombah et al., 2021). Recently, a tropical gene therapy known as Vyjuvek has been approved for dystrophic epidermolysis bullosa a condition affecting the skin (Guide et al., 2022).

A significant proportion of current gene therapy efforts are focused on treating neurodegenerative and central nervous system (CNS) disorders. However, the blood-brain barrier poses a significant challenge for efficient delivery into the CNS. Current efforts are concentrated on developing highly CNS-tropic AAVs that can bypass this barrier. AAVs can be introduced systematically by intravenous injection for wide CNS transduction. However, this typically requires higher vector doses. Delivery into the CSF offers several advantages over systemic delivery. Delivery into the CSF can be achieved via intrathecal (lumbar puncture), intracisternal magna, intracerebroventricular space for targeted CNS delivery at significantly lower doses versus IV (Perera et al., 2024). Intraparenchymal delivery has also been used for targeted brain regions i.e. injections into the subthalamic nucleus or putamen regions in the brain in Parkinson's disease (Hwu et al., 2021) (Fig. 2). All routes of administration have several advantages and disadvantages. Systemic intravenous delivery can lead to adverse events due to off-targeting, immunogenicity and cytotoxicity. (L. Xu et al., 2024). Intraparenchymal injections are highly technical and invasive but achieve high transduction of localized area (Hudry & Vandenberghe, 2019). Ocular diseases are also a great target for gene therapies due to their size and general immune privileged nature (Hudry & Vandenberghe,

2019). Various injections can target specific region of the eye such as the vitreous, retinal and choroid regions and similar developments are occurring in the ear (Morgan et al., 2020; Sahu et al., 2021). For metabolic disorders, the brain, retina and skeletal muscles are the organs most often affected and therefore various strategies could be employed in patients. Many challenges associated with the route of administration are currently being resolved with the discovery of novel AAV capsids capable in transducing specific tissues efficiently and de-targeting susceptible organs such as the liver (Fig. 2).

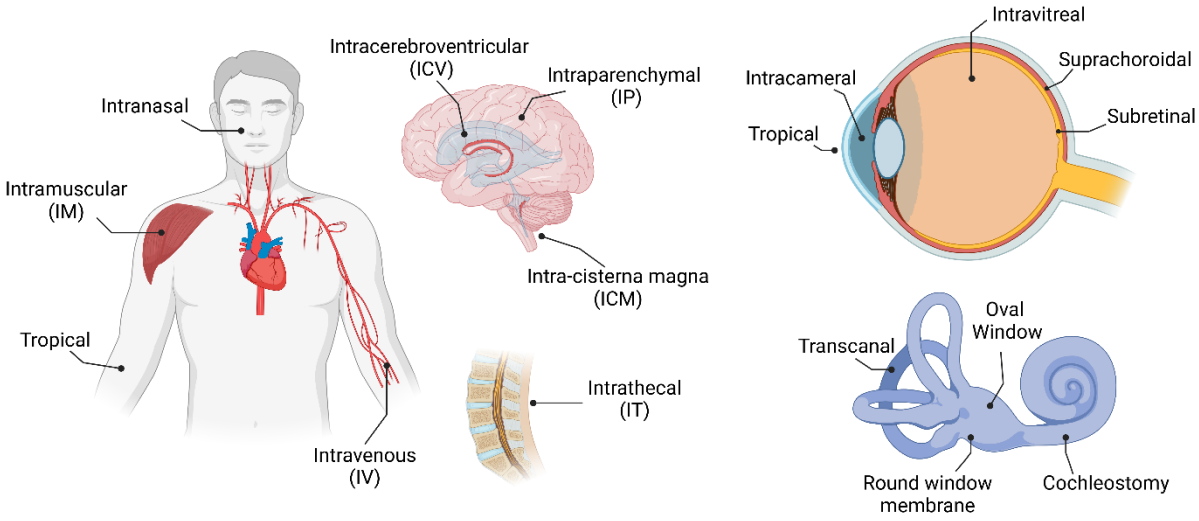

Figure 2: The delivery routes of in vivo gene therapies into the CNS and specialized organs.

The illustration was generated by BioRender.com.

AAV gene expression cassette

The gene expression cassette is the most critical component of any gene therapy drug, whether delivered by viral or non-viral vehicles. The gene expression cassette is composed of the ITR regions, promoter region, exogenous gene and downstream post-transcriptional and regulatory elements (Fig. 3). There are various engineering strategies for the gene expression cassette, each tailored to the specific etiology of the disease. The first is the simplest which is gene augmentation. Gene augmentation involves the delivery of a new therapeutic gene to replace a mutant nonfunctional gene without the disruption of the genetic makeup of an organism. A well-known example is Zolgensma, which uses an AAV9 to deliver the human survival motor neuron gene 1 (SMN1) for spinal muscular atrophy patients lacking SMN1(Pane et al., 2023). Gene augmentation is the most common strategy currently being utilized for neurological diseases (J. Gao et al., 2024). Furthermore, gene silencing and modulation can also be achieved by targeting and degradation of toxic mRNA. This strategy is employed for RNA gain of function diseases. Small interfering RNAs, short hairpin RNAs, micro RNAs can be used to target toxic mutant RNA species leading to degradation. Recently, RNA-targeting Cas endonucleases can achieve this goal efficiently i.e. type IV Cas13d and type II Cas9 endonucleases (Burmistrz et al., 2020). One ongoing clinical trial for neovascular age-related macular degeneration is utilizing CRISPR-Cas13Y system that fits into an AAV (Luk et al., 2024). Furthermore, the capability to edit genes with the arrival of CRISPR-Cas based editing technologies has expanded the toolkit for diseases for single base pair mutation or a portion of DNA within a gene. Base editors are capable of precisely altering a single DNA base pair to correct a mutant gene. There are two main base editors: Cytosine base editor alters a cytosine-guanine pairing to a thymine-adenine pairing and Adenine base editor alters a thymine-adenine pairing to cytosine-guanine pairing (Porto et al., 2020). Base editing is currently being investigated for familial hypercholesterolemia and

sickle cell disease (ClinicalTrials.gov, IDNCT05456880) (Horie & Ono, 2024). However, many diseases are caused by genes with extensive mutations across multiple loci. As a result, correcting a significant portion of the mutant gene is required, this can be achieved by Prime editing. Prime editing can precisely modify DNA sequences by the use of a gene correction template and a Cas nikase fused to a reverse transcriptase (P. J. Chen & Liu, 2023). This gene editing strategy is currently being investigated for chronic granulomatous disease (ClinicalTrials.gov, NCT06559176) (Fig. 3).

A crucial element of the gene cassette is the promoter region located upstream of the transgene or gene of interest. The promoter region can include enhancers, core promoter region and introns. The promoter region strength dictates the level of the expression of the exogenous gene. Ubiquitous promoters lead to expression in all transduced cell while cell-specific promoters are only active in specific cells. Cell specific promoters can mitigate the side effects associated with expression in undesired cells. Promoter selection is integral to the overall therapeutic strategy and therefore is disease dependent. The most commonly used ubiquitous promoters are the CAG promoter and the CMV promoter (Au et al., 2022). Both promoters are classified as strong promoters, resulting in high levels of exogenous gene expression. Some examples of moderate to weak promoters include CBA, PGK, UBC which will drive expression at moderate to weak level (Qin et al., 2010). Various cell specific promoters have been used such as Synapsin I (Syn 1) for neurons, muscle creatine kinase (CK8) for muscle, Transthyretin (TTR) for liver and others (Chuah et al., 2014; Hart et al., 2024; McLean et al., 2014). Current efforts within gene therapy aims to identifying novel promoters and developing synthetic promoters. Synthetic promoters can be designed to drive precise regulation of gene expression and overcome the limitations of natural promoters.

Along with the promoter region, the inclusion of downstream post-transcriptional regulatory elements is vital in the gene expression cassette. These elements enhance the stability, export

and translation of mRNA intro therapeutic protein. The Woodchuck Hepatitis Virus Post-Transcriptional Regulatory Element (WPRE) can be included immediately downstream of the stop codon functioning as the 3' untranslated region (UTR) along with poly adenylation signal. The WPRE element enhances gene expression stability, nuclear export, and enhancement of viral gene expression (Mouzannar et al., 2024; Patrício et al., 2017). Poly adenylation signals are commonly found in many gene cassette designs which are vital for transcriptional termination, mRNA stability, nuclear export and translation. Other elements that can be included are microRNA binding sites in the gene expression cassette for gene silencing (Hordeaux, Buza, Jeffrey, et al., 2020). Overall, all components of the gene expression cassette are essential to ensure the expression of the therapeutic cargo gene.

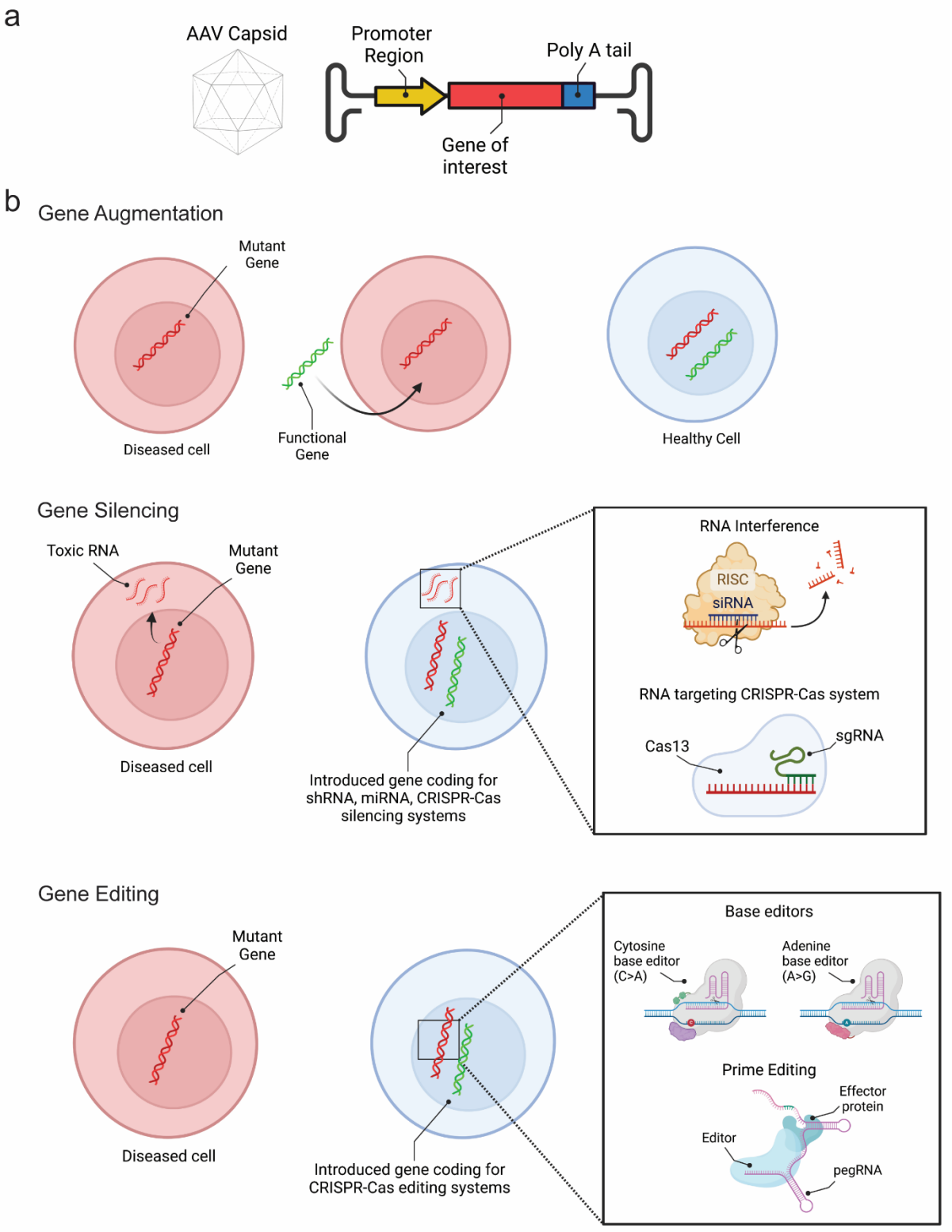
a
AAV Capsid
Promoter Region
Poly A tail
Gene of interest
b
Gene Augmentation
Mutant Gene
Diseased cell
Functional Gene
Healthy Cell
Gene Silencing
Toxic RNA
Mutant Gene
Diseased cell
Introduced gene coding for shRNA, miRNA, CRISPR-Cas silencing systems
RNA Interference
RISC
siRNA
RNA targeting CRISPR-Cas system
Cas13
sgRNA
Gene Editing
Mutant Gene
Diseased cell
Introduced gene coding for CRISPR-Cas editing systems
Base editors
Cytosine base editor (C>A)
Adenine base editor (A>G)
Prime Editing
Effector protein
Editor
pegRNA

Figure 3: Gene therapy strategies with a focus on recombinant AAV based gene therapies. **a.** The components of the recombinant AAV gene expression cassette. **b.** Gene augmentation involves the introduction of a therapeutic gene which restores function in diseased cells. Gene silencing strategies involves targeting toxic mRNA species in the cytoplasm by various mechanisms such as via the RNA interference pathway by RISC complex guided by siRNA. Also, RNA-targeting Cas endonucleases such as Cas13d can efficiently target and degrade toxic RNA. Direct DNA editing technologies focus on the use of base editors to alter a single base and correct mutations in genes. Prime editing technologies can alter large DNA sequences. These editing technologies alter the DNA without as opposed to the double-strand breaks associated with traditional CRISPR-Cas9 systems. Note that current Prime editors do not fit AAVs. Prime editor can be delivered into diseased cells via lipid nanoparticle or directly as ribonucleoprotein. The illustration was generated by BioRender.com.

AAV-based modality for the treatment of neurodegenerative diseases

The World Health Organization estimates that there are 50 million people currently affected with debilitating neurodegenerative disorders worldwide (Lamptey et al., 2022; *Neurological Disorders Affect Millions Globally*, n.d.). The most common CNS diseases are Alzheimer's, Parkinson's, Huntington's, Amyotrophic Lateral Sclerosis and Multiple Sclerosis. Neurodegenerative diseases are defined as a group of conditions affecting the central nervous system and specifically loss of neurons. Neurodegenerative diseases are progressive with symptoms generally emerging slowly with age. In many cases, the disease process involves accumulation of dysfunctional proteins leading to cellular damage and death (Disorders et al., 2013). These are typically caused by genetic mutations in one or more genes. This process is aggravated with inflammatory responses driven by the activation of microglia, astrocytes and other cell types (Kwon & Koh, 2020). In early stages of the disease, inflammation is hypothesized to be protective, however, as the disease progresses, chronic inflammation leads to acceleration of disease pathology and clinical phenotypes. It is expected that the population of individuals suffering from these diseases to rise as the population ages in the next decades. Currently, there are no existing disease modifying therapies to treat the underlying causes of the disease. The need for novel interventions will be vital for tackling these diseases.

The advancement of gene therapy over the past decades has created new opportunities for treating neurodegenerative diseases, particularly those with identified genetic basis (J. Gao et al., 2024). With gene therapy, drug developers can correct a disease mechanism to protect neurons from degeneration. Gene therapy can also be used to regulate to prevent chronic inflammation, promote neuromodulation and promote regeneration by overexpression of key neurogenesis genes. AAVs is the vehicle of preference for therapeutic transgene delivery as they have been shown to be effective for loss of function genetic diseases. AAV based gene

silencing strategies and also gene editing are also being employed. The most common AAV serotypes used in neurodegenerative disease are AAV2, AAV9, AAVrh10, AAV5, AAV1 (J. Gao et al., 2024). The most common route of administration for the ongoing clinical trials is intrathecal dosing into the CSF space. A single dose regimen is the most common for all gene therapy clinical. This is typical as neutralizing antibodies can pose a create risk for patients despite the use of immune suppression for patients. A summary of AAV-based gene therapies for neurodegenerative diseases is provided in Table 1.

Disease	Gene Therapy#	Strategy	Route of Administration	Dosing Frequency	Study Phase	Trial Identifier
Alzheimer's Disease	AAV2-BDNF	Gene augmentation	MRI guided stereotaxic delivery to entorhinal cortex	Single Dose	I	NCT05040217
Alzheimer's Disease	AAVrh10- APOE2	Gene augmentation	IT	Single Dose	I/II	NCT03634007
Huntington's Disease	AAVrh10 - CYP46A1	Gene augmentation	ICV	N/A	I/II	NCT05541627
Huntington's Disease	rAAV5-miHTT	Gene silencing	MRI guided stereotaxic brain delivery	Single Dose	I/II	NCT04120493
Huntington's Disease	rAAV5-miHTT	Gene silencing	MRI guided stereotaxic bilateral delivery to striatum	Single Dose	I/II	NCT05243017
Parkinson's Disease	AAV9-GBA1	Gene augmentation	IC	Single Dose	I/II a	NCT04127578
Parkinson's Disease	AAV –GAD	Gene augmentation	Bilateral infusion to subthalamic nuclei	Single Dose	I/II	NCT05603312
Parkinson's Disease	AAV2-GDNF	Gene augmentation	Bilateral infusion into putamen	Single Dose	I	NCT04167540
Parkinson's Disease	AAV2- AADC	Gene augmentation	Bilateral infusion into putamen	Single Dose	II	NCT03562494
Amyotrophic Lateral Sclerosis (ALS)	AAVrh10- miRNA- SOD1	Gene silencing	IT	Single Dose	I/II	NCT06100276
Frontotemporal Dementia (FTD)	AAV9- GRN	Gene augmentation	MRI guided intrathalamic delivery	Single Dose	I/II	NCT06064890
Frontotemporal Dementia (FTD)	AAV1-GRN	Gene augmentation	IC	Single Dose	I/II	NCT04747431
Frontotemporal Dementia (FTD)	AAV9-GRN	Gene augmentation	IC	Single Dose	I/II	NCT04408625
Spinal Muscular Atrophy (SMA) Type 1	AAV9-SMN	Gene augmentation	IT	Single Dose	I/II	NCT05824169
SMA Type 2	AAV9-SMN	Gene augmentation	IT	Single Dose	I/II	NCT05901987
SMA Type 2	AAV9-SMN	Gene augmentation	IT	Single Dose	III	NCT05089656
SMA	AAV9-SMN	Gene augmentation	IT	Single Dose	IIIb	NCT05386680
Unilateral Refractory Mesial Temporal Lobe Epilepsy (MTLE)	AAV9-miRNA- GRIK2	Gene silencing	MRI-Guided Convection- enhanced Delivery (CED)	Single Dose	I//IIa	NCT06063850

Hereditary Spastic Paraplegia	AAV9-AP4M1	Gene augmentation	IT	Single Dose	I/II	NCT05518188
Giant Axonal Neuropathy	scAAV9-Gigaxonin	Gene augmentation	IT	Single Dose	I	NCT02362438
Metachromatic Leukodystrophy (MLD)	AAVrh10-ARSA	Gene augmentation	Bilateral intracerebral injections to white matter	Single Dose	I/II	NCT01801709
Adrenomyeloneuropat hy	AAV9-ABCD1	Gene augmentation	IT	Single Dose	I/II	NCT05394064
GM1 Gangliosidosis	AAV9-GLB1	Gene augmentation	IV	Single Dose	I/II	NCT03952637
GM2 Gangliosidosis	AAV9-Hexokinase A	Gene augmentation	IT	Single Dose	I/II	NCT04798235
Krabbe Disease	AAVrh10-GALC-Hematopoietic stem cells	Gene augmentation	IV	N/A	I/II	NCT04693598
Krabbe Disease	AAVrh10-GALC	Gene augmentation	IV	Single Dose	I/II	NCT05739643
Canavan Disease	AAV9-ASPA	Gene augmentation	IV	Single Dose	I/II	NCT04998396
Canavan Disease	rAAV-ASPA	Gene augmentation	Intracranial	Single Dose	I/II	NCT04833907
Batten Disease	scAAV9-CLN3	Gene augmentation	IT	Single Dose	I/II	NCT03770572
Batten Disease	AAV9-TPP	Gene augmentation	Subretinal	Single Dose	I/II	NCT05791864
Batten Disease	AAV9-CLN5	Gene augmentation	ICV, ICT	Single dose per administration route	I/II	NCT05228145
Batten Disease	AAV9-MFSD8	Gene augmentation	IT	Single Dose	I	NCT04737460
Fabry Disease	AAV-C102 - GLA	Gene augmentation	IV	Single Dose	I/II	NCT04519749
Fabry Disease	AAV2/6- GLA	Gene augmentation	IV	Single Dose	I/II	NCT04046224
Fabry Disease	AAVS3- GLA	Gene augmentation	IV	Single Dose	I/II	NCT04455230
Mucopolysaccharidosi s Type I (Hurler Syndrome)	rAAV9- IDUA	Gene augmentation	IC	Single Dose	I/II	NCT03580083
Mucopolysaccharidosi s Type II (Hunter Syndrome)	rAAV9-IDS	Gene augmentation	IC or ICV	Single and Multiple Doses	II/III	NCT03566043

Mucopolysaccharidosi s Type III (Sanfilippo Syndrome)	scAAV9- SGSH	Gene augmentation	IV	Single Dose	II/III	NCT02716246
Dravet Syndrome	rAAV9- reGABA and eTFSCN1A	Gene augmentation	ICV	Single Dose	I/II	NCT05419492
Rett Syndrome	AAV9- Mini- MECP2	Gene augmentation	IT	Single Dose	I/II	NCT05606614
Rett Syndrome	AAV9-MECP2	Gene augmentation	ICV	Single Dose	I/II	NCT05898620

Table 1: Current ongoing AAV-based clinical trials for neurodegenerative diseases as of 2024. The table was adapted from Gao et al., 2024. Intracerebroventricular (ICV), Intrathecal (IT), Intravenous (IV), Intracisternal (IC), Intravitreal (ICT).

Current safety challenges of AAV-based in-vivo gene therapy

In vivo recombinant AAV gene therapies possess much greater challenge than ex vivo gene therapies (Shirley et al., 2020). Ex vivo gene therapy circumvents immune responses which significantly reduces toxicity. The process of introducing AAV into the organism is complex, presenting numerous challenges and requiring consideration of factors. One of these challenges is the route of administration, this is dependent on the target tissue and disease. For example, intravenous delivery targets multiple organs which increases the risk of toxicity while localized delivery limits the potential for toxicity.

Certain toxicities have been observed in clinical trials and preclinical animal models:

- **Genotoxicity:** Although rare, insertional mutagenesis could occur post AAV administration (Martins et al., 2023). At high doses, insertions may take place in organs with high transduction rates like the liver. A recent sequencing study revealed that other tissues, including the kidney, heart, lung, and spleen, can also be impacted (Martins et al., 2023).
- **Hepatotoxicity:** systemic delivery of high vector doses leads to liver injury. Elevation of liver enzymes such as aminotransferases have been observed in preclinical animal models and patients in clinical trials (Chand et al., 2021).
- **Thrombotic microangiopathy:** formation of blood clots in blood vessels due to the aggregation of platelets. The innate immune system is thought to contribute to this injury which can progress to ischemia (Salabarria et al., 2024).
- **Immunogenicity:** the AAV capsid and gene expression cassette components can activate innate and adaptive immune responses leading to inflammation and tissue injury (T. Yang et al., 2022). Immune responses can eliminate transduced cells thereby reducing efficacy.
- **Neurotoxicity:** high AAV titers can cause local or widespread neurotoxicity in the CNS and peripheral nervous system. Intraparenchymal delivery damages the blood brain barrier

due to immune cell infiltration (Guo et al., 2023). Cerebellar toxicity has been observed in NHPs (Keiser et al., 2021). Neuronal degeneration has been observed in the trigeminal ganglia and the DRG following AAV delivery into the CSF. Consistent axonal degeneration in the spinal cord and peripheral sensory nerves have been reported (Fader et al., 2022; Hordeaux, Buza, Dyer, et al., 2020; Johnson et al., 2023).

Dorsal root ganglia toxicity in the patients following AAV administration

Reports of neurotoxicity characterized in the CNS and peripheral nervous system in patients have been noted in clinical studies administering high doses of AAV. Dosing into the CSF like in many ongoing clinical trials increases the risk of this toxicity. Typically, these findings are not accompanied by clinical manifestations. In an investigational clinical study to measure the safety, an AAV9 coding for microRNA targeting the human SOD1 gene was injected intrathecally into two SOD1 ALS patients (Mueller et al., 2020). One patient developed tingling in both hands after 3 weeks and painful electric shocks in his right foot at 4 weeks post-dosing. It was found that sural and left median sensory-nerve potentials were absent 10 weeks post-dosing. The amplitude of superficial peroneal nerve was reduced at 10 weeks post-dosing. The conduction velocities of the peroneal motor conduction velocity were reduced. The patient succumbed to ALS 15.6 months post-dosing. At autopsy, along with motor neuron loss in the spinal cord, neuronal loss was noted in the bilateral dorsal root ganglia and evidence of T cell infiltration in the proximal nerve roots. The second patient in this clinical study did not suffer from DRG toxicity and was given immunosuppression regimen.

Dorsal root ganglia toxicity may also been observed in a clinical trial for Giant axonal neuropathy where patients were injected intrathecally scAAV9 to deliver the GAN gene along with immunosuppression regimen (Farrar et al., 2022; Mullard, 2021). One patient succumbed 8 months post-dosing with severe neuronal loss noted in the DRG without inflammatory signal.

It is not known if this finding is test article related, or disease related since sensory neuropathy occurs in Giant axonal neuropathy patients. Overall, evidence of DRG toxicity in patients are rare and current clinical trials closely monitor patients for evidence of sensory neuron changes and neuropathy related to the test article.

Overview of the dorsal root ganglia

The dorsal root ganglia (DRG) is located within or in close proximity to the intervertebral foramina in the spinal column (Haberberger et al., 2019). Each spinal nerve has a pair of DRGs that are lateral to the spinal cord and connect to the spinal cord via the dorsal nerve root. Mice have 30 to 31 pairs of DRGs, with 8 cervical, 13 thoracic, 5 or 6 lumbar, and 4 sacral. The DRG is part of the peripheral somatosensory nervous system, housing the sensory neuronal bodies of peripheral nerves. The DRGs conduct sensory neuronal signals from the periphery to the central nervous system. Neurons in the DRG have a unipolar morphology that bifurcates into two processes. One process projects into the spinal cord and the other into the periphery (Crawford & Caterina, 2019). The neuronal soma occupies the peripheral regions of the DRG, while the central regions are composed of bundles of nerve fibers. Sensory neurons in the DRG are surrounded by satellite glial cells, which form a close unit that allows for modulation of the microenvironment and supports neurons by expressing specific receptors and ion channels (Hanani & Verkhratsky, 2021). Fibroblasts and Schwann cells make up a significant proportion of the DRG, along with other cell types such as endothelial cells, pericytes, and resident immune cells (macrophages, T cells, and B cells) (Haberberger et al., 2019). The blood vessels form a vast network of arterioles and capillaries within the DRG. Capillaries in the DRG are fenestrated, allowing easy penetration of small and large molecules (Fig. 4).

Sensory neurons are distinguished by morphology, physiology, transcription factors, expressed G-protein coupled receptors, myelination, neurotransmitters, and ion channels (Jung et al., 2023; Meltzer et al., 2021, 2021; Renthal et al., 2020; Sharma et al., 2020). Traditionally,

sensory neurons were originally defined by their soma size, degree of myelination and nerve conduction velocity (Bhuiyan et al., 2024). A-fiber neurons have large diameter and have high conduction velocity while C-fiber neurons are unmyelinated and have slow conduction velocities. Currently, distinct neuronal subtypes are defined by their gene expression based on recent studied in single cell and single nucleus RNA sequencing methodologies. Due to technical differences between the sequencing studies, the number of distinct neurons varies from one study to another, and the nomenclature is not consistent for cross-species comparisons (Bhuiyan et al., 2024). This is because researchers assign neuronal type labels based on their cutaneous physiology. Bhuiyan and colleagues recently developed a harmonized atlas of the dorsal root ganglia and trigeminal ganglia from six species generating concise nomenclature. A total of 18 neuronal subtypes were classified based on molecular gene markers only as opposed to cutaneous physiology. The atlas nomenclature defines marker genes across species, the fiber type and the known cutaneous physiology. At least one known function has been identified for fifteen of these neuronal subtypes, based on knock-in mice expressing Cre recombinase. The A-fiber neurons are Pvalb proprioceptors, Ntrk3^{high}+Ntrk2 Aβ-rapid-adapting (RA)–low-threshold mechanoreceptors (LTMRs), Ntrk3^{high}+S100a16 Aβ-field/slow-adapting (SA)–LTMRs, Ntrk3^{low}+Ntrk2 Aδ-LTMRs, Calca+Bmpr1b Aδ–high-threshold mechanoreceptors (HTMRs) expressing, Calca+Smr2 Aδ-HTMRs. The C-fiber neurons are Calca+Sstr2 nociceptors, Calca+Adra2a nociceptors, Trpm8 cold thermoreceptors, Th cLTMRs, Mrgprd nociceptors, Mrgpra3+Mrgprb4 cLTMRs, Mrgpra3+Trpv1 pruriceptors, Sst pruriceptors and a cluster specific to injury expressing Atf3, Sox11 and Jun. It is expected that this nomenclature will evolve as new datasets are generated along with novel sequencing and analysis methods emerge.

In this thesis, the neuronal annotations adhere to the nomenclature established by Jung and colleagues, as the same sequencing strategy and platform were utilized. (Jung et al., 2023).

Jung and colleagues utilized a single nucleus-based strategy to sequence DRG neurons using 10x Genomics platform. Jung and colleagues identified 11 transcriptionally distinct neuronal clusters in mice. These were defined as proprioceptors and Aβ SA-LTMRs, AβRA-LTMRs, Aδ-LTMRs, C-LTMR, cold thermoreceptors, non-peptidergic nociceptors 1 (NP1), NP2, NP3, peptidergic nociceptors 1 (PEP1), PEP2, and PEP3. This classification was compared to Guinea pig, Cynomolgus monkey and human datasets to determine homology of neurons and a cross-species atlas.

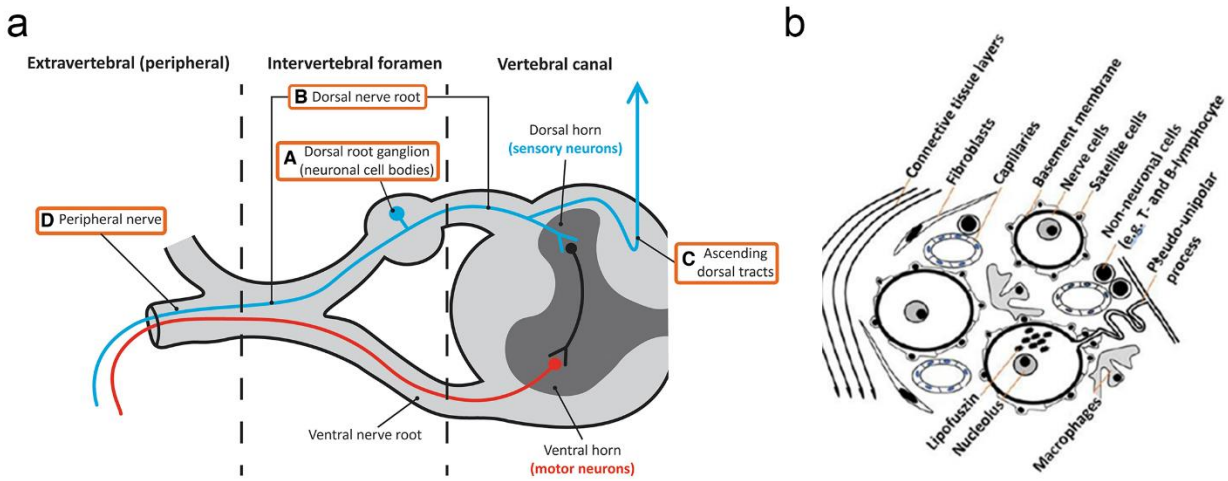

Figure 4: Neuroanatomy of the dorsal root ganglia and related nervous system components. **a.** sensory neuron processes extend into the central nervous system into the dorsal horn and towards the periphery. Figure is adapted from Hordeaux et al., 2020 **b.** Cell types found in the dorsal root ganglia. Figure is adapted from Haberberger et al., 2019.

The dorsal root ganglia and the sensorimotor system

The sensorimotor system is composed of motor and sensory neurons in the brain, spinal cord and the dorsal root ganglia. Sensory information such as, pressure, heat, proprioception, nociception is carried from the periphery into the spinal cord and to the brain. This is where integration and interaction with the somatosensory and motor cortex occurs (Kaas, 2012). Motor output is subsequently generated in the brain or the spinal cord, leading to muscle contraction by efferent nerves (Flanders, 2011).

Muscles are controlled by motor units, which are defined as a motor neuron and the downstream bundle of efferent fibers it controls. Muscle spindles and Golgi tendons form the specialized afferent fibers in the muscle and enable proprioception (Tuthill & Azim, 2018). The muscle spindle detects stretching, while the Golgi tendon senses tension in the muscle. Both specialized organs generate sensory action potentials in afferent nerves, which ultimately either activate or suppress motor neuron firing to counteract overextension or over-flexion of the muscle (Tuthill & Azim, 2018).

Muscles are organized in groups, and these muscle groups work in agonistic and antagonistic pairs, allowing for the coordination of contraction and relaxation. Injury to sensory and motor neurons, along with their fibers, can alter the regulation of muscle contraction, potentially leading to muscle atrophy and weakness or paralysis. This, in turn, can alter locomotion and gait behavior.

AAV-induced dorsal root ganglia toxicity in animal models

Toxicity within the dorsal root ganglia following AAV administration has traditionally been documented in non-human primates (NHPs) (Hordeaux et al., 2020; Johnson et al., 2023; Tukov et al., 2022). Non-human primates are thought to be a sensitive model for studying DRG toxicity along with rabbit. However, this class of toxicity has also been observed in pigs (Hinderer et al., 2018), rabbits (Tien et al., 2024), and rodents (Alstyne et al., 2021; Fader et

al., 2022; Tyszkiewicz et al., 2024; Hawley et al., 2024). In general, the pathology observed is minimal (percentage of neurons and axons affected is less than 10%) to moderate (25-50%) in the NHP. The pathology is characterized as transient/acute, resolving over time. Peripheral nerve axonal degeneration is generally more consistent than DRG neuronal findings. DRG toxicity is associated with high titers of neurotropic AAV such as AAV9. It occurs when AAV is administered either systemically or into the CSF, resulting in efficient transduction of sensory neurons. As opposed to systemic delivery, dosing into the CSF is associated with greater DRG lesion severity scores and incidence. The following histopathological findings have been noted in animal models:

1. **Neuronal cell body degeneration:** decrease in soma size and irregularly shaped morphology. It involves the formation of chromatolysis and eosinophilic granules in neurons.
2. **Infiltration of mononuclear cells***:* These are found in degenerating neurons in NHPs, piglets, and rabbits. However, rodents show increased cellularity with no infiltration of mononuclear cells.
3. **Axonal degeneration in the dorsal nerve root:** axonopathy characterized by myelin sheath dilation, with and without myelomacrophages.
4. **Central axonal degeneration in the dorsal funiculus in the spinal cord:** bilateral and multifocal axonopathy and myelin dilation in the white matter sensory nerve tracts of the spinal cord.
5. **Reactive glial proliferation:** This occurs at the site of neuronal degeneration, leading to an increase in population and altered morphology.
6. **Axonal degeneration in peripheral nerves:** axonopathy in the sciatic nerve and the saphenous nerve, characterized by myelin sheath dilation.

Along with the capsid, dose and route of administration (ROA), it is thought that the genomic cargo and its components, such as: promoters, therapeutic gene product, and transcriptional elements, impact DRG toxicity. The age of animals can impact toxicity, as younger NHPs have been shown to exhibit lower severity. DRG findings are not uniform and are not consistently bilateral. All DRGs levels are equally affected (Hordeaux, Buza, Dyer, et al., 2020). Not much is known about the mechanism of toxicity, however, it is hypothesized that high transduction of sensory neurons leads to cell injury due to the overexpression of the transgene (Hordeaux, Buza, Jeffrey, et al., 2020). This is thought to be followed by the degenerative process seen in histopathological assessments. Damage to neurons likely leads to pro-inflammatory immune responses and exacerbation of the pathology.

Neurofilament light chain

Neurofilament protein is comprised of four neurofilament subunits: neurofilament light, medium, heavy and α-internexin (Yuan et al., 2017). These subunits form a heteropolymers which assemble to generate neurofilaments. Neurofilaments are expressed in neurons and serve as cytoskeletal proteins in axons and the soma. Axonal degeneration causes the disassembly of neurofilaments into individual subunits and are released into the CSF and serum. Elevation of CSF and serum neurofilaments proteins are detected in many neurodegenerative preclinical animal models which is vital for monitoring disease progression (Loeffler et al., 2020). AAV-induced DRG toxicity leads to a robust surge in neurofilament levels. In fact, neurofilament light chain has recently been shown to be a biomarker of DRG toxicity, and serum neurofilament light (NfL) levels correlate with the severity of histopathological findings (Fader et al., 2022; Johnson et al., 2023; Tyszkiewicz et al., 2024). This enables the use of serum NfL as proxy for DRG toxicity in animal models.

Immune responses to AAV

The neurotoxic effects of AAVs, particularly neuronal degeneration, have been associated with immune reactions. Various factors such as the capsid, gene expression cassette components, expressed gene product, and impurities can contribute to the risk of eliciting an immune response against AAVs. The initial response of the innate immune system plays a crucial role in triggering subsequent adaptive immune responses. Studies have indicated that shortly after AAV administration, innate immunity responds to the presence of the vectors. AAV vectors have been observed to activate the complement system and Toll-Like Receptor signaling pathways, which in turn initiate interferon response cascades, resulting in the release of cytokines and chemokines (Arjomandnejad et al., 2021; Muhuri et al., 2021; Shirley et al., 2020; T. Yang et al., 2022).

At high doses, pre-existing neutralizing antibodies (NAb) can bind to circulating AAVs, forming NAb-AAV complexes. These NAb-AAV complexes can be detected by the C1 complex, part of the classical complement pathway, and initiate the downstream cascades. Cleavage of C3 to C3a and C3b by C3 convertase is vital for downstream processes, which leads to the activation of the membrane attack complex (MAC). The MAC creates openings in the plasma membrane of pathogens or targeted cells, which results in osmolysis. At low doses, AAV can also directly bind to C3 (alternative pathway), leading to the activation of MAC. C3-bound AAV can directly activate macrophages and dendritic cells and initiate the humoral immune response. Macrophages, dendritic cells, and neutrophils can also uptake the NAb-AAV complex and increase the inflammatory response by releasing pro-inflammatory cytokines and chemokines.

The innate immune system can detect Pathogen-Associated Molecular Patterns (PAMPs) in AAVs by toll-like receptor 2 (TLR2) on the cell surface and TLR9 recognition of genomic cargo with CpG dinucleotides in the endosome. Both receptors activate the TLR adaptor

Myd88, leading to downstream cascades initiating NF-κB and inducing type 1 interferon (IFN) response genes. These processes cause the release of proinflammatory cytokines and chemokines such as TNF, IL-1β, and IFN α/β. When IFN α/β interacts with IFNAR-1 on antigen-presenting cells (APCs), such as dendritic cells or macrophages, it leads to the activation of these cells. Activated APCs in turn, prime cytotoxic CD8+ T cells by antigen presentation of AAV peptides on major histocompatibility complex class 1 (MHCI). APCs can prime helper CD4+ T cells by antigen presentation of AAV peptides on MHCII. Primed cytotoxic CD8+ T cells identify and eliminate AAV-transduced cells by the release of cytokines such as IFNγ and TNFα. Long-term adaptive immunity is achieved by helper CD4+ T cells priming B cells to promote antibody formation against the AAV. Adaptive immune responses occur within days/weeks post AAV-administration. Regulatory T cells (Treg) can modulate the adaptive responses by the release of anti-inflammatory cytokines. Tregs can also promote tolerance to the expressed genomic cargo, which aids in controlling neuroinflammatory responses arising from long-term expression. Immune suppression strategies have been employed in trials to evade and reduce immune responses and prevent serious adverse events in patients.

AAV vectors to model dorsal root ganglia toxicity in mice

The use of two distinct AAV9 vector with similar genomic cargo components enabled toxicity modeling in mice (Fig. 3). AAV-miR-SOD1 encodes a duplex artificial microRNA targeting the human and mouse superoxide dismutase gene and AAV-mCherry encodes the mCherry reporter protein. Intrathecal injection of AAV-miR-SOD1 and AAV-mCherry in C57BL/6J mice displayed histopathological lesions characterized by minimal neuronal degeneration, increased cellularity, and chromatolysis in the lumbar DRGs at 6 weeks post-injection (Hawley et al., 2024). AAV-mCherry-injected mice showed eosinophilic intracytoplasmic granules; these were not found in AAV-miR-SOD1-treated mice. For both test articles, axonal degeneration was also

observed in the sciatic nerve (motor and sensory) and the saphenous nerves (sensory) and appeared to be more consistent compared to the findings in the DRGs. In the dorsal funiculus of the spinal cord, lesions consisting of axonal dilation and degeneration were found in mice. Lesions coincided with a serum neurofilament surge at 6- and 13-weeks post-dosing. DRG toxicity was acute, and the severity along with the incidence of lesions generally decreased at around 6 to 9 months post-injection. Transcriptional analysis revealed a large proportion of differentially activated genes noted at 6- and 13-weeks post-injection. Innate immune response-associated genes, specifically complement, were noted along with cell-mediated T-cell genes that were upregulated. Several pro-inflammatory cytokines and chemokines were elevated indicating inflammatory responses in the DRG.

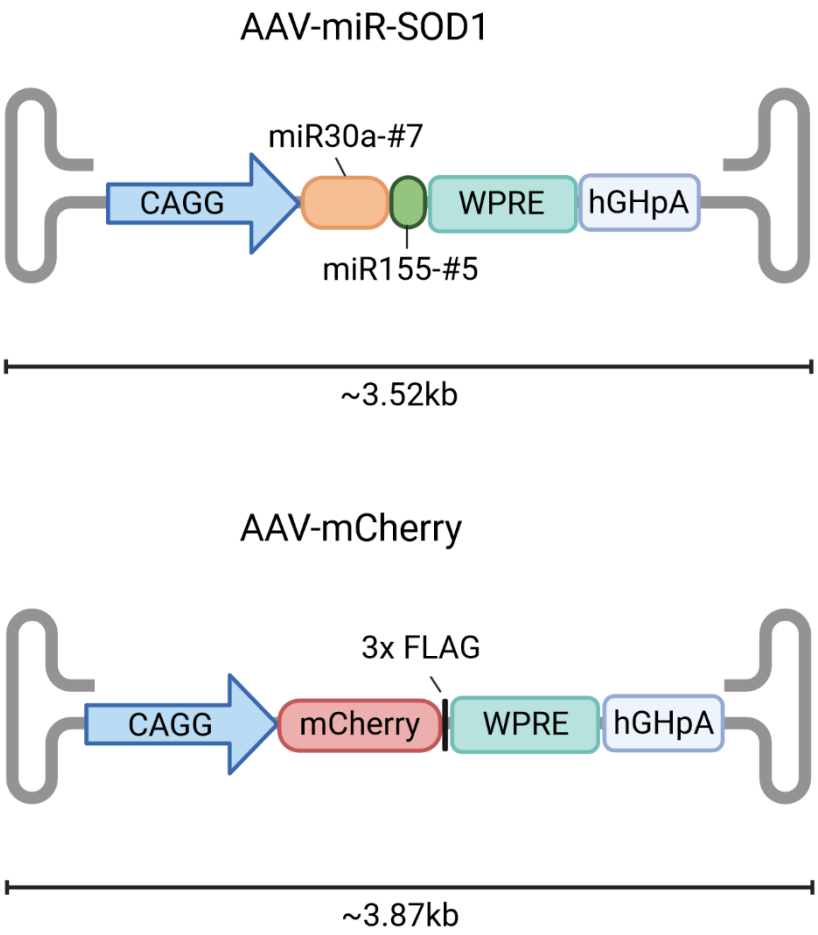

Figure 5: Vector maps of the test articles. The transgenes were packaged in AAV9. CAGG- CMV enhancer element, chicken-beta actin promoter, and intron gene. miR30a-#7- artificial microRNA with seed sequence #7. miR155-#5 – artificial microRNA with seed sequence #5. WPRE- Woodchuck hepatitis virus post-transcriptional regulatory element. hGHpA- human growth hormone poly A tail. The vector maps are to scale. The illustration was created by BioRender.com.

Research objectives

Many of the studies rely on histopathology to characterize DRG toxicity. However, this leaves inherent gaps, histopathological analysis is semi-quantitative and requires experienced pathologists to detect the subtle changes. In addition, tissue sections are not entirely representative of the entire DRG, thereby allowing for the potential underestimation of pathological severity. Alterations in non-abundant and small cell types may not be easily detected via histopathology analysis (Din et al., 2020). Therefore, quantitative methods such as transcriptomics and proteomic analyses are vital in providing a comprehensive view encompassing all cell types. RNA sequencing has recently been used to uncover RNA expression profiles in the DRG. Additionally, functional phenotypes have been rarely observed in patients and animal studies. The dose levels used in all studies ranged from 5.0E11 GC to 1.6E12 GC per mouse at 6 weeks of age. These doses are comparable to the doses used in intrathecal studies in animal models and in patients (Bharucha-Goebel et al., 2024; X. Chen et al., 2022; Fader et al., 2022; Johnson et al., 2023; Mueller et al., 2020; Tukov et al., 2022).

Two key objectives:

- Explore the cell-specific transcriptional alteration in the DRG following AAV-induced toxicity in mice. Identify the key gene expression signatures in neurons, satellite glia, immune cells, and the relevant enriched pathways.

  This was achieved in Chapter 2. Intrathecal AAV dosing and lumbar DRG collection for nuclei isolation and single nucleus RNA sequencing.
- Examine whether mice display functional deficits, particularly physiological and behavioral alterations in response to AAV-induced DRG toxicity in mice.

  This was achieved in Chapter 3-5. Mice were intrathecally dosed with high titers of AAV to induce DRG toxicity and were subjected to diverse physiological and behavior testing.

The dissertation is structured as follows: it begins with a general introduction in Chapter 1, followed by standalone body Chapters 2, 3, 4 and 5. Each body chapter includes an introduction, methods, results, and discussion. Chapter 6 focuses on a general discussion, which connects the primary findings of all body chapters of this thesis.

Chapter 2

Single Nucleus Transcriptomic Characterization of AAV-induced Dorsal Root Ganglia Toxicity in C57BL/6J Mice

Introduction

Gene therapy has revolutionized treatment for life-threatening diseases, altering the outcomes dramatically. In the last decade, many *in vitro* and some *in vivo* gene therapies have been approved and are currently prescribed to patients. Overall, *in vitro* interventions dominate the landscape as challenges continue to persist with *in vivo* therapies. Currently, Adeno-associated virus (AAV) is the most widely employed vehicle of *in vivo* gene therapy trials (Kuzmin et al., 2021). While AAV has various advantages over alternative viral-based vectors, it also has several drawbacks, including immunogenicity, hepatoxicity, and neurotoxicity (Ertl, 2023). Toxicity in animals is dependent on key variables such as the dose, gene cargo, age, and route of administration (Hordeaux, Buza, Dyer, et al., 2020). Dorsal root ganglia (DRG) toxicity is one of these class toxicities first identified in non-human primates (NHPs) and later observed in other animal models. AAVs at high titers were found to elicit neuronal cell body loss, mono-nuclear cell infiltration, axonal degeneration in the spinal cord and peripheral nerves in NHPs (Hordeaux, Buza, Dyer, et al., 2020). Similar findings have been recorded in pigs, rabbits, rats and recently mice (Fader et al., 2022; Hawley et al., 2024; Hinderer et al., 2018; Tien et al., 2024; Tyszkiewicz et al., 2024). The significance of these findings remains unknown and clinical manifestation is rare. However, some patients treated with various gene therapies were found to exhibit DRG toxicity and presented a clinical phenotype (Mueller et al., 2020). Almost all studies utilize histopathological assessments to identify DRG toxicity as these studies provide a clear visual representation of the anatomical changes occurring in response to AAV-induced injury. Histopathological evaluation is semi-quantitative, and the interpretation of results undergo validation by a second pathologist. Subtle changes can potentially by missed and/or underestimated.

Recent studies have employed RNA sequencing methods to study DRG toxicity in mice and NHPs. This has facilitated comprehensive study of transcriptomic profiles in the DRG, and the

pathways associated with AAV-induced changes. Wild type C57BL/6J mice injected with AAV9 carrying the survival motor neuron 1 (SMN1) gene have alterations in splicing and upregulation of genes associated with the innate immune response and inflammatory pathways (Alstyne et al., 2021). The authors note an upregulation of all the subunits of the C1q complex, a component of the classical complement pathway. However, the sequencing study probes at 10 months post-injection, which is far removed from the acute responses with AAV treatments. In a recent comprehensive investigation focusing on acute and chronic impact of AAV dosing, mice were intrathecally dosed with AAV-amiR-SOD1 (AAV9 serotype expressing the artificial duplex microRNA targeting the human superoxide dismutase 1 gene) and AAV-mCherry reporter protein (Hawley et al., 2024). Lumbar DRGs were collected at 3-, 6-, 13-, 27- and 38-weeks post-injection for RNA sequencing. A transient elevation of differentially activated genes occurs at 6- and 13- weeks post-injection which notably declines at 27- and 38- weeks post-injection. Upregulated genes indicate activation of the complement immune system, toll-like receptor signaling and macrophages activation leading to cell-mediated to T cell immunity. Upregulation of cytokines and chemokines indicate robust inflammatory signal. These innate and adaptive immune events are transient, starting at 6-weeks and peaks at 13-weeks post-injection and parallel observations from prior studies (T. Yang et al., 2022). Deconvolution analysis hint to a reduction in the number of neurons, elevation of macrophages, fibroblast, pericytes, and satellite glia, and no changes to Schwann cells. Some enriched pathways following AAV treatment are preserved in NHP DRGs, indicating some translatability between the two species.

RNA-sequencing serves as a valuable tool for examining gene profile alterations in bulk tissue; nonetheless, it lacks cellular resolution, and the transcriptomic profile represents an average across all cell types. The aim was to explore how a toxic AAV vector induces transcriptomic changes in the DRG and unravel how different cell types respond to injured and degenerating

neurons. Single nucleus RNA sequencing enabled investigation of cell specific changes in the DRG and the key altered pathways in each cell type thereby allowing the study of biological complexity of this class toxicity. This was achieved by intrathecally dosing wild type C57BL/6J mice at 6 weeks of age and collecting lumbar DRGs for nuclei isolation and sequencing. Neuronal and axonal injury in the DRG was assessed via serum neurofilament light levels (NfL), recently shown to be a biomarker of DRG toxicity in rodents and NHPs (Fader et al., 2022; Hawley et al., 2024; Johnson et al., 2023; Tukov et al., 2022). Novel and comparable findings to prior studies were noted such as neuronal cell loss, activation of repair processes in activated satellite glia and innate and adaptive immune responses. This research broadens our understanding of DRG toxicity in preclinical models and reinforces mice as an early model for DRG toxicity.

Materials and Methods

Animals

Wild type C57BL/6J (Stock #:000664) females were obtained from the Jackson Laboratory and were housed in a 12/12 hrs light/dark cycle temperature-controlled room (22-24 ºC) with access to food pellet and water provided *ad libitum*. Mice were also given diet gels to prevent the loss of bodyweight as the study progressed. All animal use and treatments were approved by the Biogen Institute of Animal Care and Use Committee (IACUC) and followed the National Institute of Health Guide for the Care and Use of Laboratory Animals.

AAV vector design and production

AAV-miR-SOD1 is a single-stranded AAV9 vector composed of ubiquitous CAGG promoter driving the expression of two artificial microRNAs designed to target human SOD1, miR30a-huSOD1_#5 and miR155-huSOD1_#7.

miR30a scaffold with mature guide huSOD1_#5 underlined:

5'TGTTTGAATGAGGCTTCAGTACTTTACAGAATCGTTGCCTGCACATCTTGGAAA
CACTTGCTGGGATTACTTCTTCAGGTTAACCCAACAGAAGGCTAAAGAAGGTATAT
TGCTGTTGACAGTGAGCGTACTTTCTTCATTTCCACCTTTTAGTGAAGCCACAGAT
GTAAAGGTGGATGAAGAAAGTATGCCTACTGCCTCGGACTTCAAGGGGCTACTTT
AGGAGCAATTATCTTGTTTACTAAAACTGAATACCTTGCTATCTCTTTGATACATTTT
TACAAAGCTGAATTAAAATGGTATAAATTAAATCACTTTA**3'**.

miR155 scaffold with mature guide huSOD1_#7 underlined:

5'CTGGAGGCTTGCTGAAGGCTGTATGCTGTCAGGATACATTTCTACAGCTTTTGGC
CACTGACTGACAAGGTGGATGAAGAAAGTACAGGACACAAGGCCTGTTACTAGC
ACTCACATGGAACAAATGGCC **3'**.

These artificial microRNAs target the human superoxide dismutase 1 (SOD1) mRNA in the cytoplasm for degradation via the RNA interference pathway. The expression and transcriptional regulation of the cassette is enhanced by the addition of the Woodchuck Hepatitis Virus Post-transcriptional Regulatory Element (WPRE), and a human growth hormone poly-A (hGHpolyA) signal downstream of the artificial microRNAs.

AAV vectors were produced by PackGene Biotech (Worcester, MA, USA) by triple plasmid transfection protocol and the protocol has been described previously (Torregrosa et al., 2021). The AAV produced was assessed for sterility, endotoxin level and purity. Qualitative empty to full capsid assessment was determined by transmission electron microscopy (TEM). The titer was determined via ddPCR method targeting the WPRE.

Intrathecal Injections

Intrathecal injections were performed at 6 weeks of age. Mice were anesthetized with isoflurane and the depth of anesthesia was assessed via a toe pinch. Ethiqua XR (buprenorphine extended-release injectable suspension) (Fidelis Animal Health, North Brunswick, NJ, USA) was administered to eliminate pain sensation. The mouse fur was clipped from the injection area and an ocular lubricant was applied. The mouse was placed on a heating source in ventral recumbency. The injection site was thoroughly cleaned, including three wipes with betadine and three wipes with isopropyl alcohol (alternating). Vertebral processes were detected by arching the spine which allows correct orientation and placement of the needle. A 29-gauge, 0.3mL syringe (Cat#: 4429-3, Smiths Medical ASD, Inc., Southington, CT, USA) was inserted in the gap between L5 and L6 or L4 and L5 and a tail flick is detected if the needle is in the correct location. The test articles or vehicle (artificial cerebrospinal fluid - CSF) was slowly administered (10 µL, 5E11, 1.0E12, 1.5E12 GC) to minimize rapid changes in CSF pressure. Mice were then transferred to a heating chamber set at 37C for recovery first and then placed in their home cages.

Neurofilament light measurement

Mice were bled (~100 µL) via facial vein puncture at -1, 3-, and 6-weeks post-injection. The blood was collected in BD Microtainer SST Clog Activator/Gel tubes (Becton Dickinson, Franklin Lakes, NJ, USA). The tube was inverted a few times and left for 30 mins for

coagulation. The tube was then centrifuged at 2000 RCF (4600 RPM) for 10 minutes to separate the serum. Neurofilament light in serum was quantified via Simple Plex Human NF-L Cartridge (Protein Simple, SPCKB-PS-002448, San Jose, CA, USA) by following the manufacturer's protocol.

Isolation of lumbar dorsal root ganglia

Mice were sacrificed at 6 weeks post-injection (12 weeks of age) and perfused with phosphate buffered saline. Removal of blood allowed for easy identification of the dorsal root ganglia which emerged from the intervertebral foramina. The mouse was pinned to a dissection board and the vertebral column was exposed by an incision from the base of the tail to approximately the cervical region of the column. Using bone cutting scissors or equivalent, an incision horizontal to the column was made to break through the vertebral processes without damaging the dorsal regions of the spinal cord. A 45-degree mini scissor was used to debone the spinal cord by cutting the vertebral processes longitudinally along with removal of the associated dorsal muscle and connective tissue. Using Dumont #5/45 Forceps (Fine Science Tools, CA, USA) and Vannas Spring Scissors (Fine Science Tools, CA, USA), the lumbar ganglia were exposed by pulling the spinal cord slightly to the side which allowed easy removal of the ganglion body. This was accomplished by cutting the spinal nerves and dorsal root. Lumbar 1-6 bilateral ganglia were collected into a 200 μL PCR tube in dry ice and then liquid nitrogen prior to -80C storage.

Nuclei isolation

Iodixanol based density gradient method was employed to isolate nuclei from tissues. The lumbar DRGs from two mice were pooled as a single biological replicate. A minimum of 2 mice was found to generate enough nuclei for sequencing. Pooling was conducted based on sex and summed serum NfL levels from week 3 and week 6 post-injection. Animals with

similar NfL levels were grouped together. For more comprehensive information regarding biological replicates and mouse pooling, please refer to Table S1 in the supplementary information. A detailed list of chemicals, reagents, and solutions required for isolations are noted in supplementary Table S2, these solutions were prepared and stored for up to a month in a 4°C fridge. On the day nuclei isolation, the solutions listed in Table S3 were prepared fresh and stored in ice. The DRGs were kept frozen in dry ice and all solutions and glassware were kept in ice. 1 mL of 40% and 1 mL 30% iodixanol was slowly layered into a 13.2 mL ultracentrifuge tube and kept in ice. Lumbar DRGs were thawed quickly using 100 µL of Hyman lysis buffer. Using a wide tip pipette, the DRGs in lysis buffer were transferred to a Dounce homogenizer filled with 400 µL of Hyman lysis buffer. The DRGs were left in lysis buffer for 1-2 mins. The DRGs were mechanically homogenized with the tight B pestle (x20 passes) slowly limiting bubble formation. 1 mL of Hyman low sucrose buffer was added to the homogenate and gently mixed. The total volume in the Dounce homogenizer was passed through a 70 µm filter into a 50 mL Falcon tube in ice. Another 1 mL of Hyman low sucrose buffer was used to wash the Dounce homogenizer. The sample (~3.5 mL) was centrifuged at 600g for 10 mins at 4°C. The supernatant was discarded, 5 mL of Complete Buffer HP was transferred to the 50 mL Falcon tube to resuspend the nuclei pellet by gentle mixing gently for 5 times. 5 mL of Working Solution was added to the 50 mL falcon tube and mixed 5x (~10 mL). Gently added the homogenate to the ultracentrifuge tube without disturbing the 30% and 40% layers. The ultracentrifuge tubes were placed in the swing bucket, balanced, and centrifuged at 10,000 g for 18 min at 4°C with the brake off. The fatty myelin top layer along with 25% iodixanol layer and some of the 30% layer was vacuum aspirated. A faint nuclei band may be apparent above the 30% layer. Used a wide tip to remove the faint nuclei layer slowly and transferred it to a 1.5 mL tube. Determined the concentration of the nuclei using Countess

II (ThermoFisher Scientific, Waltham, MA, USA) and kept the sample in ice prior to library preparation, droplet generation and sequencing.

Generation of single-nuclei libraries, processing and sequencing

Single nuclei RNAseq Library preparation used the 10X Genomics Chromium Next GEM Single Cell 3' HT Kit v3.1 (PN-1000348, 10X Genomics, CA, USA), following the manufacture protocol (User Guide, CG000416). The aim was to sequence 10,000 nuclei/sample, sufficient Cell-RT mix was prepared for the GEM generation step. This Cell-RT mix, the 3' HT Kit v3.1 gel beads, and emulsion oil were subsequently loaded on a Chromium Next GEM Chip M following the loading procedure in the user guide. GEM generation was achieved using the Chromium-X Controller. The samples underwent a post-GEM-RT cleanup, cDNA amplification (comprising 12 cycles with v3.1), and library construction. The sample index PCR was performed with 13 cycles, using the Dual Index Kit TT Set A, PN-1000215. The libraries were quantified using the Qubit dsDNA HS Assay Kit (Thermo Fisher Q33230) and profiled with the Bioanalyzer High Sensitivity DNA kit (Agilent Technologies 5067-4626). Illumina's NovaSeq6000 was used to sequence the libraries.

CellRanger version 7.0.1 was used to process the sequencing raw data. The transcriptome cell reference used 'Mouse.GRCm38.vM25' which was modified to include the AAV-miR-SOD1 transgene noted as *SOD1_ITR2ITR*. The quality of the sequencing per sample was assessed by the Cell Ranger output metrics such as: median genes per cell, estimated number of cells, mean reads per cell, total genes detected, median UMI counts and percent of reads mapped confidently to genome. A summary of all Cell Ranger quality control metrics can be found in Table S3.

Ambient RNA removal

Ambient RNA removal was achieved by CellBender (Fleming et al., 2023). The Cell Ranger output 'raw_feature_bc_matrix.h5' files were used as input. The Cell Ranger summary metrics output "Estimated Number of Cells" was used as "expected_cells" when running CellBender. The number of "total_droplets_included" was set to values between 5,000 to 7,000 nuclei which represented the point with the plateau of the barcode rank plots.

scRNASequest pipeline: single nucleus RNA sequencing analysis

The scRNASequest (https://github.com/interactivereport/scRNASequest) is an automated single-cell and single-nucleus RNA-seq data analysis workflow allowing for preprocessing, harmonization, reference-based cell label transfer, embedding projection and gene expression analysis (K. Li et al., 2023). The output of the pipeline generates results in h5ad format and visualization can be achieved by cellxgene VIP with data hosting on CellDepot (Lin et al., 2022). The main configuration file, *config.yml*, included 2 reference datasets: Jung and colleagues and Renthal and colleagues for label transfer (Jung et al., 2023; Renthal et al., 2020). In the *config.yml* file, the percent mitochondrial gene cutoff was 20%. The number of genes per cell cutoffs of was >5 and <6,000. The minimum number of genes per cell was 50. The cuffoff for UMI counts was 80,000. The data harmonization was achieved by SCT normalization followed by Harmony (set as *sctHarmony* in the *config.yml* file) The *clusterResolution* value was set to 0.6. A detailed *config.yml* file is provided at the end of this chapter after the biblography. *sctHarmony_umap* embedding plot provided the most optimal representation of the dataset. The first run generated a total of 305,968 nuclei and 41 sctHarmony clusters. Specific cutoffs were selected to remove cytoplasmic RNA (low intron rate/ high exon rate), remove doublets, remove low quality nuclei to eliminate/limit the granularity and improve the quality of the dataset. The second filtration step included the following cutoffs: $intron\_rate \geq 0.5$, $CBkeepR \geq 0.7$, $predicted.Jung.celltype \geq 0.7$, $scDblFinder.score \leq 0.4$. The resulting nuclei subset post-secondary filtering yielded 219,442

nuclei and 28 defined sctHarmony clusters. Label transfer from the two references cited above successfully labeled almost all clusters. Manual labelling was required for a few clusters with unclear labels. This was achieved by finding the top gene markers and comparing the expression level of each marker gene(s) in the unidentified clusters. Other marker genes from previously published research articles were used to confirm the cluster labels. For the neuronal sub-clustering, cluster labels were solely based on Jung et al., 2023 annotations.

Differential gene expression, gene ontology and pseudobulk generation

The scRNASequest pipeline allows differential expression analysis using various software methods. NEBULA-HL was selected for comparison between neurofilament light quartiles for each cell type with HL mode (He et al., 2021). The output gene lists were filtered by FDR <0.05 and |log2FC| >1.2. Gene ontology and GO enrichment analysis were determined using ShineyGO 0.80 (http://bioinformatics.sdstate.edu/go/) (Ge et al., 2020). The pseudobulk was generated by extracting the UMI raw counts, the count per million normalized expression and count per 1k cell normalized expression from the h5ad object. The counts and the metadata were aggregated into each biological replicate. An R Shiny app known as Quickomics was used to generate heatmaps and boxplots (B. Gao et al., 2021).

Statistical analysis

In addition to the tools described above, GraphPad Prism 8 (San Diego, CA, USA), RStudio 4.3.0 (Posit, Boston, MA, USA), Python via Project Jypyter (jupyter.org) were used to plot and analyze the data.

Results

Single nucleus RNA sequencing of the dorsal root ganglia of mice

In this study, wild type C57BL/6J mice were intrathecally dosed at 6 weeks of age with AAV-miR-SOD1 at 5E11, 1.0E12 and 1.5E12 GC, a vector known to cause DRG injury (Fig. 1a). Serum neurofilament light (NfL) was measured at -1, 3-, 6- weeks post-injection to track DRG and nerve injury (Fig. 1a). Lumbar DRGs from each mouse were collected for downstream nuclei isolation, droplet generation and sequencing (Fig. 1a). Each biological replicate represented nuclei from pooled lumbar DRGs from two mice (Table S1).

A pipeline known as scRNASequest was used to process the data from the Cell Ranger pipeline generated UMI count matrix files to generate quality control metrics, perform harmonization, label transfer and produce an h5ad input file for visualization using cellxgene in CellDepot (K. Li et al., 2023; Lin et al., 2022). Cell Ranger quality control metrics for each biological replicate was examined to ensure successful sequencing, these are summarized in Table S4. The first filtration step was achieved with setting cutoffs in the pipeline. It consisted of removal of objects with low likelihood of being true nuclei: having high mitochondrial gene expression hinting at the presence of cytoplasm minimal features or too many genes expressed indicative of duplexes. Gene expression was corrected with CellBender to remove likely ambient RNAs (Fleming et al., 2023). The second filtration step focused on the output and established another set of cutoffs to improve data quality. The second filtration step removed nuclei with low intron rate (and high exon rate), and nuclei with low predicated cell type scores based on the references Jung et al., 2023. The number of nuclei post-filtrations was 219,442 in 11 distinct clusters represented in the UMAP (Uniform Manifold Approximation and Projection for Dimension Reduction) plot (Fig. 1b). Fibroblasts and satellite glia represented ~50% of all nuclei per replicate followed by Schwann cells and neurons (Fig. 1c, Table S5). AAV-miR-SOD1 preferentially transduced neurons as indicated by ~60% median percent transduction

rate in neurons (Fig. 1d, e). Determination of cluster annotations was achieved by a combination of automated label transfer (from Jung et al, 2023 and Renthal et al., 2020) part of the scRNASequest pipeline and de novo manual marker identification (Fig. 1f). Interestingly, a novel population of cells was noted to be closely related to satellite glia, which expressed genes that were associated with development and regeneration post-AAV-induced DRG injury such as *Epha5*, *Tnc*, *Runx2* (Das et al., 2016; R. Hu et al., 2024; Tucić et al., 2021) (Fig. 1f,g). Comparing the top marker genes from activated satellite glia and satellite glia showed the expression of distinct genes and commonly expressed genes in both clusters (Fig. 1f). Activated satellite glia seems to emerge post-AAV treatment, closely explored in this study (Fig. 1c). Satellite glial cells exhibited close anatomical proximity to neurons and as they fulfill diverse supportive functions for neuronal activity. Consequently, the emergence of this novel cluster is not an unexpected occurrence as gliosis and reactive glia have been reported to accompany post-neuronal injury previously.

Sub-clustering and determination of neuronal subtypes

There are distinct types of sensory neurons in the DRG differentiated by their physiology (stimuli detected), anatomy (degree of myelination and axonal projections) and molecular marker genes (neurotransmitters, ion channels, G-protein coupled receptors and transcription factors) (Meltzer et al., 2021). Neuronal nuclei were isolated and clustered separately to yield 11 distinct clusters (Fig. 2a). The labels and naming convention followed Jung et al., 2023. The sensory neurons annotated were three types of low threshold mechanoreceptors (AβRA-LTMR, Aδ-LTMR, and C-LTMR), cold thermoreceptors, three types of none-peptidergic nociceptors (NP1 NP2, NP3), three types of peptidergic nociceptors (PEP1, PEP2.1, PEP2.2), and an unknown cluster (Fig. 2a). The largest populations of sensory neurons were Aβ RA-LTMR and NP1 in all biological replicates (Fig. 2b). The difference found in the present dataset has led to uncertainties regarding the labels attributed to Aβ RA-LTMR and PEP2.1, font color in red.

Also, this dataset revealed two distinct and separated populations of PEP2 neurons that were labelled as PEP2.1 and PEP2.2 deviating from Jung et al., 2023 designations. The top marker genes for some neuronal subtypes overlap with other closely related subtypes, this is seen with the LTMRs with the expression of *Ntrk3* and *Scn1a* (Fig. 2c). Distant neuronal subtypes such as NP3, PEP2.2 and Cold thermoreceptors exhibited distinct expression of marker genes (Fig. 2c). It is important to note that the top marker genes used by Jung and colleagues were not sufficient in distinguishing the neuronal subtypes (Fig. S1). For example, the expression levels of marker genes previously identified by Jung et al. showed low expression, and certain markers such as *Pvalb*, *Zpf521/ZNF521*, and *Fam19a1* were absent in this dataset (Fig. S1). Therefore, additional markers gathered from the supplementary material of Jung et al. were used for cluster labeling (Fig. 2c). Furthermore, the median percent (± IQR) transduction in neurons was 56.41 ± 20.87% for 5E11 GC AAV-treated mice and peaked to 65.70 ± 3.71% for 1.5E12 GC treated mice (Kruskal-Wallis Test followed by Dunn's Multiple Comparison test, **P>0.05*, ***P>0.01*) (Fig. 2d). The median transduction within neuronal cell types ranged from 48% to 76% with Cold thermoreceptors having the lowest and AβRA-LTMR having the highest transduction rates (Fig. 2e).

Neurofilament light is associated with DRG toxicity

Neurofilament is a cytoskeletal component found in the cytoplasm of soma and the axons of neurons. Neurofilament light (NfL) has been found to be elevated in the cerebrospinal fluid and blood following neuronal degeneration in many models of disease (Gaiani et al., 2017). Neurofilament has been shown to be an indicator of DRG toxicity following AAV delivery in animal models (Fader et al., 2022; Johnson et al., 2023; Tien et al., 2024; Tyszkiewicz et al., 2024). Mean serum NfL levels significantly surged to 4074.58 ± 1908.73 pg/mL for 1.5E12 GC AAV-treated mice compared to 183.80 ± 100.09 pg/mL for vehicle-treated mice (one-way ANNOVA followed by Tukey's Honest Significant Difference test, ***P<0.01*) (Fig. 3a). The

wide standard deviation within dosage for all AAV-treated mice indicated a large variability in the observed levels of damage severity among the mice. Plotting the percent neuron for each biological replicate against serum NfL showed a weak negative correlation (R=-0.35) (Fig. 3b). This is partly driven by the variability in neuronal percent within each replicate which is evident in the vehicle-treated mice (Fig. 1c) and the variability of NfL within dose (Fig. 3b). The variability in NfL levels might indicate differences in the amount of AAV reaching the DRG. Mice were assigned quartiles (0-0.25, 0.25-.50, 0.75-1.00) based on serum NfL to assess trends as an alternative to AAV dosage (Fig. 3c, d). Animals assigned for quartile 1 (Q1) represented mice with no AAV-induced DRG toxicity and mice assigned for quartile 4 (Q4) represented animals with severe AAV-induced DRG toxicity as represented with neuronal cell body loss (Fig. 3c, d).

The cell type percentages for all replicates were computed and graphed against both dosage and NfL quartiles. The neuronal content remained constant when measured against dosage, contrasting with the decrease observed in NfL quartiles from a median of 14.4% to 5.9% (Fig. 3g, h). The reduction in satellite glia and Schwann cells by dosage was mirrored in the NfL quartile. The rise in macrophages and T cells was more pronounced by NfL quartile compared to dosage. Fibroblasts remained unchanged by dosage, unlike the increase seen by NfL quartile. The increase in the percentage of activated satellite glia by NfL quartile was notably distinct, unlike the unclear pattern by dosage. The median contribution of activated satellite glia by NfL quartile rose from less than 1% in Q1 to 11.21% in Q4. In general, grouping animals by NfL quartiles significantly enhanced the trends observed by dosage (one-way ANNOVA followed by Tukey's Honest Significant Difference test, $*P<0.05$, $**P<0.01$, $***P<0.001$). Given that AAV-induced toxicity is closely linked to the temporary increase in serum NfL, it was more effective to perform the transcriptomic analysis by NfL quartile rather than dosage. This method facilitated the discovery of amplified transcriptomic signatures related to DRG toxicity

and avoided the dilution of signal that would have occurred if analyzed by dosage. After all, serum NfL surge is a strong indicator of DRG toxicity, and the absence of serum NfL is associated with a resolved state of DRG toxicity. Hawley et al. demonstrated that pathological lesions decreased at 27- and 38-weeks post-injection, which coincided with a decrease in serum neurofilament (Hawley et al., 2024). To conclude, grouping by NFL quartiles increased the significance and resolution of the trends relative to grouping by AAV dosages.

Differentially activated genes in response to AAV treatment

The observed variations in the ratio of DRG cell types are probably influenced by modifications in gene expression. How do the various types of cells respond to DRG-induced injury? A computationally efficient method, NEBULA, was used to conduct differential expression analysis for each cell type by NfL quartiles (Q2, Q3 and Q4) compared to Q1. Quartile 1 mice represented no DRG toxicity while Q4 represented animals with severe DRG toxicity. The highest differentially expressed gene (DEG) counts were found in activated satellite glia (1047), macrophages (107) and T cells (98) in the comparison of NfL Q4 versus Q1 using a Log_2 fold change cutoff of 1.2 and false discovery rate (FDR) < 0.05 (Fig. 4a, Table S6). The number of DEGs was found to increase by quartile (Fig. 4a, Table S6). Interestingly, DEGs in neurons were minimal. Many of the DEGs overlapped across quartiles, as seen with activated satellite glia where 400 genes were found in all comparisons (Fig. 4b). Activated satellite glia is likely sensitive to neuronal damage as large transcriptomic alterations were observed Q2 relative to Q1. Similarly, many genes were found altered in macrophages and less so in T cells (Fig. 4c, d).

Neurons undergo cell death in injured DRG

As reported in previous histopathology-based studies, neurons degenerate following the administration of stressor AAVs into the blood or the cerebrospinal fluid. In this study, a sharp and dramatic decline was observed in neurons, a median of 14.39% at NfL Q1 to 5.91% in NfL

Q4 (Fig. 4h). Focusing on DEGs, 41 genes were observed in the comparison NfL Q4 vs Q1. Many of these genes were associated with developmental and neurogenesis processes and have been reported as such: *Lrrc4c* (Zhang et al., 2021), *Mir6236* (Y.-J. Chen et al., 2021), *Resf1* (Vojtek & Chambers, 2021), *Capsn1* (Amini et al., 2013), *Gprasp2* (Edfawy et al., 2019), *Trpv1* (Ramírez-Barrantes et al., 2016), *Ncl* (Perry et al., 2016) and *Tcp1* (X.-Q. Chen et al., 2018) (Fig. 5a). Some downregulated genes were associated with cell morphology and cytoskeletal organization - *Cnn3* (Junghans & Herzog, 2018), axonal integrity – *Zfp36l2* (Cargnin et al., 2014), myelination-*Gap1* (Loughner et al., 2016) and downregulation of potassium channel – *Kcng2* (Fig. 5a). Consistent upregulation of cell death genes in neurons (associated with GO term Biological "Neuron Apoptotic Process") were particularly evident in NfL Q4, (see Fig. 5b, c). Some of these upregulated genes like *Bax*, *Cdk5* and *Diablo* and downregulated *Adnp* were noted (Fig. 5c). However, it was not clear whether all or just select neuronal subtypes were susceptible to degeneration. After identifying and quantifying ten different neuronal subtypes in these DRG samples, if became evident that all neuronal subtypes declined from NfL Q1 to Q4 (Fig. 5d). The largest population, AβRA-LTMR declined from a mean of 5.54 ± 2.10% to 3.03 ± 1.89% and the second largest NP1 declined from 3.90 ± 1.03% to 1.77 ± 0.97% (Fig. 5d). NP neurons were all found to reach significance with the Q1 vs Q4 comparisons which may suggest they could be the most sensitive to AAV toxicity (one-way ANNOVA followed by Tukey's Honest Significant Difference test, $*P<0.05$).

Activated satellite glia alleviated AAV-induced DRG injury

Activated satellite glia emerged as a novel cluster in response to AAV-induced toxicity (Fig. 3h). It is the cluster that showed the largest number of DEGs especially at the Q4 vs. Q1 comparison with more genes downregulated (697) than upregulated (350) (Fig. 4a, Table S6). To investigate these genes further, Gene Set Enrichment Analysis was employed to determine the pathways and biological processes altered. Robust enrichment of the “neurogenesis” term

along with other processes such as “cell migration” were noted (Fig. 6a). The pseudobulk heatmap of the “neurogenesis” process genes showed consistent upregulation of a subset of genes in NfL Q2, Q3 and Q4 mice and downregulation of another, slightly larger subset (Fig. 6b). Interestingly, upregulated genes had similar expression levels from NfL Q2 to Q4. A similar trend was observed for the "cell migration” process. Investigating a subset of these genes in embedding plots of activated satellite glia showed high expression of *Dok4*, *Gdnf* , and *Wnt10b,* genes that are important for neurite outgrowth and neuronal development (Airaksinen & Saarma, 2002; Garcia et al., 2018) (Fig. 5d). The central nervous system cytokine, *Tafa2*, which plays an essential role on neuronal survival, was also highly expressed in activated satellite glia and neurons (Liang et al., 2023) (Fig. 5d). Other examples of notable genes that were highly upregulated in activated satellite glia are known to be vital for proliferation, differentiation and axonal guidance: *Nrcam* (Sakurai, 2012), *Epha5* (Das et al., 2016), *Tgfbi* (Meyers & Kessler, 2017), *Ngfr* (Siddiqui et al., 2023), and *Runx2* (Shirai et al., 2019) (Fig. 6e). On the other hand, some examples of the downregulated genes like *Adam23* (Markus-Koch et al., 2017), *Nrp2* (Eisenberg et al., 2021, p. 2), *Sema6d* (Thomas et al., 2021), *Plce1* (Yu et al., 2020) and *Ntrk2* (Roussel-Gervais et al., 2023) are essential in axonal guidance, proliferation and differentiation and cell migration. In summary, the proportion of activated satellite glia increases and processes associated with neurodevelopment, axonal guidance and differentiation are significantly affected following neuronal injury and axonal degeneration.

AAV-miR-SOD1 induced inflammation in the dorsal root ganglia

Macrophages are the immune resident cells in the peripheral nervous system with diverse roles, mainly digesting debris/dead cells and managing the inflammatory response. In the mouse DRG, monocytes cell marker *Cx3cr1*, anti-inflammatory macrophages (M2) cell marker *Mrc1* and pro-inflammatory macrophages (M1) by *Cd86* were noted in the macrophage cluster (Fig.

7a). Typically, monocytes circulate in the blood before the migrating into tissues. Monocytes differentiate to either pro-inflammatory (M1) or anti-inflammatory (M2) macrophages in response to changes in the microenvironment such as tissue damage or infection (J. Yang et al., 2014). A shift in the expression of monocytes and macrophages specific genes was observed from NfL Q1 to Q4. A subset of monocyte specific genes were downregulated in NfL Q1 to Q4, such as *Csf1r* and *Ccr2* (Fig. 7b). Interestingly, the anti-inflammatory macrophage (M2) markers such as *Cd163* and *Irf4* were also down-regulated coinciding with the upregulation of pro-inflammatory (M1) macrophage gene signatures, *Cd80* and *Cd38* (Fig. 7c, d). It's worth noting that there was a decrease in *Tlr4* expression, indicating that not all markers were uniform or changed in the same direction. The innate immune response has been known to be involved in responding to AAV (Muhuri et al., 2021). A subset of the Toll like receptor (TLR) cascades genes were upregulated in macrophages indicating the detection of AAV and activation of downstream signaling players. Macrophages showed several TLR receptors (*Tlr8*, *Tlr1*, *Tlr3*, *Tlr12*) that were upregulated with no changes to *Tlr9* and a subset of their downstream components (Fig. S2). This in turn stimulates the interferon pathways and a subset of genes, including *Irf1*, *Stat1*, *Irak1* and *Irf7,* were upregulated in NfL Q4 vs NfL Q1 mice (Fig. 7e). These genes are vital in the antiviral response, the interferon regulatory factors *Irf1* and *Irf7*, for example, are known to modulate the response against viral infections (Irving et al., 2020), while *Irak1* is involved in activating *Stat1* in *Il-1R* signaling (Y. Zheng & He, 2022). Looking at the complement activation system, only a subset of genes exhibited a trend of upregulation, including *C4b*, *C6*, *Itgax*, *C1qc*, *C1qb,* which are components of the classical complement system (Fig. 7f). Collectively, these changes in the innate immune processes activated Nuclear Factor Kappa B (NF- κB) which led to the upregulation of several chemokines (*Ccl5*, *Ccl22*, *Cxcl13*) and cytokines (*Il1a* and *Osm*) (Fig. 7g). These released chemokines and cytokines can then influence the microenvironment and activate/recruit other immune cells such as T Cells

to initiate the adaptive immune response. Gene Set Enrichment Analysis indicated that processes related to “cell migration” (specifically, the clearance of deceased neurons), activation of T cells and “lipoprotein particle clearance” (related to myelin elimination following axonal degeneration) were enriched in dysregulated genes. These processes collectively illustrate the diverse activities in which macrophages engage in response to AAV-induced DRG toxicity. (Fig. 7h). This is clearly seen with some of the highlighted and well-studied genes such as *Gpnmb* (inflammation) (Saade et al., 2021), *Mmp14* (proteolysis) (Llorente et al., 2020), and *Trem2* (Jay et al., 2017) which is involved in diverse roles in macrophages (Fig. 7i).

Fibroblasts are supporting cells in tissues as the maintain the structure integrity and are involved in various functions such as development, repair and immune responses. Fibroblasts were found to increase following AAV-miR-SOD1 dosing by NfL quartiles which is expected due to the loss of neurons. Innate immune responses were observed in fibroblasts where a subset of Toll-Like Receptor (TLR) signaling genes were upregulated such as *Traf3*, *Tlr12*, *Tlr4*, *Tlr7*, *Ripk2* and *Tnf* (Fig. S3). Components of the classical complement pathways were noted like macrophages except for *C3* which was only upregulated in fibroblasts (Fig. S4). A large subset of the interferon (IFN) responses genes were upregulated in NfL Q4 mice, some notable mentions include *Ifngr2*, *Myd88*, *Infnar2*, *Stat2*, *Stat1* and *Jak1* (Fig. S5). Interestingly, *Myd88* which is an adaptor protein to most TLR receptors was only upregulated in fibroblasts but not macrophages. Many cytokines and chemokines were upregulated in fibroblasts which strengthens the inflammatory response and contributes to the activation of the adaptive response (Fig. S6).

T cells induced the cell mediated immune response

T cells play a vital role in the adaptive immune response and coordinate with macrophages and to carry out their functions. In this dataset, three populations of T cells are predicted to be present in the T cell cluster, cytotoxic CD8+ T cell (*Cd8a*), helper CD4+ T cell (*Cd4*) and T regulatory cell (*Foxp3*) (Fig. 8a). The expression of these markers increased from NfL Q1 to Q4 which coincides with the increase in the population of T cells from Q1 (median of 0.81%) to Q4 (median of 8.08%) (Fig. 8b, Fig. 3h). The DEGs detected in T cells in NfL Q4 vs. Q1 comparison translated to increase in lymphocyte activation (Fig. 8c, d), with several cytokines and chemokines such as *Ccl3*, *Cxcl9*, *Il21*, *Il10, Ifng* and *Ccl5* upregulated in the NfL Q4 mice (Fig. 8e). Antigen presenting cells such as macrophages activate helper CD4+ T cells and cytotoxic CD8+ T cells. The presentation of AAV components on major histocompatibility complex class II (MHC-II) for helper T cells and MHC-I for cytotoxic T cells (Muhuri et al., 2021). This is supported by the upregulation of a subset genes associated with each cell type as noted in the pseudobulk heatmaps (Fig. 5f, g). Helper CD4+ T cells prime cytotoxic CD8+ T cells which enables their activity in eliminating transduced cells (Arjomandnejad et al., 2023). In summary, T cells play a significant role in the inflammatory and immune responses triggered by high doses of AAV.

Effects in satellite glia and Schwann cells

Satellite glial cells establish a close association with sensory neurons, thereby offering an array of neurotropic functions. The number of DEGs found in NfL Q4 vs. Q1 was limited to only 80 genes. Gene set enrichment analysis showed that “antigen processing and presentation” was one of the most significantly upregulated process in satellite glia (Fig. S7a). Histocompatibility 2 genes were highly elevated in NfL Q4 relative to Q1 mice as shown in the pseudobulk heatmaps (Fig. S7b). As for Schwann cell, there is pathological evidence of demyelination

following axonal degeneration. This was reflected by the downregulation of the “cholesterol metabolic processes” where many genes important for lipoprotein formation, component of myelin, were downregulated in NfL Q4 relative to Q1 mice (Fig. S7c, d). Overall, the changes in satellite glia and Schwann cells complement the changes that are occurring in the DRG with the immune response and axonal degeneration and demyelination due to AAV.

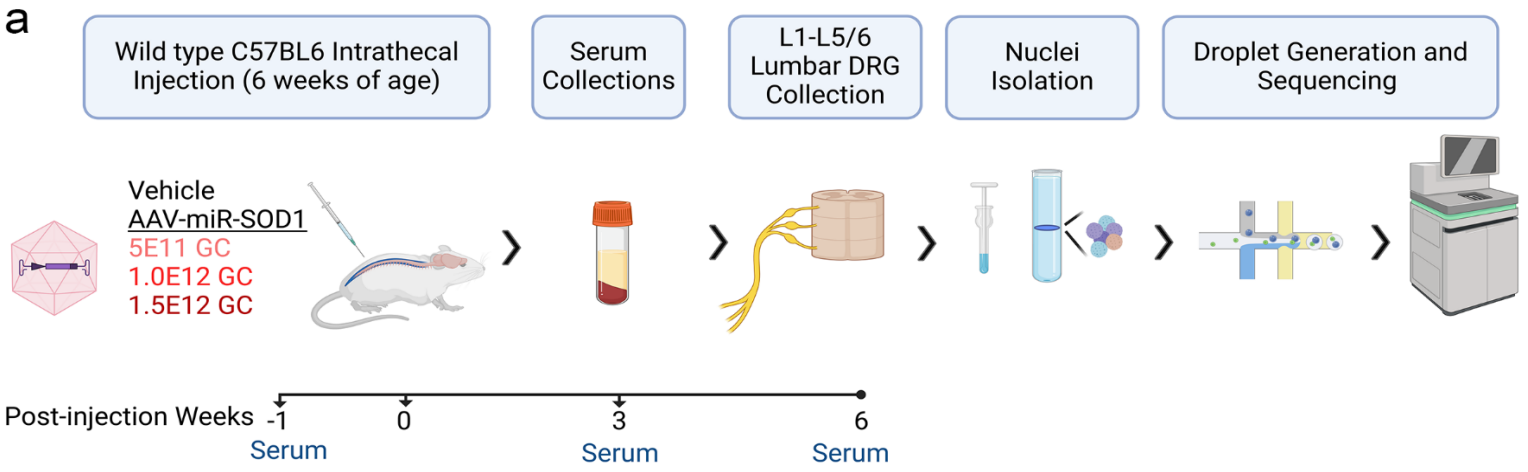
a
Wild type C57BL6 Intrathecal Injection (6 weeks of age)
Serum Collections
L1-L5/6 Lumbar DRG Collection
Nuclei Isolation
Droplet Generation and Sequencing
Vehicle
AAV-miR-SOD1
5E11 GC
1.0E12 GC
1.5E12 GC
Post-injection Weeks
-1
0
3
6
Serum
Serum
Serum

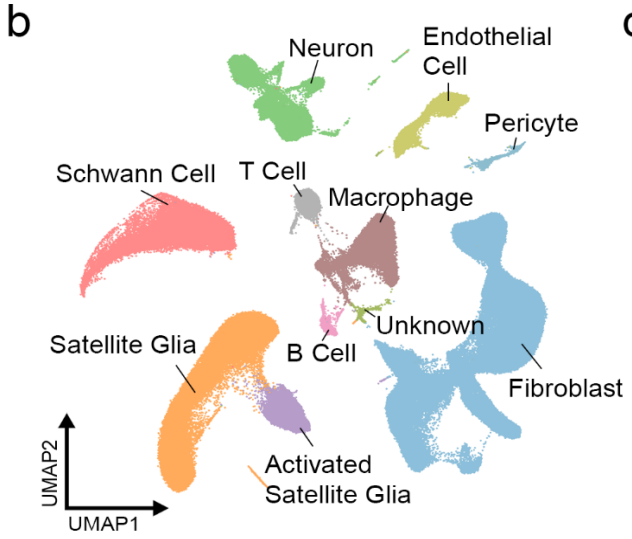
b
Neuron
Endothelial Cell
Pericyte
Schwann Cell
T Cell
Macrophage
Unknown
Satellite Glia
B Cell
Fibroblast
Activated Satellite Glia
UMAP2
UMAP1

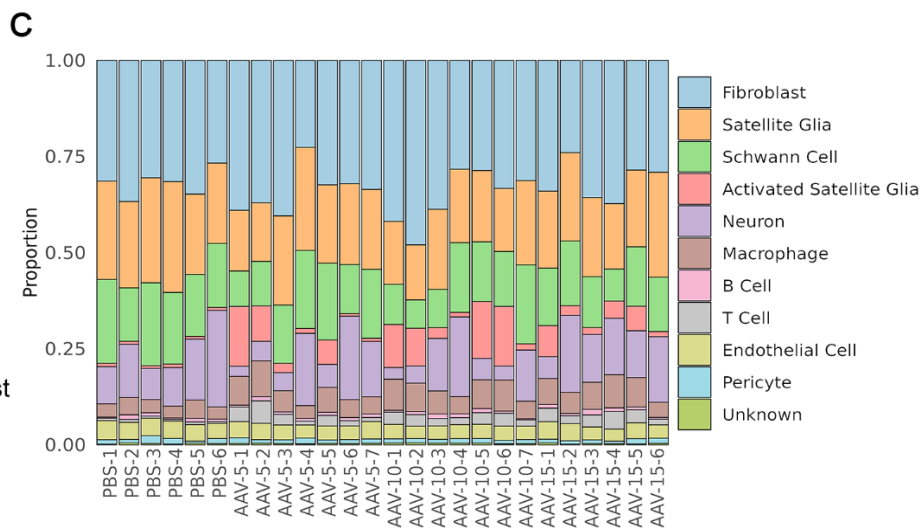
c
Proportion
1.00
0.75
0.50
0.25
0.00
Fibroblast
Satellite Glia
Schwann Cell
Activated Satellite Glia
Neuron
Macrophage
B Cell
T Cell
Endothelial Cell
Pericyte
Unknown
PBS-1
PBS-2
PBS-3
PBS-4
PBS-5
PBS-6
AAV-5-1
AAV-5-2
AAV-5-3
AAV-5-4
AAV-5-5
AAV-5-6
AAV-5-7
AAV-10-1
AAV-10-2
AAV-10-3
AAV-10-4
AAV-10-5
AAV-10-6
AAV-10-7
AAV-15-1
AAV-15-2
AAV-15-3
AAV-15-4
AAV-15-5
AAV-15-6

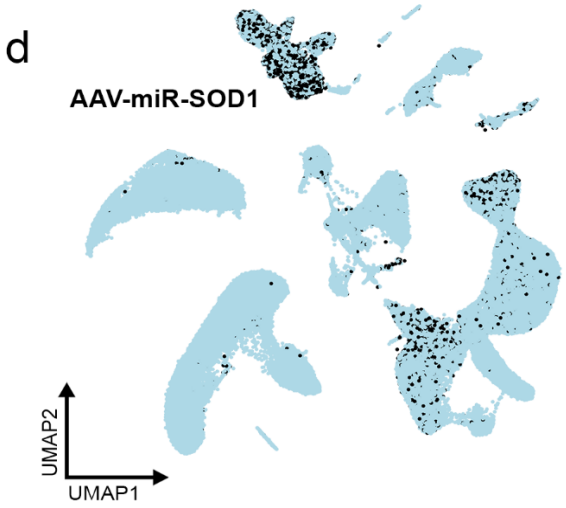
d
AAV-miR-SOD1
UMAP2
UMAP1

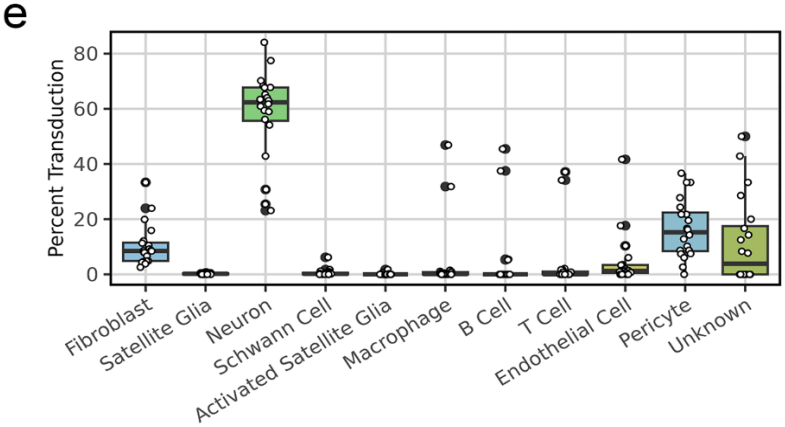
e
Percent Transduction
80
60
40
20
0
Fibroblast
Satellite Glia
Neuron
Schwann Cell
Activated Satellite Glia
Macrophage
B Cell
T Cell
Endothelial Cell
Pericyte
Unknown

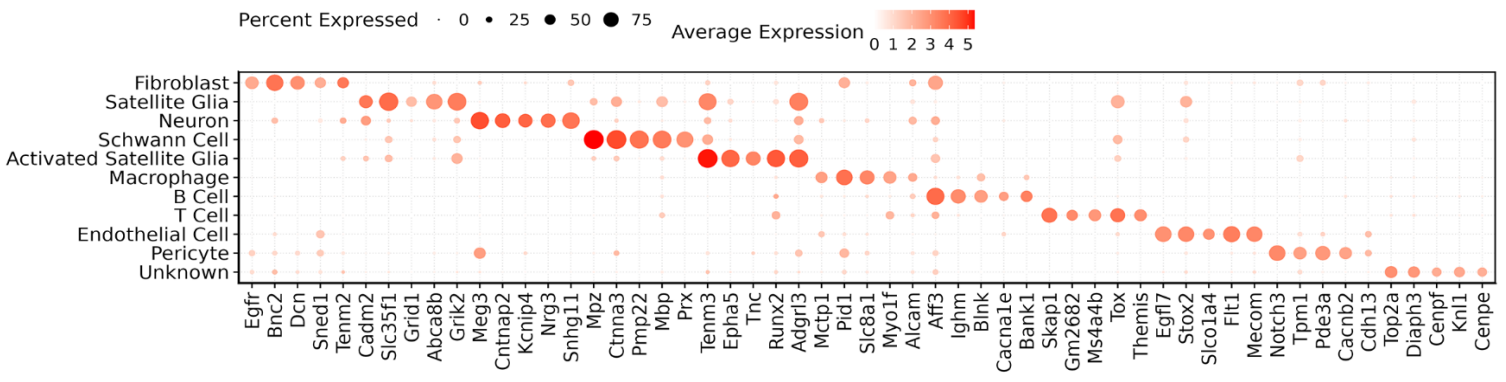
Percent Expressed
0
25
50
75
Average Expression
0 1 2 3 4 5
f
Fibroblast
Satellite Glia
Neuron
Schwann Cell
Activated Satellite Glia
Macrophage
B Cell
T Cell
Endothelial Cell
Pericyte
Unknown
Egfr
Bnc2
Dcn
Sned1
Tenm2
Cadm2
Slc35f1
Grid1
Abca8b
Grik2
Meg3
Cntnap2
Kcnip4
Nrg3
Snhg11
Mpz
Ctnna3
Pmp22
Mbp
Prx
Tenm3
Epha5
Tnc
Runx2
Adgrl3
Mctp1
Pid1
Slc8a1
Myo1f
Alcam
Aff3
Ighm
Blnk
Cacna1e
Bank1
Skap1
Gm2682
Ms4a4b
Tox
Themis
Egfl7
Stox2
Slco1a4
Flt1
Mecom
Notch3
Tpm1
Pde3a
Cacnb2
Cdh13
Top2a
Diaph3
Cenpf
Knl1
Cenpe

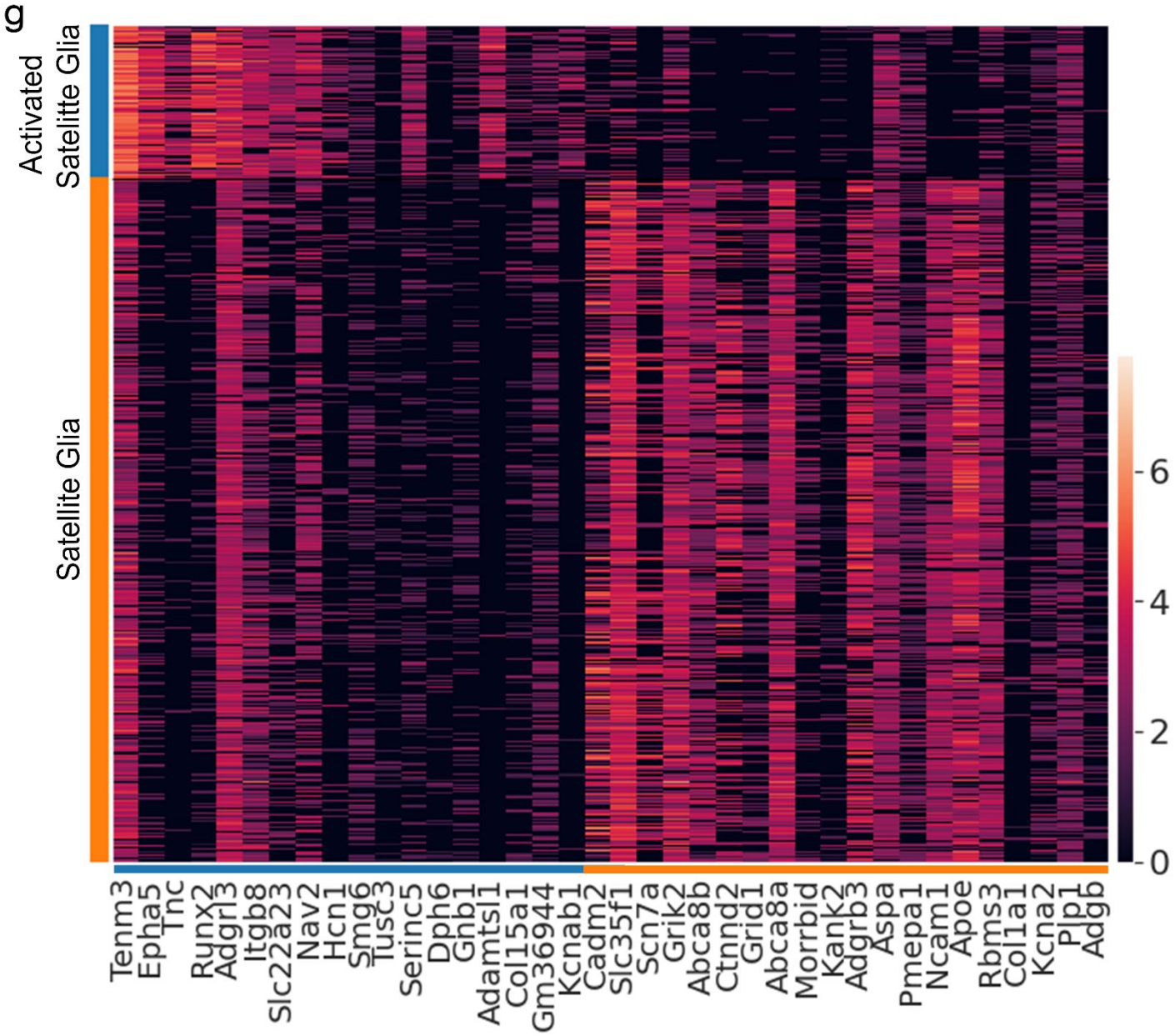
g
Activated Satelitte Glia
Satellite Glia
6
4
2
0
Tenm3
Epha5
Tnc
Runx2
Adgrl3
Itgb8
Slc22a23
Nav2
Hcn1
Smg6
Tusc3
Serinc5
Dph6
Gnb1
Adamtsl1
Col15a1
Gm36944
Kcnab1
Cadm2
Slc35f1
Scn7a
Grik2
Abca8b
Ctnnd2
Grid1
Abca8a
Morrbid
Kank2
Adgrb3
Aspa
Pmepa1
Ncam1
Apoe
Rbms3
Col1a1
Kcna2
Plp1
Adgb

Figure 1: Single-nucleus RNA-seq analysis of dorsal root ganglia (DRG) treated with AAV in C57BL/6J mice. **a.** Experimental timeline and workflow from intrathecal injections to droplet generation (10x Genomics) and sequencing. Serum was collected at -1, 3 and 6-weeks post-injection. **b.** UMAP embedding plot of all sequenced nuclei representing the distinct populations of cells in the DRG. **c.** The percentage proptortion of each cell type per biological sample. Vehicle represents PBS **d.** Embedding plot showing the AAV-miR-SOD1 transduction predominantly in neurons. Each black dot represents transduced nuclei relative to untransduced nuclei (light blue). **e.** Boxplots of percent transduction for all cell types in the DRG. **f.** Dotplot of enriched genes per cell type showing expression represented the color black. **g.** Single nucleus heatmap of the top 20 marker gene expession for each activated satellite glia (blue) and satellite glia (orange). The rows represents individual nuclei. The legend indicates gene expression.

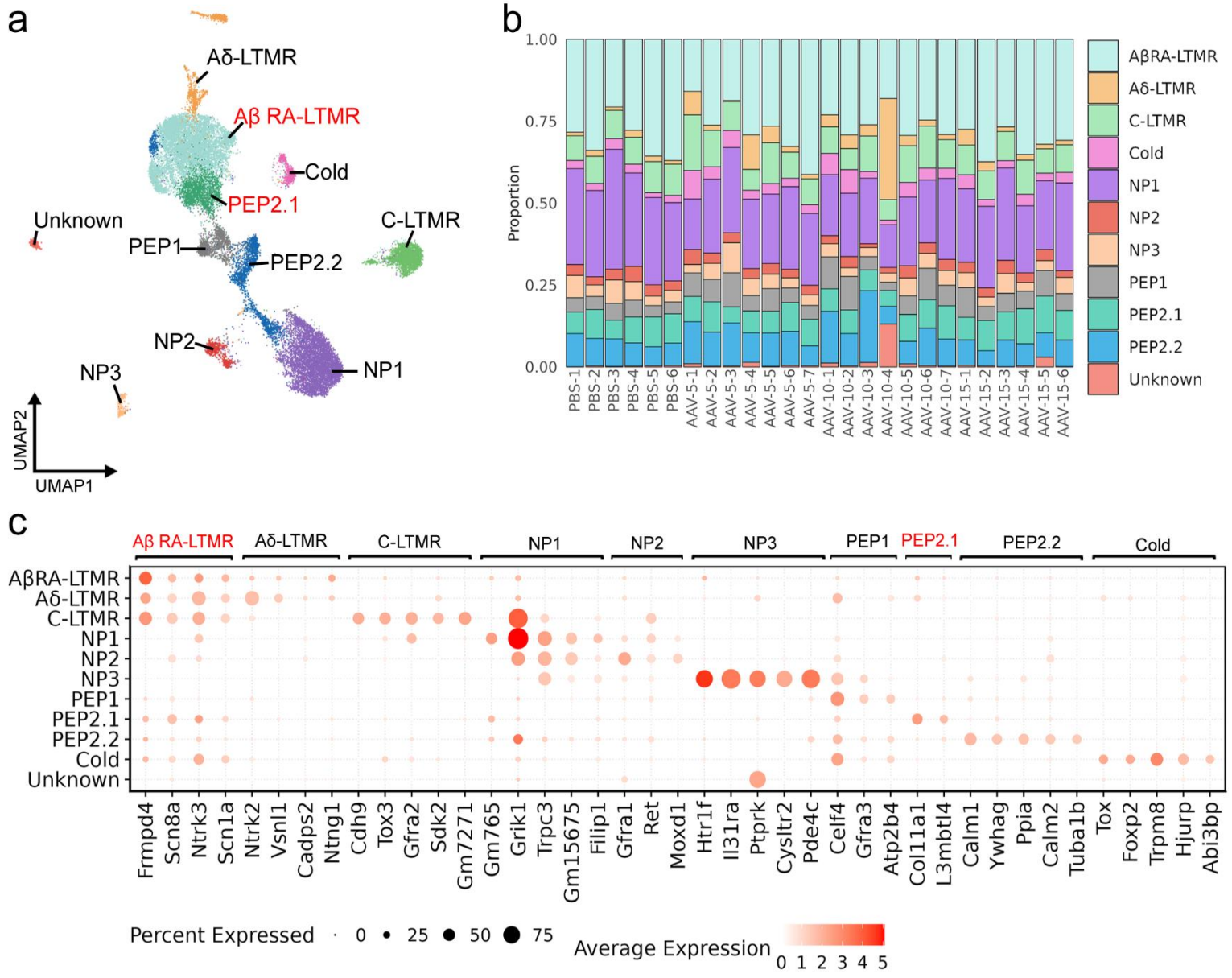
a
Aδ-LTMR
Aβ RA-LTMR
Cold
PEP2.1
Unknown
C-LTMR
PEP1
PEP2.2
NP2
NP3
NP1
UMAP2
UMAP1
b
Proportion
1.00
0.75
0.50
0.25
0.00
PBS-1
PBS-2
PBS-3
PBS-4
PBS-5
PBS-6
AAV-5-1
AAV-5-2
AAV-5-3
AAV-5-4
AAV-5-5
AAV-5-6
AAV-5-7
AAV-10-1
AAV-10-2
AAV-10-3
AAV-10-4
AAV-10-5
AAV-10-6
AAV-10-7
AAV-15-1
AAV-15-2
AAV-15-3
AAV-15-4
AAV-15-5
AAV-15-6
AβRA-LTMR
Aδ-LTMR
C-LTMR
Cold
NP1
NP2
NP3
PEP1
PEP2.1
PEP2.2
Unknown
c
Aβ RA-LTMR
Aδ-LTMR
C-LTMR
NP1
NP2
NP3
PEP1
PEP2.1
PEP2.2
Cold
AβRA-LTMR
Aδ-LTMR
C-LTMR
NP1
NP2
NP3
PEP1
PEP2.1
PEP2.2
Cold
Unknown
Frmpd4
Scn8a
Ntrk3
Scn1a
Ntrk2
Vsnl1
Cadps2
Ntng1
Cdh9
Tox3
Gfra2
Sdk2
Gm7271
Gm765
Grik1
Trpc3
Gm15675
Filip1
Gfra1
Ret
Moxd1
Htr1f
Il31ra
Ptprk
Cysltr2
Pde4c
Celf4
Gfra3
Atp2b4
Col11a1
L3mbtl4
Calm1
Ywhag
Ppia
Calm2
Tuba1b
Tox
Foxp2
Trpm8
Hjurp
Abi3bp
Percent Expressed
0
25
50
75
Average Expression
0 1 2 3 4 5
d
Percent Transduction in Neurons
100
75
50
25
0
*
**
**
Vehicle
5.0E11 GC
1.0E12 GC
1.5E12 GC
e
Percent Transduction of Neuron Subtypes
100
75
50
25
0
AβRA-LTMR
Aδ-LTMR
C-LTMR
NP1
NP2
NP3
PEP1
PEP2.1
PEP2.2
Cold
Unknown

Figure 2: Efficient transduction of neuronal subtypes in the dorsal root ganglia of C57BL/6J mice. **a.** UMAP embedding plot of 10 identified neuronal subtypes and 1 unknown population. Neuronal subtypes in red indicate lower confidence in label relative to others. **b.** Proportion of individual sensory neuron subtypes per biological sample. **c.** Dotplot of distinctly expressed genes for each neuronal subtypes, 2-5 marker genes are shown for each population. Neuronal subtypes in red indicate lower confidence in the final label. **d.** AAV-miR-SOD1 efficiently transduces neurons (Kruskal-Wallis Test followed by Dunn's Multiple Comparison test, **P>0.05*, ***P>0.01*) **e.** Variable transduction of neuronal subtypes in the DRG. C – c-fiber, LTMR – Low Threshold Mechanoreceptor, PEP – Peptidergic nociceptor, NP- None-Peptidergic nociceptor, Cold – Cold thermoceptor. The name designations are based on Jung et al., 2023.

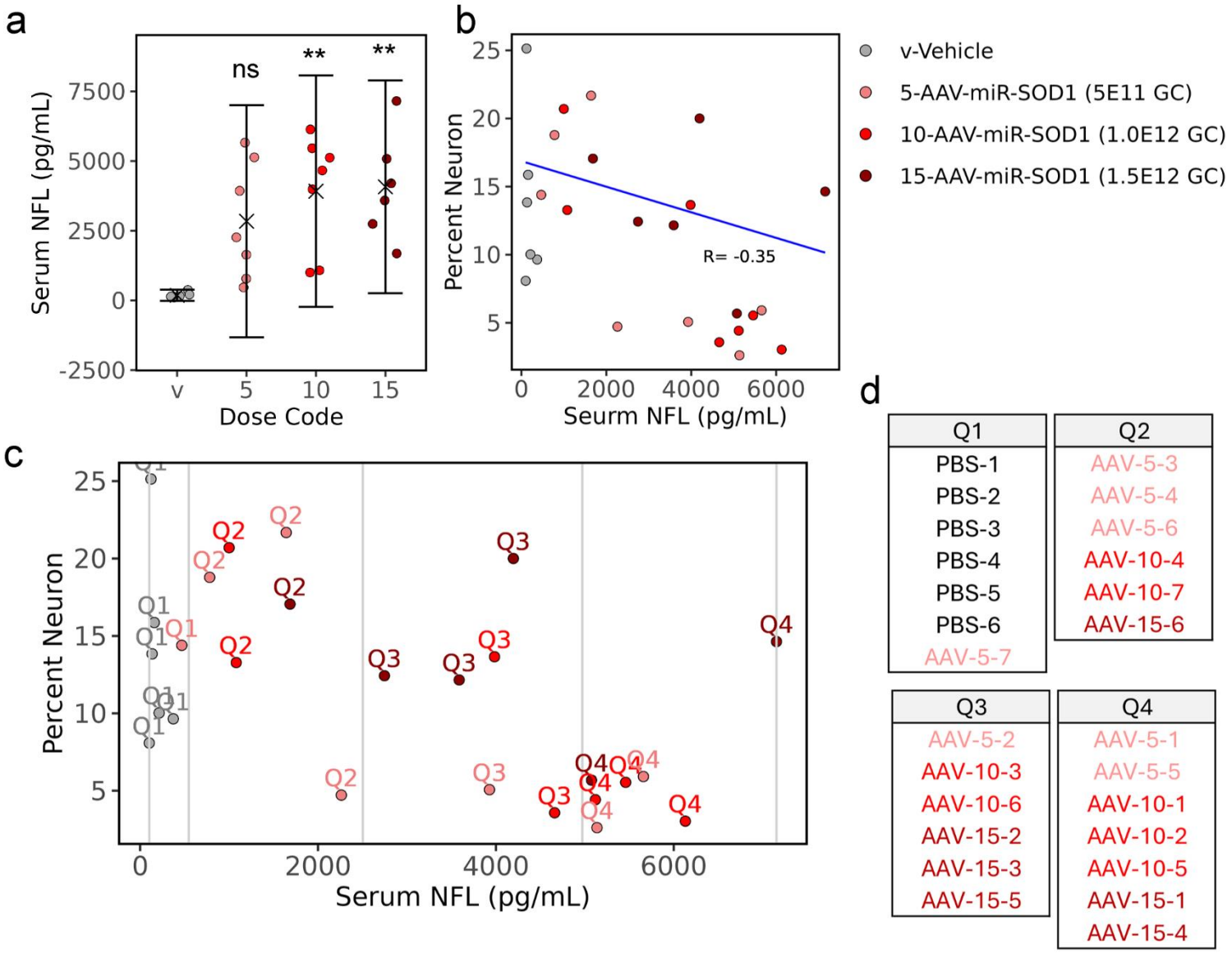
a
Serum NFL (pg/mL)
7500
5000
2500
0
-2500
ns
**
**
v
5
10
15
Dose Code
b
Percent Neuron
25
20
15
10
5
R= -0.35
0
2000
4000
6000
Seurm NFL (pg/mL)
v-Vehicle
5-AAV-miR-SOD1 (5E11 GC)
10-AAV-miR-SOD1 (1.0E12 GC)
15-AAV-miR-SOD1 (1.5E12 GC)
c
Percent Neuron
Serum NFL (pg/mL)
Q1
Q2
Q3
Q4
d
Q1
PBS-1
PBS-2
PBS-3
PBS-4
PBS-5
PBS-6
AAV-5-7
Q2
AAV-5-3
AAV-5-4
AAV-5-6
AAV-10-4
AAV-10-7
AAV-15-6
Q3
AAV-5-2
AAV-10-3
AAV-10-6
AAV-15-2
AAV-15-3
AAV-15-5
Q4
AAV-5-1
AAV-5-5
AAV-10-1
AAV-10-2
AAV-10-5
AAV-15-1
AAV-15-4

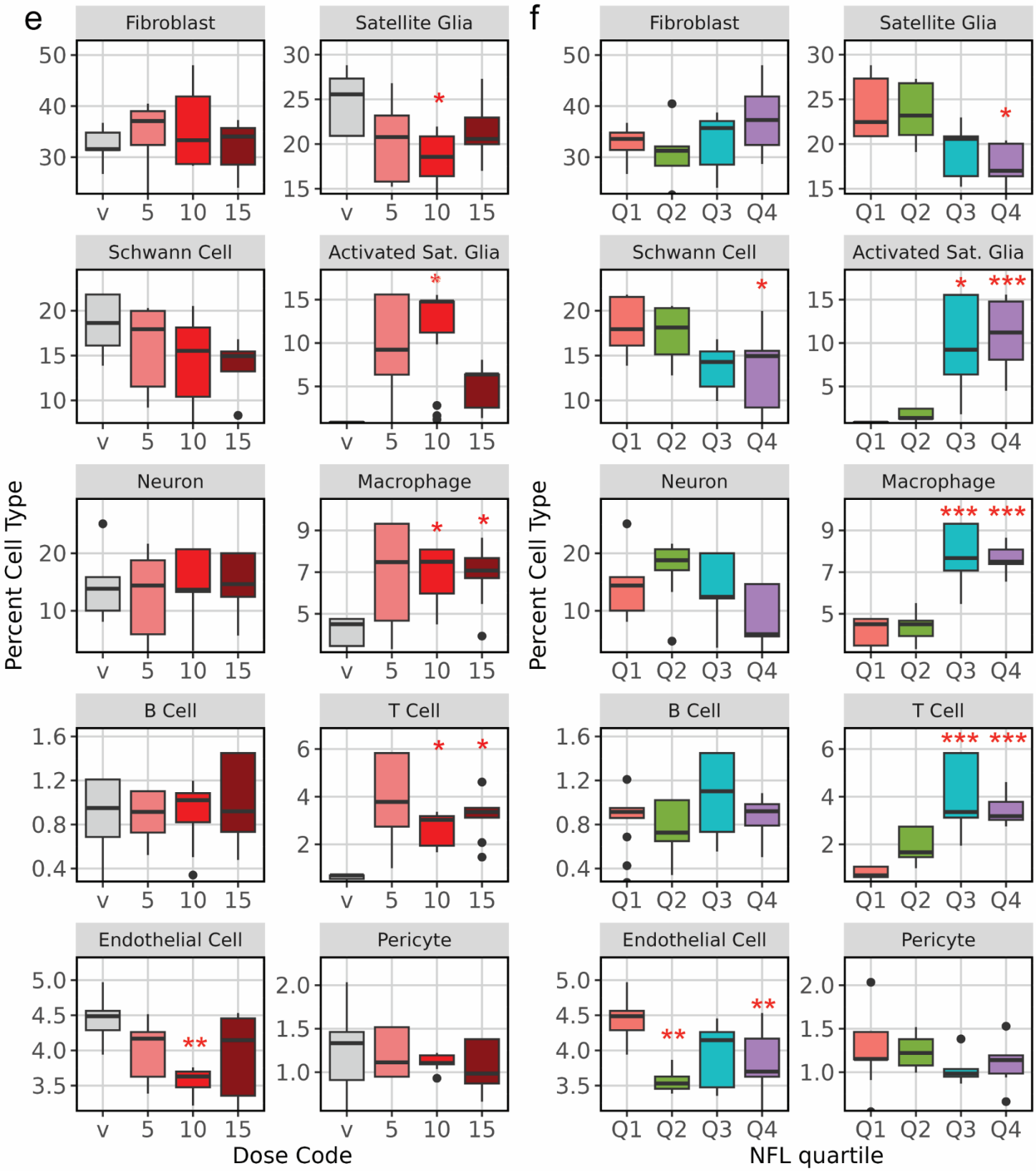
e
f
Fibroblast
Satellite Glia
Schwann Cell
Activated Sat. Glia
Neuron
Macrophage
B Cell
T Cell
Endothelial Cell
Pericyte
Percent Cell Type
Dose Code
NFL quartile
v
5
10
15
Q1
Q2
Q3
Q4

Figure 3: Serum neurofilament light levels surge in response to AAV treatment in C57BL/6J mice. **a.** All dose levels led to an increase in serum neurofilament light (NfL) levels. Neurofilament light levels plotted is the sum of week 3 and 6 post-injection per biological replicate. Data is mean ± SD **b.** Pearson correlation between NfL and percent neuron per biological sample. **c.** A plot showing the quartile divisions and the assignment of each biological sample to an NfL quartile range. Vertical grey lines indicate the quartile ranges. **d.** The assignment of each biological sample to a NfL quartile division. **e.** Boxplot of percent cell type for each cell population by dose code (v – Vehicle, 5 – 5E10 GC, 10 – 10E10 GC, 15 – 15E10 GC). **f.** Boxplot of percent cell type for each cell population by NfL quartile. ns – not significant. For all statistical tests conducted, one-way ANNOVA followed by Tukey's Honest Significant Difference test, **P<0.05, **P<0.01, ***P<0.001*) with all comparisons to vehicle or NFL Q1.

a

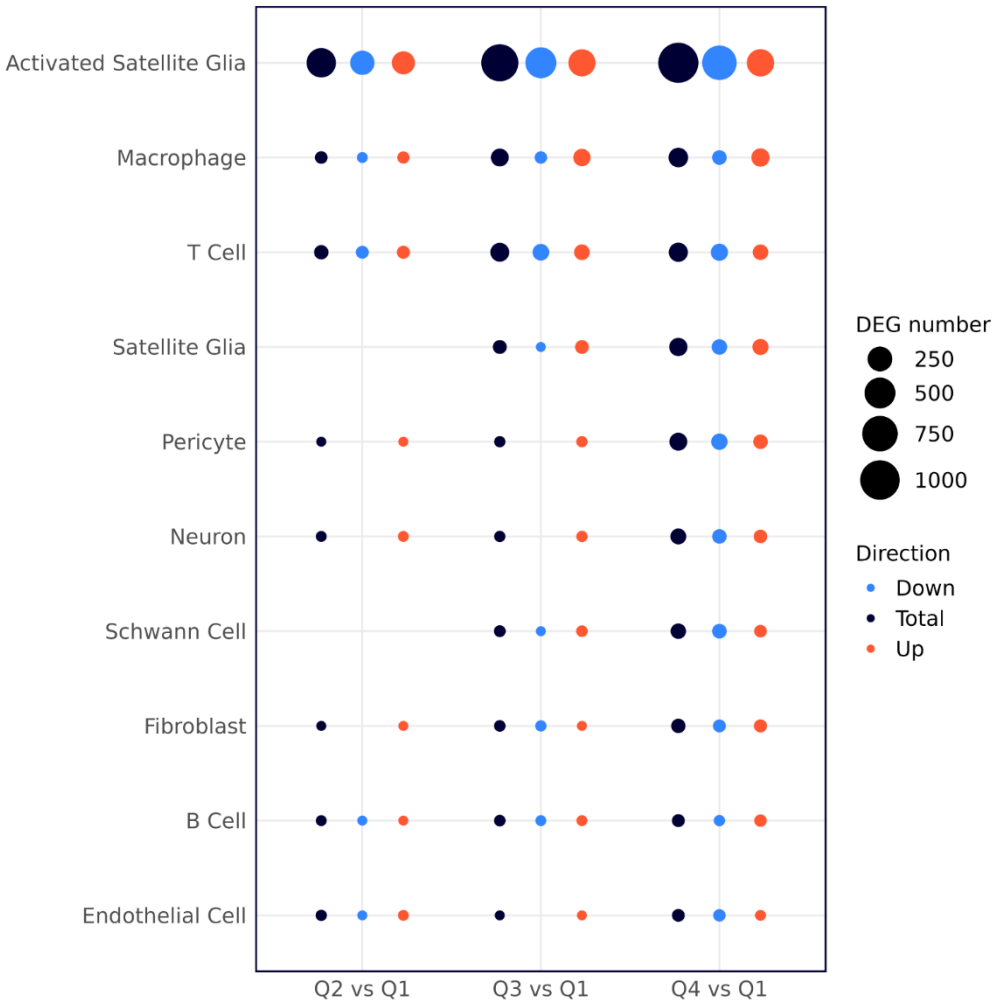
Activated Satellite Glia
Macrophage
T Cell
Satellite Glia
Pericyte
Neuron
Schwann Cell
Fibroblast
B Cell
Endothelial Cell
Q2 vs Q1
Q3 vs Q1
Q4 vs Q1
DEG number
250
500
750
1000
Direction
Down
Total
Up

b

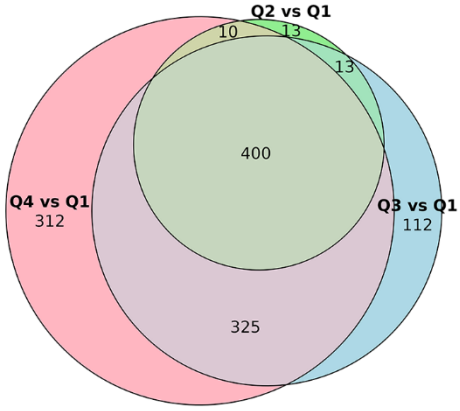
Activated Satellite Glia
Q2 vs Q1
10
13
13
400
Q4 vs Q1
312
Q3 vs Q1
112
325

c

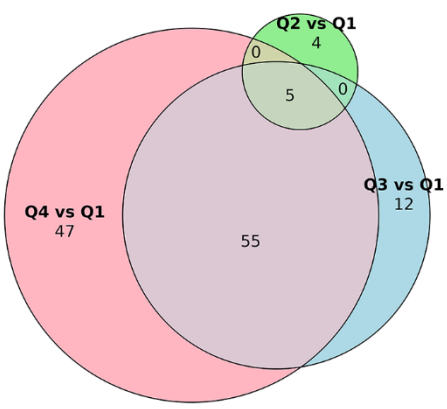
Macrophage
Q2 vs Q1
4
0
5
0
Q4 vs Q1
47
Q3 vs Q1
12
55

d

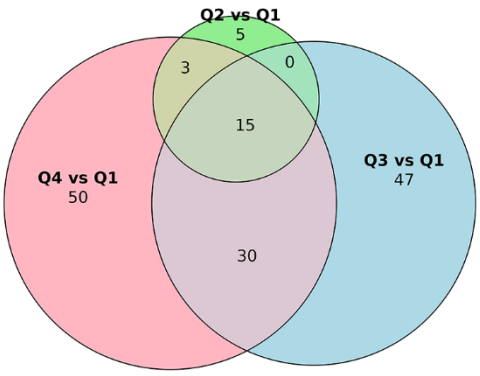
T Cell
Q2 vs Q1
5
3
0
15
Q4 vs Q1
50
Q3 vs Q1
47
30

Figure 4: Activated satellite glia and immune cells display large differentially activated genes by neurofilament light quartile in C57BL/6J mice. **a.** Dotplot representing differentially activated genes by size and direction noted via color. Differential gene expression analysis was conducted by NEBULA. The cutoffs were set $|Log_2FC| > 1.2$ and FDR <0.05. Euler diagram for **b.** Activated satellite glia, **c.** Macrophage and **d.** T Cell showing the overlap of differentially activated genes in each NfL quartile (Q) comparison.

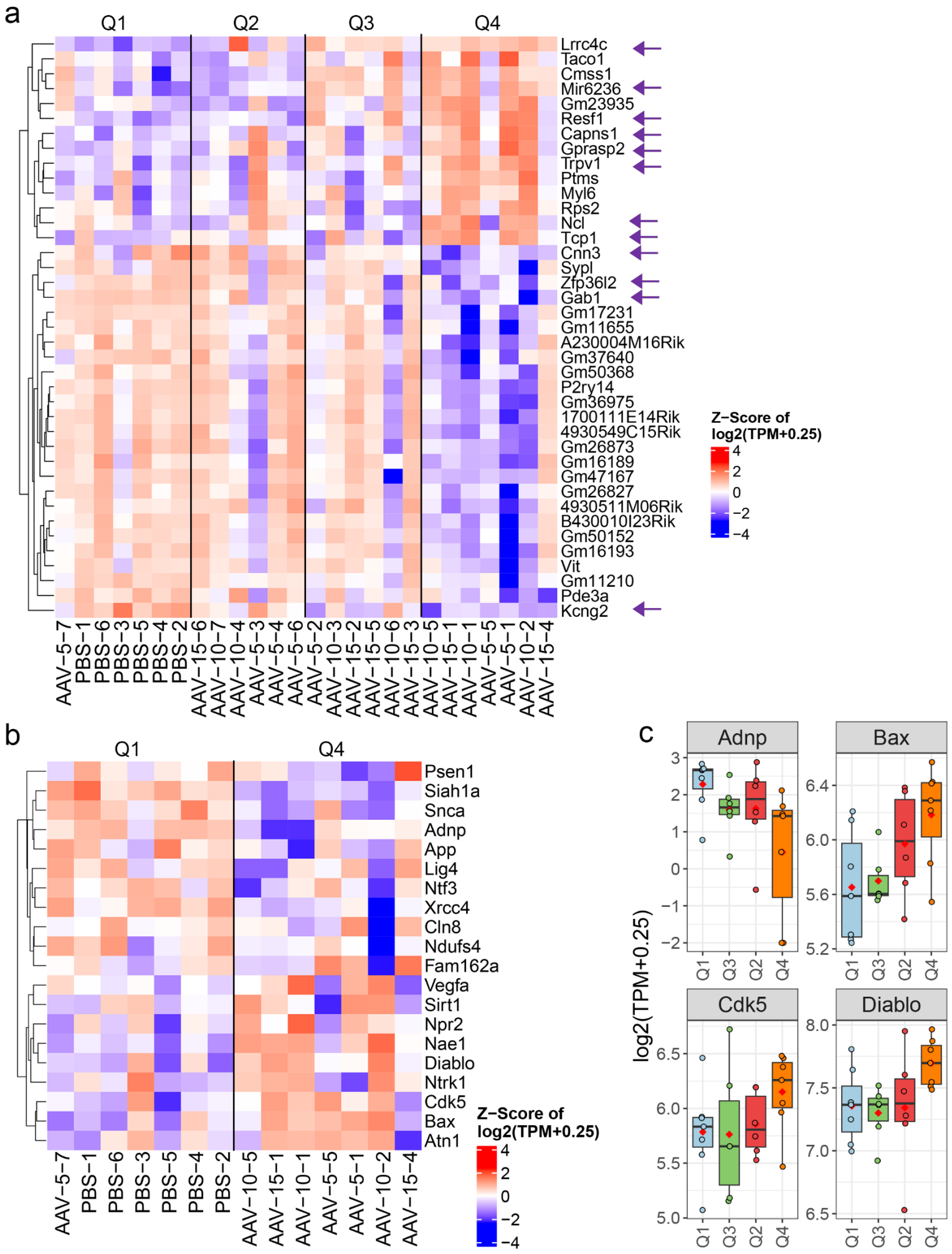
a
Q1
Q2
Q3
Q4
Lrrc4c
Taco1
Cmss1
Mir6236
Gm23935
Resf1
Capns1
Gprasp2
Trpv1
Ptms
Myl6
Rps2
Ncl
Tcp1
Cnn3
Sypl
Zfp36l2
Gab1
Gm17231
Gm11655
A230004M16Rik
Gm37640
Gm50368
P2ry14
Gm36975
1700111E14Rik
4930549C15Rik
Gm26873
Gm16189
Gm47167
Gm26827
4930511M06Rik
B430010I23Rik
Gm50152
Gm16193
Vit
Gm11210
Pde3a
Kcng2
AAV−5−7
PBS−1
PBS−6
PBS−3
PBS−5
PBS−4
PBS−2
AAV−15−6
AAV−10−7
AAV−10−4
AAV−5−3
AAV−5−4
AAV−5−6
AAV−5−2
AAV−10−3
AAV−15−2
AAV−15−5
AAV−10−6
AAV−15−3
AAV−10−5
AAV−15−1
AAV−10−1
AAV−5−5
AAV−5−1
AAV−10−2
AAV−15−4
Z−Score of log2(TPM+0.25)
4
2
0
−2
−4
b
Q1
Q4
Psen1
Siah1a
Snca
Adnp
App
Lig4
Ntf3
Xrcc4
Cln8
Ndufs4
Fam162a
Vegfa
Sirt1
Npr2
Nae1
Diablo
Ntrk1
Cdk5
Bax
Atn1
AAV−5−7
PBS−1
PBS−6
PBS−3
PBS−5
PBS−4
PBS−2
AAV−10−5
AAV−15−1
AAV−10−1
AAV−5−5
AAV−5−1
AAV−10−2
AAV−15−4
Z−Score of log2(TPM+0.25)
4
2
0
−2
−4
c
Adnp
Bax
Cdk5
Diablo
log2(TPM+0.25)
Q1
Q3
Q2
Q4

d

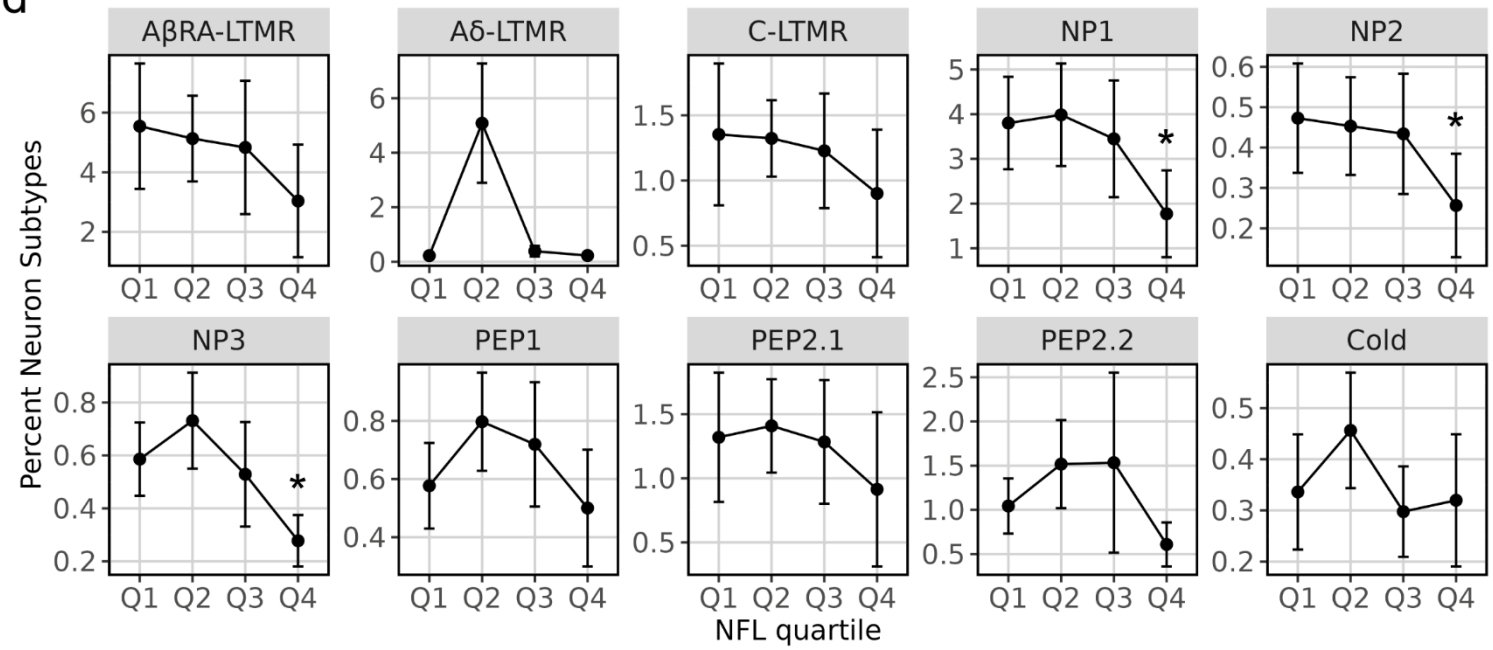
AβRA-LTMR
Aδ-LTMR
C-LTMR
NP1
NP2
NP3
PEP1
PEP2.1
PEP2.2
Cold
Percent Neuron Subtypes
NFL quartile
Q1 Q2 Q3 Q4
*

Figure 5: Genes associated with cell death are upregulated in sensory neurons of C57BL/6J mice. **a.** Pseudobulk heatmap of differentially activated genes in neurons by neurofilament light (NfL) quartile 1 (Q1) to quartile 4 (Q4). The purple arrows indicate genes of interest with known functional annotation. **b.** Pseudobulk heatmap showing a subset of Neuron Apoptotic genes (Go Biological Term) for NfL quartile 1 and quartile 4. **c.** Boxplots of necrosis related genes and change in bulk expression by NfL quartile. Red diamonds indicate the mean **d.** The mean percent of neuronal subtype by NfL quartile. For all statistical tests conducted, one-way ANNOVA followed by Tukey's Honest Significant Difference test, $*P<0.05$ with all comparisons to NFL Q1. Data represents mean ± SD. C – c-fiber, LTMR – Low Threshold Mechanoreceptor, PEP – Peptidergic nociceptor, NP- None-Peptidergic nociceptor, Cold – Cold thermoceptor. The name designations are based on Jung et al., 2023.

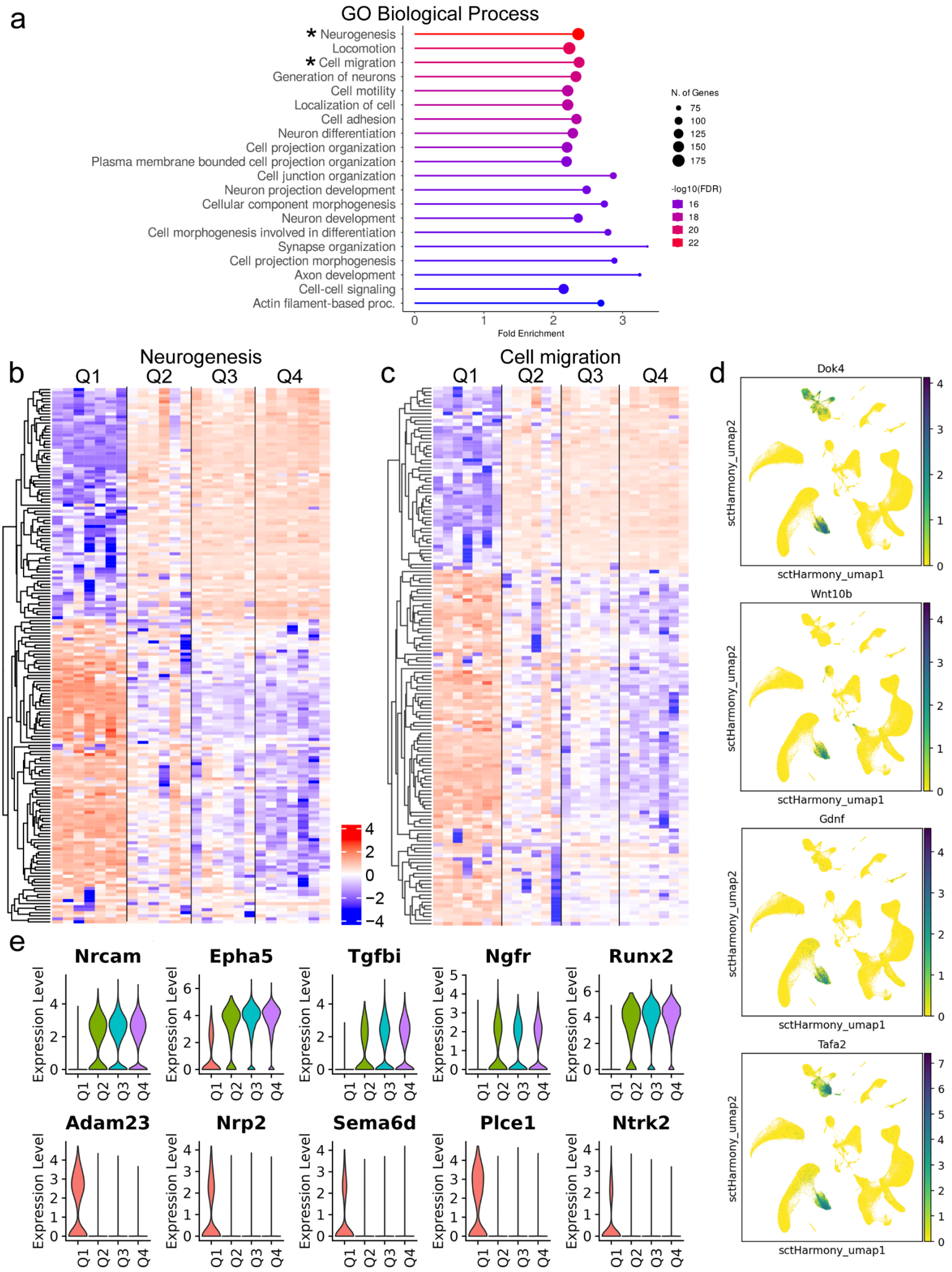
a
GO Biological Process
* Neurogenesis
Locomotion
* Cell migration
Generation of neurons
Cell motility
Localization of cell
Cell adhesion
Neuron differentiation
Cell projection organization
Plasma membrane bounded cell projection organization
Cell junction organization
Neuron projection development
Cellular component morphogenesis
Neuron development
Cell morphogenesis involved in differentiation
Synapse organization
Cell projection morphogenesis
Axon development
Cell-cell signaling
Actin filament-based proc.
0
1
2
3
Fold Enrichment
N. of Genes
75
100
125
150
175
-log10(FDR)
16
18
20
22
b
Neurogenesis
Q1
Q2
Q3
Q4
4
2
0
−2
−4
c
Cell migration
Q1
Q2
Q3
Q4
d
Dok4
Wnt10b
Gdnf
Tafa2
sctHarmony_umap1
sctHarmony_umap2
e
Nrcam
Epha5
Tgfbi
Ngfr
Runx2
Adam23
Nrp2
Sema6d
Plce1
Ntrk2
Expression Level
Q1
Q2
Q3
Q4

Figure 6: Activated satellite glia express genes associated with regeneration and neurodevelopment. **a.** Go Term Biological process showing the top enriched pathways in the dorsal root ganglia of C57BL/6J mice. **b.** Pseudobulk heatmap of differentially activated genes (DEGs) in activated satellite glia. **c.** Pseudobulk heatmap of DEGs specific for cell migration in activated satellite glia. Biological sample labels avoided for clarity, neurofilament quartile 1 (Q1) while the black rectangles note the upregulated and downregulated genes in Q2, Q3 and Q4. **d.** Embedding UMAP plots for the expression of specific genes in activated satellite glia. **e.** Violin plots of a subset highly altered genes related to the enriched pathways in activated satellite glia. The scale in heatmaps is Z-Score of $\log_2$FC (TPM + 0.25). TPM – transcripts per million. FC – fold change. Asterisks indicate processes in focus.

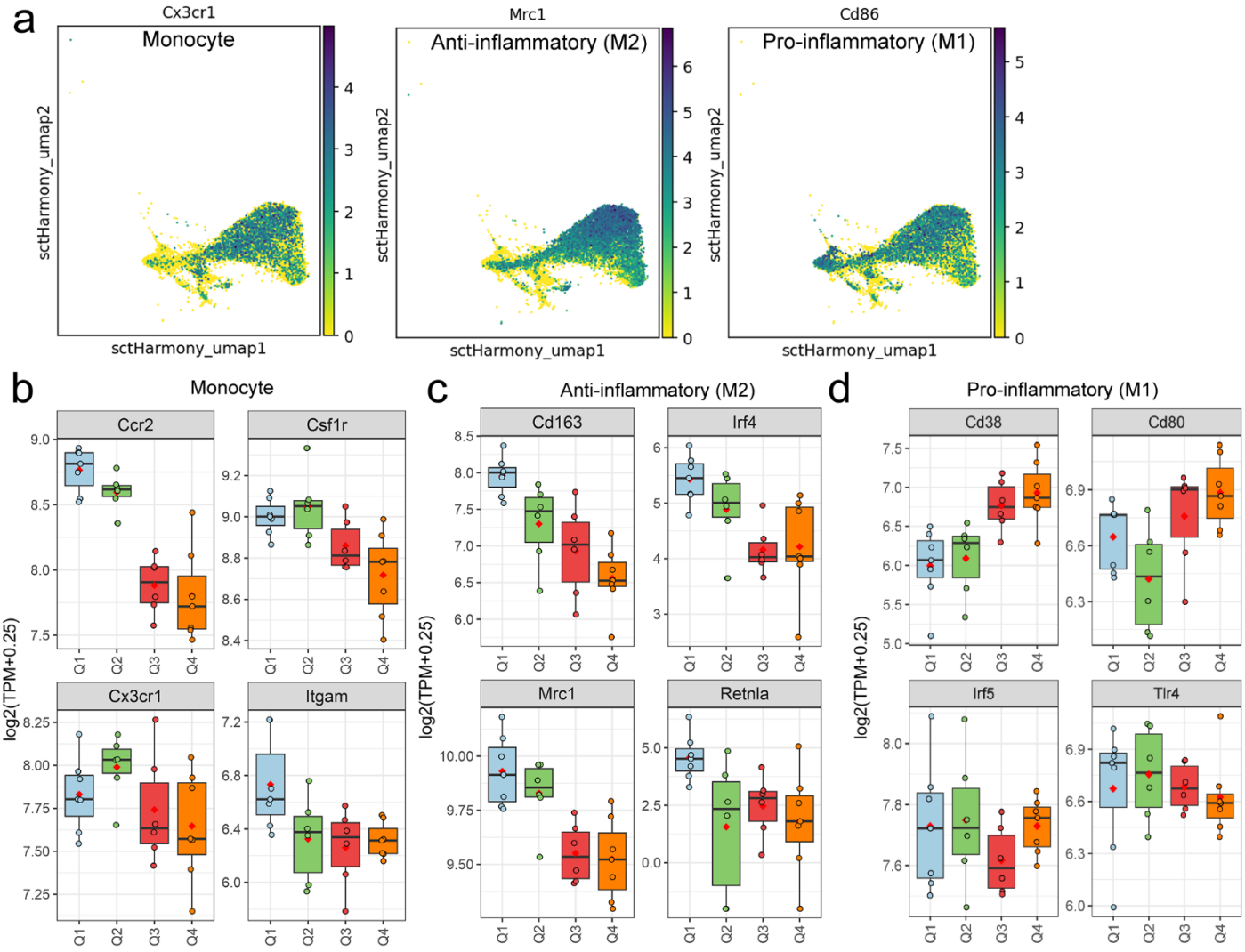
a
Cx3cr1
Monocyte
Mrc1
Anti-inflammatory (M2)
Cd86
Pro-inflammatory (M1)
sctHarmony_umap1
sctHarmony_umap2
b
Monocyte
c
Anti-inflammatory (M2)
d
Pro-inflammatory (M1)
Ccr2
Csf1r
Cx3cr1
Itgam
Cd163
Irf4
Mrc1
Retnla
Cd38
Cd80
Irf5
Tlr4
log2(TPM+0.25)
Q1
Q2
Q3
Q4

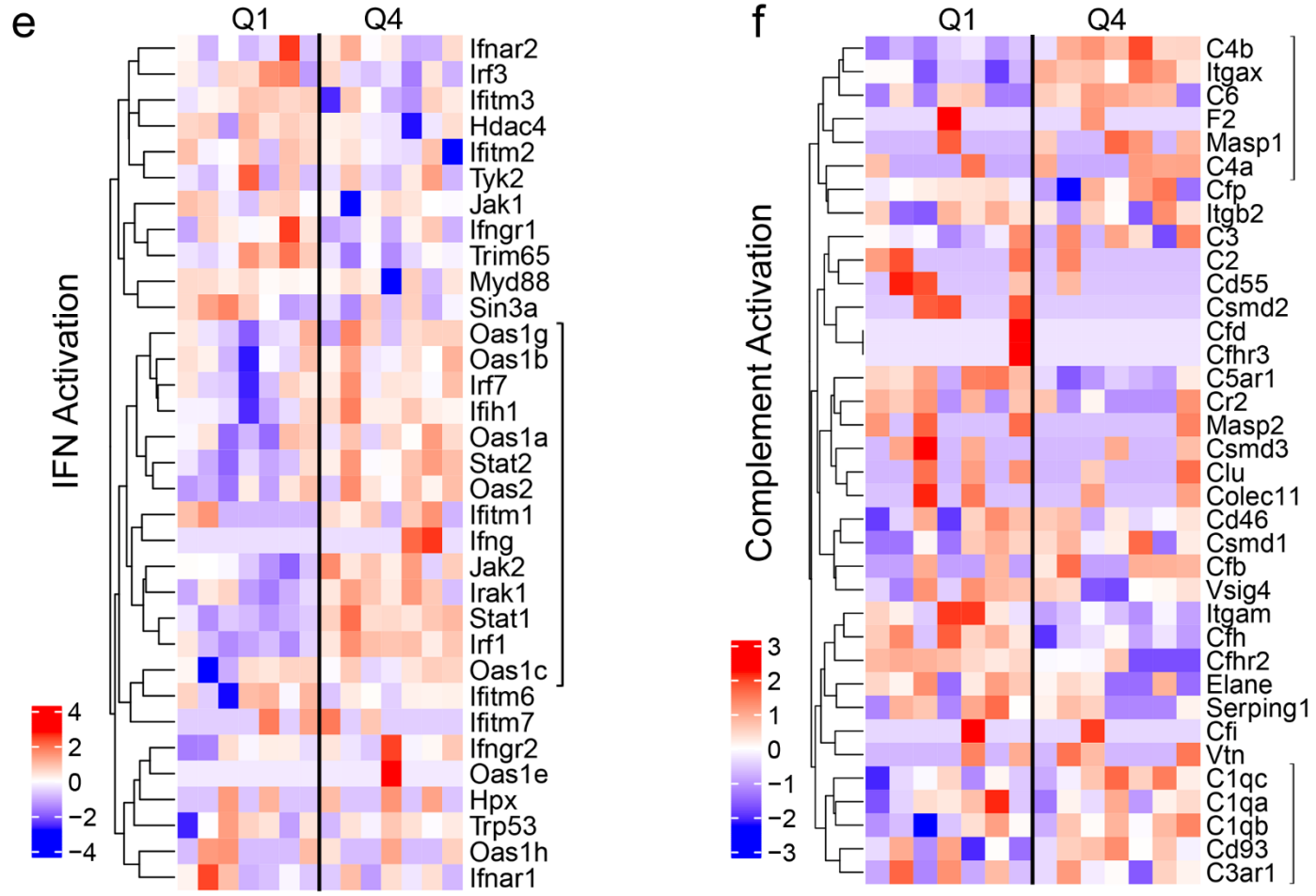
e
Q1
Q4
IFN Activation
Ifnar2
Irf3
Ifitm3
Hdac4
Ifitm2
Tyk2
Jak1
Ifngr1
Trim65
Myd88
Sin3a
Oas1g
Oas1b
Irf7
Ifih1
Oas1a
Stat2
Oas2
Ifitm1
Ifng
Jak2
Irak1
Stat1
Irf1
Oas1c
Ifitm6
Ifitm7
Ifngr2
Oas1e
Hpx
Trp53
Oas1h
Ifnar1
f
Complement Activation
C4b
Itgax
C6
F2
Masp1
C4a
Cfp
Itgb2
C3
C2
Cd55
Csmd2
Cfd
Cfhr3
C5ar1
Cr2
Masp2
Csmd3
Clu
Colec11
Cd46
Csmd1
Cfb
Vsig4
Itgam
Cfh
Cfhr2
Elane
Serping1
Cfi
Vtn
C1qc
C1qa
C1qb
Cd93
C3ar1

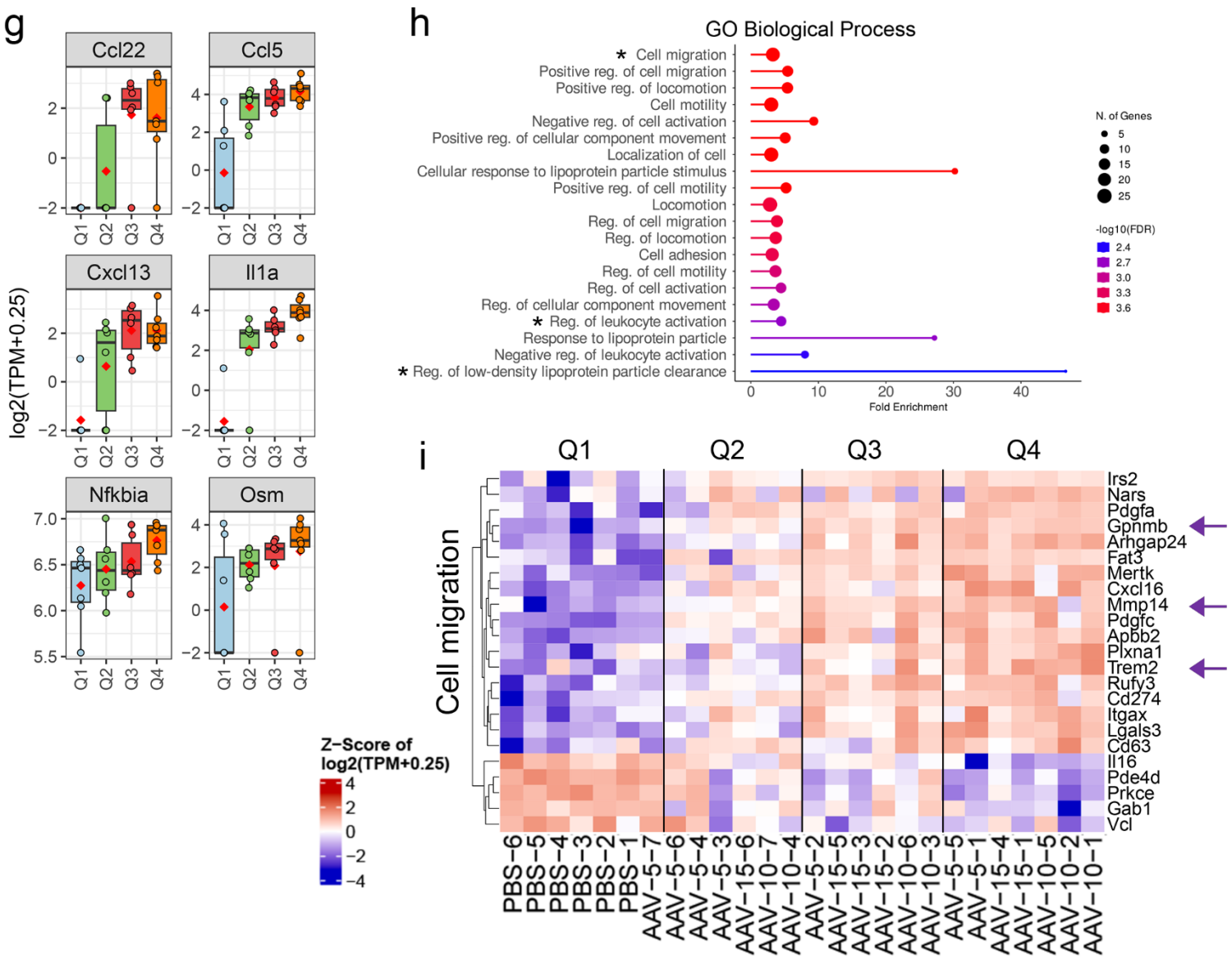
g
Ccl22
Ccl5
Cxcl13
Il1a
Nfkbia
Osm
log2(TPM+0.25)
Q1
Q2
Q3
Q4
Z−Score of
log2(TPM+0.25)
h
GO Biological Process
* Cell migration
Positive reg. of cell migration
Positive reg. of locomotion
Cell motility
Negative reg. of cell activation
Positive reg. of cellular component movement
Localization of cell
Cellular response to lipoprotein particle stimulus
Positive reg. of cell motility
Locomotion
Reg. of cell migration
Reg. of locomotion
Cell adhesion
Reg. of cell motility
Reg. of cell activation
Reg. of cellular component movement
* Reg. of leukocyte activation
Response to lipoprotein particle
Negative reg. of leukocyte activation
* Reg. of low-density lipoprotein particle clearance
Fold Enrichment
N. of Genes
-log10(FDR)
i
Cell migration
Irs2
Nars
Pdgfa
Gpnmb
Arhgap24
Fat3
Mertk
Cxcl16
Mmp14
Pdgfc
Apbb2
Plxna1
Trem2
Rufy3
Cd274
Itgax
Lgals3
Cd63
Il16
Pde4d
Prkce
Gab1
Vcl
PBS−6
PBS−5
PBS−4
PBS−3
PBS−2
PBS−1
AAV−5−7
AAV−5−6
AAV−5−4
AAV−5−3
AAV−15−6
AAV−10−7
AAV−10−4
AAV−5−2
AAV−15−5
AAV−15−3
AAV−15−2
AAV−10−6
AAV−10−3
AAV−5−5
AAV−5−1
AAV−15−4
AAV−15−1
AAV−10−5
AAV−10−2
AAV−10−1

Figure 7: Inflammatory response in macrophages following treatment with AAV in C57BL/6J mice. **a.** Embedding UMAP plots of monocytes and macrophages. Pseudobulk boxplots of **b.** monocytes **c.** Anti-inflammatory (M2) macrophages and **d.** pro-inflammatory (M1) macrophages in the dorsal root ganglia (DRG) by neurofilament light (NfL) quartiles 1 (Q1) to Q4. Red diamonds indicate the mean **e.** Pseudobulk heatmap showing the interferon (IFN) response genes in macrophages by NfL quartiles. **f.** Pseudobulk heatmap of the complement system part of the innate immune response by NfL quartiles. Box bracket indicates genes of interest. **g.** Pseudobulk boxplots of chemokines and cytokines in response to Nuclear Factor Kappa B (NF-kB) surge by neurofilament quartile. **h.** Biological Go Term processes enriched in macrophages. Asterisk indicates process of interest. Differentially activated genes (DEGs) in Q4 vs Q1 comparison in macrophages was used in Gene Set Enrichment Analysis. **i.** Pseudobulk heatmap of the cell migration GO Term process. Purple arrows indicate genes of interest. The scale in heatmaps is Z-Score of $\log_2$FC(TPM + 0.25). TPM – transcripts per million. FC – fold change.

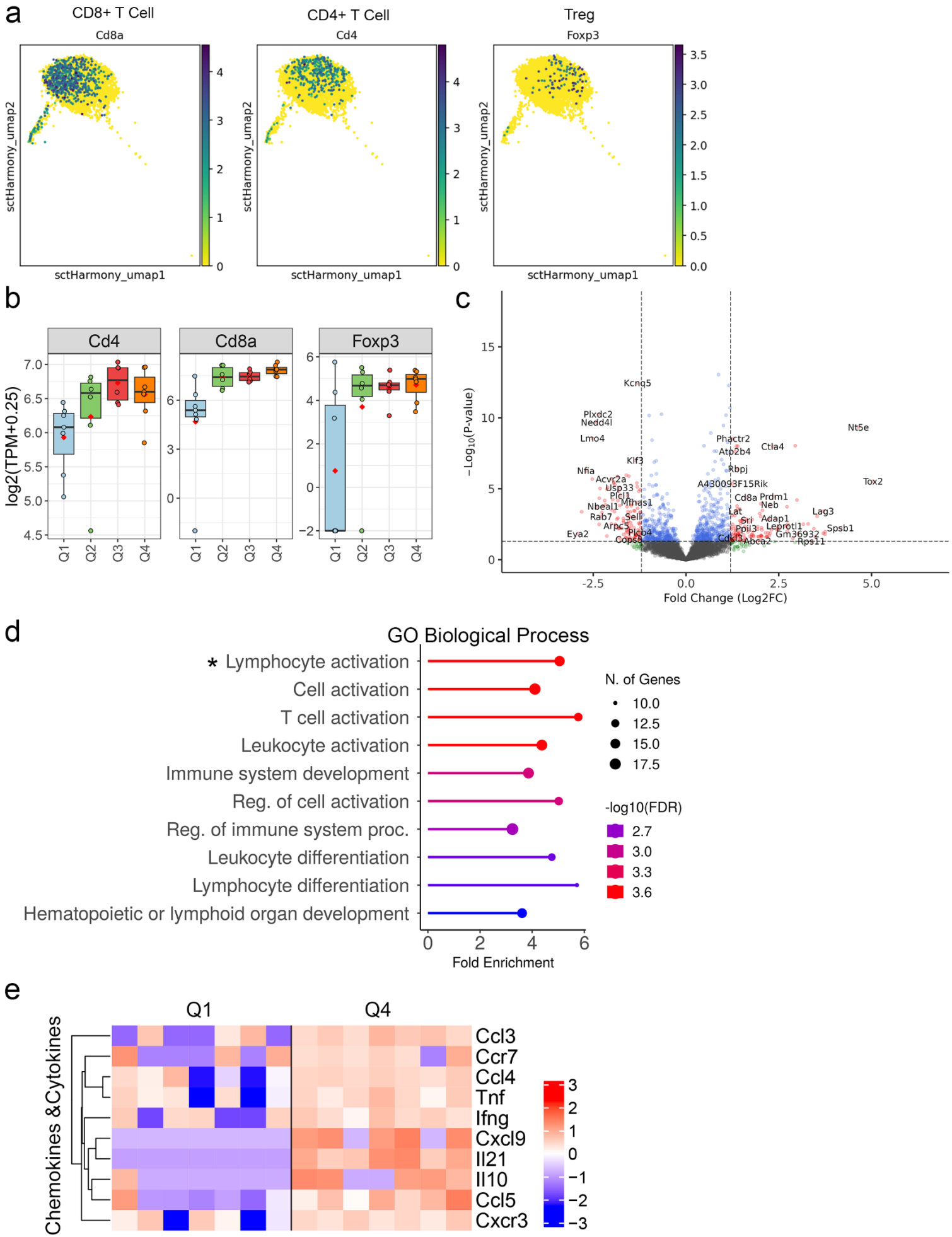
a
CD8+ T Cell
Cd8a
CD4+ T Cell
Cd4
Treg
Foxp3
sctHarmony_umap1
sctHarmony_umap2
b
Cd4
Cd8a
Foxp3
log2(TPM+0.25)
Q1
Q2
Q3
Q4
c
−Log10(P-value)
Fold Change (Log2FC)
Kcnq5
Plxdc2
Nedd4l
Lmo4
Klf3
Nfia
Acvr2a
Usp33
Plcl1
Mfhas1
Nbeal1
Rab7
Sell
Arpc5
Plcb4
Copb2
Eya2
Phactr2
Atp2b4
Ctla4
Rbpj
A430093F15Rik
Cd8a
Prdm1
Neb
Lat
Sri
Adap1
Ppil3
Leprotl1
Gm36932
Cdkl5
Abca2
Rps11
Lag3
Spsb1
Nt5e
Tox2
d
GO Biological Process
* Lymphocyte activation
Cell activation
T cell activation
Leukocyte activation
Immune system development
Reg. of cell activation
Reg. of immune system proc.
Leukocyte differentiation
Lymphocyte differentiation
Hematopoietic or lymphoid organ development
Fold Enrichment
N. of Genes
10.0
12.5
15.0
17.5
-log10(FDR)
2.7
3.0
3.3
3.6
e
Q1
Q4
Chemokines &Cytokines
Ccl3
Ccr7
Ccl4
Tnf
Ifng
Cxcl9
Il21
Il10
Ccl5
Cxcr3

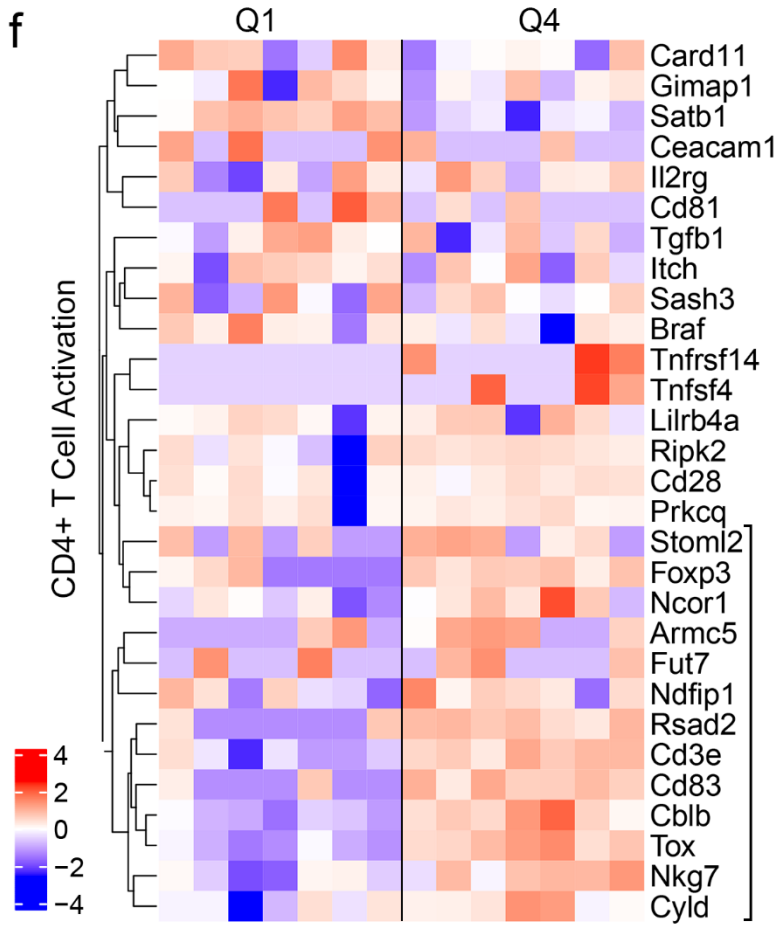
f
Q1
Q4
CD4+ T Cell Activation
Card11
Gimap1
Satb1
Ceacam1
Il2rg
Cd81
Tgfb1
Itch
Sash3
Braf
Tnfrsf14
Tnfsf4
Lilrb4a
Ripk2
Cd28
Prkcq
Stoml2
Foxp3
Ncor1
Armc5
Fut7
Ndfip1
Rsad2
Cd3e
Cd83
Cblb
Tox
Nkg7
Cyld
4
2
0
−2
−4

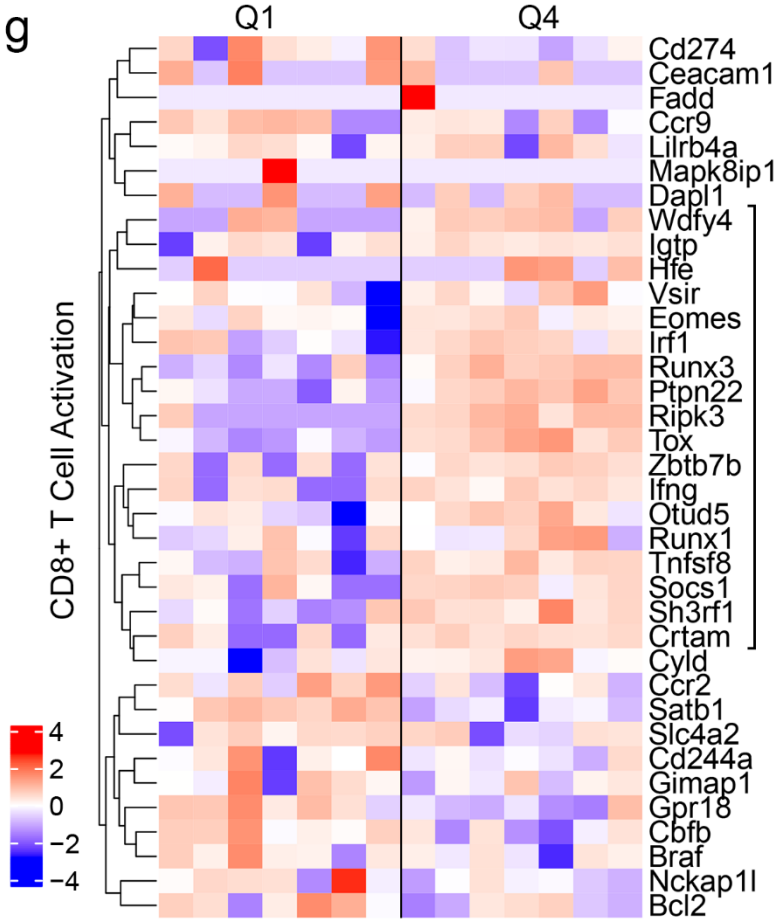
g
Q1
Q4
CD8+ T Cell Activation
Cd274
Ceacam1
Fadd
Ccr9
Lilrb4a
Mapk8ip1
Dapl1
Wdfy4
Igtp
Hfe
Vsir
Eomes
Irf1
Runx3
Ptpn22
Ripk3
Tox
Zbtb7b
Ifng
Otud5
Runx1
Tnfsf8
Socs1
Sh3rf1
Crtam
Cyld
Ccr2
Satb1
Slc4a2
Cd244a
Gimap1
Gpr18
Cbfb
Braf
Nckap1l
Bcl2
4
2
0
−2
−4

Figure 8: Activation of T cell responses in the dorsal root ganglia of AAV-treated C57BL/6J mice. **a.** Embedding UMAP plots of different populations of T cells found in the dorsal root ganglia (DRG). **b.** Pseudobulk boxplots of T cell gene markers by neurofilament light (NfL) quartiles (Q). Red diamond indicates the mean. **c.** Volcano plot of differentially activated genes (DEGs) in T cells for the comparison between NfL Q4 vs Q1. **d.** Go Biological enrichment plot of the top processes in the T cell cluster. DEGs in Q4 vs Q1 comparison in macrophages was used in Gene Set Enrichment Analysis. Asterisk indicates a process of interest. **e.** Pseudobulk heatmap of chemokines and cytokines found in the T Cells cluster. Pseudobulk heatmaps for **f.** helper CD4+ T Cell activation and **g.** Cytotoxic CD8+ T Cell activation. Square bracket indicates genes of interest. Scale on heatmaps indicates Z-Score of $\log_2$FC(TPM + 0.25). TPM – transcripts per million. FC – fold change.

Discussion

This work revealed cell-specific changes in response to AAV-induced toxicity in the dorsal root ganglia (DRG) of wild-type mice. AAV transduced neurons most efficiently at all dose levels, with approximately 65% of neurons transduced at the highest dose of 1.5E12 GC. Serum neurofilament light chain (NfL) was used as a proxy for DRG toxicity, despite the large standard deviation in serum NfL measurements within each dose group. To eliminate dilution and loss of the gene expression signal, mice were grouped by NfL quartiles (Q1 to Q4, from low to high NfL), rather than by AAV dosage. Mice in Q4 exhibited neuronal loss and reduction in Schwann cells, indicative of neuronal and axonal degeneration. Interestingly, activated satellite glia emerged in response to neuronal injury, with key neurogenesis and neurodevelopmental processes enriched, suggesting an attempt at repair and regeneration. The immune response in macrophages, fibroblasts, and T cells was evident, with the expression of a multitude of cytokines and chemokines contributing to inflammation in the microenvironment of the DRG, likely playing a role in responding to injured and degenerating neurons.

The key findings presented by single nucleus RNA sequencing (snRNA-seq) dataset aligns with the histopathological findings from prior studies. A meta-analysis looking at all non-human primate (NHP) DRG toxicity studies showed neuronal loss, axonal degeneration, proliferation of satellite glia, mono-nuclear cell infiltration and fibrosis in peripheral nerves by histopathology (Hordeaux, Buza, Dyer, et al., 2020). These findings were comparable to the decline in neuronal and Schwann cell populations as well as the surge in activated satellite glia and immune cells in present dataset. Fibroblast in this report clearly show an increase number that is not detectable by histopathology. Fibrosis has been detected in rat DRG following sciatic nerve compression (Q. Li et al., 2016). Similar findings have been observed in rats, pigs, and rabbits with varied severity and consistency (Fader et al., 2022; Hordeaux, Buza, Dyer, et al.,

2020; Tien et al., 2024). In mice, Hawley and colleagues showed that neuronal degeneration was graded as minimal by histopathology (Hawley et al., 2024). This is in opposition to the dramatic reduction in the number of neurons seen in the snRNA-seq dataset. The contrast was attributed to the greater quantitative precision and sensitivity of snRNA-seq compared to histopathology. On the other hand, the higher doses used in this study (1.0E12 and 1.5E12 GC compared to 8E11 GC in the prior mentioned mouse study) could also be responsible for the greater neuronal degeneration detected in this study. Also, mice in this study were grouped by NfL quartiles as opposed to AAV dosage. Interestingly, many of the histopathology-based studies classify satellite glia surrounding injured neurons as 'reactive satellite glia' or 'proliferating', which likely represented the distinct activated satellite glia population noted in this report. Overall, the snRNA-seq dataset provided a greater resolution of changes associated with DRG toxicity and confirmed the prior histopathological findings in many preclinical models.

The transcriptomic profile of neurons offer a glimpse into the different states of neurons, while those of the activated satellite glia reflect the extent of the injury in the DRG. The number of differentially expressed genes (DEGs) in neurons was relatively small compared to other cell types. The toxic AAV transduced sensory neurons at a high rate, resulting in their degeneration. The DEGs detected might be dominated by the expression profiles of surviving neurons. Upregulation of neurodevelopmental and neurogenesis genes such as *Lrrc4c, Mir6236, Resf1* and others indicate that there could be injured neurons evading cell death or attempting to recover from the damage. *Lrrc4c* has been shown to be upregulated post-injury (Matson et al., 2022). However, upregulation of apoptotic genes such as *Bax* and *Cdk5* and *Diablo* indicated that neurons were destined for cell death. Axotomized DRG neurons have been found to activate *Bax* in mice and *Cdk5* upregulation was noted in post-sciatic nerve crush in rats (Hwang & Namgung, 2021; Thippeswamy et al., 2001). Interestingly, the classical neuronal

injury signatures such as *Atf3, Jun, Sox11,* and *Fosl1* were not found to be dysregulated in the neurons in this study, while these genes have been detected in various reports post-ligation and transection of peripheral nerves (Barry et al., 2023; G. Hu et al., 2016; Patodia & Raivich, 2012). In brief, neurons showed upregulation of neurogenesis genes which hints of repair process and upregulation of cell death genes indicating degeneration.

Undoubtedly, the large number of DEGs found in activated satellite glia along with the ~10% surge in their proportions signaled the severity of injury and loss of neurons in the DRG. The lack of AAV transduction in activated satellite glia suggested that changes in their activity were driven by injury and alterations in the microenvironment of the DRG. Gene set enrichment analysis of the DEGs indicated activated satellite glia role in supporting recovery and regeneration of neurons. Activated satellite glia showed highly altered expression of essential genes such as *Dok4, Gdnf, Nrcam, Ngfr, Epha5,* all vital for these roles. *Gdnf* signaling is known to promote neuron and axon regeneration after peripheral nerve injury: upon the binding of *Gdnf* to *Ret* receptor, *Dok4* is recruited to *Ret* receptor to initiate the downstream cascades (Cintrón-Colón et al., 2021; Uchida et al., 2006). Axonal degeneration from various models of injury have revealed the upregulation of *Nrcam, Epha5,* and *Ngfr* are vital for regenerative processes (Barrette et al., 2010; Kalinski et al., 2020). The transcriptional programs initiated following axonal degeneration caused by AAV toxicity are similar to those detected in various nerve injury models.

Despite the substantial difference between the immune systems of mice compared to human and NHP, key aspects of AAV-induced immune response can be replicated in mice. The complement system, part of the innate immune response, has been characterized following AAV in patients and non-human primates (NHPs) (Arjomandnejad et al., 2023; Schmitz et al., 2021). In this study, activation of the classical complement pathway in macrophages and

fibroblasts (*C1q, C4b, Itgax, C6* in macrophages and *C1q, C3, C2* in fibroblasts) was shown in mice in NfL Q4 vs. Q1. Interestingly, fibroblast also showed *Cfb* and *Cfp* upregulation which are components of the alternative pathway. The classical complement activation findings align with those of Hawley and colleagues using the same test article as well as earlier studies (Alstyne et al., 2021; Hawley et al., 2024; Vukojicic et al., 2019). Interestingly, the noted Toll Like Receptors (TLR) upregulated are distinct to what has been reported previously. The detection of viral DNA by TLR9 within the endosome and/or the direct binding of AAV to TLR2 on the cell surface has been thoroughly investigated (Muhuri et al., 2021). Macrophages showed an upregulation of *Tlr1, Tlr3, Tlr8, Tlr12, Tlr13* while fibroblasts showed *Tlr3* and *Tlr7*. Only a few mice showed upregulation of *Tlr2* and one mouse showed upregulation of *Tlr9* in macrophages. *Tlr8* was recently reported to be upregulated in mice following treatment with the same test article (Hawley et al., 2024). *Tlr2* and *Tlr9* were not found in the highly transduced neurons either (data not shown). *Myd88,* an adaptor for most TLRs, was consistently upregulated in fibroblasts but not macrophages. The distinct gene expression profiles of TLR signaling could be due to AAV-miR-SOD1 modest transduction of fibroblasts but not macrophages. Overall, the downstream components of TLR signaling such as *Irak1, Irak2, Traf3,* and *Tnf* were upregulated in macrophages and fibroblasts.

The activation and signaling of Toll-like receptors led to the induction of interferons (IFN). Type I IFN was noted with the upregulation of *Irf1, Irf7, Stat1 and Stat2* in macrophages and more pronounced upregulation in fibroblasts with *Tyk2, Jak1, Ifnar2, Irf7, Irf1, ifngr2* and others. All of these innate immune events led to the activation of Nuclear factor kappa B (NF-kB) noted with the upregulation of NF-kB inhibitor gene – *Nfkbia,* and the release of chemokines and the cytokines in macrophages. Some of these cytokines and chemokines such as *Cd69, Cxcl10, Cxcl9, Il12b, Tnfrsf14* upregulated in this were also found to be significantly upregulated in an O-link proteomic analysis of NHP cerebrospinal fluid samples treated with

AAV-miR-SOD1 (Fig. S8) (Hawley et al., 2024). Collectively, these innate immune mechanisms collaborate to drive the transition towards a pro-inflammatory macrophage (M1) state. The alterations observed in macrophages resemble those found in models of neurodegenerative disease and peripheral nerve injury, as macrophages are mobilized to sites of injury (X. Xu et al., 2021).

Pro-inflammatory macrophages mount a cellular immune response as seen with the elevation of helper CD4+ T cell, cytotoxic CD8+ T cells and T regulatory cells (Treg) gene expression markers. Upregulation of *Cd86, Cd80, Cd38* were noted in macrophages, which are key in inducing CD8+ T cells. In addition, helper CD4+ T cells further induce the inflammatory response by priming CD8+ T cells. Ultimately, cytokine and chemokines specific to CD8+ T cells (i.e. *Tnf, Ifnγ, Cxcl9*) were upregulated along with CD4+ T cell (*Il21, Il10*). The cytotoxic T cell activation in this study occurs independent of TLR9. This is in opposition to the cytotoxic T cell activation via TLR9-Myd88 and type I IFN signaling reported in mice and previously (Zhu et al., 2009). Activation of cytotoxic CD8+ T cell can occur independent of TLR9. A recent study showed that a TLR9 independent pathway and IL-1R1-MyD88 signaling is sufficient to induce CD8+T cells (Kumar et al., 2024). Ultimately, cytotoxic T cell activity can lead to the elimination of infected cells by the release of perforin and granzymes (Arjomandnejad et al., 2023). Tregs, upregulation of *Foxp3,* is not surprising as it modulates cytotoxic and helper T cell activities. Also, Tregs here can aide in tolerance for long term expression of the transgene, especially with strong ubiquitous promoters such as CAG, the promoter used in AAV-miR-SOD1 and many ongoing clinical trials (Arjomandnejad et al., 2021; Au et al., 2022).

It was shown that mice replicate many key features of AAV-induced DRG toxicity, a model which could be a workhorse for early screening of gene therapy candidates. The vector used in

this report replicated the neuronal cell loss, activation of a novel population of satellite glia and the innate and adaptive immune responses seen in other preclinical models. Neuronal degeneration occurs in the absence of mononuclear cell infiltration in mice (as opposed to NHPs) (Fader et al., 2022; Hawley et al., 2024). Indeed, neuronal cell death is likely intrinsic stemming from high transduction rate which could lead to the activation of necrosis related genes. However, extrinsic signaling by immune cells also likely contribute to injury of neurons. The use of snRNA-seq expanded the understanding of DRG toxicity and the underlying biological processes in animal models. It added valuable mechanistic details and greater resolution derived from cell type transcriptomic profiles to the previous histopathological observations. However, this method also has some limitations: Single nucleus transcriptomics only captures the RNA profile of the nuclei and not of the whole cell. While this is not specific to single nucleus methods, it is well known that gene expression does not correlate very strongly with protein expression. Also, the relatively shallow depth of sequencing of snRNA-seq compared to bulk RNA-seq limits the detection to the more highly expressed genes. It would be highly beneficial to selectively enrich for neurons or employ a strategy to deplete abundant cell types such as fibroblasts or Schwann cells. This would enhance the depth and coverage for the clusters of interest such as neuron, satellite glia and immune cells. Despite these limitations, this study has provided insightful findings on DRG toxicity in mice. The hope is that better understanding of the mechanism of this AAV class toxicity in early animal models. This will enable objective assessment of gene therapy drug candidates for various diseases and will contribute to finding novel strategies to mitigate this problem in patients.

Supplementary Information

Sample ID	Animal Eartag	Sex	Treatment	Summed Serum NfL from 3 and 6 week post injection NfL (pg/mL)	Avg. Serum NfL / Sample (pg/mL)
PBS-1	803	F	Vehicle	564.1	372.65
	4467/825	F	Vehicle	181.2	
PBS-6	827	M	Vehicle	148.7	121.55
	4402	M	Vehicle	94.4	
PBS-3	829	F	Vehicle	108.8	102.3
	890	F	Vehicle	95.8	
PBS-4	4496	M	Vehicle	232.8	213.1
	888	M	Vehicle	193.4	
PBS-2	889	F	Vehicle	148.9	134.55
	828	F	Vehicle	120.2	
PBS-5	811	M	Vehicle	162	158.65
	810	M	Vehicle	155.3	
AAV-5-1	290	F	AAV-miR-SOD1 (5E11 GC)	5618	5137
	4477/891	F	AAV-miR-SOD1 (5E11 GC)	4656	
AAV-5-4	895	F	AAV-miR-SOD1 (5E11 GC)	901	781.5
	893	F	AAV-miR-SOD1 (5E11 GC)	662	
AAV-5-7	824	M	AAV-miR-SOD1 (5E11 GC)	856	468.1
	300	M	AAV-miR-SOD1 (5E11 GC)	80.2	
AAV-5-3	4462	F	AAV-miR-SOD1 (5E11 GC)	3450	2262.5
	4478/892	F	AAV-miR-SOD1 (5E11 GC)	1075	
AAV-5-5	801	M	AAV-miR-SOD1 (5E11 GC)	7286	5659
	4493	M	AAV-miR-SOD1 (5E11 GC)	4032	
AAV-5-2	826	F	AAV-miR-SOD1 (5E11 GC)	4093	3928
	894	F	AAV-miR-SOD1 (5E11 GC)	3763	
AAV-5-6	809	M	AAV-miR-SOD1 (5E11 GC)	2127	1642.5
	823	M	AAV-miR-SOD1 (5E11 GC)	1158	
AAV-10-1	4451	F	AAV-miR-SOD1 (1E12 GC)	6455	6130.5
	813	F	AAV-miR-SOD1 (1E12 GC)	5806	
AAV-10-4	4476-f	F	AAV-miR-SOD1 (1E12 GC)	1161	1000.5
	4482	F	AAV-miR-SOD1 (1E12 GC)	840	
AAV-10-5	898	M	AAV-miR-SOD1 (1E12 GC)	5650	5459.5
	4405	M	AAV-miR-SOD1 (1E12 GC)	5269	
AAV-10-2	814	F	AAV-miR-SOD1 (1E12 GC)	5182	5119
	815	F	AAV-miR-SOD1 (1E12 GC)	5056	
AAV-10-7	830	M	AAV-miR-SOD1 (1E12 GC)	1629	1080.5
	897	M	AAV-miR-SOD1 (1E12 GC)	532	
AAV-10-3	4457	F	AAV-miR-SOD1 (1E12 GC)	5035	3985
	4485	F	AAV-miR-SOD1 (1E12 GC)	2935	
AAV-10-6	4494/896	M	AAV-miR-SOD1 (1E12 GC)	4916	4660.5
	807	M	AAV-miR-SOD1 (1E12 GC)	4405	
AAV-15-2	819	F	AAV-miR-SOD1 (1.5E12 GC)	4685	4196.5
	4454	F	AAV-miR-SOD1 (1.5E12 GC)	3708	
AAV-15-5	817	M	AAV-miR-SOD1 (1.5E12 GC)	4497	3587.5
	822	M	AAV-miR-SOD1 (1.5E12 GC)	2678	
AAV-15-1	804	F	AAV-miR-SOD1 (1.5E12 GC)	5273	5075.5
	806	F	AAV-miR-SOD1 (1.5E12 GC)	4878	
AAV-15-6	4414	M	AAV-miR-SOD1 (1.5E12 GC)	1888	1685.5
	4488	M	AAV-miR-SOD1 (1.5E12 GC)	1483	
AAV-15-3	4453	F	AAV-miR-SOD1 (1.5E12 GC)	2807	2747
	4480	F	AAV-miR-SOD1 (1.5E12 GC)	2687	
AAV-15-4	808	M	AAV-miR-SOD1 (1.5E12 GC)	7554	7155.5
	4495	M	AAV-miR-SOD1 (1.5E12 GC)	6757	

Table S1: Pooling of mouse lumbar dorsal root ganglia samples to generate biological samples. Serum neurofilament light levels was averaged from 3- and 6-weeks post-injection for each biological replicate. Vehicle – PBS. In the Sample ID column, AAV/PBS indicates the treatment, the first number in AAV treatments indicated the dose code (5 – 5E11 GC, 10 – 1.0E12 GC, 15 – 1.5E12 GC) and the second number indicated the biological replicate.

Reagents	Company	Cat#
Dithiothreitol (DTT) (@4°C)	Sigma-Aldrich	D0632
Spermine tetrahydrochloride (SMN)	Sigma-Aldrich	S1141
Spermidine trihydrochloride (SMD)	Sigma-Aldrich	S2501
Triton X-100	Sigma-Aldrich	9036-19-5
OptiPrep Density Gradient Medium (60% iodixanol)	Sigma-Aldrich	D1556
Cell Strainer, 70um, blue	Becton Dickinson	Falcon 352340 352350
RNasin Plus RNase Inhibitor (@-20C; ~250ul /vial)	Promega	N2611 N2615
Tricine	Sigma-Aldrich	T0377
Centrifuge tubes	Beckman Coulter	344059
30% BSA (@ 4°C)	Sigma-Aldrich	A9576
2mL Dounce homogenizer	Bellco	1984-10002

Solutions	Molarity
Hyman Low Surcrose Buffer	0.32M Sucrose, 5mM CaCl2, 3.0mM Mg(Acetate)2, 0.1mM EDTA, 10mM Tris-HCl,
Buffer HB	0.25M sucrose, 25mM KCl, 5mM MgCl2, 20mM Tricine-KOH, pH 7.8
Diluent Buffer	150mM KCl, 30mM MgCl2, 120mM Tricine-KOH, pH 7.8
10% Triton X-100	
Dithiothreitol (DTT) (1000X)	1M
spermine	0.15 M
spermidine	0.5 M
17.5% BSA	

Equipment	Company	Cat#
Sorvall™ WX+ Ultracentrifuge (with SW 40 Ti rotor and swing buckets)	ThermoFisher Scientific	
2mL Dounce homogenizer	Bellco	1984-10002

Table S2: A list of chemicals, reagents, solutions and equipment required for single nucleus isolation from the dorsal root ganglia for the 10x Genomics Chromium Single Cell 3” RNA sequencing platform.

Hyman Low Sucrose Buffer	Hyman LSB base (mL)	1M DTT (uL)	RNAse inhibitor (uL)
4 samples (16.6 mL)	16.6	16.6	16.6
Hyman Lysis Buffer	Hyman LSB (mL)	10% Triton X-100 (uL)	
4 samples (2.6 mL)	2.6	26	
Working Solution	Optiprep (mL)	Diluent (mL)	RNAse inhibitor (uL)
4 samples (36 mL)	30	6	36
Complete Buffer HB	Buffer HB (mL)	17.5% BSA (uL)	RNAse inhibitor (uL)	1M DTT (uL)	spermidine (uL)	spermine (uL)
4 samples (27 mL)	27	64.8	27	27	27	27
30% Iodixanol	Working solution (mL)	Complete Buffer HB (mL)	17.5% BSA (uL)
4 samples (4.8 mL)	2.88	1.92	11.52
40% Iodixanol	Working solution (mL)	Complete Buffer HB (mL)	17.5% BSA (uL)
4 samples (4.8 mL)	3.84	0.96	5.76
Resuspension Buffer	PBS + 2% BSA (mL)	RNAse inhibitor (uL)
4 samples (42 mL)	42	42

Table S3: A list of fresh reagents prepared prior to the start of single nuclei isolation workflow from the dorsal root ganglia of mice. The volumes are for 4 samples.

Sample ID	Estimated Number of Cells	Mean Reads per Cell	Median Genes per Cell	Number of Reads	Valid Barcodes	Sequencing Saturation	Q30 Bases in Barcode	Q30 Bases in RNA Read	Q30 Bases in UMI	Reads Mapped to Genome	Reads Mapped Confidently to Genome	Reads Mapped Confidently to Intergenic Regions	Reads Mapped Confidently to Intronic Regions	Reads Mapped Confidently to Exonic Regions	Reads Mapped Confidently to Transcriptome	Reads Mapped Antisense to Gene	Fraction Reads in Cells	Total Genes Detected	Median UMI Counts per Cell
AAV-10-1	11,992	34,435	1,387	412,946,237	97.70%	65.40%	97.00%	94.20%	96.70%	94.10%	91.80%	5.40%	46.70%	39.60%	76.40%	8.80%	45.30%	33,013	2,159
AAV-10-2	8,046	46,892	986	377,297,634	98.10%	82.20%	96.70%	94.40%	96.40%	95.50%	92.80%	5.10%	42.80%	44.90%	79.00%	7.50%	42.00%	29,492	1,382
AAV-10-3	10,276	36,693	1,121	377,060,477	97.00%	65.70%	96.80%	94.20%	96.50%	94.90%	92.20%	5.70%	46.50%	40.00%	66.70%	18.80%	45.00%	33,364	1,611
AAV-10-4	13,100	34,953	1,436	457,892,671	97.50%	60.90%	97.00%	94.50%	96.70%	95.40%	92.70%	5.40%	48.50%	38.70%	72.90%	13.30%	50.40%	34,591	2,350
AAV-10-5	13,120	41,597	1,464	545,755,680	97.20%	69.20%	96.70%	94.50%	96.40%	95.10%	92.50%	5.40%	50.10%	37.00%	70.30%	15.70%	56.20%	34,737	2,466
AAV-10-6	8,358	55,068	1,234	460,261,926	97.80%	77.10%	97.10%	94.40%	96.80%	94.00%	91.60%	5.20%	45.80%	40.60%	74.90%	10.30%	42.90%	31,687	1,887
AAV-10-7	10,403	43,054	1,106	447,891,788	97.90%	75.10%	96.80%	94.10%	96.50%	95.60%	92.90%	5.30%	43.60%	44.10%	71.80%	14.80%	46.60%	32,282	1,637
AAV-15-1	9,709	39,974	1,030	388,116,214	97.90%	77.00%	97.00%	94.60%	96.60%	95.10%	92.60%	5.60%	44.00%	43.00%	76.10%	9.80%	43.60%	31,166	1,485
AAV-15-2	14,477	31,371	1,331	454,170,359	95.60%	54.70%	96.80%	94.30%	96.50%	94.30%	91.30%	5.80%	55.70%	29.90%	49.50%	35.20%	64.10%	35,991	2,213
AAV-15-3	17,957	19,710	1,203	353,948,854	96.40%	43.60%	96.80%	94.50%	96.50%	95.70%	93.00%	5.60%	48.20%	39.30%	63.30%	23.30%	51.80%	35,064	1,769
AAV-15-4	10,974	34,893	1,246	382,918,452	96.60%	67.60%	96.90%	94.40%	96.60%	95.30%	92.60%	5.30%	49.10%	38.20%	60.10%	26.20%	54.30%	33,991	1,936
AAV-15-5	14,922	31,952	1,460	476,799,692	96.60%	57.30%	96.80%	94.00%	96.50%	95.00%	92.60%	5.50%	53.80%	33.30%	61.90%	24.20%	61.20%	35,735	2,418
AAV-15-6	11,354	40,099	1,290	455,284,645	97.50%	64.60%	96.80%	94.30%	96.40%	96.10%	93.20%	5.10%	42.60%	45.50%	67.70%	19.40%	50.40%	33,800	1,991
AAV-5-1	10,700	38,587	1,220	412,889,828	97.70%	72.40%	96.70%	94.40%	96.30%	93.40%	90.70%	5.00%	40.80%	45.00%	78.70%	5.80%	41.00%	31,326	1,840
AAV-5-2	19,659	18,680	1,290	367,230,894	96.80%	47.20%	96.80%	94.30%	96.50%	95.90%	93.40%	5.60%	48.60%	39.30%	70.90%	15.90%	49.10%	34,842	1,884
AAV-5-3	10,397	38,651	917	401,854,975	98.20%	76.60%	96.80%	94.30%	96.40%	95.50%	93.10%	5.60%	44.80%	42.70%	79.90%	6.40%	39.30%	30,254	1,240
AAV-5-4	10,270	41,569	1,268	426,919,966	96.80%	63.00%	96.60%	94.40%	96.30%	95.30%	92.90%	5.80%	51.90%	35.30%	63.00%	23.30%	60.50%	34,861	2,069
AAV-5-5	9,672	40,659	1,052	393,257,875	98.20%	77.10%	96.70%	94.30%	96.40%	96.00%	93.20%	4.90%	41.70%	46.50%	76.40%	10.70%	44.50%	31,302	1,525
AAV-5-6	8,568	38,379	1,107	328,834,961	96.90%	65.30%	96.80%	94.00%	96.50%	95.50%	92.50%	5.20%	44.00%	43.20%	63.30%	23.00%	49.00%	33,061	1,671
AAV-5-7	14,195	33,094	1,336	469,771,922	96.90%	62.90%	96.70%	94.20%	96.30%	95.20%	92.90%	5.70%	52.10%	35.10%	63.90%	22.30%	61.40%	35,144	2,139
PBS-1	14,894	29,885	1,428	445,111,611	97.10%	54.00%	96.80%	94.40%	96.50%	94.90%	92.30%	5.50%	46.60%	40.30%	68.20%	17.70%	56.70%	34,921	2,290
PBS-2	12,877	38,428	1,430	494,841,225	97.20%	59.50%	96.80%	94.40%	96.50%	95.80%	93.10%	5.40%	45.60%	42.10%	66.20%	20.50%	52.30%	34,797	2,307
PBS-3	7,989	62,655	1,079	500,553,018	98.20%	80.90%	96.80%	94.20%	96.50%	95.50%	93.10%	5.50%	44.40%	43.30%	76.80%	9.70%	38.60%	30,450	1,576
PBS-4	9,335	41,692	1,140	389,199,660	97.80%	71.00%	96.70%	94.20%	96.40%	95.80%	93.30%	5.20%	44.80%	43.40%	72.10%	15.10%	48.70%	31,970	1,704
PBS-5	18,363	21,953	1,228	403,138,644	96.40%	49.10%	96.50%	94.70%	96.30%	95.30%	92.70%	5.60%	50.80%	36.30%	58.30%	27.90%	58.60%	35,103	1,873
PBS-6	6,859	62,337	1,333	427,572,017	96.20%	75.20%	96.90%	94.30%	96.60%	94.10%	91.60%	5.50%	52.40%	33.70%	53.60%	31.70%	64.60%	33,777	2,295
Average	*11,864*	*38,356*	*1,235*	*425,058,509*	*97.24%*	*65.95%*	*96.80%*	*94.33%*	*96.48%*	*95.17%*	*92.56%*	*5.42%*	*47.15%*	*40.01%*	*68.53%*	*17.59%*	*50.70%*	*33,335*	*1,912*

Table S4: Cell Ranger quality control metrics per biological sample. Vehicle – PBS. In the Sample ID column, AAV/PBS indicates the treatment, the first number in AAV treatments indicated the dose code (5 – 5E11 GC, 10 – 1.0E12 GC, 15 – 1.5E12 GC) and the second number indicated the biological replicate.

Cell Type	Cell Number	Percentage
Fibroblasts	73,026	33.28
Satellite glia	45,602	20.78
Schwann cells	33,321	15.18
Neurons	25,551	11.64
Macrophages	12,938	5.9
Activated satellite glia	10,224	4.66
Endothelial cells	8,693	3.96
T cells	5,160	2.35
Pericytes	2,427	1.11
B cells	1,799	0.82
Unknown	701	0.32

Table S5: Nuclei and percentage counts for each cell type in the dorsal root ganglia of C57BL/6J.

a

	Q2 vs Q1			Q3 vs Q1			Q4 vs Q1		
Cell Type	Total	Down	Up	Total	Down	Up	Total	Down	Up
Activated Satellite Glia	436	237	199	850	507	343	1047	697	350
Macrophage	9	2	7	72	8	64	107	26	81
T Cell	23	11	12	92	53	39	98	61	37
Satellite Glia				19	1	18	80	36	44
Pericyte	1	0	1	3	0	3	73	48	25
Neuron	2	0	2	3	0	3	41	25	16
Schwann Cell				5	1	4	35	26	9
Fibroblast	1	0	1	4	3	1	23	11	12
B Cell	2	1	1	4	2	2	11	3	8
Endothelial Cell	3	1	2	1	0	1	10	8	2

b

Cell Type	**Q1**	**Q2**	**Q3**	**Q4**
Fibroblast	19407	13584	20546	19489
Satellite Glia	13910	10347	12062	9283
Schwann Cell	10662	7604	8520	6535
Neuron	8021	7251	7060	3219
Endothelial Cell	2658	1590	2475	1970
Macrophage	2366	1959	4637	3976
Pericyte	670	546	641	570
Activated Satellite Glia	473	637	3722	5392
B Cell	455	305	612	427
T Cell	402	747	2201	1810
Unknown	189	136	175	201

Table S6: Comparisons and the number of nuclei in each neurofilament light chain quartile. **a.** The total number of differentially activated genes of comparison between neurofilament quartiles for each cell type. NEBULA was used for the differential analysis. $|Log_2FC| > 1.2$ and FDR < 0.05. **b.** The number of nuclei for each cell type by quartile.

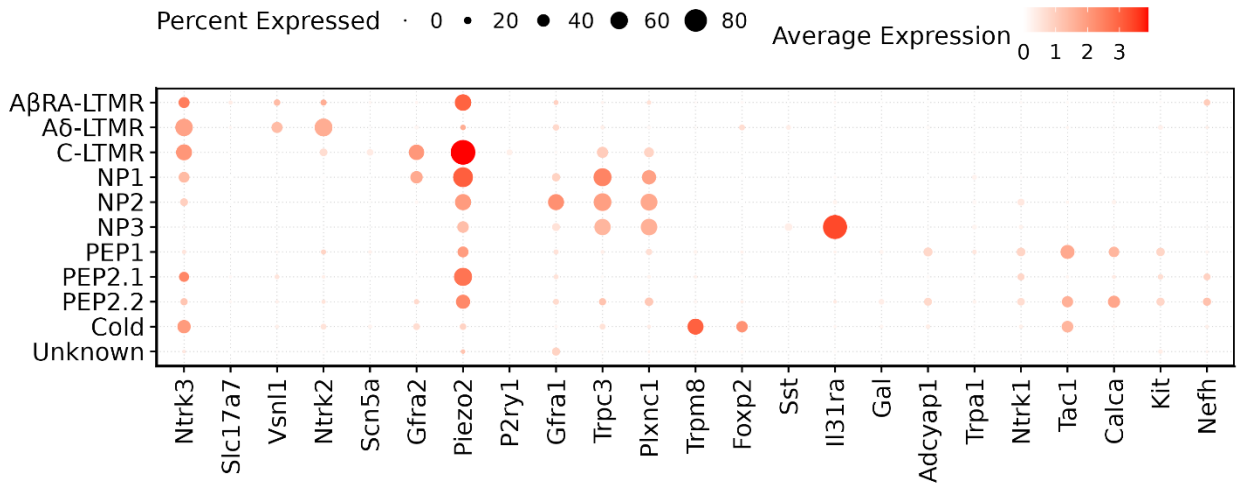

Figure S1: Marker genes expressed by the sensory neurons in the dorsal root ganglia of C57BL/6J mice. Gene markers were obtained from Jung et al. 2023.

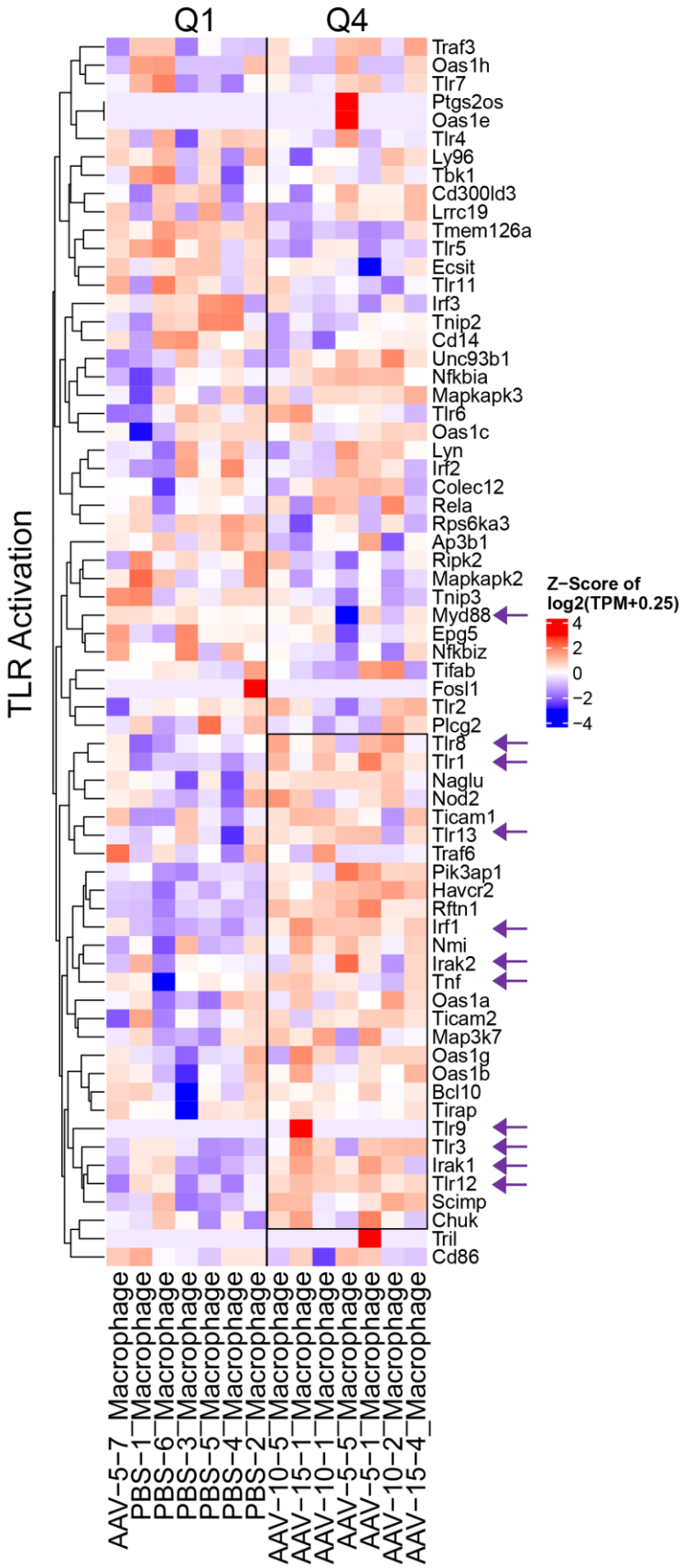
Q1
Q4
TLR Activation
Traf3
Oas1h
Tlr7
Ptgs2os
Oas1e
Tlr4
Ly96
Tbk1
Cd300ld3
Lrrc19
Tmem126a
Tlr5
Ecsit
Tlr11
Irf3
Tnip2
Cd14
Unc93b1
Nfkbia
Mapkapk3
Tlr6
Oas1c
Lyn
Irf2
Colec12
Rela
Rps6ka3
Ap3b1
Ripk2
Mapkapk2
Tnip3
Myd88
Epg5
Nfkbiz
Tifab
Fosl1
Tlr2
Plcg2
Tlr8
Tlr1
Naglu
Nod2
Ticam1
Tlr13
Traf6
Pik3ap1
Havcr2
Rftn1
Irf1
Nmi
Irak2
Tnf
Oas1a
Ticam2
Map3k7
Oas1g
Oas1b
Bcl10
Tirap
Tlr9
Tlr3
Irak1
Tlr12
Scimp
Chuk
Tril
Cd86
Z−Score of
log2(TPM+0.25)
4
2
0
−2
−4
AAV−5−7_Macrophage
PBS−1_Macrophage
PBS−6_Macrophage
PBS−3_Macrophage
PBS−5_Macrophage
PBS−4_Macrophage
PBS−2_Macrophage
AAV−10−5_Macrophage
AAV−15−1_Macrophage
AAV−10−1_Macrophage
AAV−5−5_Macrophage
AAV−5−1_Macrophage
AAV−10−2_Macrophage
AAV−15−4_Macrophage

Figure S2: Pseudobulk heatmap of Toll Like Receptor (TLR) Activation in macrophages of C57BL/6J dorsal root ganglia. TPM – Transcripts Per Million. Box and purple arrows indicate genes of interest. Gene set obtained from GO Biological Gene Ontology TPM – Transcripts Per Million. Q1 – neurofilament light quartile 1. Q4- neurofilament light quartile 4.

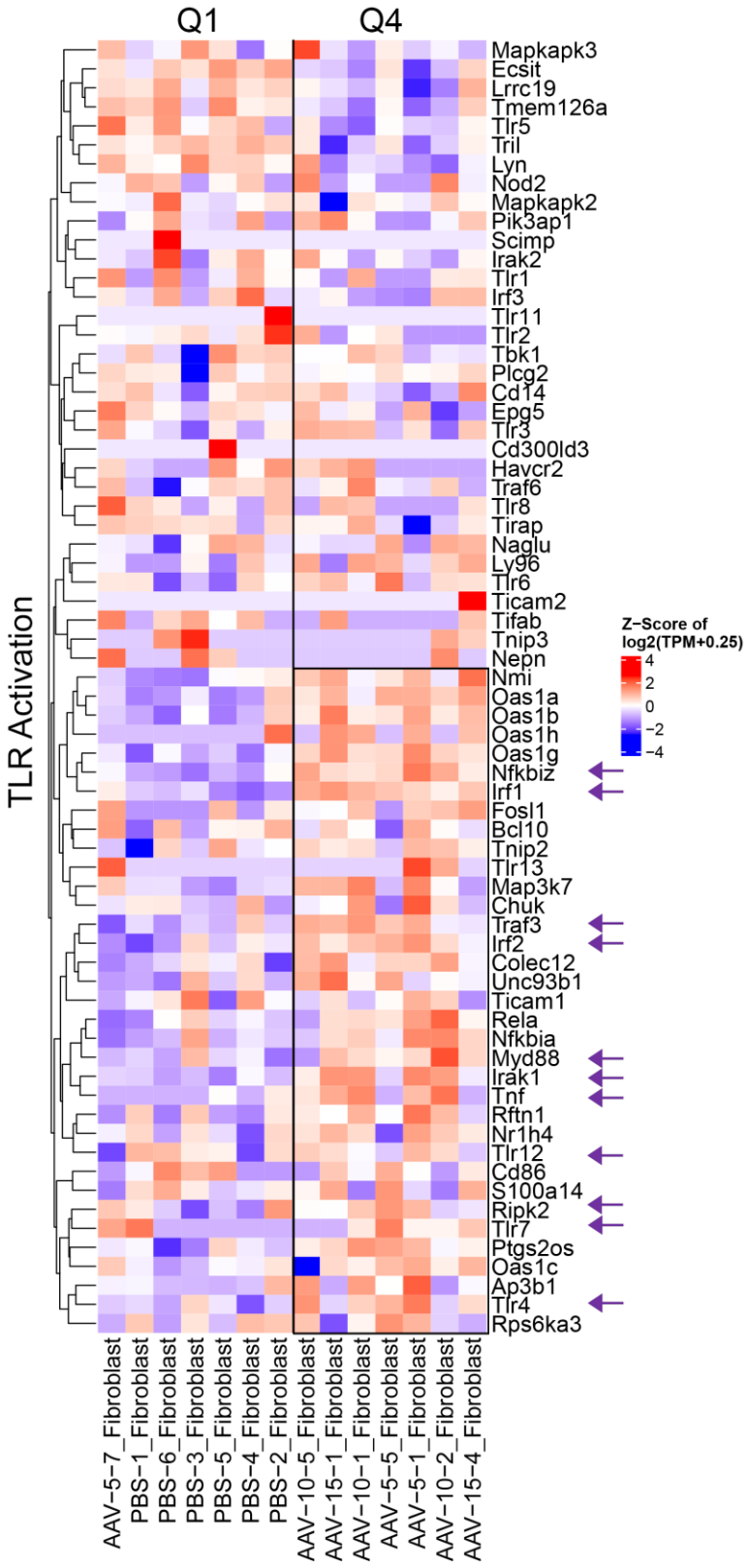

Figure S3: Pseudobulk heatmap of Toll Like Receptor (TLR) Activation in fibroblasts of C57BL/6J dorsal root ganglia. TPM – Transcripts Per Million. Box and purple arrows indicate

genes of interest. Gene set obtained from GO Biological Gene Ontology. Q1 – neurofilament light quartile 1. Q4- neurofilament light quartile 4.

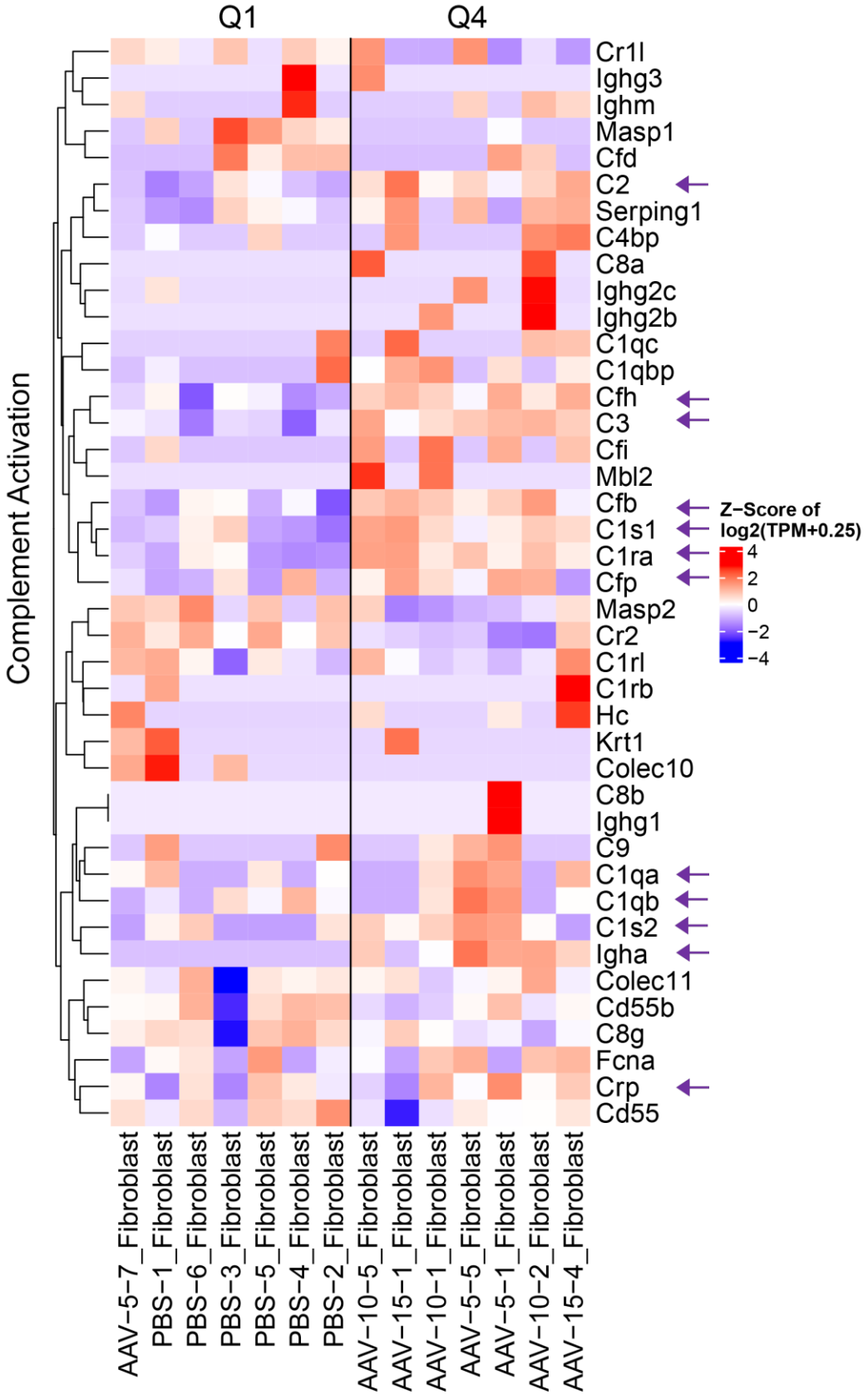
Q1
Q4
Complement Activation
Cr1l
Ighg3
Ighm
Masp1
Cfd
C2
Serping1
C4bp
C8a
Ighg2c
Ighg2b
C1qc
C1qbp
Cfh
C3
Cfi
Mbl2
Cfb
C1s1
C1ra
Cfp
Masp2
Cr2
C1rl
C1rb
Hc
Krt1
Colec10
C8b
Ighg1
C9
C1qa
C1qb
C1s2
Igha
Colec11
Cd55b
C8g
Fcna
Crp
Cd55
Z−Score of
log2(TPM+0.25)
4
2
0
−2
−4
AAV−5−7_Fibroblast
PBS−1_Fibroblast
PBS−6_Fibroblast
PBS−3_Fibroblast
PBS−5_Fibroblast
PBS−4_Fibroblast
PBS−2_Fibroblast
AAV−10−5_Fibroblast
AAV−15−1_Fibroblast
AAV−10−1_Fibroblast
AAV−5−5_Fibroblast
AAV−5−1_Fibroblast
AAV−10−2_Fibroblast
AAV−15−4_Fibroblast

Figure S4: Pseudobulk heatmap of Complement Activation in fibroblasts of C57BL/6J dorsal root ganglia. TPM – Transcripts Per Million. Box and purple arrows indicate genes of interest. Gene set obtained from GO Biological Gene Ontology Q1 – neurofilament light quartile 1. Q4- neurofilament light quartile 4.

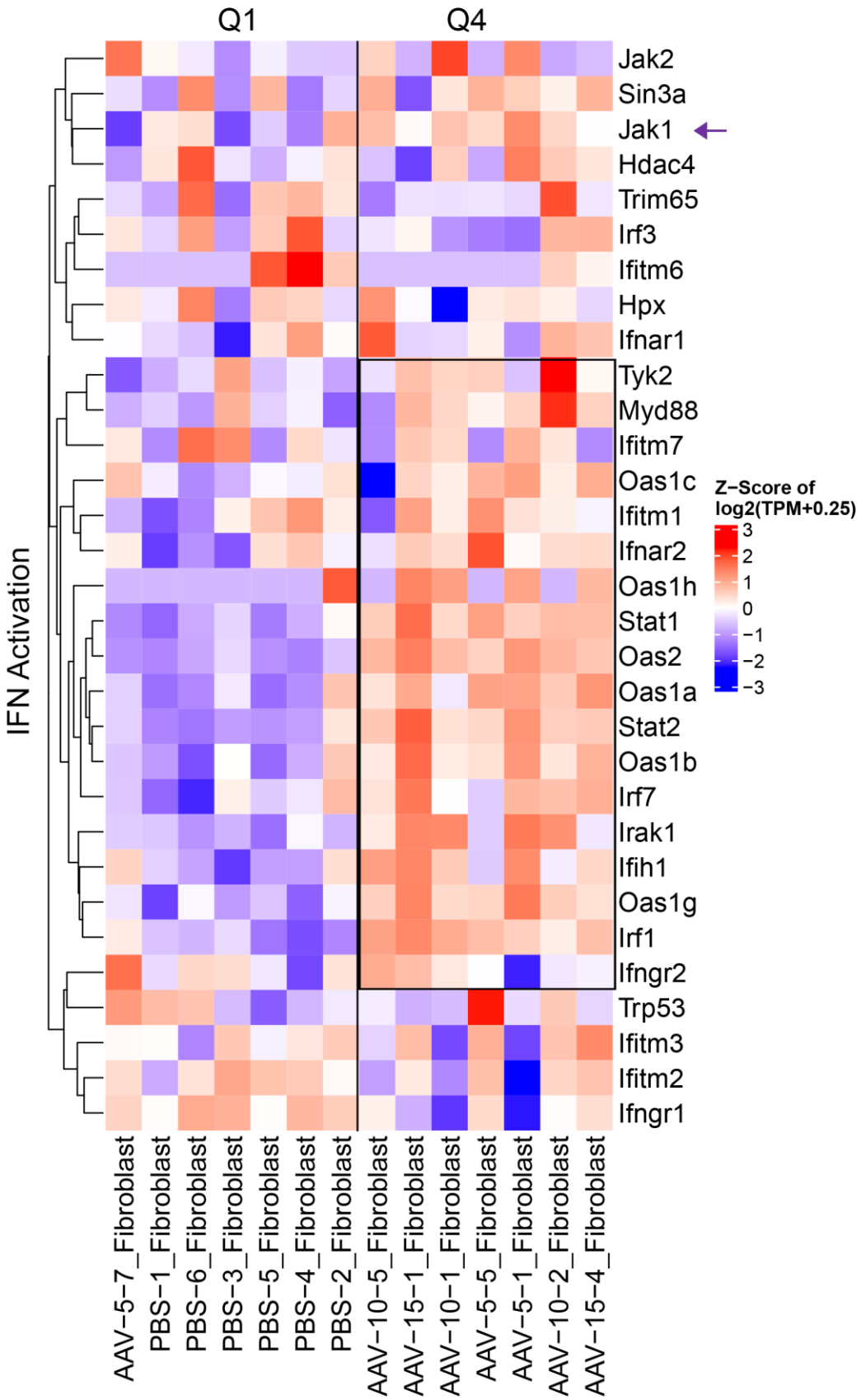
Q1
Q4
IFN Activation
Jak2
Sin3a
Jak1
Hdac4
Trim65
Irf3
Ifitm6
Hpx
Ifnar1
Tyk2
Myd88
Ifitm7
Oas1c
Ifitm1
Ifnar2
Oas1h
Stat1
Oas2
Oas1a
Stat2
Oas1b
Irf7
Irak1
Ifih1
Oas1g
Irf1
Ifngr2
Trp53
Ifitm3
Ifitm2
Ifngr1
Z−Score of log2(TPM+0.25)
3
2
1
0
−1
−2
−3
AAV−5−7_Fibroblast
PBS−1_Fibroblast
PBS−6_Fibroblast
PBS−3_Fibroblast
PBS−5_Fibroblast
PBS−4_Fibroblast
PBS−2_Fibroblast
AAV−10−5_Fibroblast
AAV−15−1_Fibroblast
AAV−10−1_Fibroblast
AAV−5−5_Fibroblast
AAV−5−1_Fibroblast
AAV−10−2_Fibroblast
AAV−15−4_Fibroblast

Figure S5: Pseudobulk heatmap of Interferon (IFN) Activation in fibroblasts of C57BL/6J dorsal root ganglia. TPM – Transcripts Per Million. Box and purple arrows indicate genes of interest. Gene set obtained from GO Biological Gene Ontology. Q1 – neurofilament light quartile 1. Q4- neurofilament light quartile 4.

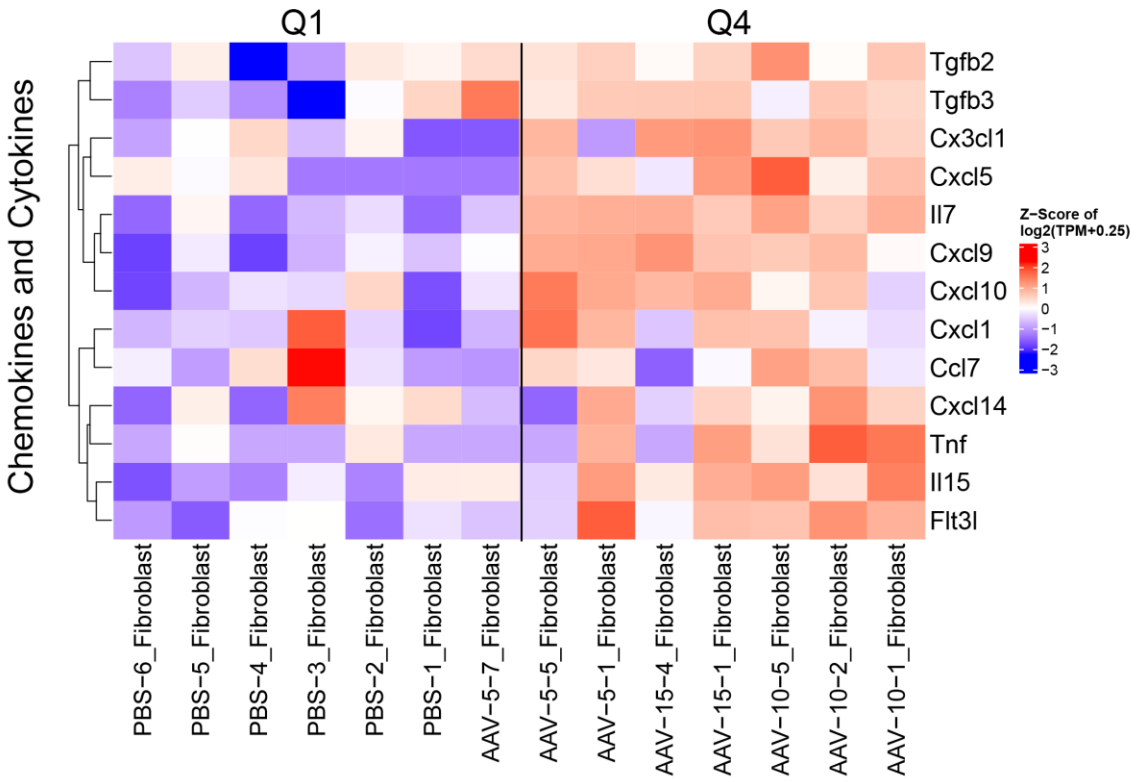

Figure S6: Pseudobulk heatmap of cytokines and chemokines in fibroblasts of C57BL/6J dorsal root ganglia. Gene set obtained from GO Biological Gene Ontology TPM – Transcripts Per Million. Q1 – neurofilament light quartile 1. Q4- neurofilament light quartile 4.

a

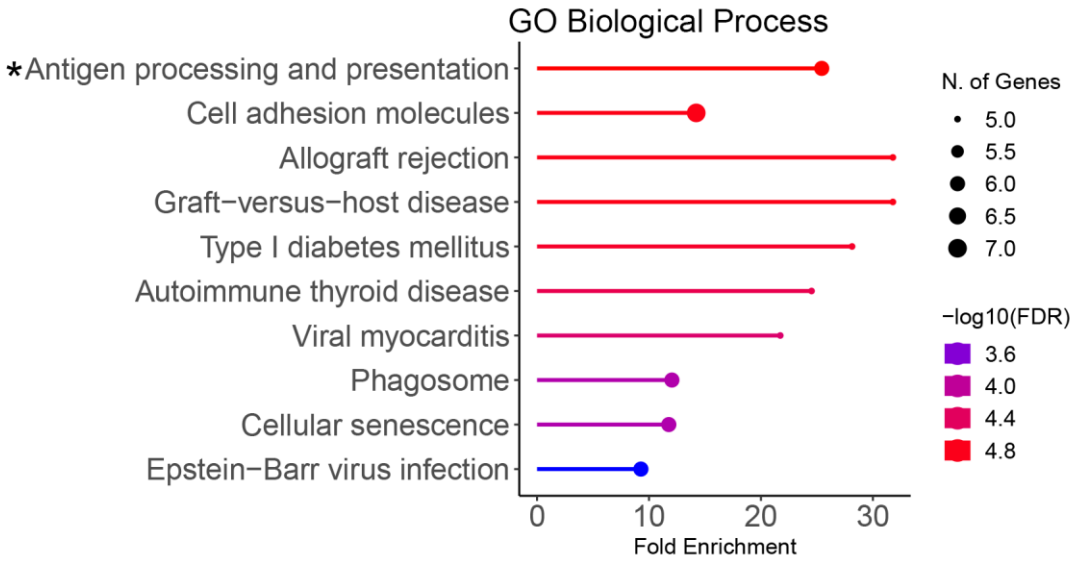
GO Biological Process
*Antigen processing and presentation
Cell adhesion molecules
Allograft rejection
Graft−versus−host disease
Type I diabetes mellitus
Autoimmune thyroid disease
Viral myocarditis
Phagosome
Cellular senescence
Epstein−Barr virus infection
0
10
20
30
Fold Enrichment
N. of Genes
5.0
5.5
6.0
6.5
7.0
−log10(FDR)
3.6
4.0
4.4
4.8

b

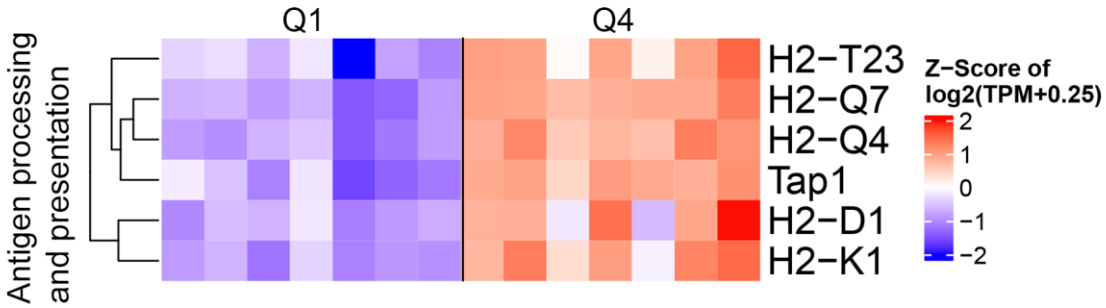
Q1
Q4
Antigen processing and presentation
H2−T23
H2−Q7
H2−Q4
Tap1
H2−D1
H2−K1
Z−Score of log2(TPM+0.25)
2
1
0
−1
−2

c

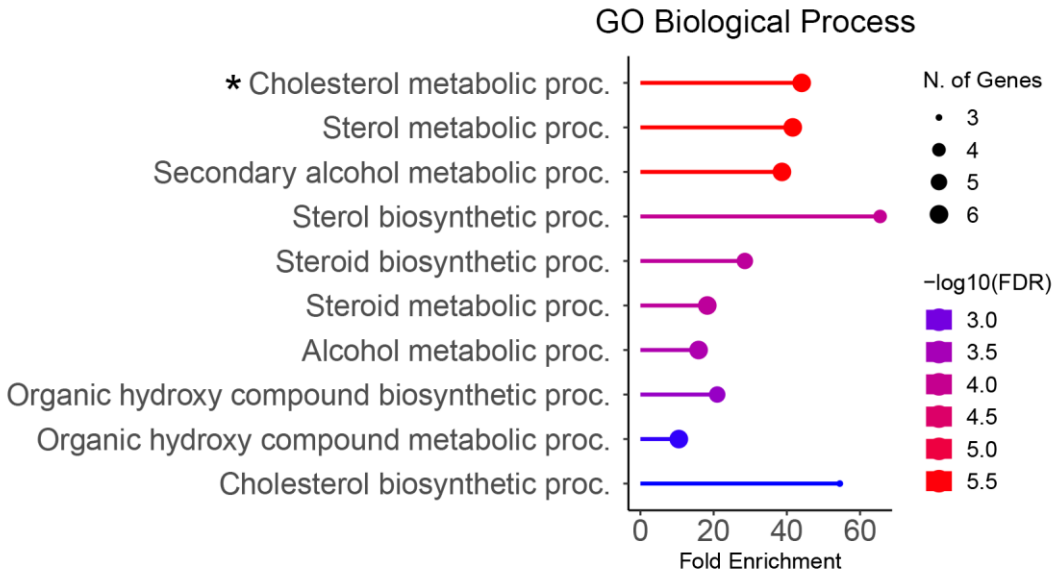
GO Biological Process
* Cholesterol metabolic proc.
Sterol metabolic proc.
Secondary alcohol metabolic proc.
Sterol biosynthetic proc.
Steroid biosynthetic proc.
Steroid metabolic proc.
Alcohol metabolic proc.
Organic hydroxy compound biosynthetic proc.
Organic hydroxy compound metabolic proc.
Cholesterol biosynthetic proc.
0
20
40
60
Fold Enrichment
N. of Genes
3
4
5
6
−log10(FDR)
3.0
3.5
4.0
4.5
5.0
5.5

d

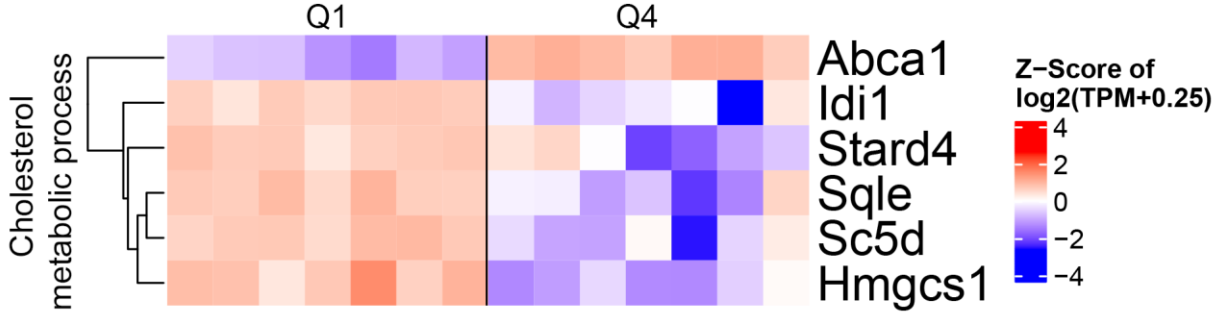
Q1
Q4
Cholesterol metabolic process
Abca1
Idi1
Stard4
Sqle
Sc5d
Hmgcs1
Z−Score of log2(TPM+0.25)
4
2
0
−2
−4

Figure S7: Enriched process in satellite glia and Schwann cells following AAV-treatment in C57BL/6J mice. **a.** Go Term enriched processes in satellite glia. Differentially activated genes (DEGs) of satellite glia from neurofilament light chain (NFL) at quartile 4 (Q4) versus quartile 1(Q1) were used for the Gene set enrichment analysis (GSEA). Asterisk indicates a pathway of interest. **b.** Pseudobulk heatmap of the Antigen processing and presentation process in satellite glia. **c.** Go Term enrichment processes in Schwann cells. DEGs of Schwann cell from NFL Q4 vs Q1 were used for the GSEA analysis. **d.** The top process in Schwann cells is represented in the pseudobulk heatmap in Schwann cells. TPM -Transcripts per million.

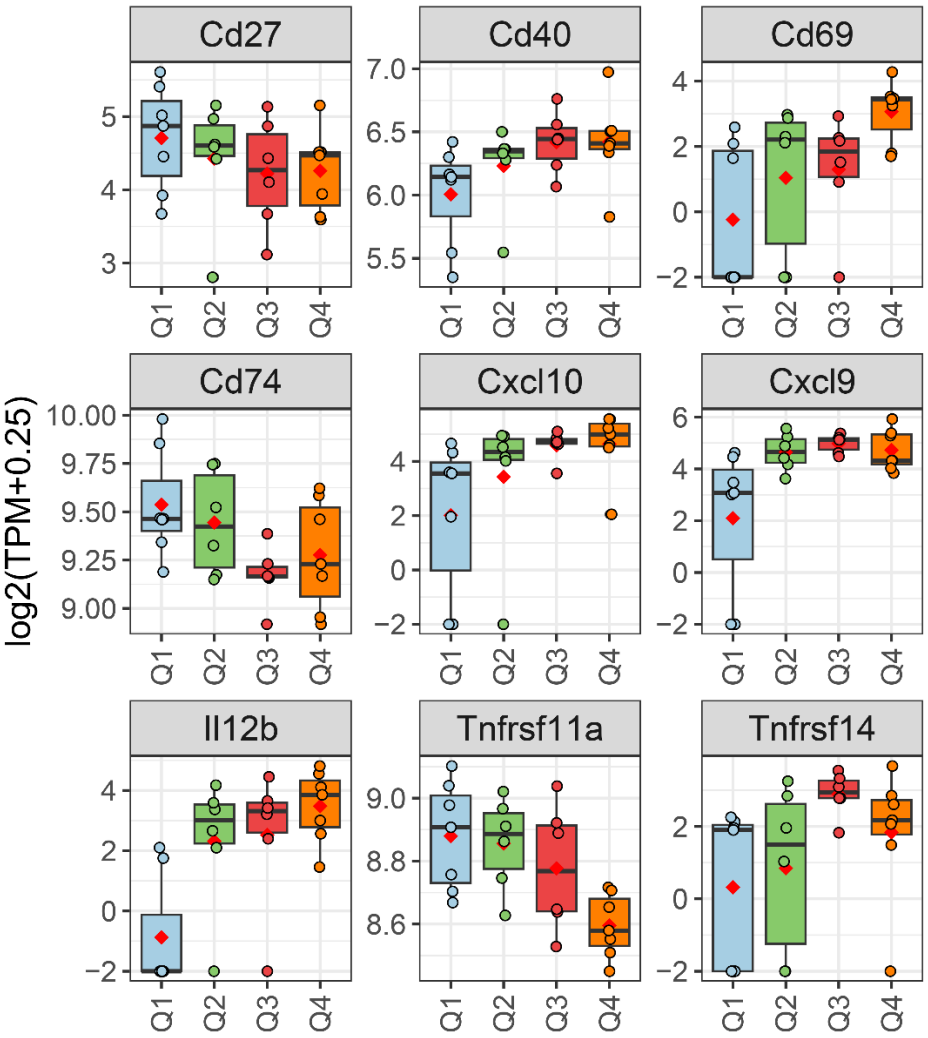

Figure S8: Alteration in the expression of immune based genes in macrophages of AAV-miR-SOD1 treated mice. These components were found to be significantly upregulated in an O-link proteomic analysis of the cerebrospinal fluid of non-human primates treated with AAV-miR-SOD1 from Hawley et al., 2024. Q – Neurofilament light quartile 1-4.

Acknowledgements

Ben Doyle, David Koske and Zachary Hawley for dissection support. Patrick Cullen for nuclei sample processing and sequencing. Zhengyu Ouyang, Yu(Henry) Sun for computational support.

Config.yml file

```
---------------------
1: # please check wiki page for the details
2: prj_name: TST11982_wAAV_cellbender_subset5 # this is the name of the project which
    will be used as prefix of all file created
3: prj_title: "TST11982 Mouse DRG snRNA-seq Study 1" # quote might be needed
4: ref_name:
    {'Renthal':/camhpc/ngs/projects/Renthal_mouse_DRG/Make_Azimuth/mouse_dr
    'Jung':/edgehpc/dept/compbio/projects/GSE201654_MouseDRG/Azimuth_ref/GS
5: output:
    /mnt/depts/dept04/compbio/projects/TST11982/dnanexus/SH/cluster_res0.6/
    #output path
6: sample_name: Sample_Name # this is the column header in the following meta file which
    specify the sample name
7: sample_meta:
    /mnt/depts/dept04/compbio/projects/TST11982/dnanexus/SH/sampleMeta.csv      8:
gene_group:
9:      MT:
10:         startwith: ["MT-","Mt-","mt-"]
11:         cutoff: 20 # percentage cutoff to filter out the cells (larger than this cutoff),
12:         rm: False # this means the genes specified "startwith" will be REMOVED
    from the downstream analysis
13:     # The following is an example (Ribosomal genes) to add additional gene set/list
    to be quantified the percentage over total UMI per cell
14:     # additional gene set/list can be added as the format
15:     RP:
16:         startwith: [MRPL,MRPS,RPL,RPS]
17:         cutoff: 50
18:         rm: False
19: filter_step: True # if False, the above 'gene_group' filtering will be skipped as well
20: dbl_filter: False # if True, the dbl finding class will be used to remove the predicted
    doublets, if a numeric (0~1), cells with larger predicted doublet scores will be removed
21: min.cells: 5 #filtering genes by minimal cell, please increase this when there is a large
    number of cells
22: min.features: 50 #filtering cells by minimal genes
23: highCount.cutoff: 80000 # any cells with higher total counts to be removed
24: highGene.cutoff: 6000 # any cells with higher number of detected genes to be removed
25: intron.cutoff: 1.0 # any cells with less intron rate will be removed if it is available
26: dblscore: True # perform scDbl to get the doublet score
27: group: #if provided, a 10X QC box plot will be ploted in QC plot
28: rasterizeFig: True # should image in pdf be rasterized
```

```
29:
30: runAnalysis: True
31: reRunQC: True # if satisfied with the above setting, please set this to False to save
    time
32: overwrite: True
33: newProcess: False
34: methods: [SCT,SeuratRef,sctHarmony] #SCT method (including log1p) is required
    expression normalization
35: expScaler: 10000 #integer value, 0: SCT (along with following option); 1-100:
    logNormal with scale.factor to be the specified quantile; >100: logNormal with
    scale.factor to be the specified value
36: PrepSCTFindMarkers: True # should the "PrepSCTFindMarkers" applied on SCT to
    be exported for visualization expression
37: clusterMethod: Louvain # the cluster methods: Louvain or Leiden
38: clusterResolution: 0.6 #A parameter value controlling the coarseness of the clustering.
    Higher values lead to more clusters
39: parallel: slurm #"sge" or "slurm"
40: core: 32
41: memory: 480G #if provided (e.g. 100G), it will be used to request cluster scheduler
42: jobID: j12 # please make sure this job id is different with your other projects which would
    be run at the same time
43:
44: major_cluster_rate: 0.7 # the proportion of cells of an integration cluster to be assigned to
    a seurat reference label
45: batchCell: 200000 # the number of cells to be put into one batch to limit memory usage
    (please remove/rename the 'tmp' folder in sctHarmony/SeuratRef, if rerun is needed)
46: harmonyBatchGene: 5000 # the number of high variable genes for each batch during
    sctHarmony step
47:
48: ## DEG analysis for an annotation (such as disease vs health) within a cell type annotation
49: DEG_desp:
    /mnt/depts/dept04/compbio/projects/TST11982/dnanexus/20231007235510_Fer
    #required for DEG analysis
50: NAstring: [] #provide a list of strings which should be considered NA and associated
    cells to be removed
51: DEG_pipeline_version: v1 #v1: implemented Sept, 2023, v0: original implemented by
    bioStats team linked to the publication below
52: # Please be causion of changing the following default filtering
53: # More details can be found: section 2.4 in https://pubmed.ncbi.nlm.nih.gov/35743881/
54: # Applies the 1st round of biostats filtering pipeline. Note that this filter is applied to all
    cells of the experiment
55: min.cells.per.gene: 3 # if `perc_filter` is FALSE, then keep only genes that have
    expression in at least min.cells.per.gene
56: min.genes.per.cell: 250 # keep cells with expression in at least min.genes.per.cell genes.
57: min.perc.cells.per.gene: 0.00 #if 'perc_filter'`' is TRUE, then keep only genes that have
    expression in at least min.per.cells.per.gene *
    100 percent of cells
58: perc_filter: TRUE #if TRUE, apply the cells.per.gene filter using percentages (expressed
    as a decimal) rather than an absolute threshold
```

59: *# Apply the 2nd round of biostats filtering. For "group" mode, the filtering is applied to `ref_group` and `alt_group` for the given cell type of interest.*
60: R6_min.cells.per.gene: 3 *#minimum cells expressed per gene. This filter is applied if `R6_perc.cells.filter` is FALSE*
61: R6_min.perc.cells.per.gene: 0.1 *# minimum % cells expressed per gene filtering (use decimal form of percentage). This threshold is applied if 'R6_perc.cells.filter' is TRUE and 'R6_cells.per.gene.filter' is TRUE*
62: R6_min.cells.per.gene.type: "or" *#The type of cell per gene filtering.If it has the value "and" then it requires the gene be expressed in both reference and non-reference groups. If it has the value "or" then it requires the gene be expressed in either group*
63: R6_cells.per.gene.filter: TRUE *#TRUE means apply cells per gene filtering*
64: R6_perc.cells.filter: TRUE *#TRUE means apply cell.per.gene filtering by use of a percentage rather than absolute threshold. If the percentage results in a number less than R6_min.cells.per.gene, the code will automatically switch to min.cells.per.gene absolute thresholding*
65: R6_perc.filter: FALSE *#If TRUE, then apply the 75th percentile gene filtering*
66: R6_perc.filter.type: "and" *#The type of percentile gene filtering. If it has the value "and" then any gene that has 75th percentile of zero in both groups will be filtered out. If it has the value "or" then any gene that has a 75th percentile of zero in either group will be filtered out.*
67: R6_perc_threshold: 0.90 *#Percentile threshold, 75th percentile is default. Express percentile as a decimal value.*
68: R6_min.ave.pseudo.bulk.cpm: 1 *#cpm filtering threshold*
69: R6_pseudo.bulk.cpm.filter: FALSE *#if TRUE, then apply a cpm filter on the pseudo-bulk counts*
70: R6_min.cells.per.subj: 3 *#Minimum cells required per subject, must be a nonzero number*
71:
72: *## publish to celldepot*
73: *## please use "Create Project" on CellDepot to add this project "File Name" is <prj_name>.h5ad*
74: *#publish: False*

Chapter 3

Exploring Sciatic Nerve Action Potentials in Response to AAV-Induced Dorsal Root Ganglia Toxicity in C57BL/6J Mice

Introduction

The sciatic nerve enables motor function i.e., muscle activation for movement and sensory function for the detection of external stimuli from the environment. In mice, the sciatic nerve is formed by the fusion of L3, L4 and L5 spinal nerves (Rigaud et al., 2008). The nerve comprises efferent motor and afferent sensory axons, leading to the detection of action potentials in both directions. Sensory axons originate from the dorsal root ganglia (DRG) while motor axons originate from the ventral horn of the spinal cord. Damage to the anatomical structure of the nerve results in alterations in the nerve's conduction properties. Mechanical damage such as spinal crush causes a reduction in the amplitude, and significantly reduces the conduction velocity of the action potential (Büttner et al., 2018). Injection of toxic agents can lead to degeneration of the sciatic nerve and reduction of the conduction velocities (Üstün et al., 2017).

Recent advances in gene therapy have uncovered novel findings on treatment-related peripheral nerve damage in patients and animal models. A familial superoxide dismutase 1 (SOD1) ALS patient treated with an AAV9-microRNA targeting the human SOD1 gene was found to have clinical symptoms likely associated with the test article (Mueller et al., 2020). These phenotypes progressed to a loss of sural sensory-nerve action potentials and left median sensory potentials along with H-reflexes 10-weeks after intrathecal dosing. The amplitude of the superficial peroneal nerve sensory action potentials was reduced. Although rare, severe cases of peripheral nerve axonal degeneration and fibrosis were associated with changes to the nerve conduction velocities in the sural nerve in non-human primates (NHP) (Hordeaux, Buza, Dyer, et al., 2020). Mice have demonstrated extensive and dose-dependent injury to the sciatic nerve following intrathecal delivery of AAV-miR-SOD1 (S. K. Chen et al., 2023; Hawley et al., 2024). Histopathological assessment demonstrated axonal degeneration and myelin dilation at 3 weeks post-injection which lasted to over 9 months post-injection (Hawley et al., 2024). The

severity of these findings varied sporadically and did not consistently affect one anatomical side, with the range of severity ranging from minimal to moderate. It is not certain if both sensory and motor axons were affected. It is predicted that sensory axons are likely affected due to similar findings in the saphenous sensory nerve in the same study. A study in Wistar Han rats investigated the plantar nerve action potential conduction velocity following intravenous dosing of AAV9 expressing the human frataxin transgene (Tyszkiewicz et al., 2024). The authors observe minimal to moderate degeneration of nerve fibers and neurons in the DRG and no discernible impact on conduction velocities. The authors speculate lack of severity potentially contributes to their findings.

Axonal degeneration and myelin dilation in the sciatic nerve is consistent and dose-dependent in mice post-AAV delivery (S. K. Chen et al., 2023; Hawley et al., 2024). High AAV titers cause substantial damage to the sciatic nerves including sensory axons. It is hypothesized that injury to sensory axons could alter peripheral sensory action potentials in the sciatic nerve. Therefore, the purpose of this study is to determine if AAV-induced sciatic nerve injury caused an alteration in the conduction properties of the sciatic nerve. Mice were intrathecally injected with a high titer, 1.5E12 GC, of AAV-miR-SOD1 and extracellular recordings of the sciatic nerve action potentials were collected longitudinally. The latencies to the biphasic waveform minima and maxima were examined. Peripheral nerve damage and axonal degeneration was confirmed by serum neurofilament light levels as it has been shown to be a robust biomarker of DRG toxicity in many animals models (Fader et al., 2022; Johnson et al., 2023; Tyszkiewicz et al., 2024). Previous reports suggest damage to the sciatic nerve leads to slowing of the conduction velocity due to the increase in the latency of the action potential (Büttner et al., 2018). Thus, it is hypothesized that mice treated with AAV would exhibit an increase in action potentials latency, or in more severe instances, a total absence of action potentials.

Materials and Methods

Animals

Wild type C57BL/6J (Stock #:000664) females were obtained from the Jackson Laboratory and were housed in a 12/12 hrs light/dark cycle temperature-controlled room (22-24 ºC) with access to food pellet and water provided *ad libitum*. Mice were also given diet gels to prevent the loss of bodyweight as the study progressed. All animal use and treatments were approved by the Biogen Institute of Animal Care and Use Committee (IACUC) and followed the National Institute of Health Guide for the Care and Use of Laboratory Animals.

AAV vector design and production

AAV-miR-SOD1 is a single-stranded AAV9 vector composed of ubiquitous CAGG promoter driving the expression of two artificial microRNAs designed to target human SOD1, miR30a-huSOD1_#5 and miR155-huSOD1_#7.

miR30a scaffold with mature guide huSOD1_#5 underlined:

5'TGTTTGAATGAGGCTTCAGTACTTTACAGAATCGTTGCCTGCACATCTTGGAAA
CACTTGCTGGGATTACTTCTTCAGGTTAACCCAACAGAAGGCTAAAGAAGGTATAT
TGCTGTTGACAGTGAGCGTACTTTCTTCATTTCCACCTTTTAGTGAAGCCACAGAT
GTAAAGGTGGATGAAGAAAGTATGCCTACTGCCTCGGACTTCAAGGGGCTACTTT
AGGAGCAATTATCTTGTTTACTAAAACTGAATACCTTGCTATCTCTTTGATACATTTT
TACAAAGCTGAATTAAAATGGTATAAATTAAATCACTTTA**3'**.

miR155 scaffold with mature guide huSOD1_#7 underlined:

5'CTGGAGGCTTGCTGAAGGCTGTATGCTGTCAGGATACATTTCTACAGCTTTTGGC
CACTGACTGACAAGGTGGATGAAGAAAGTACAGGACACAAGGCCTGTTACTAGC
ACTCACATGGAACAAATGGCC **3'**.

These artificial microRNAs target the human superoxide dismutase 1 (SOD1) mRNA in the cytoplasm for degradation via the RNA interference pathway. The expression and transcriptional regulation of the cassette is enhanced by the addition of the Woodchuck Hepatitis Virus Post-transcriptional Regulatory Element (WPRE), and a human growth hormone poly-A (hGHpolyA) signal downstream of the artificial microRNAs.

AAV vectors were produced by PackGene Biotech (Worcester, MA, USA) by triple plasmid transfection protocol and the protocol has been described previously (Torregrosa et al., 2021). The AAV produced was assessed for sterility, endotoxin level and purity. Qualitative empty to full capsid assessment was determined by transmission electron microscopy (TEM). The titer was determined via ddPCR method targeting the WPRE.

Intrathecal Injections

Intrathecal injections were performed at ~6 weeks of age. Mice were anesthetized with isoflurane and the depth of anesthesia was assessed via a toe pinch. Ethiqua XR (buprenorphine extended-release injectable suspension) (Fidelis Animal Health, North Brunswick, New Jersey) was administered to eliminate pain sensation. The mouse fur was clipped from the injection area and an ocular lubricant was applied. The mouse was placed on a heating source in ventral recumbency. The injection site was thoroughly cleaned, including three wipes with betadine and three wipes with isopropyl alcohol (alternating). Vertebral processes were detected by arching the spine which allows correct orientation and placement of the needle. A 29-gauge, 0.3mL syringe (Cat#: 4429-3, Smiths Medical ASD, Inc., Southington, CT, USA) was inserted in the gap between L5 and L6 or L4 and L5 and a tail flick is detected if the needle is in the correct location. The test article or vehicle (artificial cerebrospinal fluid) was slowly administered (10 µL, 1.5E12 GC) to minimize rapid changes in CSF pressure. Mice were then transferred to a heating chamber set at 37C for recovery first and then placement in their home cages.

Neurofilament light measurement

Mice were bled (~100 µL) via facial vein puncture at -1, 3-, 6- and 11-weeks post-injection. The blood was collected in in BD Microtainer SST Clog Activator/Gel tubes (Becton Dickinson, Franklin Lakes, NJ, USA). The tube was inverted a few times and left for 30 mins

for coagulation. The tube was then centrifuged at 2000RCF (4600RPM) for 10 minutes to separate the serum for neurofilament light measurement (NFL). Neurofilament in serum was quantified via Simple Plex Human NF-L Cartridge (Protein Simple, SPCKB-PS-002448, San Jose, CA, USA) by following the manufacturer's protocol.

Sciatic nerve action potential recordings

The mouse was anesthetized, and a light foot pinch was used to assess the depth of anesthesia. Ointment was placed on the eyes to prevent dryness and the mouse was relocated to an isoflurane nose cone. The mouse was placed on a heating pad. The fur covering the hindlimbs was sometimes shaved with an electric razor to allow easy probe placement, however, this was not always needed to record an action potential. The stimulating electrode (cathode) was inserted under the skin at the dorsum or at the ankle of the foot and a reference electrode (anode) was inserted distal from the cathode. Note that the electrodes are not pushed into the muscle. The recording electrode (G1) was inserted at the sciatic notch and a reference electrode (G2) was inserted distal from the recording electrode (G1). A ground electrode was inserted dorsally (Fig. 2). From the foot to the dorsal midline of the mouse the placement of electrodes in order is anode, cathode, G1 and G2. The exact location of the electrodes can be slightly adjusted to generate cleaner electrophysiological recordings. Custom software was written using LabView (National Instruments, Woburn, MA, USA) to operate a portable digital acquisition device (DAQmx, USB-6343, National Instruments, Woburn, MA, USA). Timing pulses were generated by the analog output of the DAQmx device and used to drive a stimulus isolator (A365, World Precision Instruments, Sarasota, FL, USA) to deliver current to the leg muscle of the mouse. Sciatic nerve activity was simultaneously acquired using a single channel, bipolar amplifier (DAM80, World Precision Instruments, Sarasota, FL, USA), subcutaneous needle electrodes and the analog input of the DAQmx device. Biopotentials were acquired at

34kHz after applying a gain of 100X, a bandpass filter 0.3Hz to 3kHz and each waveform was constructed from the average of three stimulus pulses repeated at 1Hz.

Statistical analysis

GraphPad Prism 8 (San Diego, CA, USA) was used to plot graphs and conduct statistical analysis. All data are expressed as means ± standard deviation (SD). Measurements from a few animals were avoided due to the inability to detect the action potential. For all amplitude measurements, all outliers were removed using the ROUT method outlier test.

Results

Intrathecal administration of AAV increases serum neurofilament light levels

To model peripheral nerve damage, mice were injected with 1.5E12 GC of AAV-miR-SOD1 intrathecally at 6 weeks of age. Neurofilament light levels (NfL) in serum was monitored to determine the degree of dorsal root ganglia (DRG) and peripheral nerve toxicity in mice, indicative damage to sensory neurons and axons. Neurofilament light levels surge at 3 weeks post-injection to 3532 ± 1385 pg/mL in AAV-miR-SOD treated versus vehicle mice (Fig. 1a). Neurofilament levels decreases in subsequent timepoints to 676 ± 1385 pg/mL at 11 weeks post-injection. Vehicle treated mice have a range of ~116 -167 pg/mL throughout the study. This NfL surge and decline is consistent with previous reports in rodents (Fader et al., 2022; Hawley et al., 2024; Tyszkiewicz et al., 2024). There is a large variability in NfL in AAV-treated mice at week 3 post-injection, but mice with high NfL had consistently high NfL levels throughout all timepoints (Fig. 1b). Overall, AAV-treated mice display elevated NfL levels, indicating DRG and peripheral nerve damage allowing studying action potentials.

AAV-miR-SOD1 had no affect the action potential latencies

The goal of longitudinally tracking sciatic nerve action potentials necessitated a non-invasive approach that had minimal impact on the study animals. Electrode placement was subdermal with without probing into the muscle. The consistency of recordings required adjustments of the stimulating and recording electrodes to generate comparable waveforms in all mice (Fig. 2a). The biphasic action potential response generated is the sum of all action potentials in individual axons. It is important to note that sample traces can vary as seen in the vehicle (artificial CSF) and AAV-miR-SOD1 treated mice (Fig. 2b), these traces were consistent with previous studies (Schulz et al., 2014). The latency to the minima and the maxima were calculated as the time between the stimulus artifact and the time to the minimum point or maximum point of the biphasic response (Fig. 2b). The mean latency to the minima for all mice

at all timepoints was ~1.0 - 1.5 msec with no clear trend in any treatment groups (Fig. 2c). The mean latency to the maxima for all timepoints is ~1.5 – 2.0 msec with no trend in any treatment groups (Fig. 2d). At 3 weeks post-injection, the latencies to the minima and maxima increased relative to control, of which one was significant (Mixed-effects analysis followed by Bonferroni Multiple Comparison test, $*P<0.05$). However, this relationship was not maintained at 6 weeks post-injection (Fig. 2c, d). The amplitude of the action potential was measured from the minima to the maxima of the biphasic waveform. The amplitude of the sciatic nerve varies, and the standard deviation was large. The mean amplitude of the action potential at 3 weeks was 2.39 ± 1.46 mV for AAV-treated mice compared to 1.07 ± 0.23 mV for vehicle treated mic (Fig. 2e). The increase in amplitude was not observed at week 6 post-injection and the baseline readings for AAV-treated mice was higher than vehicle. High doses of AAV did not affect sensory action potentials in the sciatic nerve.

The action potential properties were not altered based on sex and anatomical side.

Toxicity in the sciatic nerve can be spotty and inconsistent requiring faceting the data by sex and anatomical side(Hawley et al., 2024). For males, the latency to the minima is similar for AAV-treated and vehicle-treated mice and it ranged from 1.0 – 1.5 msec without a trend in all timepoints (Fig. 3a). There could be a change in the latency to the maxima for males at 3- and 6-weeks post-injection, however, the relationship was inconsistent (Fig. 3b). The standard deviation of the amplitude was large, there was no distinct trend between AAV-treated mice and those treated with the vehicle. (Fig. 3c). In females, the latency to the minima and the maxima was similar for AVV-treated and vehicle-treated mice (Fig. 3d, e). The amplitude for two female mice was higher in AAV-treated mice, this increased the mean values AAV-treated mice (Fig. 3f).

Sciatic nerve axonal degeneration and dilation of myelin was not consistent in the left and right sciatic nerves (Hawley et al., 2024). Therefore, the left and right sciatic nerve action potentials were assessed at 3- and 6- weeks post-injection. Note that the -1 week post-injection timepoint was excluded because only one side was tested at week -1 post-injection. In the right sciatic nerve, the latency to the minima and maxima was similar in AAV and vehicle-treated mice (Fig. 4a, b). This trend was repeated for the left sciatic nerve (Fig. 4d, e). The amplitudes for the right and left sciatic nerves was higher for AAV-treated mice when compared to vehicle with large standard deviation (Fig 4c, e). The left and right sciatic nerves did not show a characteristic trend in response to AAV dosing and for both sex and side analysis, the number of animals was small to detect trends.

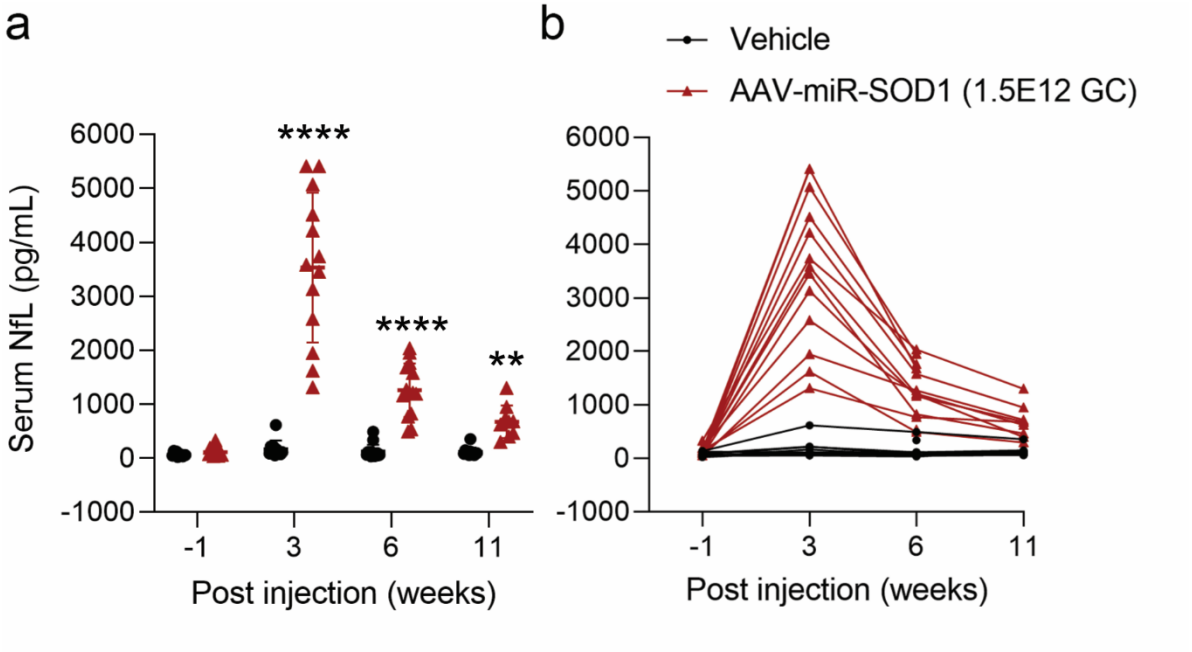

Figure 1: Neurofilament light chain (NfL) surges post AAV-miR-SOD1 intrathecal dosing. **a.** Plot showing the variation in serum NfL levels at different timepoints post-injection. **b.** Individual mice tracked over overtime. Mixed-effects analysis followed by Bonferroni Multiple Comparison test, $^{**}P<0.01$, $^{*}P<0.0001$. Data are mean ± SD with n=10-15/treatment.

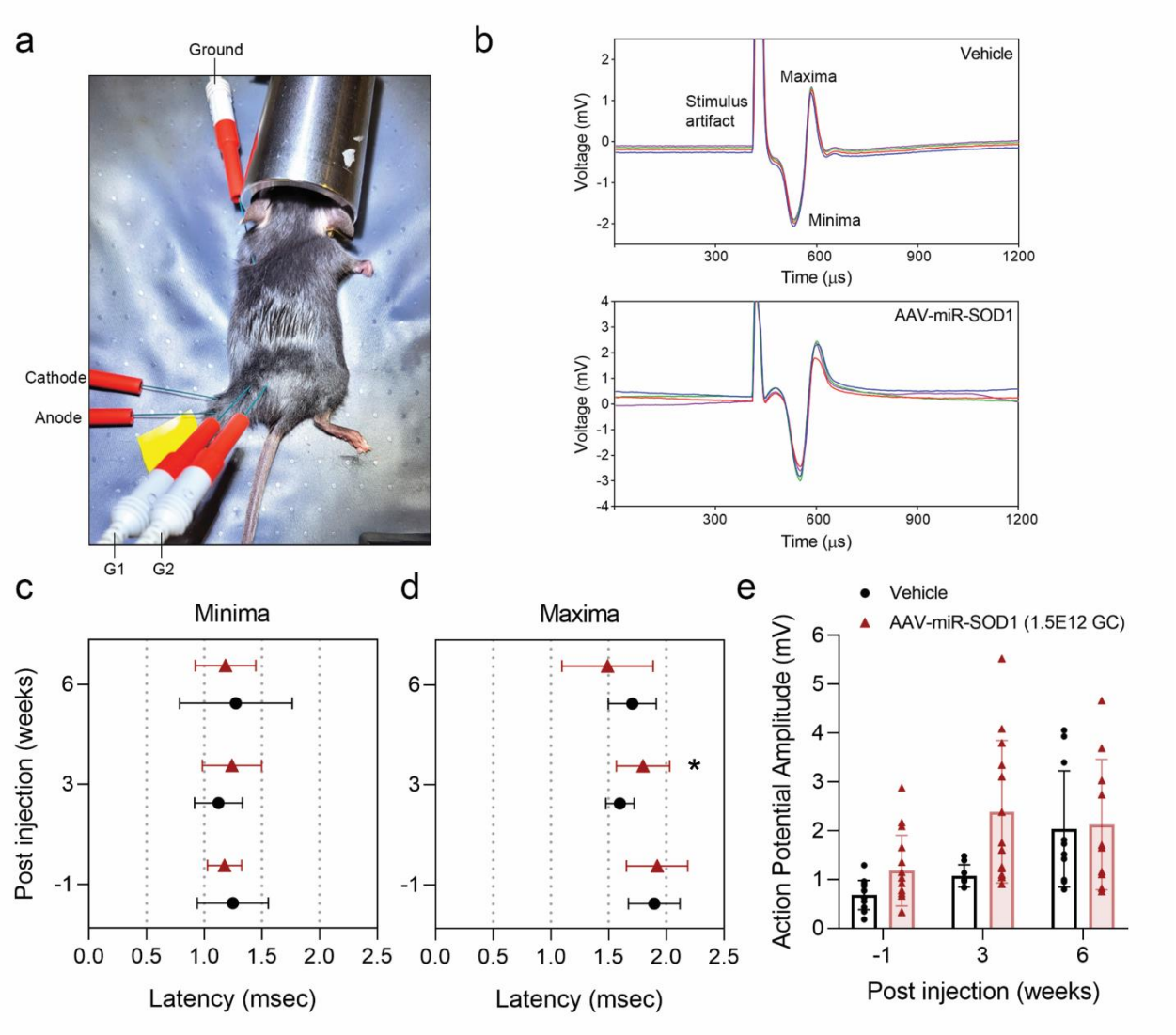

Figure 2: Electrophysiological design for the detection of mouse sciatic nerve action potentials. **a.** The stimulating electrodes are placed at the ankle while the recording electrodes are placed at the sciatic notch near the spinal cord. **b.** Sample traces from mice treated with vehicle and AAV-amiR-SOD1. **c.** Latency measurements to the minima, **d.** the maxima, and **e.** the amplitude of the biphasic sciatic nerve action potential for all mice. Data are mean ± SD with n=10-15/treatment. Mixed-effects analysis followed by Bonferroni Multiple Comparison test, *$P<0.05$, was conducted for panels c and d at each timepoint. All to other comparisons were not significant.

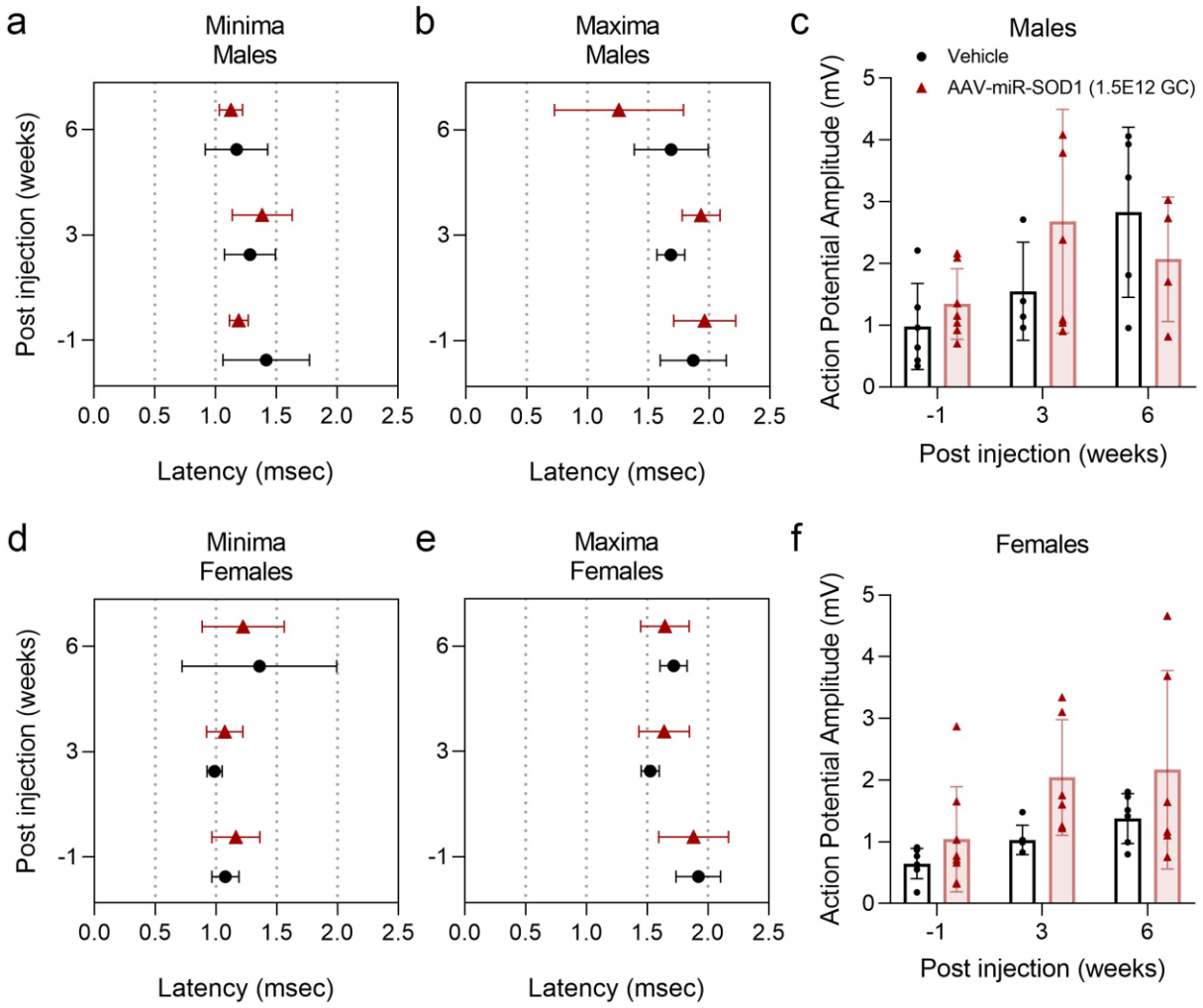

Figure 3: Latency measurements to the minima and maxima of sciatic nerve action potential separated by sex. **a.** The latency for the minima, **b.** maxima for males, and **c.** the amplitude of the action potential. **d.** The latency for the minima, **e.** maxima for females, and **f.** the amplitude for females. Only one side was recorded for week -1 post-injection while the average of both legs was calculated for 3- and 6-weeks post-injection. Data are mean ± SD with n=4-6/treatment. Mixed-effects analysis followed by Bonferroni Multiple Comparison test was conducted at each timepoint for panels a, b, d and e with not significance noted. No significance tests were conducted for e and f.

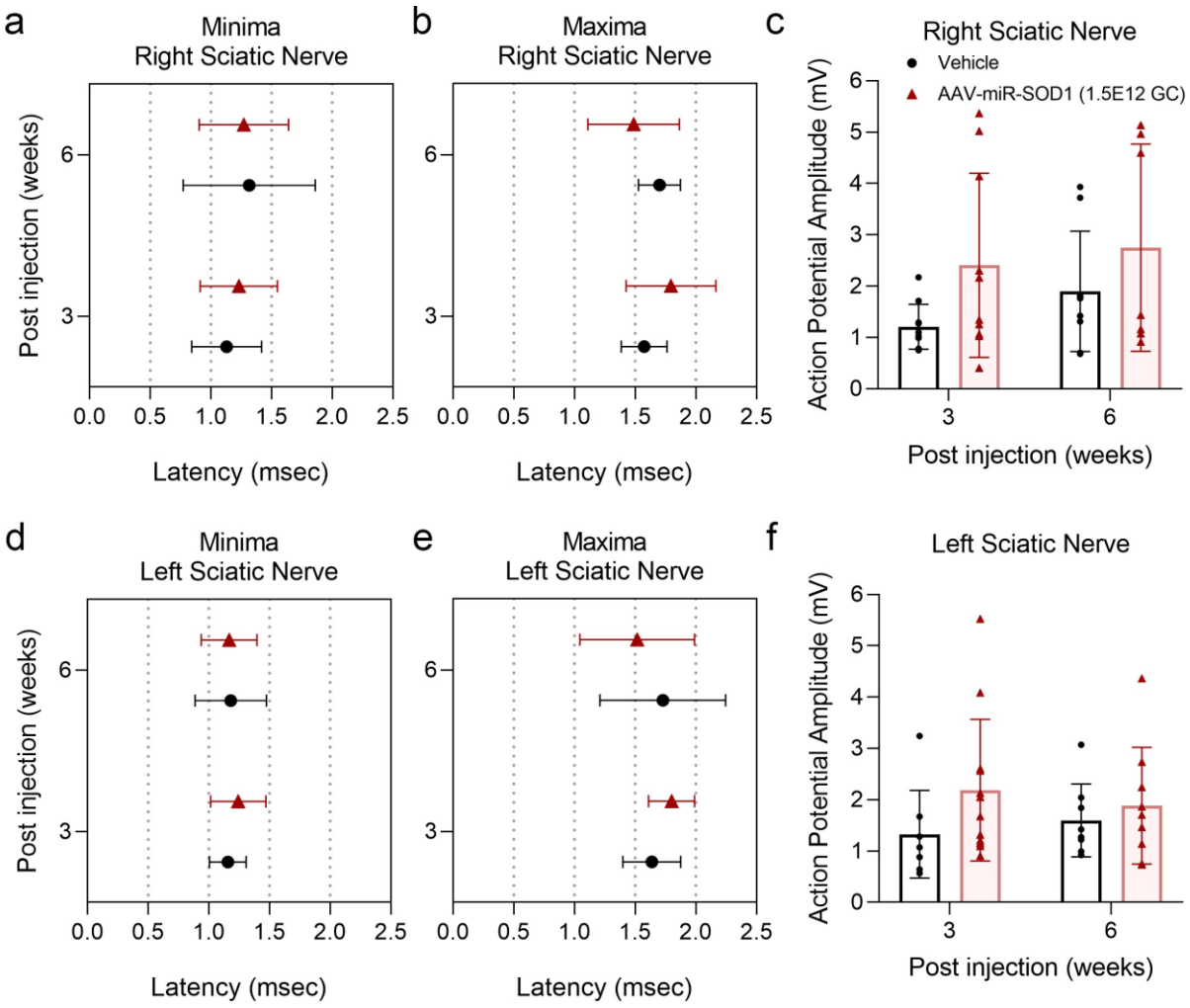

Figure 4: Latency measurements to the minima and maxima of sciatic nerve action potential separated by anatomical side. **a.** The latency for the minima, **b.** maxima for the right, and **c.** the amplitude of the right sciatic nerve. **d.** The latency for the minima, **e.** the maxima for females. and **f.** the amplitude for the left sciatic nerve. Note that the -1 week post-injection timepoint is excluded because only one side was tested. Data are mean ± SD with n=10-15/treatment. Two-way ANNOVA followed by Bonferroni Multiple Comparison test was conducted for at each timepoint for panels a, b, d and e with not significance noted. No significance tests were conducted for e and f.

Discussion

In this report, the aim was to understand the physiological effect of sciatic nerve injury in response to AAV-miR-SOD1 dosing in wild type mice. The study design emphasized sensory action potentials originating from the periphery, which then propagate towards the dorsal root ganglia (DRG) and into the spinal cord. Therefore, it is important to understand if the histopathological findings would translate to sciatic nerve action potential changes or in extreme cases, the loss of the action potential.

AAV-injected mice showed a consistent elevation in serum neurofilament light (NfL) levels indicting peripheral nerve injury. Mice showed a wide range of NfL levels within a dose group. This phenomenon has also been seen in a recent mouse study using the same AAV vector (Hawley et al., 2024). The severity of axonal degeneration is predicted to be proportional to the degree of serum NfL levels in mice as seen previously in rats (Fader et al., 2022). This is expected, neurofilaments are integral cytoskeletal components of the axon. Results from this study showed that the latencies to the minima and the maxima of the biphasic response were not affected by AAV. These findings were separated by sex and the anatomical side, and no changes or distinctive trends were detected. The amplitude in majority of the recordings varied, the amplitude is likely dependent on the proximity of the electrodes to the nerve and anatomical variability in mice. These results are consistent with recent findings in Wistar Han rats, where nerve conduction velocities remained unchanged following AAV9-frataxin administration. (Tyszkiewicz et al., 2024). The test article, dose and the route of administration differed between the two studies, intrathecal versus intravenous delivery in the rat study. In summary, mice injected with AAV exhibited changes in serum NfL levels; however, these alterations did not manifest in any observable physiological differences in the conduction properties.

Several limitations likely contributed to the observations in this short report. The sensitivity of the experimental design to detect changes and the degree of axonal degeneration needed to

yield electrophysiological deficit in the nerve is unknown. This approach might not effectively evaluate smaller, inadequately myelinated nerve fibers in comparison to larger, well-myelinated fibers. The changes in the latencies if present could be miniscule and not detectable using the current experimental design. Extracellular recordings measure the potential changes outside of the nerve meaning both damaged and healthy axons would be captured. Healthy axons could overshadow damaged or degenerating axons. Furthermore, it is not clear what proportion of damaged or degenerating axons is necessary for a change in the action potential to observable. Previous studies have shown that when the sciatic nerve is crushed, the changes can be seen in slowed conduction velocity (Büttner et al., 2018). The degree of damage caused by AAV is not likely equivalent and consistent as the damage achieved by nerve crush. Only 2 NHPs have showed a decline in the amplitude of sensory compound action potentials of the median nerve out of 56 NHPs surveyed, both NHPs exhibited severe axonopathy and fibrosis (Hordeaux, Buza, Dyer, et al., 2020). In another NHP study, intravenous delivery of AAV9 encoding the motor neuron survival gene did not show any changes to the conduction velocities to the sural, fibular/peroneal, saphenous and tibial nerves (Tukov et al., 2022). The current experimental design can be improved, a single and terminal action potential recording at the height of nerve damage can improve the consistency. The sciatic nerve would be exposed by removing the skin and the surrounding muscle, the electrodes can be placed around the nerve at consistent location within the nerve track for recordings. To avoid potential variability, only one sex could be selected, and the study cohort can be increased to detect a small effect size. Most importantly, histological analysis for each mouse undergoing physiological is critical to compare to the observed physiology, perhaps analyzing the data based on lesion severity could improve resolution. Also, tissue collection for molecular analysis could further substantiate electrophysiological results. In summary, the sciatic nerve action potentials were measured

from wild type mice. AAV treatment induced NfL surge indicative of damage in the sciatic nerve, and changes to the action potential were not detected.

Acknowledgements

Brain Harvey for his collaboration with running the sciatic nerve action potential assay on mice. Ayan Ghoshal for supporting this study and reviewing this chapter and Elena Morozova for helping with setting up the method from sciatic nerve action potential detection.

Chapter 4

Intrathecal Administration of Stressor Adeno-Associated Viruses (AAVs) Causes Hindlimb Muscle Weakness in C57BL/6J Mice

Introduction

Recombinant adeno-associated virus (rAAV) is a commonly used vector for the delivery of therapeutic genes for the treatment of various diseases. AAVs are non-pathogenic and induce limited host immune responses relative to other viral vectors (Shirley et al., 2020). However, only a few *in vivo* gene therapies have been approved in patients in the last decades as many challenges continue to persist (Bolt et al., 2021). One of these hurdles affects the somatosensory nervous system. Dorsal root ganglia (DRG) toxicity post-AAV administration has been noted in clinical and periclinal animal models such as non-human primates (NHP), pigs, rats and mice (Alstyne et al., 2021; S. K. Chen et al., 2023; Fader et al., 2022; Hinderer et al., 2018; Hordeaux, Buza, Dyer, et al., 2020). AAV delivery into the cerebrospinal fluid (CSF) and bloodstream results in roust transduction in sensory neurons and expression of a foreign gene. At high doses, this process subsequently leads to neuronal and axonal injury (Hordeaux, Buza, Dyer, et al., 2020). In rodents, neuronal degeneration in the DRG, axonal degeneration in the dorsal nerve root and axonal degeneration in the dorsal funiculus of the spinal cord have been reported previously (Fader et al., 2022; Hawley et al., 2024; Tyszkiewicz et al., 2024). Additionally, peripheral nerves are also affected, axonal degeneration in the sciatic nerve and the saphenous nerve have been observed in mice months post-AAV administration (Hawley et al., 2024). The extent of DRG toxicity and peripheral nerve damage is evaluated by monitoring the levels of neurofilament light (NfL) in the serum (Fader et al., 2022; Johnson et al., 2023; Tyszkiewicz et al., 2024). Serum NfL levels are correlated with degeneration/necrosis and nerve fiber degeneration in rats and NHPs (Fader et al., 2022).

Although rare, functional deficits have been previously recorded in patients and animal models. A familial ALS patient treated with an AAV9 targeting the human SOD1 gene felt a transient tingling sensation in his hands and ‘electric’ shocks in his foot 1-week post-injection (Mueller et al., 2020). This patient also suffered from loss of sensory action potentials in the

sural and the left median nerves (Mueller et al., 2020). Pigs intravenously injected with AAVhu68-SMN (survival motor neuron gene) showed proprioceptive deficits and ataxia which required euthanasia (Hinderer et al., 2018). Mice treated with high dose of AAV9-survival motor neuron gene 1 displayed clasping behavior and deficits in muscle performance (Alstyne et al., 2021). Mice displayed a sharp and significant decline in grip strength and rotarod activity mice (Alstyne et al., 2021). Alstyne and colleagues also showed electrophysiological alterations in compound muscle action potentials (CMAP), specifically in H-reflexes, noting loss in proprioceptive neurons. Compound muscle action potentials measures the summated action potentials in muscle fibers and is a commonly used to assess motor nerves and neuromuscular junction function in neurodegenerative diseases (Bogdanik et al., 2015; Y. A. Chen et al., 2022; J. Li et al., 2014; McCampbell et al., 2018).

The purpose of this report was to investigate the effects of stressor AAVs on hindlimb muscle contractions and signal conduction in the hindlimbs. This was achieved by intrathecally dosing mice with stressor AAVs and measuring muscle action potential and the muscle force generated by the foot. Triggered muscle dual lever was used to assess the muscle force and closely study excitation-contraction coupling and neuromuscular function (Zhao et al., 2017). It was shown that hindlimb muscle weakness was detected in mice. Various correlation analyses were conducted to unravel the relationship between serum NfL, CMAP and hindlimb muscle weakness.

Materials and Methods

Animals

Wild type C57BL6/J (Stock #:000664) females were obtained from the Jackson Laboratory and were housed in a 12/12 hrs light/dark cycle in a temperature-controlled room (22-24 ºC) with access to food pellet and water provided *ad libitum*. Mice were also given diet gels to prevent the loss of bodyweight as the study progressed. All animal use and treatments were approved by the Biogen Institute Animal Care and Use Committee (IACUC) and followed the National Institute of Health Guide for the Care and Use of Laboratory Animals.

AAV vector design and production

AAV-miR-SOD1 is a single-stranded AAV9 vector composed of ubiquitous CAGG promoter driving the expression of two artificial microRNAs designed to target human SOD1, miR30a-huSOD1_#5 and miR155-huSOD1_#7.

miR30a scaffold with mature guide huSOD1_#5 underlined:

5'TGTTTGAATGAGGCTTCAGTACTTTACAGAATCGTTGCCTGCACATCTTGGAAA
CACTTGCTGGGATTACTTCTTCAGGTTAACCCAACAGAAGGCTAAAGAAGGTATAT
TGCTGTTGACAGTGAGCGTACTTTCTTCATTTCCACCTTTTAGTGAAGCCACAGAT
GTAAAGGTGGATGAAGAAAGTATGCCTACTGCCTCGGACTTCAAGGGGCTACTTT
AGGAGCAATTATCTTGTTTACTAAAACTGAATACCTTGCTATCTCTTTGATACATTTT
TACAAAGCTGAATTAAAATGGTATAAATTAAATCACTTTA**3'**.

miR155 scaffold with mature guide huSOD1_#7 underlined:

5'CTGGAGGCTTGCTGAAGGCTGTATGCTGTCAGGATACATTTCTACAGCTTTTGGC
CACTGACTGACAAGGTGGATGAAGAAAGTACAGGACACAAGGCCTGTTACTAGC
ACTCACATGGAACAAATGGCC **3'**.

These artificial microRNAs target the human superoxide dismutase 1 (SOD1) mRNA in the cytoplasm for degradation via the RNA interference pathway. The expression and transcriptional regulation of the cassette is enhanced by the addition of the Woodchuck Hepatitis Virus Post-Transcriptional Regulatory Element (WPRE), and a human growth

hormone poly-A (hGHpolyA) signal downstream of the artificial microRNAs. AAV-mCherry was packaged into a single stranded AAV9 vector, mCherry protein expression was driven by the ubiquitous strong CAGG promoter, the expression was enhanced and regulated by WPRE and hGHpolyA downstream of mCherry reporter protein.

AAV vectors were produced by PackGene Biotech (Worcester, MA, USA) by triple plasmid transfection protocol and the protocol has been described previously (Torregrosa et al., 2021). The AAV produced was assessed for sterility, endotoxin level and purity. Qualitative empty to full capsid assessment was determined by transmission electron microscopy (TEM). The titer was determined via ddPCR method targeting the WPRE.

Intrathecal Injections

Intrathecal injections were performed at ~6 weeks of age. Mice were anesthetized with isoflurane and the depth of anesthesia was assessed via a toe pinch. Ethiqua XR (buprenorphine extended-release injectable suspension) (Fidelis Animal Health, North Brunswick, NJ, USA) was administered to eliminate pain sensation. The mouse fur was clipped from the injection area and an ocular lubricant was applied. The mouse was placed on a heating source in ventral recumbency. The injection site was thoroughly cleaned, including three wipes with betadine and three wipes with isopropyl alcohol (alternating). Vertebral processes were detected by arching the spine which allows correct orientation and placement of the needle. A 29-gauge, 0.3mL syringe (Cat#: 4429-3, Smiths Medical ASD, Inc., Southington, CT, USA) was inserted in the gap between L5 and L6 or L4 and L5 and a tail flick was detected if the needle was in the correct location. The test articles or vehicle, artificial cerebrospinal fluid (CSF), was slowly administered (10 µL, 8E11 and 1.6E12 GC) to minimize rapid changes in CSF pressure. Mice were then transferred to a heating chamber set at 37C for recovery first and then placement in their home cages.

Neurofilament light measurement

Mice were bled (~100 µL) via facial vein puncture at -1, 4-, and 13-weeks post-injection. The blood was collected in in BD Microtainer SST Clog Activator/Gel tubes (Becton Dickinson, Franklin Lakes, NJ, USA). The tube was inverted a few times and left for 30 mins for coagulation. The tube was then centrifuged at 2000RCF (4600RPM) for 10 minutes to separate the serum. Neurofilament light in serum was quantified via Simple Plex Human NF-L Cartridge (Protein Simple, SPCKB-PS-002448, San Jose, CA, USA) by following the manufacturer's protocol.

Compound muscle action potential

Compound muscle action potential (CMAP) recordings were performed under isoflurane anesthesia, animals were maintained at 37 °C using a thermostatic heating and ophthalmic ointment was applied to the eyes to prevent dryness. Disposable monopolar 28-gauge needle electrodes were used for stimulation and recording of electrical signals. The sciatic nerve was stimulated near the sciatic notch with constant-current monophasic square-wave pulses (0.1 millisecond duration, 2-second intervals). For CMAP recordings, the recording electrode was placed intramuscularly 1 mm deep in the tibialis anterior. The stimulation current was increased until a maximum CMAP was obtained, and recordings were performed using a current level 0.5 mA above this value (supramaximal stimulation). The amplitude represents the peak-to-peak amplitude of the biphasic CMAP waveform (averaged over 4 stimuli). For each animal, right and left leg amplitudes were recorded and averaged for -1-, 3- and 11-weeks post-injection.

Triggered dual lever muscle strength

Dual lever recordings were performed under isoflurane anesthesia animals were maintained at 37 °C with eye ointment to prevent dryness. The animal was placed in a supine position on a

heated platform and the leg was shaved and cleaned with 70% alcohol and iodine wipes. A conductive gel was applied to the skin where electrodes are placed. *In vivo* force measurements were performed using the dual mode lever (model 300C-LR; Aurora Scientific) (Palla et al., 2021). The foot was positioned onto a footplate; the foot was held in place by medical tape. The knee was clamped to stabilize and immobilize the leg during recordings. The knob adjustments were modified such that the mouse's hindlimbs are positioned 90°. The electrodes, 28-gauge, were inserted subcutaneously. The electrodes were placed on the lateral side of the leg, one electrode was placed near the head of the fibula and the other electrode was placed more distally on the lateral side of the leg. The tibial nerve was stimulated resulting in a maximum plantarflexion torque. The stimulation and the muscle length parameters were optimized to ensure the muscle was able to generate a maximal force (0.5 ms 100 Hz). For tetanic contractions, the frequency of stimulation was varied from 10-150 Hz to generate force frequency curves. Recordings from the plantarflexion torque using the dual lever were completed for -1-, 4- and 12-week post-injection for all animals. Data were collected with the Aurora Scientific Dynamic Muscle Data Acquisition and Analysis Software (Aurora, ON, Canada).

Statistical analysis

GraphPad Prism 8 (San Diego, CA, USA) and RStudio (Posit, Boston, MA, USA) were used to generate graphs and conduct statistical analysis. All data is expressed as means ± standard deviation.

Results

AAV-miR-SOD1 elevated serum neurofilament and reduced survival

In this study, mice were injected with two doses, 8E11 and 1.6E12 GC, of AAV-miR-SOD1 and 1.6E12 GC with AAV-mCherry at intrathecally at 6 weeks of age. Mice were subjected to two physiological assessments at various timepoints along with blood serum collections (Fig.1a). Neurofilament light levels (NfL) in serum was monitored to determine the degree of dorsal root ganglia (DRG) and peripheral nerve injury in mice, indicative of neuronal and axonal damage. Neurofilament light levels significantly surge at 4 weeks post-injection (p.i.) to 1900 ± 800 pg/mL in 8E11 GC and 2197 ± 1324 pg/mL in 1.6E12 GC AAV-miR-SOD1-treated mice (Mixed-effects analysis followed by Tukey's Multiple Comparison Test, $*P<0.05$, $**P<0.01$) (Fig. 1b, c). Neurofilament levels were lower for mice treated with 1.6E12 GC AAV-mCherry vector (Fig. 1b, c). As shown previously, NfL levels decreases in the subsequent 12 weeks post-injection timepoint. The standard deviation within group was large at 4 p.i. Mice treated with AAV exhibit heightened NfL levels, suggesting damage to DRG and peripheral nerves, facilitating the investigation of muscle physiology.

Bodyweight is indicative of the general condition of mice and sharp changes post dosing can be indicative of toxicity (Hoffman, 2002). AAV-treated mice were supplemented with diet and hydrogels to alleviate loss of bodyweight (Alstyne et al., 2021). Mice bodyweight was tracked one-week p.i. and subsequent measurements were completed twice weekly for the study duration. Overall, AAV-miR-SOD1-treated mice-maintained bodyweight while AAV-mCherry treated mice gained weight relative to control mice starting at 78 days (Fig. 1d). This finding must be viewed with caution due to mice being euthanized or found dead in the AAV-miR-SOD1 1.6E12 GC treated group. Also, AAV-treated mice were provided with diet gels to supplement bodyweight (Fig. 1g). At day 136, mice were sacrificed for tissue collection and for terminal weight measurement of the soleus and gastrocnemius muscle of the hindlimbs.

The average soleus and gastrocnemius weight was comparable for all treatments (Fig. 1e). The normalized mean bodyweight for the soleus and gastrocnemius was lower than vehicle-treated mice, especially for the remaining 1.6E12 GC AAV-miR-SOD1 mice (Fig. 1f). These findings were not significant (Kruskal-Wallis Test followed by Dunn's Multiple Comparison test, ns - not significant). Interestingly, the soleus and gastrocnemius muscle were purple in color for one AAV-mCherry treated mouse indicating possible transduction of skeletal muscle. Although not closely tracked in this study, hindlimb clasping in AAV-treated mice appeared early and worsened overtime (Alstyne et al., 2021). Clasping is characterized by the retraction of the limbs towards the body and clenching of the digits (Cahill et al., 2019). The majority of mice survived the duration of the study, but the high-dosed 1.6E12 GC AAV-miR-SOD1-treated mice showed a significant reduction of median survival, measured at 127 days (Long-rank test, $**P<0.01$) (Fig. 1g).

AAV-miR-SOD1 reduced muscle force in the hindlimbs

Two main physiological recordings were collected to probe for nerve and muscle health in AAV-treated mice (Fig. 1a). Compound muscle action potential (CMAP) assess the function of the sciatic nerve motor axons and the neuromuscular junctions, reduction in CMAP amplitude indicates neurodegeneration (McCampbell et al., 2018; Weng et al., 2021). The sciatic nerve was stimulated, and electromyogram recordings were collected from the tibialis anterior muscle. Mean CMAP activity ranged between ~60-80 mV for all mice with a significant reduction noted in 8E11 GC AAV-miR-SOD1 treated mice at 11 weeks p.i. compared to vehicle-treated mice (Fig. 2a-c). Baseline corrected CMAP values also displayed this relationship with 8E11 GC AAV-miR-SOD1 treated mice noted at below baseline (Fig. 2d). Furthermore, triggered muscle dual lever enables examination of muscle contractions and thereby investigating nerve motor activity and muscle function. The tibial nerve was stimulated to generate plantar flexor force, these flexions are mostly the result of gastrocnemius muscle

force. All mice showed an increase in normalized muscle force throughout the study, this was expected due to maturation of mice. AAV-treated mice had lower normalized force at 12 weeks p.i. relative to vehicle-treated mice, none reaching significance (Fig. 2e-g). The force exerted onto the lever was lower in AAV-treated mice indicating muscle weakness. The force difference normalized to pre-treatment baseline was lower for 8E11 GC AAV-miR-SOD1-treated mice (25.43 ± 18.81%) versus vehicle-treated mice (48.31± 18.67%) reaching significance at 12 weeks p.i. (Mixed-effects analysis with Bonferroni's multiple comparison test, $*P<0.05$). This indicates that AAV-treated mice were not able to gain equivalent muscle strength as vehicle-treated mice controls.

AAV treatment did not alter muscle contractile properties.

Muscle contractions can summate in response to an increase in the frequency of action potentials. This occurs due to the inability for the muscle to fully relax before the next wave of contraction and at high frequencies, muscle tetanus is observed. The frequency at which muscle reaches tetanus can be altered in response to muscle injury and disease. Mice were stimulated with increasing frequency from 10-140 Hz to lead to tetanic summation and complete tetanus. AAV-treated mice displayed a left shift at 4 weeks p.i. relative to vehicle indicated at 50-100 Hz, however this shift was not observed at 12 weeks p.i. (Fig. 3). The administration of AAVs appeared to have no discernible impact on the properties of muscle contraction.

Correlations of serum neurofilament light with physiological endpoints

The aim was to understand how serum NfL levels correlated with muscle force and CMAP changes. Using Pearson correlations analyses, serum NfL was investigated at 4 weeks p.i in relation to the physiological tests. This timepoint was the height of neurofilament surge in mice which is indicative of the severity of DRG and peripheral nerve injury. For CMAP, the correlation observed at 11 weeks p.i. for raw values (-0.36) and baseline corrected values (-

0.31) was weak, indicating that elevation of NfL signal was weakly correlated with lower CMAP activity (fig. 4a-d). Similarly, NfL was weakly correlated with muscle activity at 12 weeks p.i. (fig. 4e-h). To summarize, CMAP and muscle dual lever force measurements were weakly correlated with serum NfL stemming from the variability in these measurements.

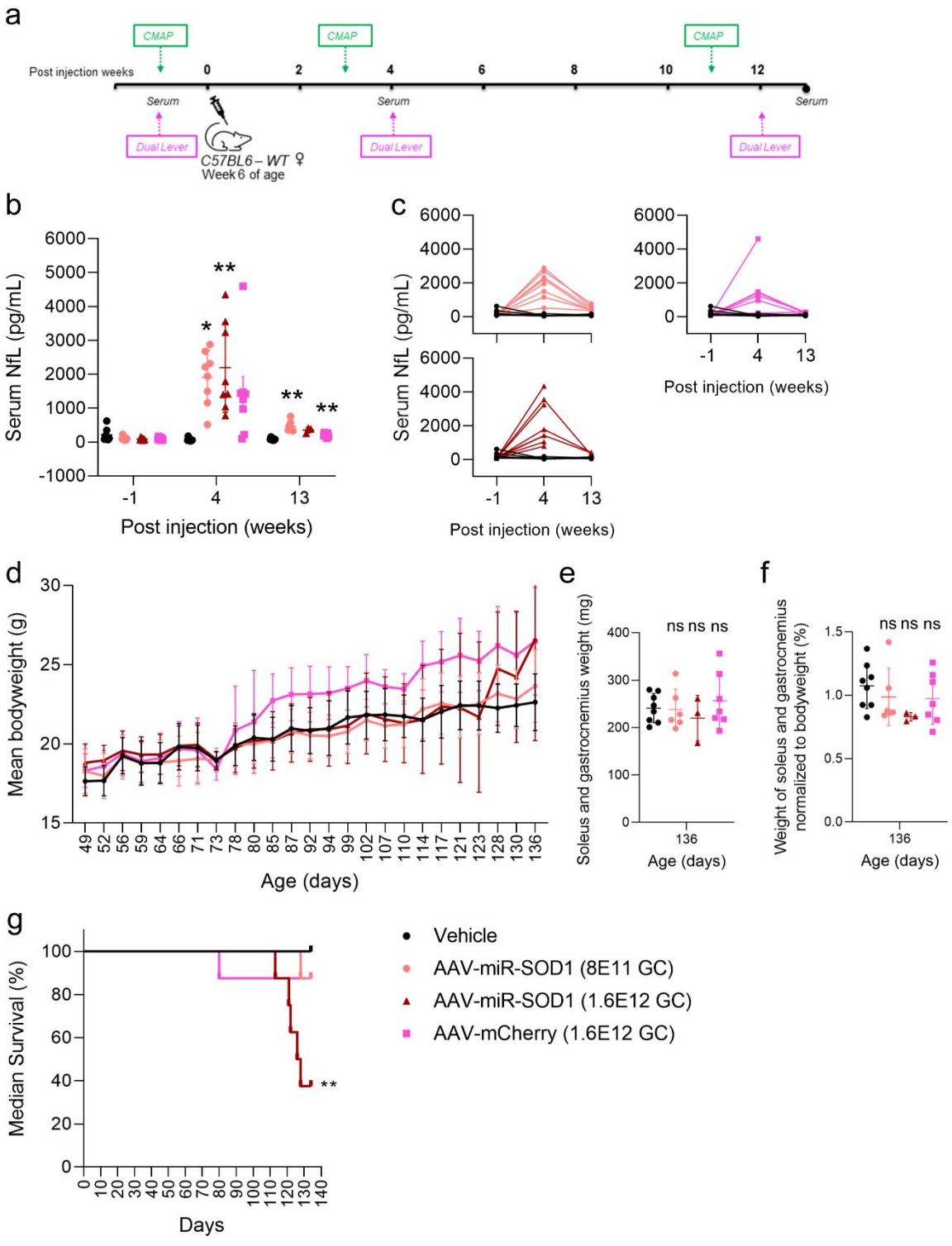
a
CMAP
CMAP
CMAP
Post injection weeks
0
2
4
6
8
10
12
Serum
Serum
Serum
Dual Lever
Dual Lever
Dual Lever
C57BL6 – WT ♀
Week 6 of age
b
Serum NfL (pg/mL)
Post injection (weeks)
c
Serum NfL (pg/mL)
Post injection (weeks)
Post injection (weeks)
d
Mean bodyweight (g)
Age (days)
e
Soleus and gastrocnemius weight (mg)
ns ns ns
Age (days)
f
Weight of soleus and gastrocnemius normalized to bodyweight (%)
ns ns ns
Age (days)
g
Median Survival (%)
Days
Vehicle
AAV-miR-SOD1 (8E11 GC)
AAV-miR-SOD1 (1.6E12 GC)
AAV-mCherry (1.6E12 GC)

Figure 1: Intrathecal dosing of AAV-miR-SOD1 causes a surge in neurofilament light chain (NfL) and alters median survival. **a.** Timeline and the experimental design of the study. **b.** Serum NfL surge in AAV treated mice post-AAV administration. Mixed-effects analysis followed by Tukey's Multiple Comparison Test, *$P<0.05$, **$P<0.01$, comparison to Vehicle **c.** Serum NfL spaghetti plots individual mice tracked over overtime per treatment. **d.** Mean bodyweight of mice throughout the study. **e.** Mean weight of soleus and gastrocnemius muscle at necropsy at day 136 (Kruskal-Wallis Test followed by Dunn's Multiple Comparison test, ns- not significant). **f.** Normalized weight of soleus and gastrocnemius relative to the bodyweight of each mouse at necropsy at day 136 (Kruskal-Wallis Test followed by Dunn's Multiple Comparison test, ns- not significant). **g.** AAV-miR-SOD1 at 1.6E12 GC reduces medial survival (Long-rank test, **$P<0.01$). Data are mean ± SD with n=3-8/treatment. CMAP, compound muscle action potential; Dual lever, triggered muscle dual lever.

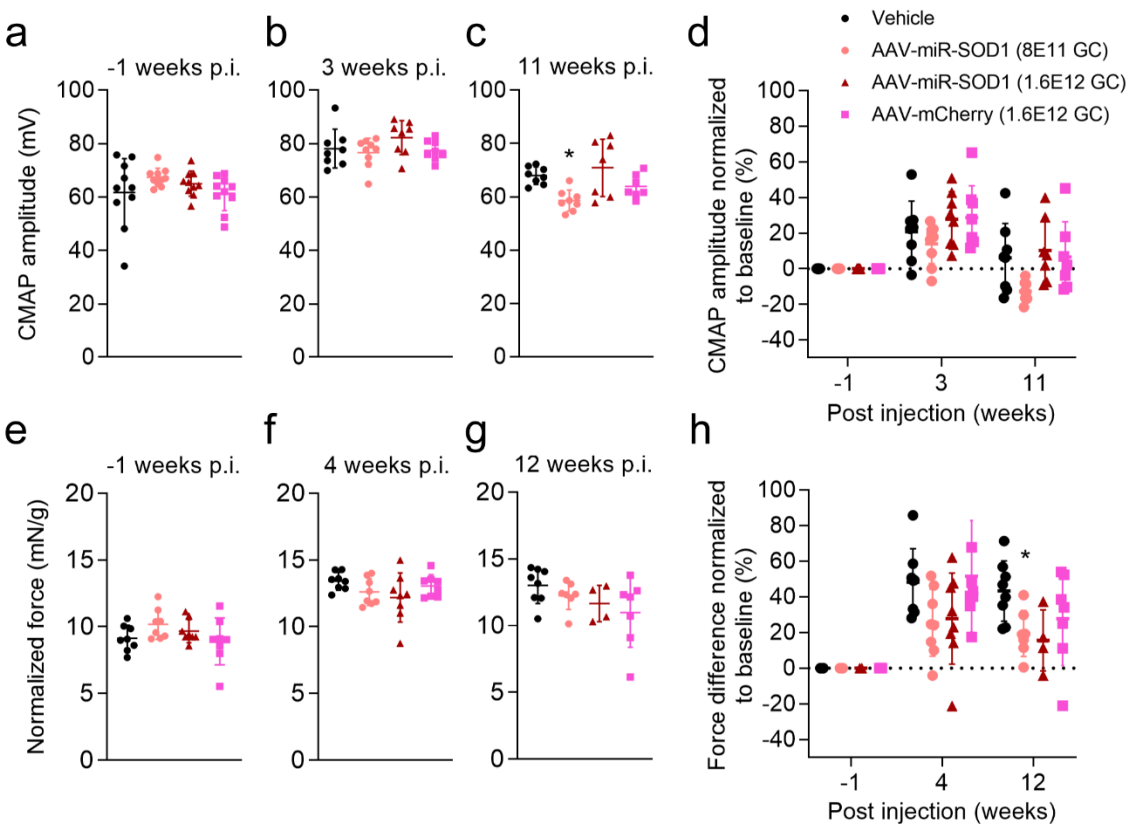

Figure 2: Physiological assessment of neuromuscular and muscle function in mice. **a-c.** Compound muscle action potential (CMAP) amplitude recorded post-injection (p.i.) of AAV (Mixed-effects analysis followed by Bonferroni's multiple comparisons test; *P<0.05). **d.** Baseline corrected CMAP for all timepoints. **e-f.** Triggered muscle dual lever measuring plantarflexor force normalized to bodyweight. **h.** Pretreatment baseline corrected force (8E11 GC AAV-miR-SOD1 vs. vehicle; Mixed-effects analysis followed by Bonferroni's multiple comparisons test; *P<0.05). Data represent mean ± SD with n=4-8/treatment. CMAP, compound muscle action potential. p.i., post-injection.

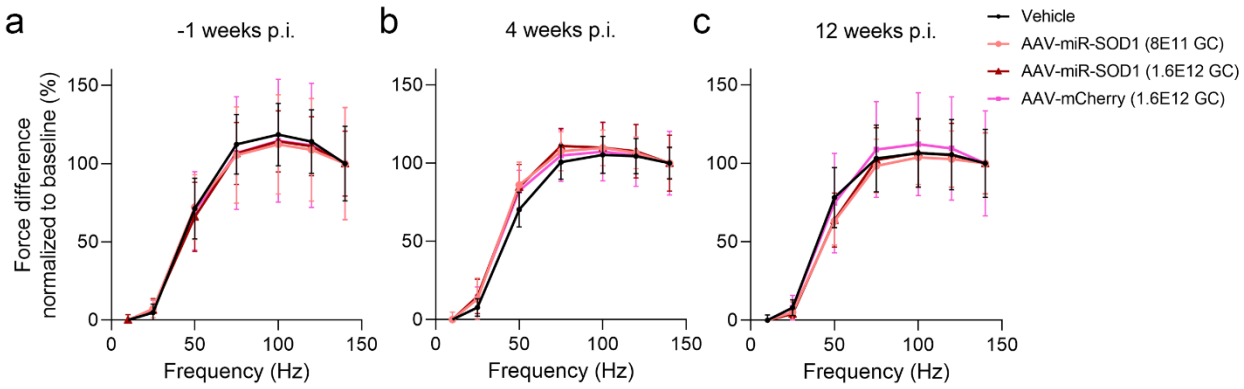

Figure 3: The normalized muscle force difference in response to escalating stimulation frequency in the gastrocnemius muscle. The force difference at **a.** -1 weeks p.i. **b.** 4 weeks p.i. **c.** 12 weeks p.i. Data represent mean ± SD with n=4-8/treatment. p.i., post-injection.

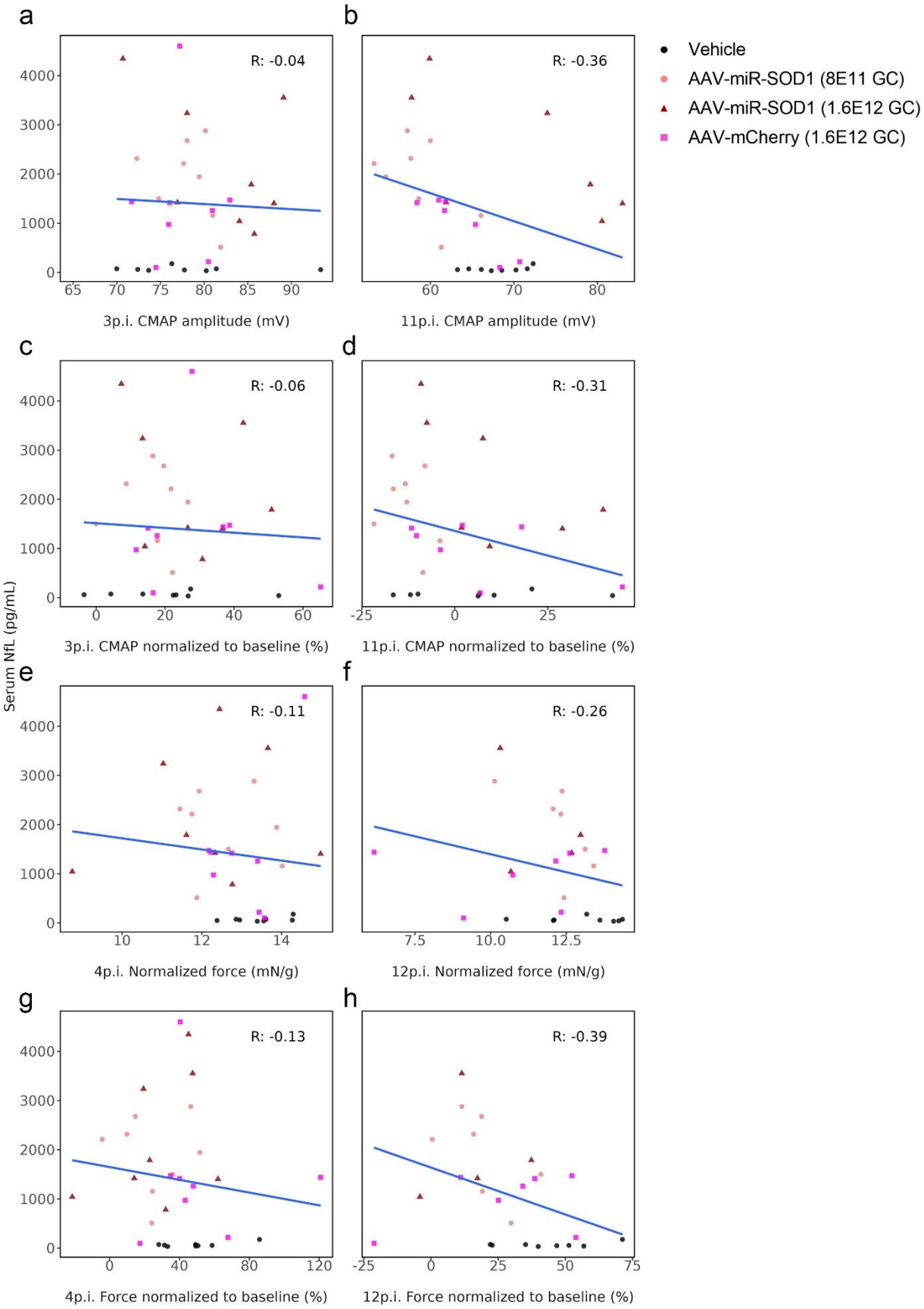
a
b
c
d
e
f
g
h
R: -0.04
R: -0.36
R: -0.06
R: -0.31
R: -0.11
R: -0.26
R: -0.13
R: -0.39
Serum NfL (pg/mL)
3p.i. CMAP amplitude (mV)
11p.i. CMAP amplitude (mV)
3p.i. CMAP normalized to baseline (%)
11p.i. CMAP normalized to baseline (%)
4p.i. Normalized force (mN/g)
12p.i. Normalized force (mN/g)
4p.i. Force normalized to baseline (%)
12p.i. Force normalized to baseline (%)
Vehicle
AAV-miR-SOD1 (8E11 GC)
AAV-miR-SOD1 (1.6E12 GC)
AAV-mCherry (1.6E12 GC)

Figure 4: Correlation analyses of compound muscle action potential (CMAP) and triggered dual muscle force against serum neurofilament (NfL) at 4 weeks post-injection. **a-d.** Correlation analyses of CMAP at 3 and 11 weeks p.i. and **c-d**. baseline-corrected CMAP at 3 and 11 weeks p.i. **e-f**. Correlation analysis of normalized force and **g-h**. baseline-corrected normalized force at 4 and 12 weeks p.i. CMAP, compound muscle action potential.

Discussion

In this report, injection of AAV vectors, known to cause dorsal root ganglia (DRG) and peripheral nerve damage, resulted in muscle weakness in the hindlimbs of mice. AAV-treated mice showed a transient elevation in serum neurofilament light (NfL) as observed previously in rodents (Fader et al., 2022; Hawley et al., 2024; Tyszkiewicz et al., 2024). AAV-treated mice were supplemented with diet gels to prevent bodyweight loss and early euthanasia, however, the average normalized weight of the soleus and gastrocnemius muscle were lower than vehicle-treated mice indicating potential myofiber atrophy. AAV-miR-SOD1 was more toxic than AAV-mCherry, this can be seen with reduction in survival, greater hindlimb muscle weakness and higher serum NfL levels. Normalized muscle force difference in AAV-treated mice was reduced with minimal changes to compound muscle action potential (CMAP) activity. CMAP and muscle force findings were weakly correlated with serum NfL at 4 weeks post-injection (p.i.). This was anticipated due to the inherent variability associated with a functional endpoint and the variability observed in serum NfL measurements in mice.

The weakness observed in hindlimb muscles is unlikely to stem from diminished motor nerve function, rather, it is more likely associated with sensory activity. CMAP activity was generally unaltered in AAV-treated mice indicating that motor axons and neuromuscular junctions were not likely affected. There was a reduction in CMAP for animals treated with 8E11 GC AAV-miR-SOD1, however, this trend was not observed in mice treated with 1.6E12 GC AAV-miR-SOD1-treated mice. The decrease in muscle force observed in AAV-treated mice could potentially stem from injury to sensory axons within the sciatic nerve, as well as to the specialized sensory receptors found in the muscle, muscle spindle fibers and Golgi tendon organs. AAV-miR-SOD1 leads to axonal degeneration in the sciatic nerve (motor and sensory) and the saphenous nerve (sensory) (Hawley et al., 2024). Muscle spindles are proprioceptors that detect stretch in the length of a muscle fiber. Upon the stretching of a muscle fiber, the

frequency of afferent action potentials in sensory nerves are altered (Tuthill & Azim, 2018). This signal is processed in the spinal cord leading to the activation of alpha motor neurons and generation of muscle contraction preventing overstretching (Tuthill & Azim, 2018). Alteration or attenuation of sensory action potentials in injured sensory axons can lead to overstretching of the muscle resulting in a defective stretch reflex (Adidharma et al., 2022; Kröger & Watkins, 2021). Also, muscle spindles are essential in inhibiting antagonistic muscles to prevent overstretching, reciprocal inhibition (Tuthill & Azim, 2018). Golgi tendons are proprioceptors that are activated in response to muscle contraction. Golgi tendons generate sensory action potentials in afferent fibers to inhibit alpha motor neurons from firing, key for muscle relaxation (Adidharma et al., 2022; Tuthill & Azim, 2018). Mice injected with AAVs may experience a loss of control over muscle relaxation. Further investigations are needed to explore these hypotheses on how defective sensory activity affects muscle force. It would be highly beneficial to include immunostainings of motor neurons in the spinal cord to aide in these conclusions.

Some mice treated with AAV experienced muscle atrophy, which likely contributed to the decline in muscle performance. Mice at 6 - 18 weeks of age (12 weeks p.i.) grow and increase in strength, evident in vehicle-treated mice. The progression in strength is slowed in AAV-treated mice despite the supplementation with diet gels on the cage floor throughout the study. For the three remaining mice treated with 1.6E12 GC of AAV-miR-SOD1, the normalized percent soleus and gastrocnemius muscle weight was lower than control animals. Also, the minor leftward shift observed in the force difference versus frequency plots (Fig. 3) in AAV-treated mice may indicate muscle atrophy. AAV-treated mice reach muscle tetanus earlier than vehicle. This observation maybe be associated with muscle atrophy and anatomical changes to myofibers. A Balb/c model subjected to bilateral ligation of femoral artery displayed a left shift, muscle atrophy, central nucleation and increased collagen disposition (Roseguini et al., 2015).

One mouse dosed with 1.6E12 GC AAV-mCherry, had purple soleus and gastrocnemius muscle at harvest indicating AAV transduction of muscle and mCherry expression. AAV9 has been shown to transduce skeletal muscle (Riaz et al., 2015, p. 9; Zincarelli et al., 2008). Peripheral leakage of AAV has been commonly observed following intrathecal delivery and as such various tissues such as the liver, heart and the sciatic nerve can be transduced (Chandran et al., 2023; Gong et al., 2019; Hawley et al., 2024). To conclude, intrathecal administration of high doses of AAV may have contributed to muscle atrophy which impacted muscle performance and this hypothesis would need further testing to confirm.

In conclusion, mice treated with two types of AAV transgenes (amiR and reporter protein) led to a functional deficit characterized by weakness in the hindlimbs without notable associations with serum NfL. Phenotypically mice struggled in later parts of the study especially the AAV-miR-SOD1 treated mice suggesting AAV transgene or cargo dictates the severity of DRG-toxicity as observed previously in NHPs (Hordeaux, Buza, Dyer, et al., 2020). Clasping behavior was observed in most AAV-treated mice. Unfortunately, many mice treated with 1.6E12 GC AAV-miR-SOD1 were either found dead or euthanized prior to the final triggered dual lever test at 12 weeks p.i. Therefore, the timepoints for future studies must account for the loss of animals as the study progresses. Traditionally, DRG toxicity has been investigated in primates with no to minimal reports of functional deficits. Unlike NHPs, mice showed a consistent muscular deficit, and it manifested 12 weeks post-dosing. Understanding the functional toxicities associated with gene therapy will allow for enhanced screening of candidates, reduce resource, and alleviate the need for NHP studies to assess toxicity.

Acknowledgements

Dora Bodnar and Taras Tuczkewycz for conducting the physiological tests on study animals and providing early analysis. Deborah Kwon for providing scientific input and Adelaida Palla Cachorro for scientific input and review of this chapter.

Chapter 5

Behavioral Investigation of AAV-induced Dorsal Root Ganglia Toxicity in C57BL/6J Mice

Introduction

The rise of gene therapy in the last decades has enabled the ability to permanently alter the course of genetic diseases. The most common vehicle of gene therapy utilizes recombinant adeno-associated virus (rAAV) due to their favorable tolerability and safety profile relative to other virus-based vehicles. Despite the advancement in therapies currently being evaluated in the clinic, only a few *in vivo* gene therapies have been granted FDA approval. Reports of treatment related adverse events have been recorded post-AAV based gene therapies (Mullard, 2021). In preclinical studies, systemic and dosing into the cerebrospinal fluid has been linked to neurotoxicity. Neurotoxicity manifests as both toxicity in the central nervous system and peripheral toxicity found in the dorsal root ganglia (DRG) and peripheral nerves (Hordeaux, Buza, Dyer, et al., 2020; Keiser et al., 2021). These reports have been shown in multiple species such as non-human primates (NHP), pigs, rats, rabbits, rats and mice (Fader et al., 2022; Hawley et al., 2024; Hordeaux, Buza, Dyer, et al., 2020; Tien et al., 2024; Tyszkiewicz et al., 2024). Administration of AAV9 into the CSF leads to a high level of transduction of sensory neurons in the DRG (Schuster et al., 2014). In mice, microscopic histopathological findings of neurodegeneration, chromatolysis, increased cellularity and eosinophilic granules are observed in the lumbar DRG along with axonal degeneration in the spinal cord (Hawley et al., 2024). Lesions in mice exhibit variability and lack consistency. Peripherally, pronounced axonal degeneration are observed in the sciatic and saphenous nerves. AAV-treated mice exhibit immune responses and transcriptional and proteomic alterations, findings common with NHPs (Hawley et al., 2024).

Functional impairments resulting from AAV administration are infrequent but have been documented in both clinical and preclinical studies. A familial ALS subject treated with an intrathecal injection of AAV vector reported tingling sensations in the hands and left foot weeks post-injection. This patient exhibited alteration in sensory nerve action potentials and loss of

DRG sensory neurons (Mueller et al., 2020). Pigs and rabbits treated intravenously with high dose of AAV display ataxia and hindlimb weakness which required euthanasia (Hinderer et al., 2018; Tien et al., 2024). Behavioral investigation in rodents have shed some light into potential deficits in response to DRG toxicity. Wistar Han rats injected with 5E13 GC/kg of AAV9 did not exhibit deficits in von Frey and rotarod measurements (Tyszkiewicz et al., 2024). The authors note that DRG findings in their study were rated as minimal to moderate neuronal and nerve fiber degeneration. The authors note that the severity was not significant for potential phenotype manifestation (Tyszkiewicz et al., 2024). In mice injected with AAV9 (2.5-10E13 GC/kg), carrying the survival motor neuron gene 1 (SMN1), mice experienced a significant and dose-dependent decline in grip strength and rotarod over the 10 months period of the study (Alstyne et al., 2021). All mice developed neurological hindlimb clasping phenotype and the age of appearance of clasping phenotype was dose dependent. Clasping is defined by drawing of hindlimbs towards the body and clenching of paws (Lalonde & Strazielle, 2011). The complete loss of proprioceptive neurons in the DRG and reduction in motor neurons in the spinal cord were observed contributed to their behavior findings (Alstyne et al., 2021). Evidently, AAV toxicity is dependent on the cargo/ exogenous gene introduced, the dose levels, age, route of administration and capsid used (Hordeaux, Buza, Dyer, et al., 2020). Although AAV-induced injury in DRG and nerves do not consistently yield functional impairments, behavior and physiology alterations have been detected in patients and animal models.

In this report, female wild type C57BL/6J were intrathecally dosed with high titers of stressor AAV vector, AAV-miR-SOD1, to induce injury to sensory neurons and peripheral nerves. This allowed for the investigation of mouse behavior with a focus on open field test, grip strength, hindlimb clasping and gait analysis via catwalk. Mice were closely tracked for 4.5 months post-injection to unravel the long-term implication of DRG toxicity on behavior. The progression of toxicity was tracked by serum neurofilament light levels as it has been shown to be a biomarker

of DRG toxicity (Fader et al., 2022; Johnson et al., 2023; Tyszkiewicz et al., 2024), bodyweight and survival. Mice displayed anxiety-like behavior, pronounced reduction in grip strength and consistent severe hindlimb clasping. It was shown that functional alteration and clinical phenotypes can manifest in mice due to DRG toxicity.

Materials and Methods

Animals

Wild type C57BL/6J (Stock #:000664) females were obtained from the Jackson Laboratory and were housed in a 12/12 hrs light/dark cycle temperature-controlled room (22-24 ºC) with access to food pellet and water provided *ad libitum*. Mice were also given diet gels to prevent the loss of bodyweight as the study progressed. All animal use and treatments were approved by the Biogen Institute of Animal Care and Use Committee (IACUC) and followed the National Institute of Health Guide for the Care and Use of Laboratory Animals.

AAV vector design and production

AAV-miR-SOD1 is a single-stranded AAV9 vector composed of ubiquitous CAGG promoter driving the expression of two artificial microRNAs designed to target human SOD1, miR30a-huSOD1_#5 and miR155-huSOD1_#7.

miR30a scaffold with mature guide huSOD1_#5 underlined:

5'TGTTTGAATGAGGCTTCAGTACTTTACAGAATCGTTGCCTGCACATCTTGGAAA
CACTTGCTGGGATTACTTCTTCAGGTTAACCCAACAGAAGGCTAAAGAAGGTATAT
TGCTGTTGACAGTGAGCGTACTTTCTTCATTTCCACCTTTTAGTGAAGCCACAGAT
GTAAAGGTGGATGAAGAAAGTATGCCTACTGCCTCGGACTTCAAGGGGCTACTTT
AGGAGCAATTATCTTGTTTACTAAAACTGAATACCTTGCTATCTCTTTGATACATTTT
TACAAAGCTGAATTAAAATGGTATAAATTAAATCACTTTA**3'**.

miR155 scaffold with mature guide huSOD1_#7 underlined:

5'CTGGAGGCTTGCTGAAGGCTGTATGCTGTCAGGATACATTTCTACAGCTTTTGGC
CACTGACTGACAAGGTGGATGAAGAAAGTACAGGACACAAGGCCTGTTACTAGC
ACTCACATGGAACAAATGGCC **3'**.

These artificial microRNAs target the human superoxide dismutase 1 (SOD1) mRNA in the cytoplasm for degradation via the RNA interference pathway. The expression and transcriptional regulation of the cassette is enhanced by the addition of the Woodchuck Hepatitis Virus Post-transcriptional Regulatory Element (WPRE), and a human growth hormone poly-A (hGHpolyA) signal downstream of the artificial microRNAs.

AAV vectors were produced by PackGene Biotech (Worcester, MA, USA) by triple plasmid transfection protocol and the protocol has been described previously (Torregrosa et al., 2021). The AAV produced was assessed for sterility, endotoxin level and purity. Qualitative empty to full capsid assessment was determined by transmission electron microscopy (TEM). The titer was determined via ddPCR method targeting the WPRE.

Intrathecal Injections

Intrathecal injections were performed at ~6 weeks of age. Mice were anesthetized with isoflurane and the depth of anesthesia was assessed via a toe pinch. Ethiqua XR (buprenorphine extended-release injectable suspension) (Fidelis Animal Health, North Brunswick, NJ, USA) was administered to eliminate pain sensation. The mouse fur was clipped from the injection area and an ocular lubricant was applied. The mouse was placed on a heating source in ventral recumbency. The injection site was thoroughly cleaned, including three wipes with betadine and three wipes with isopropyl alcohol (alternating). Vertebral processes were detected by arching the spine which allows correct orientation and placement of the needle. A A 29-gauge, 0.3mL syringe (Cat#: 4429-3, Smiths Medical ASD, Inc., Southington, CT, USA) was inserted in the gap between L5 and L6 or L4 and L5 and a tail flick is detected if the needle is in the correct location. The test articles or vehicle (artificial cerebrospinal fluid) was slowly administered (10 µL, 8E11, 1.2E12, 1.6E12 GC) to minimize rapid changes in CSF pressure. Mice were then transferred to a heating chamber set at 37C for recovery first and then placement in their home cages.

Neurofilament light measurement

Mice were bled (~100 µL) via facial vein puncture at -1, 3, 7 and 18 -weeks post-injection. The blood was collected in in BD Microtainer SST Clog Activator/Gel tubes (Becton Dickinson, Franklin Lakes, NJ, USA). The tube was inverted a few times and left for 30 mins for

coagulation. The tube was then centrifuged at 2000RCF (4600RPM) for 10 minutes to separate the serum for neurofilament light measurement (NfL). Neurofilament in serum was quantified via Simple Plex Human NF-L Cartridge (Protein Simple, SPCKB-PS-002448, San Jose, CA, USA) by following the manufacturer's protocol.

Open Field

Prior to the start of each behavioral test, mice were acclimated to the procedure rooms for approximately 30 minutes. The cylindrical arena was cleaned by 70% ethanol prior for each run. Mice were individually placed in the arena (~43 cm in diameter) and allowed to move freely for 30 min. An overhead camera was used to capture mouse distance traveled, rearing, center duration and grooming by Noldus Ethovision XT15 (Noldus, Wageningen, Netherlands).

Clasping

For hindlimb clasping, mice were suspended by the tail and the number of limbs retracted towards the body. Each mouse was given a score (0 = no clasp, 1 = 1 limb, 2 = 2 limbs, 3 = 3 limbs, 4 = 4 limbs, 5 = mouse curled up into ball – all limbs and head).

Grip Strength

To assess grip strength, mice were positioned to grip a small bar connected to a force-measuring Grip Strength Meter (TSE Systems, Chesterfield, MO, USA) with all four limbs. Each mouse was then gently pulled horizontally until it lost its grip on the bar. The device measures the maximum mechanical force exerted on the bar until it is released. This process was repeated until 3 successful measurements were recorded for each mouse and the average determined. The force was measure in grams and was normalized to the bodyweight in grams.

Gait

Gait was analyzed using the Noldus CatWalk XT system (Noldus, Wageningen, Netherlands). Mice were individually placed at one end of the runway and allowed to walk across it toward the goal box to their home cage. Each mouse traversed the runway until 3 successful runs were recorded. A maximum run speed variation of 60% was set to ensure an accurate representation of a mouse's natural gait. If a mouse was unable to complete any compliant runs after 10 minutes of testing, the mouse was removed from the runway and excluded.

Statistical analysis

GraphPad Prism 8 (San Diego, CA, USA) and RStudio (Posit, Boston, MA, USA) were used to plot graphs and conduct statistical analysis. Statistical test used for each figure are noted in the caption. All data are expressed as means ± standard deviation of the data.

Results

AAV-miR-SOD1 caused a dose-dependent reduction in survival

Female wild-type C57BL/6J mice were enrolled in a battery of behavioral tests post induction of dorsal root ganglia (DRG) injury by the delivery of a stressor AAV. Mice were intrathecally dosed, free hand bolus injection, with AAV-miR-SOD1 at 8E11 GC, 1.2E12 GC and 1.6E12 GC at 6 weeks of age. Mice were subjected to open field, grip strength, clasping, and gait analysis at non-overlapping timepoints to minimize stress and allow recovery time (Fig. 1a). Neurofilament light chain (NfL) is a biomarker of DRG toxicity as AAV vectors are known to cause axonal degeneration and induce NfL release (Fader et al., 2022). Serum NfL levels significantly surged to ~2000 pg/mL for AAV-miR-SOD1 treated-mice relative to vehicle at 3 weeks post-injection (p.i.) (Mixed-effects analysis followed by Dunnett Multiple Comparison test, ****P<0.001, ****P<0.0001*) (Fig. 1b). Neurofilament peak occurred at 3 weeks p.i. for most mice, spaghetti plots reveal this transient relationship and highlights substantial reduction in survival after 7 weeks p.i. (Fig. 1c). Mean bodyweight for 1.2E12 GC and 1.6E12 GC AAV-miR-SOD1 treated mice trended below vehicle despite diet gel supplementation throughout study duration (Fig. 1d). The median survival for 1.6E12 GC and 1.2E12 GC AAV-miR-SOD1 treated mice was 105 and 170 days of age (Fig. 1e). These findings translated to a significant and dose-dependent reduction in the survival of mice (Long-rank test, ***P<0.01, ***P<0.001*) (Fig. 1e). During necropsy, some AAV-treated mice showed evidence of minor self-mutilation in their hindlimbs. Injection of AAV-miR-SOD1 induced neuronal and nerve injury which resulted in decline in bodyweight and survival.

AAV-miR-SOD1 alters key open field measurements in treated mice

Open field is a widely used behavioral test to assess exploratory behavior, locomotion and anxiety-like behaviors in mice. The open field test offers a means to assess the tolerability and safety of novel drugs in mice (Hutter-Saunders et al., 2012). Mice were placed in the open field

arena left to explore for 30 min for distance, center duration, grooming duration and rearing duration measurements were collected. All AAV-miR-SOD1-treated mice displayed a dose-dependent decline in the distance travelled at 3 weeks p.i. (Fig. 2a). At 13 weeks p.i., mice treated with 1.2E12 GC AAV-miR-SOD1 traveled a significantly shorter distance compared to vehicle, 512.2 ± 281.8 cm versus 1017.4 ± 212.2 cm (Mixed-effects analysis followed by Bonferroni's multiple comparisons test, **P<0.01*) (Fig. 2a). A similar trend was observed with 1.6E12 GC AAV-miR-SOD1, however no significance was not observed due to only 3 mice remaining in the study. On average, AAV-miR-SOD1-treated mice spent less time in the center relative to vehicle-treated mice at 13 weeks p.i., a dose dependent effect that was not significant (Fig. 2b). Grooming activity for 1.2E12 GC and 1.6E12 GC AAV-treated mice displayed substantial deviation as some mice were recorded to groom for very long periods relative to vehicle at 13-week p.i. (Fig. 2c). The mean for 1.2E12 GC (535.9 ± 450.7 sec) and 1.6E12 GC (528.8 ± 702.3 sec) was significantly longer than vehicle (94.5 ± 702.3 sec) at 13 weeks p.i. (Mixed-effects analysis followed by Bonferroni's multiple comparisons test, **P<0.01, ***P<0.001*). Rearing duration was significantly lower in all AAV-miR-SOD1 treated-mice at 13 weeks p.i. (Mixed-effects analysis followed by Bonferroni's multiple comparisons test, **P<0.05, **P<0.01, ***P<0.001*) (Fig. 2d). The rearing for 1.2E12 GC AAV-treated mice had an average duration of 99.2 ± 45.9 sec compared to vehicle-treated mice,192.8 ± 83.4 sec (Mixed-effects analysis followed by Bonferroni's multiple comparisons test, ****P<0.001*) (Fig 2d). AAV-miR-SOD1 alters open field metrics, mice covered shorter distances and exhibited reduced rearing behavior.

Mice showed deficits in grip strength and hindlimb clasping

Cage observations in earlier studies revealed that mice showed a characteristic weakness that was most consistent in the hindlimbs. To investigate this, the grip strength test was employed to assess the gripping for all limbs. Mice were positioned to grip a mesh connected to a force

transducer and were then pulled by their tails. Mice displayed a significant reduction in normalized grip strength in all dose levels (Mixed-effects analysis followed by Bonferroni's multiple comparisons test, ***P<0.01, ***P<0.001*) (Fig. 3 a, b). At 9 weeks p.i., vehicle-treated mice maintained a mean normalized grip strength score of 6.65 ± 0.46 g_{Force} /$g_{bodyweight}$ compared to 4.99 ± 1.40 g_{Force} /$g_{bodyweight}$ for 8E11 GC, 5.82 ± 0.69 g_{Force} /$g_{bodyweight}$ for 1.2E12 GC and 4.68 ± 0.93 g_{Force} /$g_{bodyweight}$ for 1.6E12 GC treated subjects (Fig. 3a, b). Muscle weakness was progressive and consistent within dose group and not dose dependent. Furthermore, mice developed clasping behavior, a neurological deficit that has been observed in neurodegenerative mouse models (Lalonde & Strazielle, 2011). Clasping in AAV-miR-SOD1-treated mice worsened in a dose dependent manner from weeks 3 to 15 p.i. (Fig 3c-f). The median clasping score for 8E11 GC AAV-treated mice hovered at ≤2 from weeks 3-11 p.i. (Fig. 3d). This is opposed to 1.6E12 GC AAV-treated mice where the median clasping score surged from score of 2 at 3 weeks p.i. to a score of 4 at 9 weeks p.i. (Fig. 3f and Fig. S1 for jittered data faceted by week). In fact, all mice treated with the highest dose of AAV-miR-SOD1 maintained a clasping score of 4 from weeks 9-15 p.i. (Fig. 3f and Fig. S1 for jittered data faceted by week). Pearson correlation analysis was used to investigate the relationship between these key functional deficits and how it aligned with serum NfL. Grip strength at 5 weeks p.i. was found to be moderately correlated with clasping scores at 9 weeks p.i. (Pearson, R = -0.644), It's crucial to recognize that the negative correlation stems from a bimodal association, where mice are located at opposing ends of the spectrum, and correlation analysis is not typically conducted on categorical variables (clasping score) (Fig. 3g). Neurofilament light was found to moderately correlate with grip strength (Pearson, R = -0.609) (Fig. 3h). There was a notable association between elevated NfL levels and severe hindlimb clasping (Fig. 3i). However, caution is warranted in interpreting this correlation, as both the vehicle-treated and the 1.6E12 GC AAV-miR-SOD1 groups were positioned at the extremes of the plot (Pearson,

R=0.799) (Fig. 3i). A summary of all Pearson correlations of grip strength, clasping and NfL are noted in Figure S2 of this report. In short, a robust decline in grip strength performance and a progressive worsening in clasping behavior were observed in response to the test article.

Mice exhibited no signs of gait abnormalities

The Catwalk XT serves as a comprehensive tool capable of detecting subtle alterations in locomotion patterns and finds extensive utilization in research (Timotius et al., 2023). Individual mice were placed on glass plate and the movement towards their home cages was recorded. Mice were tracked for various locomotion metrics: stand time, swing time, swing speed, stride length for each paw and stance width and paw position for the front and hind limbs (Fig. 4a) (Pitzer et al., 2021). Examining the overall patterns, AAV-miR-SOD1-treated mice did not exhibit any characteristic deficiencies in stand time, swing time, swing speed and stride length (Fig. 4b-e). For the stance width, some AAV-miR-SOD1 treated mice had an overall wider stance and 6 and 10 weeks p.i., however these findings were minor and showed deviation (Fig. 4f). No obvious trends were observed with print position despite some AAV-miR-SOD1-treated mice showing a higher mean right print position than vehicle (Fig. 4g). Gait measurements are dependent on mice successfully completing the task, the number of mice that failed the task was tracked (Fig. S3a). A few mice from 8E11 GC and 1.6E12 GC groups failed to complete the task at 6, 10 and 18 weeks p.i. (Fig. S3a). Interestingly, these mice exhibited NfL levels that were above the mean average along with severe clasping (score = 4) at 9 weeks p.i., a summary of key metrics for these mice is noted in Figure S3b.

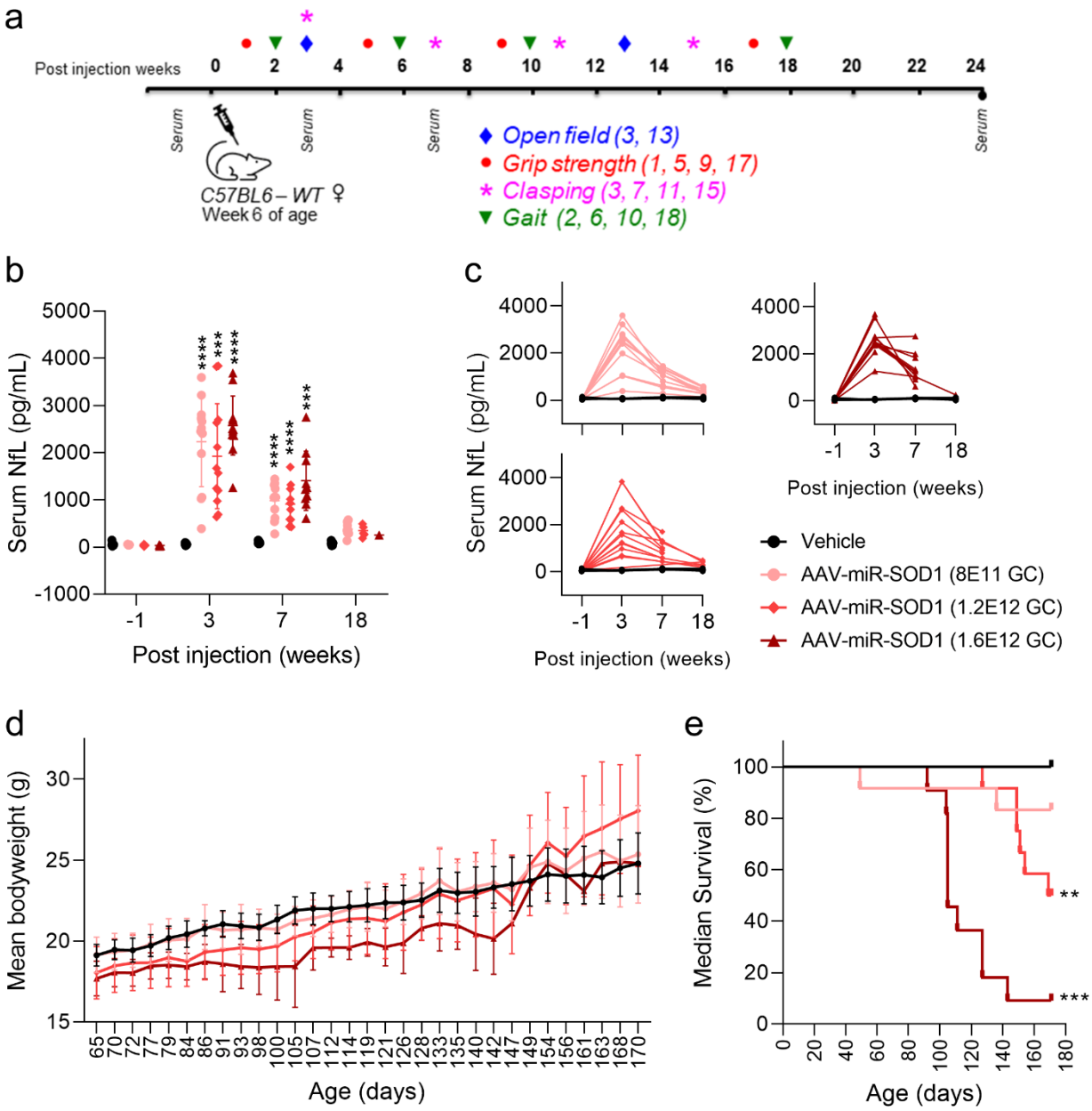
a
Post injection weeks
0 2 4 6 8 10 12 14 16 18 20 22 24
Serum
C57BL6 – WT ♀
Week 6 of age
Open field (3, 13)
Grip strength (1, 5, 9, 17)
Clasping (3, 7, 11, 15)
Gait (2, 6, 10, 18)
b
Serum NfL (pg/mL)
Post injection (weeks)
c
Serum NfL (pg/mL)
Post injection (weeks)
Vehicle
AAV-miR-SOD1 (8E11 GC)
AAV-miR-SOD1 (1.2E12 GC)
AAV-miR-SOD1 (1.6E12 GC)
d
Mean bodyweight (g)
Age (days)
e
Median Survival (%)
Age (days)

Figure 1: Intrathecal dosing of AAV-miR-SOD1 increased serum neurofilament light level and significantly reduced survival in female C57BL/6J mice. **a.** Experimental design and timeline for behavior tests. **b.** Serum neurofilament light levels surge in response to AAV treatment (n=1-15/treatment. Mixed-effects analysis followed by Dunnett Multiple Comparison test, ****P<0.001, ****P<0.0001*. **c.** Spaghetti plots for each treatment. **d.** Line plots showing the mean bodyweight of mice. **e.** High and intermediate dose of AAV-miR-SOD1 reduced medial survival (Long-rank test, ***P<0.01, ***P<0.001*). Data are mean ± SD with n=1-12/treatment unless stated.

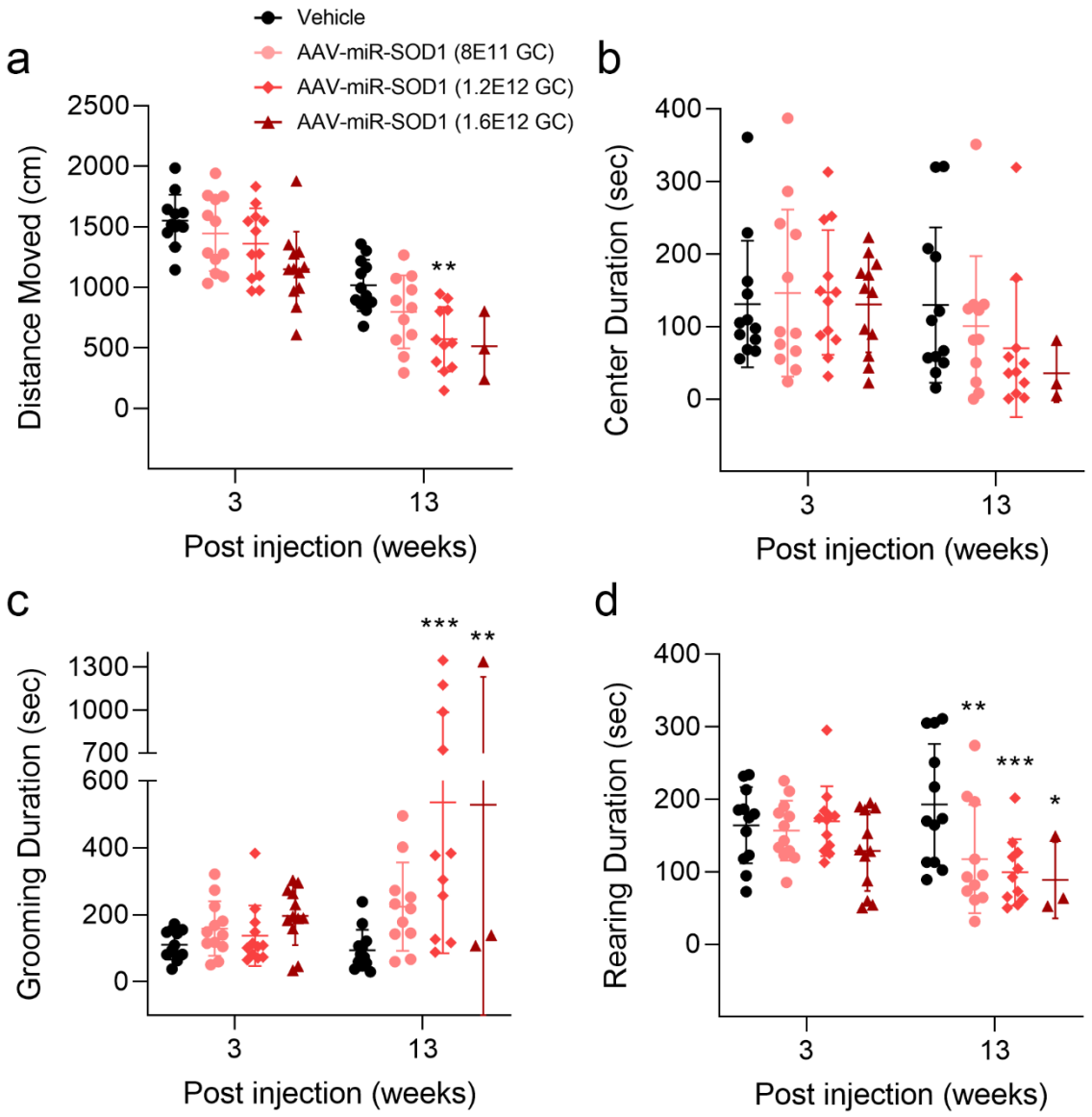

Figure 2: Open field test for female C57BL/6J mice dosed with AAV-miR-SOD1 at 6 weeks of age. Plots of **a.** distance travelled, **b.** center duration, **c.** grooming duration and **d.** rearing duration (Mixed-effects analysis followed by Bonferroni's multiple comparisons test; **P<0.05, **P<0.01, ***P<0.001*). Mice were recorded for 30 minutes for each timepoint. Data represent the mean ± SD with n=3-12/treatment.

a

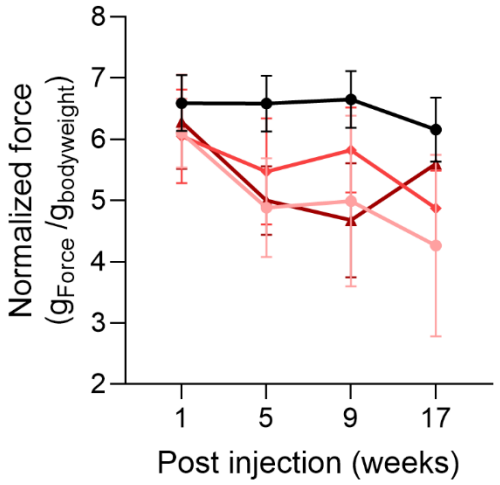

b

Weeks post injection	Bonferroni's multiple comparisons test	adjusted P-value	Significance
1	Vehicle vs. AAV-miR-SOD1 (8E11 GC)	0.0995	ns
1	Vehicle vs. AAV-miR-SOD1 (1.2E12 GC)	0.1476	ns
1	Vehicle vs. AAV-miR-SOD1 (1.6E12 GC)	0.7399	ns
5	Vehicle vs. AAV-miR-SOD1 (8E11 GC)	<0.001	***
5	Vehicle vs. AAV-miR-SOD1 (1.2E12 GC)	0.003	**
5	Vehicle vs. AAV-miR-SOD1 (1.6E12 GC)	<0.001	***
9	Vehicle vs. AAV-miR-SOD1 (8E11 GC)	0.005	**
9	Vehicle vs. AAV-miR-SOD1 (1.2E12 GC)	0.008	**
9	Vehicle vs. AAV-miR-SOD1 (1.6E12 GC)	<0.001	***
17	Vehicle vs. AAV-miR-SOD1 (8E11 GC)	0.005	**
17	Vehicle vs. AAV-miR-SOD1 (1.2E12 GC)	0.002	**
17	Vehicle vs. AAV-miR-SOD1 (1.6E12 GC)		

0.12(ns), 0.033(*), 0.002(**), <0.001(***)

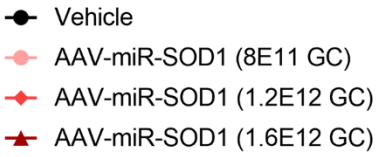

c d e f

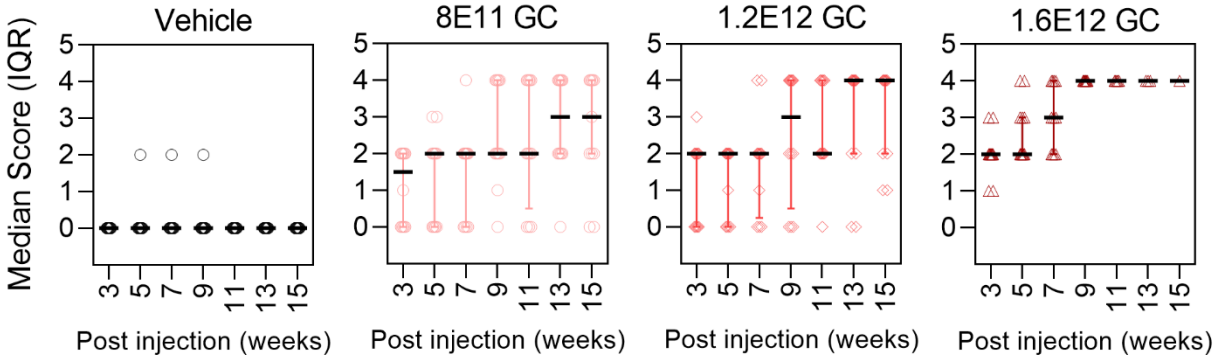

g h i

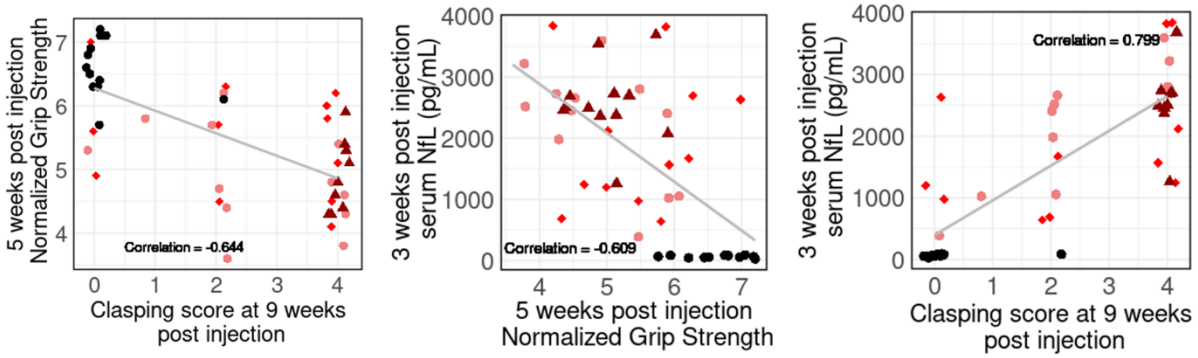

Figure 3: Female C57BL/6J mice showed muscle weakness and neurological hindlimb clasping in response to AAV treatment. **a.** All AAV-miR-SOD1 dose levels significantly reduced the normalized grip force. **b.** A summary of statistical tests and significance levels for all timepoints (Mixed-effects analysis followed by Bonferroni's multiple comparison test). Median of hindlimb clasping for **c.** Vehicle, **d.** 8E11 GC, **e.** 1.2E12 GC and **f.** 1.6E12 GC showed progressive increase in the severity of clasping. **g.** Pearson correlation of normalized grip strength at 5 weeks p.i. and clasping scores at 9 weeks p.i. for all treatments (R=-0.644). **h.** Pearson correlation of neurofilament light levels at 3 weeks post-injection versus normalized grip strength at 5 weeks postinjection (R=-0.609). **i.** Pearson correlation of neurofilament light levels at 3 weeks post-injection versus clasping scores at 9 weeks post-injection (R=0.799). Data are mean ± SD with n=1-12/treatment. Correlation means R value.

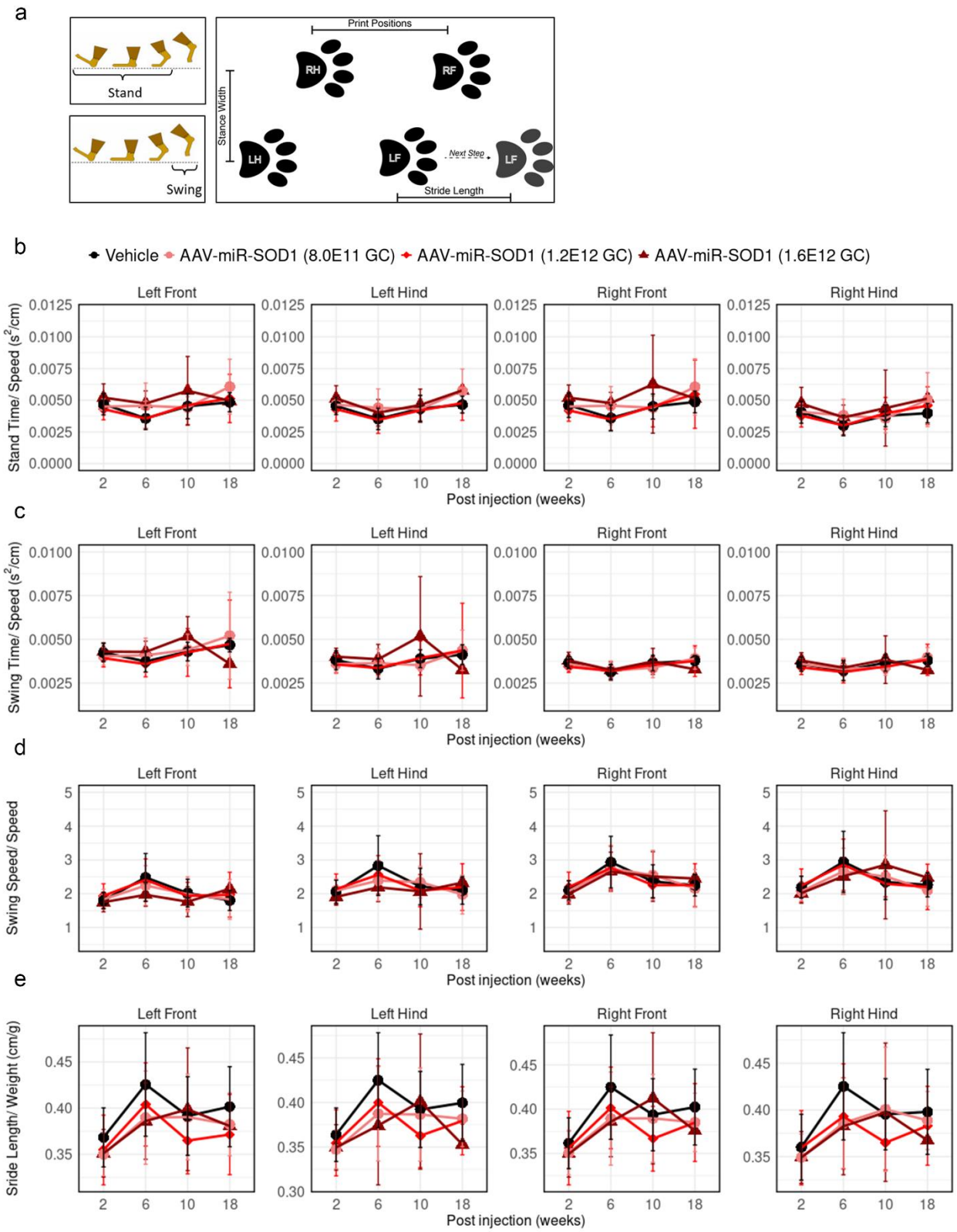
a
Stand
Swing
Print Positions
RH
RF
LH
LF
LF
Next Step
Stance Width
Stride Length
b
Vehicle
AAV-miR-SOD1 (8.0E11 GC)
AAV-miR-SOD1 (1.2E12 GC)
AAV-miR-SOD1 (1.6E12 GC)
Left Front
Left Hind
Right Front
Right Hind
Stand Time/ Speed (s²/cm)
Post injection (weeks)
c
Swing Time/ Speed (s²/cm)
d
Swing Speed/ Speed
e
Sride Length/ Weight (cm/g)

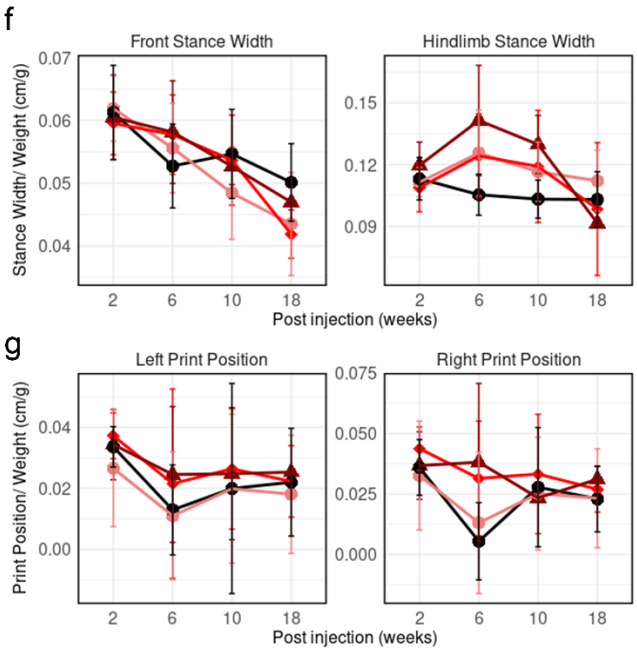

Figure 4: Gait parameters of female C57BL/6J mice in response to intrathecal administration of AAV-miR-SOD1. **a.** Images showing a representation of individual measurements from the Noldus CatWalk XT, image modified from Pitzer et al., 2021. Normalized measurements for all limbs as indicated per panel for **b.** stand time, **c.** swing time, **d.** swing speed, **e.** stride length, **f.** stance width and **g.** print position. Each metric was normalized as indicated on the y-axis. Data are mean ± SD with n=1-12/treatment.

Discussion

In this study, intrathecal administration of AAV-miR-SOD1 in female C57BL/6J mice affected key behavioral functional measures. AAV-injected mice showed the characteristic and transient surge in neurofilament light (NfL) which is indicative of dorsal root ganglia (DRG) and nerve injury. Mice were found to trend lower in mean bodyweight and showed significant decline in survival. AAV-treated mice exhibited anxiety-like behavior, reduction of grip strength and development of hindlimb clasping. Grip strength and clasping were pronounced and moderately correlated with serum NfL. Interestingly, gait measures were unaltered despite the high sensitivity of the Catwalk instrument (G. Zheng et al., 2021). The observed variability in mice was expected, given the substantial variability observed in NfL and the inconsistency of neuronal degeneration in microscopic histopathological findings (Hawley et al., 2024).

AAV toxicity consistently affected clasping and grip strength**.** Unlike other measurements, the severity of clasping was dose-dependent and did not resolve. It emerges at the highest doses in all animals at 3 weeks post-injection (p.i.) and worsens over the study duration. This finding mirrors the recent findings in mice treated with AAV9 expressing the survival motor neuron gene 1 (SMN1) (Alstyne et al., 2021). The mechanisms of how this occurs is not known, but it is likely that high doses of AAV9 transduces and effects neurons in the spinal cord and key brain regions such as the cerebellum, basal ganglia and the neocortex (Lalonde & Strazielle, 2011). Furthermore, grip strength was found to decline sharply from 1 to 5 weeks post-injection, normalized force continues to drop slightly for the following weeks. This trend aligned with wild type mice treated with AAV9-SMN at high doses where grip strength and rotarod declined rapidly after treatment (Alstyne et al., 2021). There seems to be an acute phase of injury where key neurons in the sensorimotor circuit are likely impacted. However, a recent study investigating behavior in rats post AAV9-frataxin dosing showed unaltered rotarod activity and labelled the histopathological findings as clinically silent (Tyszkiewicz et al.,

2024). Although the differences in AAV cargo, dose levels and route of administration in this study and the rat study significantly contribute to the differing outcomes (Hordeaux, Buza, Dyer, et al., 2020). Moderate correlations were found between grip strength vs. clasping, NfL vs. grip strength and strong correlation for NfL vs clasping. However, these correlations were driven by a bimodal relationship as animals were found in the extremes. The correlations do predict that these functional measures are related to serum NfL levels. This strengthens the use of these functional tests as markers of AAV-induced DRG toxicity and nerve injury.

Open field measurements indicate that AAV-treated mice may experience anxiety-like behavior. Reduction of distance moved the decline in the rearing duration and increased grooming behavior in some animals were detected at 13 weeks post dosing. Anxiety-like behavior was not as consistent as grip strength and clasping. The decrease in rearing duration is complicated by muscle weakness in animals, which is why diet gels are placed on the cage floor. Gait is a measure of coordination and muscle function; gait overall was found to be inconclusive in this study. Standard measures of gait were normalized appropriately and hindlimb stand width was found to be representative of the phenotype observed in some AAV-treated mice. Furthermore, some mice were not able to complete the gait test and those are noted in Figure S3. These animals were found to have NfL levels that were above the group mean and clasping scores of 4. To conclude, open field data suggests mice could suffer from anxiety-like behavior, but this is likely confounded by muscle weakness.

In conclusion, key behavioral measures are impacted due to the injection of stressor AAV vector in wild type mice. Grip strength and hindlimb clasping could be used as a functional biomarker for AAV-induced DRG toxicity in WT mice. Traditionally, functional phenotypes have rarely been observed in animal models such as NHP where toxicological assessments of candidate drugs are intensely studied. Several limitations were identified and require improvement for future studies. The number of mice in the highest dose groups declined as the

study progressed beyond the 7-week p.i. timepoint due to early euthanasia and found dead cases. Free hand intrathecal bolus injections likely leads to peripheral leakage which contributes to the variability in all measurements (Chandran et al., 2023; Gong et al., 2019; Hawley et al., 2024). This report presents mice as an early model to assess the tolerability of candidate AAV vectors early in discovery prior to NHP use. Hence, it is crucial to perform extensive studies with robust statistical power to minimize variability. Mice have the advantage over NHPs with larger studies can be conducted and diverse behavioral and physiological experiments have already been established. Translatability of DRG toxicity has not been firmly established, understanding the potential toxic effects and impact on behavior in an early animal model is crucial for developing safe and effective gene therapies.

Supplementary Figures

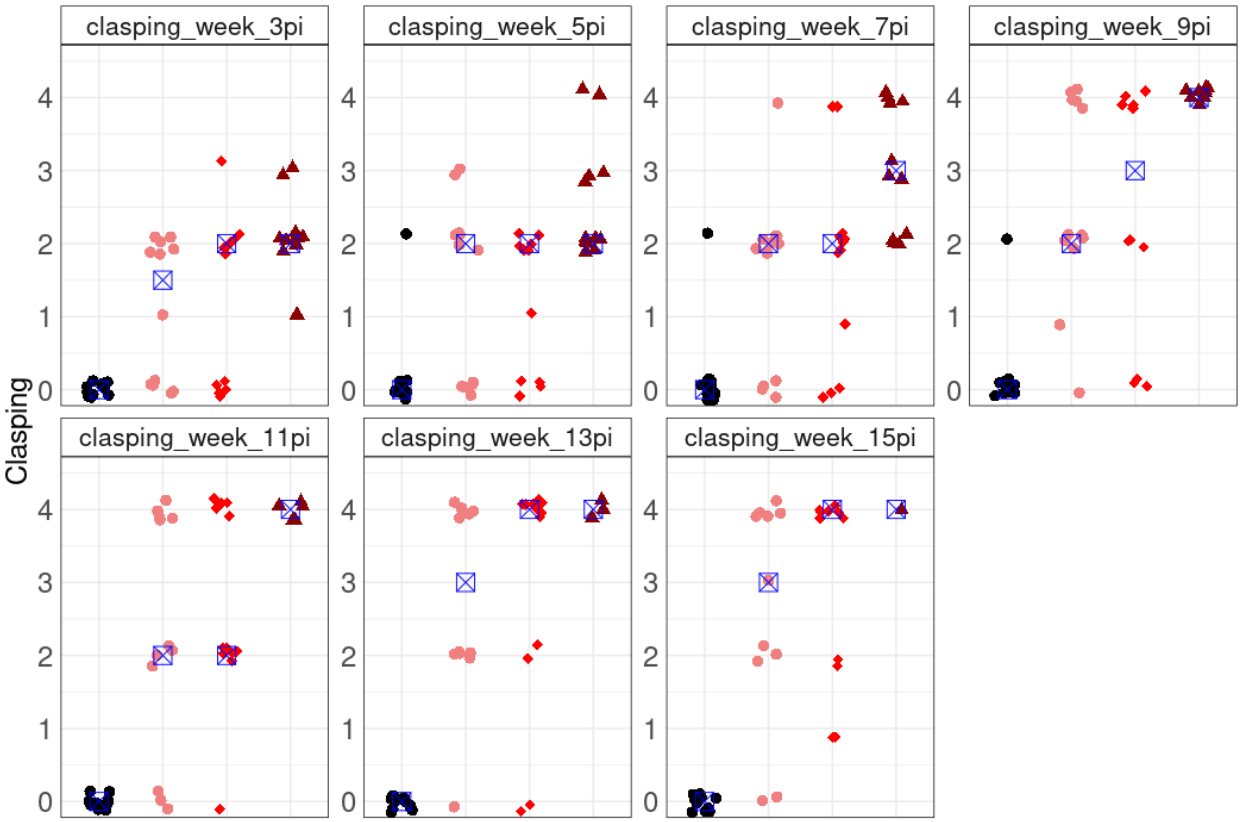

Figure S1: AAV-miR-SOD1 leads to the neurological hindlimb clasping phenotype that progresses with age in female C57BL/6J mice. Each data point represents an individual mouse and data points are faceted by post-injection weeks. The blue box with x represents the median for each group. p.i. – post-injection

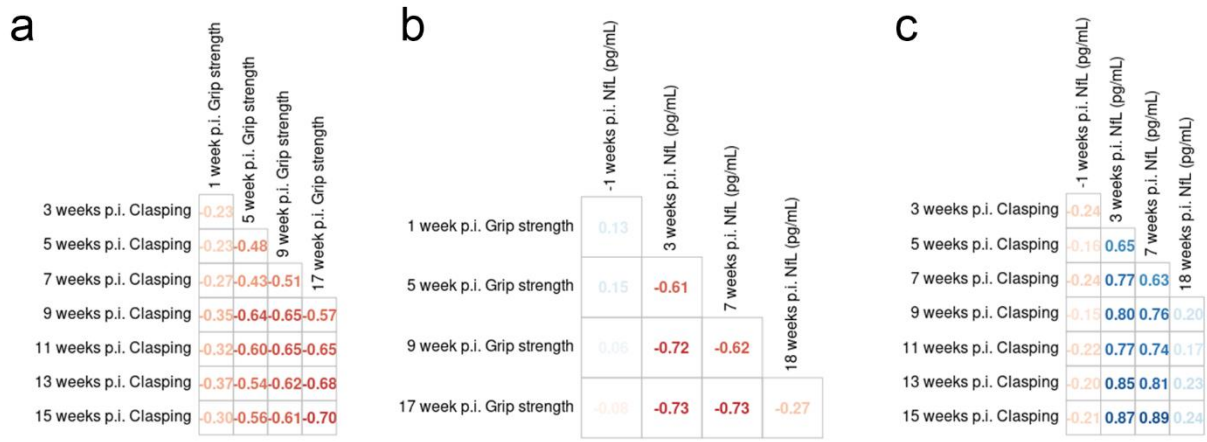

Figure S2: Pearson correlation matrices of grip strength, neurofilament light and hindlimb clasping with corresponding R values color coded red (negative) and blue (positive). **a.** Correlation of normalized grip strength versus clasping scores. **b.** Correlation matrix of NfL and normalized grip strength. **c.** correlation matrix of NfL and clasping scores in mice. p.i. – post-injection, NfL – Neurofilament light.

a

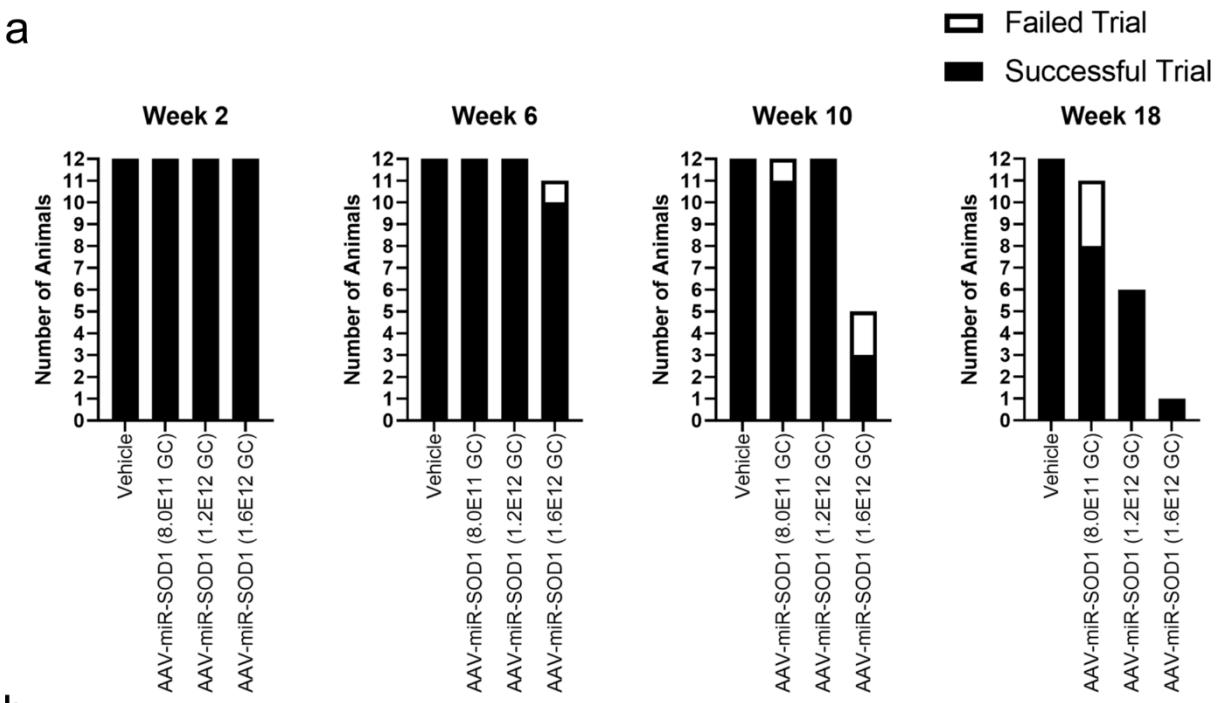

b

Weeks post injection	Mouse ID	Treatment	3 weeks p.i. NfL (pg/mL) (Group Mean)	Survival (days) (Group Medial Survival)	3 weeks p.i. Distance Moved (cm) (Group Mean)	5 weeks p.i. Normalized Grip Strength (Group Mean)	9 weeks p.i. Clasping Score (Group Median)
6	9237	AAV-miR-SOD1 (1.6E12 GC)	3543 (2573.8)	92 (105)	1292.0 (1150.8)	4.9 (5.0)	N/A (4)
10	9270	AAV-miR-SOD1 (8.0E11 GC)	2728 (2235.8)	171 (N/A)	1114.8 (1445.6)	4.3 (4.9)	4 (2)
10	9226	AAV-miR-SOD1 (1.6E12 GC)	3686 (2573.8)	127 (105)	1155.2 (1150.8)	5.9 (5.0)	4 (4)
10	9246	AAV-miR-SOD1 (1.6E12 GC)	2686 (2573.8)	111 (105)	1353.9 (1150.8)	4.3 (5.0)	4 (4)
18	9270	AAV-miR-SOD1 (8.0E11 GC)	2728 (2235.8)	171 (N/A)	1114.8 (1445.6)	4.3 (4.9)	4 (2)
18	9278	AAV-miR-SOD1 (8.0E11 GC)	2802 (2235.8)	171 (N/A)	1276.5 (1445.6)	5.4 (4.9)	4 (2)

N/A indicates not applicable values or not available data

Figure S3: All animals that have participated in gait analysis **a.** Barplots showing the number of animals that successfully completed the CatWalkXT trials for all weeks post-injection. **b.** A summary of mice that failed in the trials for all timepoints and their corresponding endpoints, the values in the brackets indicate the mean group value.

Acknowledgements

Adam Sheehy and Kevin Ghaemi for conducting the behavior tests on study animals and providing early analysis. Moore Arnold for supporting this study.

Chapter 6

General Discussion

Summary

The aim of this dissertation was to elucidate the molecular underpinnings of dorsal root ganglia (DRG) toxicity in C57BL/6J mice following intra-cerebrospinal fluid administration. Furthermore, it sought to determine whether these mice would exhibit phenotypes associated with Adeno-Associated Virus (AAV)-induced DRG injury. The elevation of neurofilament light chain (NfL) suggested AAV-induced DRG toxicity, a finding consistent with other animal models. While mice generally tolerated the toxic AAV, a decline in survival and bodyweight were observed, especially mice receiving the highest dose.

In Chapter 2, the application of single nucleus RNA sequencing (snRNA-seq) revealed significant neuronal and Schwann cell loss, along with an increase in activated satellite glia, fibroblasts, and immune cell proliferation. Neurons exhibited gene signatures associated with cell death, while activated satellite glia demonstrated a robust upregulation of neurodevelopmental genes and neurogenesis processes, suggesting a response to alleviate and repair injured neurons. Many axonal guidance genes were elevated. Both innate and adaptive immune responses were evident aligning with previous reports in mice and other species (Fig. 1). snRNA-seq provided quantitative and comprehensive resolution of the molecular and population changes which confirmed histopathological findings.

Chapter 3 posed the question of the significance of these molecular changes especially for the Schwann cell decline which is associated with axonal degeneration. Mice were subjected to sciatic nerve action potential assessment to ascertain the presence of electrophysiological deficits. Despite evidence of DRG injury as indicated by serum NfL elevations, no changes were detected in action potential latencies suggesting either lack of changes or potentially lack of sensitivity of the test. Improvements to the experimental design would be needed and a focus on sensory nerves such as the sural or the saphenous nerves would be optimal for future electrophysiological experiments.

In Chapter 4, the use of compound muscle action potential (CMAP) and triggered muscle dual lever physiological techniques on the hindlimbs of AAV-treated mice allow for assessment of motor and sensory function. AAV treated mice exhibited loss of plantar flexor strength force relative to controls a few months post-injection with no changes to CMAP activity. This indicated muscle weakness due to sensory dysfunction rather than motor dysfunction.

In Chapter 5 focused on a battery of behavior tests. Mice displayed a robust decline in grip strength and consistent clasping behavior were observed as early as 5 weeks post-injection. These findings were moderately correlated with serum NfL. Key open field test also hints to potential anxiety like behaviors in AAV-treated mice, but these finding should be treated with caution due the grip strength data.

Phenotypic and functional deficits

Several in life measurements in mice were consistently altered due to AAV-induced DRG toxicity aligned with some prior findings. All AAV-treated mice received diet gel supplementation to prevent bodyweight loss and early euthanasia. High doses significantly reduced survival in the behavior and the triggered muscle dual lever studies. Muscle weakness originally observed in cages translated to a reduction in force measures on the foot plate in the triggered dual lever study (Chapter 4) which was consistent with decline in grip strength in the behavior study (Chapter 5). Grip strength was more sensitive than triggered muscle dual lever as significant reduction in grip strength was noted at 5 weeks post-injection versus 12 weeks post-injection for the dual lever. Interestingly, clasping behavior was the most striking and consistent phenotype in all AAV-treated mice. Mice manifested this neurological phenotype early and progressed with time, observed in all treated mice at 3 weeks post-injection. Clasping behavior seemed to be dose dependent as opposed to other functional measures. These functional deficits paralleled some of the phenotypes observed in mice and other species. Clasping behavior observed after AAV dosing has been documented in mice, with the onset

varying depending on the AAV dosage (Alstyne et al., 2021). Furthermore, in other species such as the New Zealand White rabbit, reduction of bodyweight, lack of activity, hindlimb weakness, reduced muscle tone, incoordination along with other phenotypes have were observed (Tien et al., 2024). In piglets, AAV administration led to hindlimb ataxia and early euthanasia of piglets (Hinderer et al., 2018). All other studies examining rats and non-human primates have not shown functional deficits (Fader et al., 2022; Johnson et al., 2023; Tukov et al., 2022).

Molecular alterations and sensorimotor dysfunction

A substantial drop in the population of sensory neurons and Schwann cells was noted in the DRG by snRNA-seq likely affecting sensorimotor function. Loss of sensory neurons and myelination contribute to the physiological and behavioral deficits observed in mice. Mechanoreceptors play a pivotal role in proprioception, touch and pressure sensation (Tuthill & Azim, 2018). All types of low-threshold mechanoreceptors declined along with the rest of the annotated sensory neurons in the DRG in the snRNA-seq study (Chapter 2). Loss of mechanoreceptor neurons reduce the magnitude of sensory input required for proper integration; processes required for effective motor function. Additionally, axonal degeneration is also evident in sensory nerves as noted by the loss of myelination in the DRG. Histopathological examinations have consistently revealed injury to sensory axons in peripheral nerves as well as in the central nervous system, particularly affecting the sensory tracts within the spinal cord. Overall, the snRNA-seq findings in the DRG likely reduce sensory input into the CNS likely affecting physiological and behavioral findings in grip strength, muscle force measurements and clasping.

While various brain regions, including the cerebellum, have been linked to clasping behavior (Lalonde & Strazielle, 2011), it is noteworthy that DRG sensory deficits have also been identified as potential contributors to hindlimb clasping. In a previous report, loss of

proprioceptive neurons in the DRG following AAV9-SMN is thought to cause clasping phenotype observed in wild type mice (Alstyne et al., 2021). In a *Hoxb8* knockout mouse, neuronal degeneration in the DRG resulted in forelimb and hindlimb clasping (van den Akker et al., 1999). The clasping behavior observed in many studies in this dissertation can arise from neuronal degeneration of proprioceptive neurons in the DRG post-AAV induced injury.

The functional impairments noted in this dissertation are unlikely to stem from motor dysfunction. In general, no anatomical or morphological alterations have been reported in motor neurons following AAV induced-DRG toxicity. In chapter 3 of this dissertation, compound muscle action potential measurements, known to probe for motor function, were generally unaltered in AAV-treated mice. Histopathological examinations across all species revealed axonal degeneration in the dorsal funiculi, with no additional observations in ventral motor neurons. (Fader et al., 2022; Hawley et al., 2024; Hordeaux, Buza, Dyer, et al., 2020; Hordeaux et al., 2018; Tien et al., 2024). Only one study in mice reported late-onset reduction in motor neuron size and number at 10 months of age in the spinal cord, a phenomenon linked to the overexpression of the transgene (Alstyne et al., 2021). Sensory neurons are more susceptible to AAV transduction as opposed to motor neurons, which was reflected in the complete loss of proprioceptive neurons in the DRG versus the modest reduction of motor neurons in the spinal cord in mice (Alstyne et al., 2021). The sensorimotor impairments discovered following DRG toxicity in mice stem from sensory dysfunction rather than motor, confirmation of these findings with future studies would be beneficial in supporting this conclusion.

Mechanistic insights in mice

Efficient transduction of sensory neurons may lead to high expression of a toxic gene product which may drive toxicity, and inflammatory responses likely exasperating DRG injury (Fig. 1). The strong constitutive promoter, CAG, drives the expression of the SOD1 targeting duplex

artificial microRNA (amiR) as seen with prior reports (Hordeaux, Buza, Dyer, et al., 2020). Interestingly, CAG is one of the most commonly used promoters to drive the expression of different transgenes products in clinical trials (Au et al., 2022). The DRG toxicity findings in this dissertation are not likely due to SOD1 knockdown. The specific SOD1 amiRs used in the cassette are predicted to be toxic (miR30a-huSOD1_#5 and miR155-huSOD1_#7). Other SOD1 targeting amiRs effectively reduced SOD1 expression in C57BL/6J mice without phenotypic findings smaller serum NfL surges relative to test article used in this dissertation (Hawley et al., 2024). Furthermore, immune responses were detected in mice and their contribution to the degree of DRG toxicity is not known. The pro-inflammatory signals noted in immune cells of the DRG. In previous NHP studies, use of immunosuppressants failed to alleviate DRG toxicity and the authors concluded that DRG toxicity is transgene driven (Hordeaux, Buza, Jeffrey, et al., 2020; Hordeaux et al., 2018; Tukov et al., 2022). While targeted reduction of transgene expression in the DRG reduces the severity of toxicity (Hordeaux, Buza, Jeffrey, et al., 2020). Perhaps the selection of immunosuppressants and the dosing regimen could impact their effectiveness in reducing DRG toxicity, therefore, more studies are need. The sequence of events and the detailed mechanism of how DRG toxicity occurs following AAV administration requires further investigation in mice.

Doses used across different species

The AAV dose levels used in this dissertation are comparable to prior studies in animal models and clinical studies. In this dissertation, the intrathecally administered dose levels ranged from 5E11 GC to 1.6E12 GC per mouse. To compare with other studies, the AAV titer can be normalized to the brain weight for each species (Stone et al., 2023). The brain weight of a mouse is 0.4g (The Jackson Laboratory). Therefore, 5E11 GC/mouse translates to a normalized dose of 1.25E12 GC/g_{brain}, and 1.6E12 GC/mouse translates to 4E12 GC/g_{brain}. In a rat study, intrathecal dosing of up to 6E12 GC has been achieved, which can be normalized to 3E12

GC/g_{brain} assuming the weight of the rat brain is 2g (X. Chen et al., 2022; Weller, 2012). In an NHP (*Macaca fascicularis*) study, an AAV dose of 9.2E13 GC/animal was injected intrathecally. The average weight of the NHP brain is 70g, yielding a normalized titer of 1.31E13 GC/g_{brain} (Johnson et al., 2023; Sakane et al., 2020). Hordeaux and colleagues reported a dose range of 1E12 to 3E14 GC injected intrathecally/intra-cisterna magna used in 33 NHP studies (Hordeaux, Buza, Jeffrey, et al., 2020). Normalizing the doses to brain weight yields 1.43E10 – 4.28E12 GC/g_{brain}. Patients in current clinical trials have been injected with comparable dose levels for various diseases (Au et al., 2022). In a Giant axonal neuropathy clinical trial, intrathecal injection of up to 3.5E14 GC of AAV has been achieved in children (Bharucha-Goebel et al., 2024). The average weight of the child's brain from 10-12 years of age is 1.45 kg (Paus, 2005). The normalized dose of 3.5E14 GC is 2.41E11 GC/g_{brain}. Another clinical study for CLN7 Batten disease is testing a dose of 1E15 GC (6.89E11 GC/g_{brain}) injected intrathecally in patients (ClinicalTrials.gov, NCT04737460). It is vital to note that different species have varying sensitivities to AAV-induced DRG toxicity findings. A recent rabbit study reported that DRG lesions were perhaps more severe than what had been traditionally reported in NHPs (Tien et al., 2024). In conclusion, the dose levels utilized in this dissertation were acceptable and not super physiological.

Significance

It was shown that mice replicate key aspects of DRG toxicity comparable to larger animal models. This dissertation introduced the first snRNA-seq study on AAV-induced DRG toxicity in a preclinical animal model. These studies added much needed resolution to the vast histopathological data of AAV-induced DRG toxicity in many model organisms. This dissertation characterized the gene expression profiles of different populations of cells following AAV-induced DRG toxicity. In fact, it was shown how the proportion of different cells are altered and how their transcriptional profiles changed in response to AAV-induced

DRG toxicity. Activated satellite glia, also referred to as reactive satellite glia in histopathological studies, were significantly stimulated in reaction to neuronal degeneration. It was shown that mice do capture aspects of the immune responses to AAV, slightly different but comparable to larger animal models. Perhaps most strikingly, this dissertation presented data on key physiological and behavioral deficits in mice which has not been reported in the literature. Use of toxic AAV transgenes/cargo can result in phenotypic manifestations easily recognizable through cage observation. Along with other tests, hindlimb clasping can be used for early identification of toxic AAV transgene candidates. Unlike prior studies, all studies in this dissertation used large sample sizes to maintain statistical power and ensured sufficient group sizes were maintained throughout the study. However, some animals were lost due to euthanasia and found dead cases which was not uncommon. Finally, this dissertation revealed that mice can be an effective and valuable early model for AAV-induced DRG toxicity.

Limitations of this thesis

These studies offer early and exploratory investigation into DRG toxicity in mice with several limitations. All the studies conducted in this thesis utilized free hand bolus injections into the CSF space as opposed to the slow infusion in other studies. Bolus injections lead to peripheral leakage which could increase exposure to sensory neurons and peripheral nerves increasing the risk and severity of DRG toxicity. Moreover, the severity of DRG toxicity is associated with the transgene used in the capsid (Hordeaux, Buza, Dyer, et al., 2020). The focus of this thesis was mainly one specific type of transgene, the duplex artificial microRNA, which is not represented of all types of transgenes designs. The studies did not provide comparisons to safer duplex artificial microRNA transgenes. Moreover, single nucleus RNA sequencing captured the transcriptomic profile of the different cell types. However, it is important to note that cytoplasmic RNA was not captured and a single cell approach would be needed to alleviate this challenge. Another limitation for the sequencing study is the focus on the 6 weeks post-

injection timepoint only. Based on Hawley's and colleagues', 13 weeks post-injection also represent significant transcriptomic findings where were not investigated in this thesis (Hawley et al., 2024). Neuronal representation in the dataset was ~11% while fibroblasts represented ~33%. This limited capturing the transcriptomic profile of neurons. Lastly, some mice were unfortunately euthanized or found dead at key timepoints in the physiology and behavior which weakened the study in addition to the unknown studies and the cause of death was not investigated in these studies.

Future directions

The next step aim to elucidate which components are critical in driving DRG injury. The use of AAV9 provides efficient transduction of sensory neurons, however, prior studies have shown that toxicity is transgene driven. Key components such as the promoter sequence play a pivotal role in driving toxicity. The use of strong ubiquitous promoters as in AAV-miR-SOD1 enables, CAGG, enable high expression which have shown to be toxic in prior studies in mice and NHPs (Alstyne et al., 2021; Hordeaux, Buza, Jeffrey, et al., 2020). It would be beneficial to determine if weaker to moderate promoters such as UBC and PGK would circumvent overexpression and molecular pathology (C. Chen et al., 2011). Also, employing different expression cassette designs (i.e. empty capsid controls, transcriptional null, non-protein coding cassette and protein coding cassette) would provide a more comprehensive study design of different types of AAV transgenes. Certainly, future sequencing studies should examine long-term time points such as 12- or 18-weeks post-injection.

An alternative approach involves utilizing recently identified neurotropic capsids that are designed to avoid targeting the DRG, aiming to assess their potential effectiveness in reducing or eliminating DRG toxicity (Stanton et al., 2023). Furthermore, intrathecal dosing in all studies in this thesis was a single bolus injection which could contribute to large standard deviation in

the severity of toxicity in mice. A slow infusion of AVV could potentially eliminate/reduce this observation and also lower the severity of toxicity (Rahman et al., 2023).

Another avenue for further research is to utilize the current large dataset generated to discover potential AAV DRG toxicity biomarker gene(s). This would be achieved be identifying specific gene(s) that closely correlated with serum NfL levels. The expression of many genes was found to be upregulated/downregulated especially in activated satellite glia cluster. Therefore, the focus would be on highly altered processes that were noted such as neurogenesis, axonal guidance, neurodevelopment. This could also be followed with proteomic analysis in the DRG, CSF and serum to see if a specific biomarker protein could be identified. Ultimately, relying solely on NfL would potentially not be adequate in clinical settings due to disease progression in a patient serving as a confounding factor.

Young mice may exhibit greater resistance to DRG toxicity compared to older or adult mice. An NHP meta-analysis study has showed that infant and juvenile NHPs showed a lower degree of pathology relative to adult NHPs (Hordeaux, Buza, Jeffrey, et al., 2020). It would be beneficial to investigate DRG toxicity in older mice compared to young mice. The regenerative capacity of young mice is greater than older mice (Cai et al., 2023). This may play a factor in the severity AAV-induced DRG lesions in mice.

Lastly, what is the contribution of innate and adaptive immune responses in the progression and aggravation of DRG toxicity in mice? Many innate immune response drugs such as Eculizumab (C5 inhibitor), hydroxychloroquine (TLR inhibitors) and other immunosuppressants such as Rapamycin/Sirolimus are effective in preventing adaptive immunity and inflammation (T. Yang et al., 2022). In a clinical study, Mueller and colleagues showed that the administration of immunosuppressants to limit B cell and T cell function with Rituximab and Rapamycin/Sirolimus likely alleviated DRG toxicity following the

administration of AAV9-artifical microRNA targeting the human SOD1 gene (Mueller et al., 2020). Glucocorticoids such as methylprednisolone and prednisolone were also used, and the dosing regimen varied for these immunosuppressants.

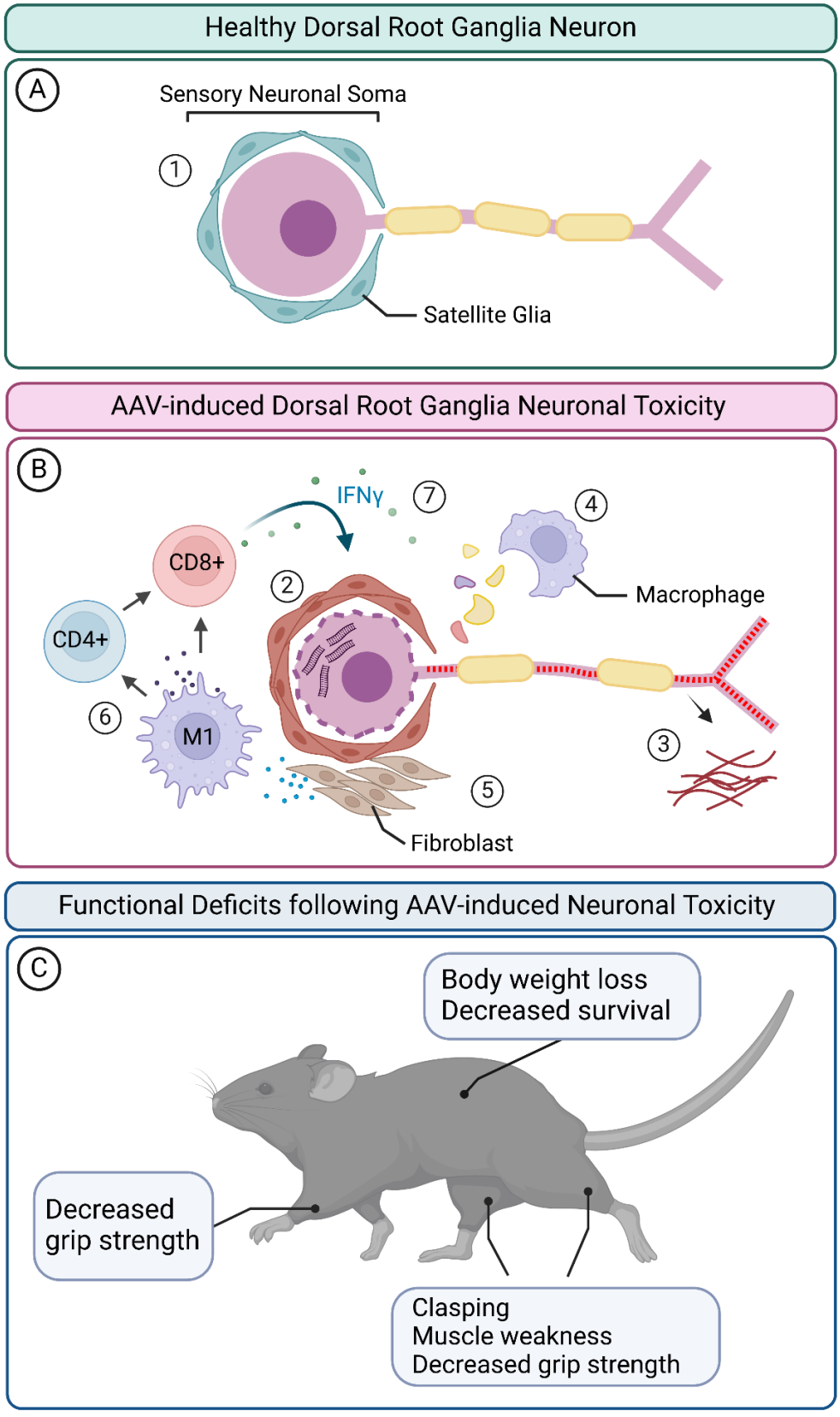
Healthy Dorsal Root Ganglia Neuron
A
Sensory Neuronal Soma
1
Satellite Glia
AAV-induced Dorsal Root Ganglia Neuronal Toxicity
B
IFNγ
7
4
CD8+
2
Macrophage
CD4+
6
M1
3
5
Fibroblast
Functional Deficits following AAV-induced Neuronal Toxicity
C
Body weight loss
Decreased survival
Decreased
grip strength
Clasping
Muscle weakness
Decreased grip strength

Figure 1: A summary of molecular and phenotypic findings following AAV-induced dorsal root ganglia toxicity in C57BL/6J mice. **A.** Healthy neuron. [1] Each sensory neuron is enveloped by supporting satellite glial cells. **B.** AAV-induced neuronal degeneration. [2] Highly transduced and degenerating neuron with accumulation of transgene product. Proliferation and activation of satellite glia in response to neuronal injury and degeneration. [3] Axonal degeneration and neurofilament light release into the CSF and serum. [4] Macrophage engulfing cell debris and myelin in response to Schwann cell loss. [5] Fibroblast proliferation and release of cytokines and chemokines. [6] Proliferation of pro-inflammatory macrophages (M1), release of cytokines & chemokines and induction of the adaptive immune response. [7] Potential cell mediated destruction of infected neuron. Further research is required to elucidate the order of these events and uncovering the detailed mechanism of how this occurs . **C.** Behavioral and physiological alterations following sensory neuron degeneration. The Illustration was generated by BioRender.com.

Bibliography

Adidharma, W., Khouri, A. N., Lee, J. C., Vanderboll, K., Kung, T. A., Cederna, P. S., & Kemp, S. W. P. (2022). Sensory nerve regeneration and reinnervation in muscle following peripheral nerve injury. *Muscle & Nerve*, *66*(4), 384–396. https://doi.org/10.1002/mus.27661

Airaksinen, M. S., & Saarma, M. (2002). The GDNF family: Signalling, biological functions and therapeutic value. *Nature Reviews Neuroscience*, *3*(5), 383–394. https://doi.org/10.1038/nrn812

Alstyne, M. V., Tattoli, I., Delestrée, N., Recinos, Y., Workman, E., Shihabuddin, L. S., Zhang, C., Mentis, G. Z., & Pellizzoni, L. (2021). Gain of toxic function by long-term AAV9-mediated SMN overexpression in the sensorimotor circuit. *Nature Neuroscience*, *24*(7), 930–940. https://doi.org/10.1038/s41593-021-00827-3

Amini, M., Ma, C., Farazifard, R., Zhu, G., Zhang, Y., Vanderluit, J., Zoltewicz, J. S., Hage, F., Savitt, J. M., Lagace, D. C., Slack, R. S., Beique, J.-C., Baudry, M., Greer, P. A., Bergeron, R., & Park, D. S. (2013). Conditional Disruption of Calpain in the CNS Alters Dendrite Morphology, Impairs LTP, and Promotes Neuronal Survival following Injury. *Journal of Neuroscience*, *33*(13), 5773–5784. https://doi.org/10.1523/JNEUROSCI.4247-12.2013

Approved Cellular and Gene Therapy Products. (2024, April 26). FDA; FDA. https://www.fda.gov/vaccines-blood-biologics/cellular-gene-therapy-products/approved-cellular-and-gene-therapy-products

Arjomandnejad, M., Dasgupta, I., Flotte, T. R., & Keeler, A. M. (2023). Immunogenicity of Recombinant Adeno-Associated Virus (AAV) Vectors for Gene Transfer. *BioDrugs*, *37*(3), 311–329. https://doi.org/10.1007/s40259-023-00585-7

Arjomandnejad, M., Sylvia, K., Blackwood, M., Nixon, T., Tang, Q., Muhuri, M., Gruntman, A. M., Gao, G., Flotte, T. R., & Keeler, A. M. (2021). Modulating immune responses to AAV by expanded polyclonal T-regs and capsid specific chimeric antigen receptor T-regulatory cells. *Molecular Therapy - Methods & Clinical Development*, *23*, 490–506. https://doi.org/10.1016/j.omtm.2021.10.010

Au, H. K. E., Isalan, M., & Mielcarek, M. (2022). Gene Therapy Advances: A Meta-Analysis of AAV Usage in Clinical Settings. *Frontiers in Medicine*, *8*. https://www.frontiersin.org/articles/10.3389/fmed.2021.809118

Barrette, B., Calvo, E., Vallières, N., & Lacroix, S. (2010). Transcriptional profiling of the injured sciatic nerve of mice carrying the Wld(S) mutant gene: Identification of genes involved in neuroprotection, neuroinflammation, and nerve regeneration. *Brain, Behavior, and Immunity*, *24*(8), 1254–1267. https://doi.org/10.1016/j.bbi.2010.07.249

Barry, A. M., Zhao, N., Yang, X., Bennett, D. L., & Baskozos, G. (2023). Deep RNA-seq of male and female murine sensory neuron subtypes after nerve injury. *PAIN*, *164*(10), 2196. https://doi.org/10.1097/j.pain.0000000000002934

Bharucha-Goebel, Todd Joshua J., Saade Dimah, Norato Gina, Jain Minal, Lehky Tanya, Bailey Rachel M., Chichester Jessica A., Calcedo Roberto, Armao Diane, Foley A. Reghan, Mohassel Payam, Tesfaye Eshetu, Carlin Bradley P., Seremula Beth, Waite Melissa, Zein Wadih M., Huryn Laryssa A., Crawford Thomas O., … Bönnemann Carsten G. (2024). Intrathecal Gene Therapy for Giant Axonal Neuropathy. *New England Journal of Medicine*, *390*(12), 1092–1104. https://doi.org/10.1056/NEJMoa2307952

Bhuiyan, S. A., Xu, M., Yang, L., Semizoglou, E., Bhatia, P., Pantaleo, K. I., Tochitsky, I., Jain, A., Erdogan, B., Blair, S., Cat, V., Mwirigi, J. M., Sankaranarayanan, I., Tavares-Ferreira, D., Green, U., McIlvried, L. A., Copits, B. A., Bertels, Z., Del Rosario, J. S.,

… Renthal, W. (2024). Harmonized cross-species cell atlases of trigeminal and dorsal root ganglia. *Science Advances*, *10*(25), eadj9173. https://doi.org/10.1126/sciadv.adj9173

Blaese, R. M., Culver, K. W., Miller, A. D., Carter, C. S., Fleisher, T., Clerici, M., Shearer, G., Chang, L., Chiang, Y., Tolstoshev, P., Greenblatt, J. J., Rosenberg, S. A., Klein, H., Berger, M., Mullen, C. A., Ramsey, W. J., Muul, L., Morgan, R. A., & Anderson, W. F. (1995). T Lymphocyte-Directed Gene Therapy for ADA− SCID: Initial Trial Results After 4 Years. *Science*, *270*(5235), 475–480. https://doi.org/10.1126/science.270.5235.475

Bogdanik, L. P., Osborne, M. A., Davis, C., Martin, W. P., Austin, A., Rigo, F., Bennett, C. F., & Lutz, C. M. (2015). Systemic, postsymptomatic antisense oligonucleotide rescues motor unit maturation delay in a new mouse model for type II/III spinal muscular atrophy. *Proceedings of the National Academy of Sciences*, *112*(43), E5863–E5872. https://doi.org/10.1073/pnas.1509758112

Bolt, M., JT, B., LO, W., & KN, K. (2021). Development challenges associated with rAAV-based gene therapies. *The Journal of Toxicological Sciences*, *46*(2), 57–68. https://doi.org/10.2131/JTS.46.57

Bryant, D. H., Bashir, A., Sinai, S., Jain, N. K., Ogden, P. J., Riley, P. F., Church, G. M., Colwell, L. J., & Kelsic, E. D. (2021). Deep diversification of an AAV capsid protein by machine learning. *Nature Biotechnology*, *39*(6), 691–696. https://doi.org/10.1038/s41587-020-00793-4

Bulcha, J. T., Wang, Y., Ma, H., Tai, P. W. L., & Gao, G. (2021). Viral vector platforms within the gene therapy landscape. *Signal Transduction and Targeted Therapy*, *6*(1), 53. https://doi.org/10.1038/s41392-021-00487-6

Burmistrz, M., Krakowski, K., & Krawczyk-Balska, A. (2020). RNA-Targeting CRISPR–Cas Systems and Their Applications. *International Journal of Molecular Sciences*, *21*(3), 1122. https://doi.org/10.3390/ijms21031122

Büttner, R., Schulz, A., Reuter, M., Akula, A. K., Mindos, T., Carlstedt, A., Riecken, L. B., Baader, S. L., Bauer, R., & Morrison, H. (2018). Inflammaging impairs peripheral nerve maintenance and regeneration. *Aging Cell*, *17*(6), e12833. https://doi.org/10.1111/acel.12833

Cahill, L. S., Zhang, M. A., Ramaglia, V., Whetstone, H., Sabbagh, M. P., Yi, T. J., Woo, L., Przybycien, T. S., Moshkova, M., Zhao, F. L., Rojas, O. L., Gomes, J., Kuerten, S., Gommerman, J. L., Sled, J. G., & Dunn, S. E. (2019). Aged hind-limb clasping experimental autoimmune encephalomyelitis models aspects of the neurodegenerative process seen in multiple sclerosis. *Proceedings of the National Academy of Sciences*, *116*(45), 22710–22720. https://doi.org/10.1073/pnas.1915141116

Cai, Y., Xiong, M., Xin, Z., Liu, C., Ren, J., Yang, X., Lei, J., Li, W., Liu, F., Chu, Q., Zhang, Y., Yin, J., Ye, Y., Liu, D., Fan, Y., Sun, S., Jing, Y., Zhao, Q., Zhao, L., … Liu, G.-H. (2023). Decoding aging-dependent regenerative decline across tissues at single-cell resolution. *Cell Stem Cell*, *30*(12), 1674-1691.e8. https://doi.org/10.1016/j.stem.2023.09.014

Cargnin, F., Nechiporuk, T., Müllendorff, K., Stumpo, D. J., Blackshear, P. J., Ballas, N., & Mandel, G. (2014). An RNA Binding Protein Promotes Axonal Integrity in Peripheral Neurons by Destabilizing REST. *Journal of Neuroscience*, *34*(50), 16650–16661. https://doi.org/10.1523/JNEUROSCI.1650-14.2014

Chand, D., Mohr, F., McMillan, H., Tukov, F. F., Montgomery, K., Kleyn, A., Sun, R., Tauscher-Wisniewski, S., Kaufmann, P., & Kullak-Ublick, G. (2021). Hepatotoxicity following administration of onasemnogene abeparvovec (AVXS-101) for the

treatment of spinal muscular atrophy. *Journal of Hepatology*, *74*(3), 560–566. https://doi.org/10.1016/j.jhep.2020.11.001

Chandran, J., Chowdhury, E. A., Perkinton, M., Jamier, T., Sutton, D., Wu, S., Dobson, C., Shah, D. K., Chessell, I., & Meno-Tetang, G. M. L. (2023). Assessment of AAV9 distribution and transduction in rats after administration through Intrastriatal, Intracisterna magna and Lumbar Intrathecal routes. *Gene Therapy*, *30*(1–2), 132–141. https://doi.org/10.1038/s41434-022-00346-1

Chen, C., Krohn, J., Bhattacharya, S., & Davies, B. (2011). A Comparison of Exogenous Promoter Activity at the ROSA26 Locus Using a PhiC31 Integrase Mediated Cassette Exchange Approach in Mouse ES Cells. *PLOS ONE*, *6*(8), e23376. https://doi.org/10.1371/journal.pone.0023376

Chen, P. J., & Liu, D. R. (2023). Prime editing for precise and highly versatile genome manipulation. *Nature Reviews Genetics*, *24*(3), 161–177. https://doi.org/10.1038/s41576-022-00541-1

Chen, S. K., Hawley, Z. C. E., Zavodszky, M. I., Hana, S., Ferretti, D., Grubor, B., Hawes, M., Xu, S., Hamann, S., Marsh, G., Cullen, P., Challa, R., Carlile, T. M., Zhang, H., Lee, W.-H., Peralta, A., Clarner, P., Wei, C., Koszka, K., … Lo, S.-C. (2023). Efficacy and safety of a SOD1-targeting artificial miRNA delivered by AAV9 in mice are impacted by miRNA scaffold selection. *Molecular Therapy - Nucleic Acids*, *34*. https://doi.org/10.1016/j.omtn.2023.102057

Chen, X., Dong, T., Hu, Y., Shaffo, F. C., Belur, N. R., Mazzulli, J. R., & Gray, S. J. (2022). AAV9/MFSD8 gene therapy is effective in preclinical models of neuronal ceroid lipofuscinosis type 7 disease. *The Journal of Clinical Investigation*, *132*(5). https://doi.org/10.1172/JCI146286

Chen, X.-Q., Fang, F., Florio, J. B., Rockenstein, E., Masliah, E., Mobley, W. C., Rissman, R. A., & Wu, C. (2018). T-complex protein 1-ring complex enhances retrograde axonal transport by modulating tau phosphorylation. *Traffic*, *19*(11), 840–853. https://doi.org/10.1111/tra.12610

Chen, Y. A., Kankel, M. W., Hana, S., Lau, S. K., Zavodszky, M. I., McKissick, O., Mastrangelo, N., Dion, J., Wang, B., Ferretti, D., Koske, D., Lehman, S., Koszka, K., McLaughlin, H., Liu, M., Marshall, E., Fabian, A. J., Cullen, P., Marsh, G., … Lo, S.-C. (2022). In vivo genome editing using novel AAV-PHP variants rescues motor function deficits and extends survival in a SOD1-ALS mouse model. *Gene Therapy*, 1–12. https://doi.org/10.1038/s41434-022-00375-w

Chen, Y.-J., Huang, Y.-A., Ho, C. T., Yang, J.-M., Chao, J.-I., Li, M.-C., & Hwang, E. (2021). A Nanodiamond-Based Surface Topography Downregulates the MicroRNA miR6236 to Enhance Neuronal Development and Regeneration. *ACS Applied Bio Materials*, *4*(1), 890–902. https://doi.org/10.1021/acsabm.0c01389

Chuah, M. K., Petrus, I., Bleser, P. D., Guiner, C. L., Gernoux, G., Adjali, O., Nair, N., Willems, J., Evens, H., Rincon, M. Y., Matrai, J., Matteo, M. D., Samara-Kuko, E., Yan, B., Acosta-Sanchez, A., Meliani, A., Cherel, G., Blouin, V., Christophe, O., … VandenDriessche, T. (2014). Liver-Specific Transcriptional Modules Identified by Genome-Wide In Silico Analysis Enable Efficient Gene Therapy in Mice and Non-Human Primates. *Molecular Therapy*, *22*(9), 1605–1613. https://doi.org/10.1038/mt.2014.114

Cintrón-Colón, A. F., Almeida-Alves, G., VanGyseghem, J. M., & Spitsbergen, J. M. (2021). GDNF to the rescue: GDNF delivery effects on motor neurons and nerves, and muscle re-innervation after peripheral nerve injuries. *Neural Regeneration Research*, *17*(4), 748–753. https://doi.org/10.4103/1673-5374.322446

Crawford, L. K., & Caterina, M. J. (2019). Functional Anatomy of the Sensory Nervous System: Updates From the Neuroscience Bench: *Https://Doi.Org/10.1177/0192623319869011*, *48*(1), 174–189. https://doi.org/10.1177/0192623319869011

Dabas, P., & Danda, A. (2023). Revolutionizing cancer treatment: A comprehensive review of CAR-T cell therapy. *Medical Oncology*, *40*(9), 275. https://doi.org/10.1007/s12032-023-02146-y

Das, G., Yu, Q., Hui, R., Reuhl, K., Gale, N. W., & Zhou, R. (2016). EphA5 and EphA6: Regulation of neuronal and spine morphology. *Cell & Bioscience*, *6*(1), 48. https://doi.org/10.1186/s13578-016-0115-5

Din, N. U., Tariq, M. U., & Pervez, S. (2020). Histopathology of Bone and Soft Tissue. In S. Pervez (Ed.), *Atlas of Diagnostic and Predictive Histopathology* (pp. 33–81). Springer. https://doi.org/10.1007/978-981-15-1220-9_2

Disorders, F. on N. and N. S., Policy, B. on H. S., & Medicine, I. of. (2013). Protein Aggregation. In *Neurodegeneration: Exploring Commonalities Across Diseases: Workshop Summary*. National Academies Press (US). https://www.ncbi.nlm.nih.gov/books/NBK208522/

Edfawy, M., Guedes, J. R., Pereira, M. I., Laranjo, M., Carvalho, M. J., Gao, X., Ferreira, P. A., Caldeira, G., Franco, L. O., Wang, D., Cardoso, A. L., Feng, G., Carvalho, A. L., & Peça, J. (2019). Abnormal mGluR-mediated synaptic plasticity and autism-like behaviours in Gprasp2 mutant mice. *Nature Communications*, *10*(1), 1431. https://doi.org/10.1038/s41467-019-09382-9

Eisenberg, C., Subramanian, D., Afrasiabi, M., Ziobro, P., DeLucia, J., Hirschberg, P. R., Shiflett, M. W., Santhakumar, V., & Tran, T. S. (2021). Reduced hippocampal inhibition and enhanced autism-epilepsy comorbidity in mice lacking neuropilin 2. *Translational Psychiatry*, *11*(1), 1–12. https://doi.org/10.1038/s41398-021-01655-6

Ertl, H. C. J. (2023). Mitigating Serious Adverse Events in Gene Therapy with AAV Vectors: Vector Dose and Immunosuppression. *Drugs*. https://doi.org/10.1007/s40265-023-01836-1

Fader, K. A., Pardo, I. D., Kovi, R. C., Somps, C. J., Wang, H. H., Vaidya, V. S., Ramaiah, S. K., & Sirivelu, M. P. (2022). Circulating neurofilament light chain as a promising biomarker of AAV-induced dorsal root ganglia toxicity in nonclinical toxicology species. *Molecular Therapy - Methods & Clinical Development*, *25*, 264–277. https://doi.org/10.1016/j.omtm.2022.03.017

Farrar, M. A., Groen, E., & Alves, C. R. R. (2022). Circulating neurofilaments to track dorsal root ganglion toxicity risks with AAV-mediated gene therapy. *Molecular Therapy Methods & Clinical Development*, *26*, 96–97. https://doi.org/10.1016/j.omtm.2022.06.005

Flanders, M. (2011). What is the biological basis of sensorimotor integration? *Biological Cybernetics*, *104*(1–2), 1–8. https://doi.org/10.1007/s00422-011-0419-9

Fleming, S. J., Chaffin, M. D., Arduini, A., Akkad, A.-D., Banks, E., Marioni, J. C., Philippakis, A. A., Ellinor, P. T., & Babadi, M. (2023). Unsupervised removal of systematic background noise from droplet-based single-cell experiments using CellBender. *Nature Methods*, *20*(9), 1323–1335. https://doi.org/10.1038/s41592-023-01943-7

Fumagalli, F., Calbi, V., Mattia, F. D., Zambon, A., Gallo, V., Recupero, S., Fratini, E. S., Ippolito, A., Ciotti, F., Fraschini, M., Sarzana, M., Scarparo, S., Montini, E., Locatelli, S., Facchini, M., Clerici, A., Morena, F., Martino, S., Yarzi, M., … Aiuti, A. (2024). P005: Atidarsagene autotemcel (hematopoietic stem cell–gene therapy) preserves cognitive and motor development in metachromatic leukodystrophy with up to 12

years follow-up*. *Genetics in Medicine Open*, *2*. https://doi.org/10.1016/j.gimo.2024.100882

Gaiani, A., Martinelli, I., Bello, L., Querin, G., Puthenparampil, M., Ruggero, S., Toffanin, E., Cagnin, A., Briani, C., Pegoraro, E., & Sorarù, G. (2017). Diagnostic and Prognostic Biomarkers in Amyotrophic Lateral Sclerosis: Neurofilament Light Chain Levels in Definite Subtypes of Disease. *JAMA Neurology*, *74*(5), 525–532. https://doi.org/10.1001/jamaneurol.2016.5398

Gao, B., Zhu, J., Negi, S., Zhang, X., Gyoneva, S., Casey, F., Wei, R., & Zhang, B. (2021). Quickomics: Exploring omics data in an intuitive, interactive and informative manner. *Bioinformatics*, *37*(20), 3670–3672. https://doi.org/10.1093/bioinformatics/btab255

Gao, J., Gunasekar, S., Xia, Z. (Judy), Shalin, K., Jiang, C., Chen, H., Lee, D., Lee, S., Pisal, N. D., Luo, J. N., Griciuc, A., Karp, J. M., Tanzi, R., & Joshi, N. (2024). Gene therapy for CNS disorders: Modalities, delivery and translational challenges. *Nature Reviews Neuroscience*, *25*(8), 553–572. https://doi.org/10.1038/s41583-024-00829-7

Garcia, A. L., Udeh, A., Kalahasty, K., & Hackam, A. S. (2018). A growing field: The regulation of axonal regeneration by Wnt signaling. *Neural Regeneration Research*, *13*(1), 43. https://doi.org/10.4103/1673-5374.224359

Ge, S. X., Jung, D., & Yao, R. (2020). ShinyGO: A graphical gene-set enrichment tool for animals and plants. *Bioinformatics*, *36*(8), 2628–2629. https://doi.org/10.1093/bioinformatics/btz931

Gong, Y., Berenson, A., Laheji, F., Gao, G., Wang, D., Ng, C., Volak, A., Kok, R., Kreouzis, V., Dijkstra, I. M., Kemp, S., Maguire, C. A., & Eichler, F. (2019). Intrathecal Adeno-Associated Viral Vector-Mediated Gene Delivery for Adrenomyeloneuropathy. *Human Gene Therapy*, *30*(5), 544–555. https://doi.org/10.1089/hum.2018.079

Guide, S. V., Gonzalez, M. E., Bağcı, I. S., Agostini, B., Chen, H., Feeney, G., Steimer, M., Kapadia, B., Sridhar, K., Sanchez, L. Q., Gonzalez, F., Ligten, M. V., Parry, T. J., Chitra, S., Kammerman, L. A., Krishnan, S., & Marinkovich, M. P. (2022). Trial of Beremagene Geperpavec (B-VEC) for Dystrophic Epidermolysis Bullosa. *New England Journal of Medicine*, *387*(24), 2211–2219. https://doi.org/10.1056/NEJMoa2206663

Guo, Y., Chen, J., Ji, W., Xu, L., Xie, Y., He, S., Lai, C., Hou, K., Li, Z., Chen, G., & Wu, Z. (2023). High-titer AAV disrupts cerebrovascular integrity and induces lymphocyte infiltration in adult mouse brain. *Molecular Therapy Methods & Clinical Development*, *31*. https://doi.org/10.1016/j.omtm.2023.08.021

Haberberger, R. V., Barry, C., Dominguez, N., & Matusica, D. (2019). Human Dorsal Root Ganglia. *Frontiers in Cellular Neuroscience*, *13*. https://www.frontiersin.org/articles/10.3389/fncel.2019.00271

Hanani, M., & Verkhratsky, A. (2021). Satellite Glial Cells and Astrocytes, a Comparative Review. *Neurochemical Research*, *46*(10), 2525–2537. https://doi.org/10.1007/s11064-021-03255-8

Hart, C. C., Lee, Y. il, Xie, J., Gao, G., Lin, B. L., Hammers, D. W., & Sweeney, H. L. (2024). Potential limitations of microdystrophin gene therapy for Duchenne muscular dystrophy. *JCI Insight*, *9*(11). https://doi.org/10.1172/jci.insight.165869

Hawley, Z. C. E., Pardo, I. D., Cao, S., Zavodszky, M. I., Casey, F., Ferber, K., Luo, Y., Hana, S., Chen, S. K., Doherty, J., Costa, R., Cullen, P., Liu, Y., Carlile, T. M., Chowdhury, T., Doyle, B., Clarner, P., Mangaudis, K., Guilmette, E., … Lo, S.-C. (2024). Dorsal root ganglion toxicity after AAV intra-CSF delivery of a RNAi expression construct into nonhuman primates and mice. *Molecular Therapy*, *0*(0). https://doi.org/10.1016/j.ymthe.2024.11.029

He, L., Davila-Velderrain, J., Sumida, T. S., Hafler, D. A., Kellis, M., & Kulminski, A. M. (2021). NEBULA is a fast negative binomial mixed model for differential or co-expression analysis of large-scale multi-subject single-cell data. *Communications Biology*, *4*(1), 1–17. https://doi.org/10.1038/s42003-021-02146-6

Hinderer, C., Katz, N., Buza, E. L., Dyer, C., Goode, T., Bell, P., Richman, L. K., & Wilson, J. M. (2018). Severe Toxicity in Nonhuman Primates and Piglets Following High-Dose Intravenous Administration of an Adeno-Associated Virus Vector Expressing Human SMN. *Human Gene Therapy*, *29*. https://doi.org/10.1089/hum.2018.015

Hoffman, W. P. (2002). Analysis of Rodent Growth Data in Toxicology Studies. *Toxicological Sciences*, *66*(2), 313–319. https://doi.org/10.1093/toxsci/66.2.313

Hordeaux, J., Buza, E. L., Dyer, C., Goode, T., Mitchell, T. W., Richman, L., Denton, N., Hinderer, C., Katz, N., Schmid, R., Miller, R., Choudhury, G. R., Horiuchi, M., Nambiar, K., Yan, H., Li, M., & Wilson, J. M. (2020). Adeno-Associated Virus-Induced Dorsal Root Ganglion Pathology. *Human Gene Therapy*, *31*(15–16), 808–818. https://doi.org/10.1089/hum.2020.167

Hordeaux, J., Buza, E. L., Jeffrey, B., Song, C., Jahan, T., Yuan, Y., Zhu, Y., Bell, P., Li, M., Chichester, J. A., Calcedo, R., & Wilson, J. M. (2020). MicroRNA-mediated inhibition of transgene expression reduces dorsal root ganglion toxicity by AAV vectors in primates. *Sci. Transl. Med*, *12*(569), 9188. https://doi.org/10.1126/scitranslmed.aba9188

Hordeaux, J., Hinderer, C., Goode, T., Katz, N., Buza, E. L., Bell, P., Calcedo, R., Richman, L. K., & Wilson, J. M. (2018). Toxicology Study of Intra-Cisterna Magna Adeno-Associated Virus 9 Expressing Human Alpha-L-Iduronidase in Rhesus Macaques. *Molecular Therapy - Methods and Clinical Development*, *10*(September), 79–88. https://doi.org/10.1016/j.omtm.2018.06.003

Horie, T., & Ono, K. (2024). VERVE-101: A promising CRISPR-based gene editing therapy that reduces LDL-C and PCSK9 levels in HeFH patients. *European Heart Journal - Cardiovascular Pharmacotherapy*, *10*(2), 89–90. https://doi.org/10.1093/ehjcvp/pvad103

Hsu, H.-L., Brown, A., Loveland, A. B., Lotun, A., Xu, M., Luo, L., Xu, G., Li, J., Ren, L., Su, Q., Gessler, D. J., Wei, Y., Tai, P. W. L., Korostelev, A. A., & Gao, G. (2020). Structural characterization of a novel human adeno-associated virus capsid with neurotropic properties. *Nature Communications*, *11*(1), 3279. https://doi.org/10.1038/s41467-020-17047-1

Hu, G., Huang, K., Hu, Y., Du, G., Xue, Z., Zhu, X., & Fan, G. (2016). Single-cell RNA-seq reveals distinct injury responses in different types of DRG sensory neurons. *Scientific Reports*, *6*(1), 31851. https://doi.org/10.1038/srep31851

Hu, R., Dun, X., Singh, L., & Banton, M. C. (2024). Runx2 regulates peripheral nerve regeneration to promote Schwann cell migration and re-myelination. *Neural Regeneration Research*, *19*(7), 1575. https://doi.org/10.4103/1673-5374.387977

Huang, Q., Chan, K. Y., Wu, J., Botticello-Romero, N. R., Zheng, Q., Lou, S., Keyes, C., Svanbergsson, A., Johnston, J., Mills, A., Lin, C.-Y., Brauer, P. P., Clouse, G., Pacouret, S., Harvey, J. W., Beddow, T., Hurley, J. K., Tobey, I. G., Powell, M., … Deverman, B. E. (2024). An AAV capsid reprogrammed to bind human transferrin receptor mediates brain-wide gene delivery. *Science*, *384*(6701), 1220–1227. https://doi.org/10.1126/science.adm8386

Hudry, E., & Vandenberghe, L. H. (2019). Therapeutic AAV Gene Transfer to the Nervous System: A Clinical Reality. *Neuron*, *101*(5), 839–862. https://doi.org/10.1016/j.neuron.2019.02.017

Hutter-Saunders, J. A. L., Gendelman, H. E., & Mosley, R. L. (2012). Murine Motor and Behavior Functional Evaluations for Acute 1-Methyl-4-Phenyl-1,2,3,6-Tetrahydropyridine (MPTP) Intoxication. *Journal of Neuroimmune Pharmacology*, *7*(1), 279–288. https://doi.org/10.1007/s11481-011-9269-4

Hwang, J., & Namgung, U. (2021). Phosphorylation of STAT3 by axonal Cdk5 promotes axonal regeneration by modulating mitochondrial activity. *Experimental Neurology*, *335*, 113511. https://doi.org/10.1016/j.expneurol.2020.113511

Hwu, P. W., Kiening, K., Anselm, I., Compton, D. R., Nakajima, T., Opladen, T., Pearl, P. L., Roubertie, A., Roujeau, T., & Muramatsu, S. (2021). Gene therapy in the putamen for curing AADC deficiency and Parkinson's disease. *EMBO Molecular Medicine*, *13*(9), e14712. https://doi.org/10.15252/emmm.202114712

Irving, A. T., Zhang, Q., Kong, P.-S., Luko, K., Rozario, P., Wen, M., Zhu, F., Zhou, P., Ng, J. H. J., Sobota, R. M., & Wang, L.-F. (2020). Interferon Regulatory Factors IRF1 and IRF7 Directly Regulate Gene Expression in Bats in Response to Viral Infection. *Cell Reports*, *33*(5), 108345. https://doi.org/10.1016/j.celrep.2020.108345

Jay, T. R., von Saucken, V. E., & Landreth, G. E. (2017). TREM2 in Neurodegenerative Diseases. *Molecular Neurodegeneration*, *12*(1), 56. https://doi.org/10.1186/s13024-017-0197-5

Johnson, E. W., Sutherland, J. J., Meseck, E., McElroy, C., Chand, D. H., Tukov, F. F., Hudry, E., & Penraat, K. (2023). Neurofilament light chain and dorsal root ganglia injury after adeno-associated virus 9 gene therapy in nonhuman primates. *Molecular Therapy - Methods & Clinical Development*, *28*, 208–219. https://doi.org/10.1016/j.omtm.2022.12.012

Jung, M., Dourado, M., Maksymetz, J., Jacobson, A., Laufer, B. I., Baca, M., Foreman, O., Hackos, D. H., Riol-Blanco, L., & Kaminker, J. S. (2023). Cross-species transcriptomic atlas of dorsal root ganglia reveals species-specific programs for sensory function. *Nature Communications*, *14*(1), Article 1. https://doi.org/10.1038/s41467-023-36014-0

Junghans, D., & Herzog, S. (2018). Cnn3 regulates neural tube morphogenesis and neuronal stem cell properties. *The FEBS Journal*, *285*(2), 325–338. https://doi.org/10.1111/febs.14338

Kaas, J. H. (2012). Chapter 30—Somatosensory System. In J. K. Mai & G. Paxinos (Eds.), *The Human Nervous System (Third Edition)* (pp. 1074–1109). Academic Press. https://doi.org/10.1016/B978-0-12-374236-0.10030-6

Kalinski, A. L., Yoon, C., Huffman, L. D., Duncker, P. C., Kohen, R., Passino, R., Hafner, H., Johnson, C., Kawaguchi, R., Carbajal, K. S., Jara, J. S., Hollis, E., Geschwind, D. H., Segal, B. M., & Giger, R. J. (2020). Analysis of the immune response to sciatic nerve injury identifies efferocytosis as a key mechanism of nerve debridement. *eLife*, *9*, e60223. https://doi.org/10.7554/eLife.60223

Keiser, M. S., Ranum, P. T., Yrigollen, C. M., Carrell, E. M., Smith, G. R., Muehlmatt, A. L., Chen, Y. H., Stein, J. M., Wolf, R. L., Radaelli, E., Lucas, T. J., Gonzalez-Alegre, P., & Davidson, B. L. (2021). Toxicity after AAV delivery of RNAi expression constructs into nonhuman primate brain. *Nature Medicine 2021 27:11*, *27*(11), 1982–1989. https://doi.org/10.1038/s41591-021-01522-3

Kröger, S., & Watkins, B. (2021). Muscle spindle function in healthy and diseased muscle. *Skeletal Muscle*, *11*(1), 3. https://doi.org/10.1186/s13395-020-00258-x

Kumar, S. R. P., Biswas, M., Cao, D., Arisa, S., Muñoz-Melero, M., Lam, A. K., Piñeros, A. R., Kapur, R., Kaisho, T., Kaufman, R. J., Xiao, W., Shayakhmetov, D. M., Terhorst, C., de Jong, Y. P., & Herzog, R. W. (2024). TLR9-independent CD8+ T cell responses

in hepatic AAV gene transfer through IL-1R1-MyD88 signaling. *Molecular Therapy*, *32*(2), 325–339. https://doi.org/10.1016/j.ymthe.2023.11.029

Kuzmin, D. A., Shutova, M. V., Johnston, N. R., Smith, O. P., Fedorin, V. V., Kukushkin, Y. S., van der Loo, J. C. M., & Johnstone, E. C. (2021). The clinical landscape for AAV gene therapies. *Nature Reviews Drug Discovery*, *20*(3), 173–174. https://doi.org/10.1038/d41573-021-00017-7

Kwon, H. S., & Koh, S.-H. (2020). Neuroinflammation in neurodegenerative disorders: The roles of microglia and astrocytes. *Translational Neurodegeneration*, *9*(1), 42. https://doi.org/10.1186/s40035-020-00221-2

Lalonde, R., & Strazielle, C. (2011). Brain regions and genes affecting limb-clasping responses. *Brain Research Reviews*, *67*(1–2), 252–259. https://doi.org/10.1016/j.brainresrev.2011.02.005

Lamptey, R. N. L., Chaulagain, B., Trivedi, R., Gothwal, A., Layek, B., & Singh, J. (2022). A Review of the Common Neurodegenerative Disorders: Current Therapeutic Approaches and the Potential Role of Nanotherapeutics. *International Journal of Molecular Sciences*, *23*(3), Article 3. https://doi.org/10.3390/ijms23031851

Li, J., Geisbush, T. R., Arnold, W. D., Rosen, G. D., Zaworski, P. G., & Rutkove, S. B. (2014). A Comparison of Three Electrophysiological Methods for the Assessment of Disease Status in a Mild Spinal Muscular Atrophy Mouse Model. *PLOS ONE*, *9*(10), e111428. https://doi.org/10.1371/journal.pone.0111428

Li, K., Sun, Y. H., Ouyang, Z., Negi, S., Gao, Z., Zhu, J., Wang, W., Chen, Y., Piya, S., Hu, W., Zavodszky, M. I., Yalamanchili, H., Cao, S., Gehrke, A., Sheehan, M., Huh, D., Casey, F., Zhang, X., & Zhang, B. (2023). scRNASequest: An ecosystem of scRNA-seq analysis, visualization, and publishing. *BMC Genomics*, *24*(1), 228. https://doi.org/10.1186/s12864-023-09332-2

Li, Q., Chen, J., Chen, Y., Cong, X., & Chen, Z. (2016). Chronic sciatic nerve compression induces fibrosis in dorsal root ganglia. *Molecular Medicine Reports*, *13*(3), 2393–2400. https://doi.org/10.3892/mmr.2016.4810

Liang, H., Tang, L. Y., Ge, H. Y., Chen, M. M., Lu, S. Y., Zhang, H. X., Shen, C. L., Shen, Y., Fei, J., & Wang, Z. G. (2023). Neuronal survival factor TAFA2 suppresses apoptosis through binding to ADGRL1 and activating cAMP/PKA/CREB/BCL2 signaling pathway. *Life Sciences*, *334*, 122241. https://doi.org/10.1016/j.lfs.2023.122241

Lin, D., Chen, Y., Negi, S., Cheng, D., Ouyang, Z., Sexton, D., Li, K., & Zhang, B. (2022). CellDepot: A Unified Repository for scRNA-seq Data and Visual Exploration. *Journal of Molecular Biology*, *434*(11), 167425. https://doi.org/10.1016/j.jmb.2021.167425

Llorente, P., Martins, S., Sastre, I., Aldudo, J., Recuero, M., Adjaye, J., & Bullido, M. J. (2020). Matrix Metalloproteinase 14 Mediates APP Proteolysis and Lysosomal Alterations Induced by Oxidative Stress in Human Neuronal Cells. *Oxidative Medicine and Cellular Longevity*, *2020*, 5917187. https://doi.org/10.1155/2020/5917187

Locatelli, F., Thompson, A. A., Kwiatkowski, J. L., Porter, J. B., Thrasher, A. J., Hongeng, S., Sauer, M. G., Thuret, I., Lal, A., Algeri, M., Schneiderman, J., Olson, T. S., Carpenter, B., Amrolia, P. J., Anurathapan, U., Schambach, A., Chabannon, C., Schmidt, M., Labik, I., … Walters, M. C. (2022). Betibeglogene Autotemcel Gene Therapy for Non–β0/β0 Genotype β-Thalassemia. *New England Journal of Medicine*, *386*(5), 415–427. https://doi.org/10.1056/NEJMoa2113206

Locke, F. L., Miklos, D. B., Jacobson, C. A., Perales, M.-A., Kersten, M.-J., Oluwole, O. O., Ghobadi, A., Rapoport, A. P., McGuirk, J., Pagel, J. M., Muñoz, J., Farooq, U., Meerten, T. van, Reagan, P. M., Sureda, A., Flinn, I. W., Vandenberghe, P., Song, K.

W., Dickinson, M., … Westin, J. R. (2022). Axicabtagene Ciloleucel as Second-Line Therapy for Large B-Cell Lymphoma. *New England Journal of Medicine*, *386*(7), 640–654. https://doi.org/10.1056/NEJMoa2116133

Loeffler, T., Schilcher, I., Flunkert, S., & Hutter-Paier, B. (2020). Neurofilament-Light Chain as Biomarker of Neurodegenerative and Rare Diseases With High Translational Value. *Frontiers in Neuroscience*, *14*. https://doi.org/10.3389/fnins.2020.00579

Loughner, C. L., Bruford, E. A., Mcandrews, M. S., Delp, E. E., Swamynathan, S., & Swamynathan, S. K. (2016). Organization, evolution and functions of the human and mouse Ly6/uPAR family genes. *Human Genomics*, *10*(10), 1–19. https://doi.org/10.1186/s40246-016-0074-2

Luk, A., Xing, D., Liu, B., Liu, W., Zhang, S., Jiang, Y., Yao, X., Shi, L., Yang, H., Yuan, Y., & Li, X. (2024). World's First CRISPR/RNA-Targeting Therapy (HG202) for Patients with Neovascular Age-Related Macular Degeneration. *Investigative Ophthalmology & Visual Science*, *65*(7), 4357.

Markus-Koch, A., Schmitt, O., Seemann, S., Lukas, J., Koczan, D., Ernst, M., Fuellen, G., Wree, A., Rolfs, A., & Luo, J. (2017). ADAM23 promotes neuronal differentiation of human neural progenitor cells. *Cellular & Molecular Biology Letters*, *22*(1), 16. https://doi.org/10.1186/s11658-017-0045-1

Martins, K. M., Breton, C., Zheng, Q., Zhang, Z., Latshaw, C., Greig, J. A., & Wilson, J. M. (2023). Prevalent and Disseminated Recombinant and Wild-Type Adeno-Associated Virus Integration in Macaques and Humans. *Human Gene Therapy*, *34*(21–22), 1081–1094. https://doi.org/10.1089/hum.2023.134

Matson, K. J. E., Russ, D. E., Kathe, C., Hua, I., Maric, D., Ding, Y., Krynitsky, J., Pursley, R., Sathyamurthy, A., Squair, J. W., Levi, B. P., Courtine, G., & Levine, A. J. (2022). Single cell atlas of spinal cord injury in mice reveals a pro-regenerative signature in spinocerebellar neurons. *Nature Communications*, *13*(1), 5628. https://doi.org/10.1038/s41467-022-33184-1

McCampbell, A., Cole, T., Wegener, A. J., Tomassy, G. S., Setnicka, A., Farley, B. J., Schoch, K. M., Hoye, M. L., Shabsovich, M., Sun, L., Luo, Y., Zhang, M., Thankamony, S., Salzman, D. W., Cudkowicz, M., Graham, D. L., Bennett, C. F., Kordasiewicz, H. B., Swayze, E. E., & Miller, T. M. (2018). Antisense oligonucleotides extend survival and reverse decrement in muscle response in ALS models. *Journal of Clinical Investigation*, *128*(8), 3558–3567. https://doi.org/10.1172/JCI99081

McLean, J. R., Smith, G. A., Rocha, E. M., Hayes, M. A., Beagan, J. A., Hallett, P. J., & Isacson, O. (2014). Widespread neuron-specific transgene expression in brain and spinal cord following synapsin promoter-driven AAV9 neonatal intracerebroventricular injection. *Neuroscience Letters*, *576*, 73–78. https://doi.org/10.1016/j.neulet.2014.05.044

Meltzer, S., Santiago, C., Sharma, N., & Ginty, D. D. (2021). The cellular and molecular basis of somatosensory neuron development. *Neuron*, *109*(23), 3736–3757. https://doi.org/10.1016/j.neuron.2021.09.004

Meyers, E. A., & Kessler, J. A. (2017). TGF-β Family Signaling in Neural and Neuronal Differentiation, Development, and Function. *Cold Spring Harbor Perspectives in Biology*, *9*(8), a022244. https://doi.org/10.1101/cshperspect.a022244

Morgan, M., Schott, J. W., Rossi, A., Landgraf, C., Warnecke, A., Staecker, H., Lesinski-Schiedat, A., Schlegelberger, B., Büning, H., Auber, B., & Schambach, A. (2020). Gene therapy as a possible option to treat hereditary hearing loss. *Medizinische Genetik*, *32*(2), 149–159. https://doi.org/10.1515/medgen-2020-2021

Mouzannar, K., Schauer, A., & Liang, T. J. (2024). The Post-Transcriptional Regulatory Element of Hepatitis B Virus: From Discovery to Therapy. *Viruses*, *16*(4), Article 4. https://doi.org/10.3390/v16040528

Mueller, C., Berry, J. D., McKenna-Yasek, D. M., Gernoux, G., Owegi, M. A., Pothier, L. M., Douthwright, C. L., Gelevski, D., Luppino, S. D., Blackwood, M., Wightman, N. S., Oakley, D. H., Frosch, M. P., Flotte, T. R., Cudkowicz, M. E., & Brown, R. H. (2020). SOD1 Suppression with Adeno-Associated Virus and MicroRNA in Familial ALS. *New England Journal of Medicine*, *383*(2), 151–158. https://doi.org/10.1056/nejmoa2005056

Muhuri, M., Maeda, Y., Ma, H., Ram, S., Fitzgerald, K. A., Tai, P. W. L., & Gao, G. (2021). Overcoming innate immune barriers that impede AAV gene therapy vectors. *Journal of Clinical Investigation*, *131*(1). https://doi.org/10.1172/jci143780

Mullard, A. (2021). Gene therapy community grapples with toxicity issues, as pipeline matures. *Nature Reviews Drug Discovery*, *20*(11), 804–805. https://doi.org/10.1038/d41573-021-00164-x

Neurological disorders affect millions globally: WHO report. (n.d.). Retrieved December 2, 2024, from https://www.who.int/news/item/27-02-2007-neurological-disorders-affect-millions-globally-who-report

Nóbrega, C., Mendonça, L., & Matos, C. A. (2020). *A Handbook of Gene and Cell Therapy*. Springer International Publishing. https://doi.org/10.1007/978-3-030-41333-0

Palla, A. R., Ravichandran, M., Wang, Y. X., Alexandrova, L., Yang, A. V., Kraft, P., Holbrook, C. A., Schürch, C. M., Ho, A. T. V., & Blau, H. M. (2021). Inhibition of prostaglandin-degrading enzyme 15-PGDH rejuvenates aged muscle mass and strength. *Science*, *371*(6528), eabc8059. https://doi.org/10.1126/science.abc8059

Pane, M., Berti, B., Capasso, A., Coratti, G., Varone, A., D'Amico, A., Messina, S., Masson, R., Sansone, V. A., Donati, M. A., Agosto, C., Bruno, C., Ricci, F., Pini, A., Gagliardi, D., Filosto, M., Corti, S., Leone, D., Palermo, C., … D'Alessandro, R. (2023). Onasemnogene abeparvovec in spinal muscular atrophy: Predictors of efficacy and safety in naïve patients with spinal muscular atrophy and following switch from other therapies. *eClinicalMedicine*, *59*. https://doi.org/10.1016/j.eclinm.2023.101997

Patodia, S., & Raivich, G. (2012). Role of Transcription Factors in Peripheral Nerve Regeneration. *Frontiers in Molecular Neuroscience*, *5*, 1–15. https://doi.org/10.3389/fnmol.2012.00008

Patrício, M. I., Barnard, A. R., Orlans, H. O., McClements, M. E., & MacLaren, R. E. (2017). Inclusion of the Woodchuck Hepatitis Virus Posttranscriptional Regulatory Element Enhances AAV2-Driven Transduction of Mouse and Human Retina. *Molecular Therapy Nucleic Acids*, *6*, 198–208. https://doi.org/10.1016/j.omtn.2016.12.006

Paus, T. (2005). Mapping Brain Development and Aggression. *The Canadian Child and Adolescent Psychiatry Review*, *14*(1), 10–15.

Perera, A., Brock, O., Ahmed, A., Shaw, C., & Ashkan, K. (2024). Taking the knife to neurodegeneration: A review of surgical gene therapy delivery to the CNS. *Acta Neurochirurgica*, *166*(1), 136. https://doi.org/10.1007/s00701-024-06028-8

Perry, R. B.-T., Rishal, I., Doron-Mandel, E., Kalinski, A. L., Medzihradszky, K. F., Terenzio, M., Alber, S., Koley, S., Lin, A., Rozenbaum, M., Yudin, D., Sahoo, P. K., Gomes, C., Shinder, V., Geraisy, W., Huebner, E. A., Woolf, C. J., Yaron, A., Burlingame, A. L., … Fainzilber, M. (2016). Nucleolin-Mediated RNA Localization Regulates Neuron Growth and Cycling Cell Size. *Cell Reports*, *16*(6), 1664–1676. https://doi.org/10.1016/j.celrep.2016.07.005

Pitzer, C., Kurpiers, B., & Eltokhi, A. (2021). Gait performance of adolescent mice assessed by the CatWalk XT depends on age, strain and sex and correlates with speed and body weight. *Scientific Reports*, *11*(1), 21372. https://doi.org/10.1038/s41598-021-00625-8

Porto, E. M., Komor, A. C., Slaymaker, I. M., & Yeo, G. W. (2020). Base editing: Advances and therapeutic opportunities. *Nature Reviews Drug Discovery*, *19*(12), 839–859. https://doi.org/10.1038/s41573-020-0084-6

Qin, J. Y., Zhang, L., Clift, K. L., Hulur, I., Xiang, A. P., Ren, B. Z., & Lahn, B. T. (2010). Systematic comparison of constitutive promoters and the doxycycline-inducible promoter. *PLoS ONE*, *5*(5), 3–6. https://doi.org/10.1371/journal.pone.0010611

Rahman, Md., Lee, J., Kim, Y., & Park, C.-K. (2023). Epidural and Intrathecal Drug Delivery in Rats and Mice for Experimental Research: Fundamental Concepts, Techniques, Precaution, and Application. *Biomedicines*, *11*(5), 1413. https://doi.org/10.3390/biomedicines11051413

Ramírez-Barrantes, R., Cordova, C., Poblete, H., Muñoz, P., Marchant, I., Wianny, F., & Olivero, P. (2016). Perspectives of TRPV1 Function on the Neurogenesis and Neural Plasticity. *Neural Plasticity*, *2016*, 1–12. https://doi.org/10.1155/2016/1568145

Renthal, W., Tochitsky, I., Yang, L., Cheng, Y. C., Li, E., Kawaguchi, R., Geschwind, D. H., & Woolf, C. J. (2020). Transcriptional Reprogramming of Distinct Peripheral Sensory Neuron Subtypes after Axonal Injury. *Neuron*, *108*(1), 128-144.e9. https://doi.org/10.1016/j.neuron.2020.07.026

Riaz, M., Raz, Y., Moloney, E. B., Putten, M. van, Krom, Y. D., Maarel, S. M. van der, Verhaagen, J., & Raz, V. (2015). Differential myofiber-type transduction preference of adeno-associated virus serotypes 6 and 9. *Skeletal Muscle*, *5*(1), 1–10. https://doi.org/10.1186/s13395-015-0064-4

Rigaud, M., Gemes, G., Barabas, M.-E., Chernoff, D. I., Abram, S. E., Stucky, C. L., & Hogan, Q. H. (2008). Species and strain differences in rodent sciatic nerve anatomy: Implications for studies of neuropathic pain. *PAIN*, *136*(1), 188. https://doi.org/10.1016/j.pain.2008.01.016

Roseguini, B. T., Silva, L. M., Polotow, T. G., Barros, M. P., Souccar, C., & Han, S. W. (2015). Effects of N-acetylcysteine on skeletal muscle structure and function in a mouse model of peripheral arterial insufficiency. *Journal of Vascular Surgery*, *61*(3), 777–786. https://doi.org/10.1016/j.jvs.2013.10.098

Roussel-Gervais, A., Sgroi, S., Cambet, Y., Lemeille, S., Seredenina, T., Krause, K.-H., & Jaquet, V. (2023). Genetic knockout of NTRK2 by CRISPR/Cas9 decreases neurogenesis and favors glial progenitors during differentiation of neural progenitor stem cells. *Frontiers in Cellular Neuroscience*, *17*, 1–14. https://doi.org/10.3389/fncel.2023.1289966

Saade, M., Araujo de Souza, G., Scavone, C., & Kinoshita, P. F. (2021). The Role of GPNMB in Inflammation. *Frontiers in Immunology*, *12*, 674739. https://doi.org/10.3389/fimmu.2021.674739

Sahu, B., Chug, I., & Khanna, H. (2021). The Ocular Gene Delivery Landscape. *Biomolecules*, *11*(8), Article 8. https://doi.org/10.3390/biom11081135

Sakane, T., Okabayashi, S., Kimura, S., Inoue, D., Tanaka, A., & Furubayashi, T. (2020). Brain and Nasal Cavity Anatomy of the Cynomolgus Monkey: Species Differences from the Viewpoint of Direct Delivery from the Nose to the Brain. *Pharmaceutics*, *12*(12), 1227. https://doi.org/10.3390/pharmaceutics12121227

Sakurai, T. (2012). The role of NrCAM in neural development and disorders—Beyond a simple glue in the brain. *Molecular and Cellular Neuroscience*, *49*(3), 351–363. https://doi.org/10.1016/j.mcn.2011.12.002

Salabarria, S. M., Corti, M., Coleman, K. E., Wichman, M. B., Berthy, J. A., D'Souza, P., Tifft, C. J., Herzog, R. W., Elder, M. E., Shoemaker, L. R., Leon-Astudillo, C., Tavakkoli, F., Kirn, D. H., Schwartz, J. D., & Byrne, B. J. (2024). Thrombotic microangiopathy following systemic AAV administration is dependent on anti-capsid antibodies. *The Journal of Clinical Investigation*, *134*(1). https://doi.org/10.1172/JCI173510

Schmitz, R., Fitch, Z. W., Schroder, P. M., Choi, A. Y., Manook, M., Yoon, J., Song, M., Yi, J. S., Khandelwal, S., Arepally, G. M., Farris, A. B., Reis, E. S., Lambris, J. D., Kwun, J., & Knechtle, S. J. (2021). C3 complement inhibition prevents antibody-mediated rejection and prolongs renal allograft survival in sensitized non-human primates. *Nature Communications*, *12*(1), 5456. https://doi.org/10.1038/s41467-021-25745-7

Schulz, A., Walther, C., Morrison, H., & Bauer, R. (2014). In Vivo Electrophysiological Measurements on Mouse Sciatic Nerves. *JoVE (Journal of Visualized Experiments)*, *86*, e51181. https://doi.org/10.3791/51181

Schuster, D. J., Dykstra, J. A., Riedl, M. S., Kitto, K. F., Belur, L. R., McIvor, R. S., Elde, R. P., Fairbanks, C. A., & Vulchanova, L. (2014). Biodistribution of adeno-associated virus serotype 9 (AAV9) vector after intrathecal and intravenous delivery in mouse. *Frontiers in Neuroanatomy*, *0*(JUN), 42. https://doi.org/10.3389/FNANA.2014.00042

Sharma, N., Flaherty, K., Lezgiyeva, K., Wagner, D. E., Klein, A. M., & Ginty, D. D. (2020). The emergence of transcriptional identity in somatosensory neurons. *Nature*, *577*(7790), 392–398. https://doi.org/10.1038/s41586-019-1900-1

Shen, S., Bryant, K. D., Brown, S. M., Randell, S. H., & Asokan, A. (2011). Terminal N-linked galactose is the primary receptor for adeno-associated virus 9. *The Journal of Biological Chemistry*, *286*(15), 13532–13540. https://doi.org/10.1074/jbc.M110.210922

Shirai, Y., Kawabe, K., Tosa, I., Tsukamoto, S., Yamada, D., & Takarada, T. (2019). Runx2 function in cells of neural crest origin during intramembranous ossification. *Biochemical and Biophysical Research Communications*, *509*(4), 1028–1033. https://doi.org/10.1016/j.bbrc.2019.01.059

Shirley, J. L., de Jong, Y. P., Terhorst, C., & Herzog, R. W. (2020). Immune Responses to Viral Gene Therapy Vectors. *Molecular Therapy*, *28*(3), 709–722. https://doi.org/10.1016/J.YMTHE.2020.01.001

Siddiqui, T., Cosacak, M. I., Popova, S., Bhattarai, P., Yilmaz, E., Lee, A. J., Min, Y., Wang, X., Allen, M., İş, Ö., Atasavum, Z. T., Rodriguez-Muela, N., Vardarajan, B. N., Flaherty, D., Teich, A. F., Santa-Maria, I., Freudenberg, U., Werner, C., Tosto, G., … Kizil, C. (2023). Nerve growth factor receptor (Ngfr) induces neurogenic plasticity by suppressing reactive astroglial Lcn2/Slc22a17 signaling in Alzheimer's disease. *Npj Regenerative Medicine*, *8*(1), 1–18. https://doi.org/10.1038/s41536-023-00311-5

Stanton, A. C., Lagerborg, K. A., Tellez, L., Krunnfusz, A., King, E. M., Ye, S., Solomon, I. H., Tabebordbar, M., & Sabeti, P. C. (2023). Systemic administration of novel engineered AAV capsids facilitates enhanced transgene expression in the macaque CNS. *Med*, *4*(1), 31-50.e8. https://doi.org/10.1016/j.medj.2022.11.002

Stone, D., Aubert, M., & Jerome, K. R. (2023). Adeno-associated virus vectors and neurotoxicity—Lessons from preclinical and human studies. *Gene Therapy*, 1–14. https://doi.org/10.1038/s41434-023-00405-1

Strings-Ufombah, V., Malerba, A., Kao, S.-C., Harbaran, S., Roth, F., Cappellari, O., Lu-Nguyen, N., Takahashi, K., Mukadam, S., Kilfoil, G., Kloth, C., Roelvink, P., Dickson, G., Trollet, C., & Suhy, D. (2021). BB-301: A silence and replace AAV-based vector for the treatment of oculopharyngeal muscular dystrophy. *Molecular Therapy Nucleic Acids*, *24*, 67–78. https://doi.org/10.1016/j.omtn.2021.02.017

Thippeswamy, T., McKay, J. S., & Morris, R. (2001). Bax and caspases are inhibited by endogenous nitric oxide in dorsal root ganglion neurons in vitro. *European Journal of Neuroscience*, *14*(8), 1229–1236. https://doi.org/10.1046/j.0953-816x.2001.01752.x

Thomas, T., Perdue, M. V., Khalaf, S., Landi, N., Hoeft, F., Pugh, K., & Grigorenko, E. L. (2021). Neuroimaging genetic associations between SEMA6D, brain structure, and reading skills. *Journal of Clinical and Experimental Neuropsychology*, *43*(3), 276–289. https://doi.org/10.1080/13803395.2021.1912300

Tien, E., Grubor, B., Kirkland, M., Chan, S. J., Van Der Munnik, N., Xu, W., Henry, K., Hamann, S., Wei, C., Lee, W.-H., Gianni, D., Brennecke, A., Nambiar, K., Chen, J., Liu, B., Shen, S., Tremblay, C., Plowey, E. D., Trapa, P., … Morris, D. (2024). Adeno-Associated Virus-Mediated Dorsal Root Ganglion Toxicity in the New Zealand White Rabbit. *Toxicologic Pathology*, 01926233241229808. https://doi.org/10.1177/01926233241229808

Timotius, I. K., Roelofs, R. F., Richmond-Hacham, B., Noldus, L. P. J. J., von Hörsten, S., & Bikovski, L. (2023). CatWalk XT gait parameters: A review of reported parameters in pre-clinical studies of multiple central nervous system and peripheral nervous system disease models. *Frontiers in Behavioral Neuroscience*, *17*. https://www.frontiersin.org/articles/10.3389/fnbeh.2023.1147784

Torregrosa, T., Lehman, S., Hana, S., Marsh, G., Xu, S., Koszka, K., Mastrangelo, N., McCampbell, A., Henderson, C. E., & Lo, S.-C. (2021). Use of CRISPR/Cas9-mediated disruption of CNS cell type genes to profile transduction of AAV by neonatal intracerebroventricular delivery in mice. *Gene Therapy*, *28*(7), Article 7. https://doi.org/10.1038/s41434-021-00223-3

Tucić, M., Stamenković, V., & Andjus, P. (2021). The Extracellular Matrix Glycoprotein Tenascin C and Adult Neurogenesis. *Frontiers in Cell and Developmental Biology*, *9*. https://doi.org/10.3389/fcell.2021.674199

Tukov, F. F., Mansfield, K., Milton, M., Meseck, E., Penraat, K., Chand, D., & Hartmann, A. (2022). Single-Dose Intrathecal Dorsal Root Ganglia Toxicity of Onasemnogene Abeparvovec in Cynomolgus Monkeys. *Human Gene Therapy*, *33*(13–14), 740–756. https://doi.org/10.1089/hum.2021.255

Tuthill, J. C., & Azim, E. (2018). Proprioception. *Current Biology*, *28*(5), R194–R203. https://doi.org/10.1016/j.cub.2018.01.064

Tyszkiewicz, C., Hwang, S.-K., DaSilva, J. K., Kovi, R. C., Fader, K. A., Sirivelu, M. P., Liu, J., Somps, C., Cook, J., Liu, C.-N., & Wang, H. (2024). Absence of functional deficits in rats following systemic administration of an AAV9 vector despite moderate peripheral nerve and dorsal root ganglia findings: A clinically silent peripheral neuropathy. *NeuroToxicology*, *101*, 46–53. https://doi.org/10.1016/j.neuro.2024.02.001

Uchida, M., Enomoto, A., Fukuda, T., Kurokawa, K., Maeda, K., Kodama, Y., Asai, N., Hasegawa, T., Shimono, Y., Jijiwa, M., Ichihara, M., Murakumo, Y., & Takahashi, M. (2006). Dok-4 regulates GDNF-dependent neurite outgrowth through downstream activation of Rap1 and mitogen-activated protein kinase. *Journal of Cell Science*, *119*(15), 3067–3077. https://doi.org/10.1242/jcs.03043

Üstün, R., Oğuz, E. K., Delilbaşı, Ç., Şeker, A., Taşpınar, F., Öncü, M. R., & Oğuz, A. R. (2017). Neuromuscular degenerative effects of Ankaferd Blood Stopper ® in mouse sciatic nerve model. *Somatosensory & Motor Research*, *34*(4), 248–257. https://doi.org/10.1080/08990220.2017.1421160

van den Akker, E., Reijnen, M., Korving, J., Brouwer, A., Meijlink, F., & Deschamps, J. (1999). Targeted inactivation of Hoxb8 affects survival of a spinal ganglion and

causes aberrant limb reflexes. *Mechanisms of Development*, *89*(1–2), 103–114. https://doi.org/10.1016/s0925-4773(99)00212-9

Vojtek, M., & Chambers, I. (2021). Loss of Resf1 reduces the efficiency of embryonic stem cell self-renewal and germline entry. *Life Science Alliance*, *4*(12). https://doi.org/10.26508/lsa.202101190

Vukojicic, A., Delestrée, N., Fletcher, E. V., Pagiazitis, J. G., Sankaranarayanan, S., Yednock, T. A., Barres, B. A., & Mentis, G. Z. (2019). The Classical Complement Pathway Mediates Microglia-Dependent Remodeling of Spinal Motor Circuits during Development and in SMA. *Cell Reports*, *29*(10), 3087-3100.e7. https://doi.org/10.1016/j.celrep.2019.11.013

Wang, J.-H., Gessler, D. J., Zhan, W., Gallagher, T. L., & Gao, G. (2024). Adeno-associated virus as a delivery vector for gene therapy of human diseases. *Signal Transduction and Targeted Therapy*, *9*(1), 1–33. https://doi.org/10.1038/s41392-024-01780-w

Weller, R. O. (2012). Fundamental Neuropathology for Pathologists and Toxicologists: Principles and Techniques. *Neuropathology and Applied Neurobiology*, *38*(5), 513–514. https://doi.org/10.1111/j.1365-2990.2012.01260.x

Weng, W.-C., Hsu, Y.-K., Chang, F.-M., Lin, C.-Y., Hwu, W.-L., Lee, W.-T., Lee, N.-C., & Chien, Y.-H. (2021). CMAP changes upon symptom onset and during treatment in spinal muscular atrophy patients: Lessons learned from newborn screening. *Genetics in Medicine*, *23*(2), 415–420. https://doi.org/10.1038/s41436-020-00987-w

Xu, L., Yao, S., Ding, Y. E., Xie, M., Feng, D., Sha, P., Tan, L., Bei, F., & Yao, Y. (2024). Designing and optimizing AAV-mediated gene therapy for neurodegenerative diseases: From bench to bedside. *Journal of Translational Medicine*, *22*(1), 866. https://doi.org/10.1186/s12967-024-05661-2

Xu, X., Zhou, X., Du, J., Liu, X., Qing, L., Johnson, B. N., & Jia, X. (2021). Macrophage Activation in the Dorsal Root Ganglion in Rats Developing Autotomy after Peripheral Nerve Injury. *International Journal of Molecular Sciences*, *22*(23), 12801. https://doi.org/10.3390/ijms222312801

Yang, J., Zhang, L., Yu, C., Yang, X.-F., & Wang, H. (2014). Monocyte and macrophage differentiation: Circulation inflammatory monocyte as biomarker for inflammatory diseases. *Biomarker Research*, *2*(1), 1. https://doi.org/10.1186/2050-7771-2-1

Yang, T., Braun, M., Lembke, W., McBlane, F., Kamerud, J., DeWall, S., Tarcsa, E., Fang, X., Hofer, L., Kavita, U., Upreti, V. V., Gupta, S., Loo, L., Johnson, A. J., Chandode, R. K., Stubenrauch, K.-G., Vinzing, M., Xia, C. Q., & Jawa, V. (2022). Immunogenicity assessment of AAV-based gene therapies: An IQ consortium industry white paper. *Molecular Therapy - Methods & Clinical Development*, *26*, 471–494. https://doi.org/10.1016/j.omtm.2022.07.018

Yu, S., Choi, W.-I., Choi, Y. J., Kim, H.-Y., Hildebrandt, F., & Gee, H. Y. (2020). PLCE1 regulates the migration, proliferation, and differentiation of podocytes. *Experimental & Molecular Medicine*, *52*(4), 594–603. https://doi.org/10.1038/s12276-020-0410-4

Yuan, A., Rao, M. V., & Nixon, R. A. (2017). Neurofilaments and Neurofilament Proteins in Health and Disease. *Cold Spring Harbor Laboratory Press*, 9:a018309. https://doi.org/10.1101/cshperspect.a018309

Zaidman, C. M., Proud, C. M., McDonald, C. M., Lehman, K. J., Goedeker, N. L., Mason, S., Murphy, A. P., Guridi, M., Wang, S., Reid, C., Darton, E., Wandel, C., Lewis, S., Malhotra, J., Griffin, D. A., Potter, R. A., Rodino-Klapac, L. R., & Mendell, J. R. (2023). Delandistrogene Moxeparvovec Gene Therapy in Ambulatory Patients (Aged ≥4 to <8 Years) with Duchenne Muscular Dystrophy: 1-Year Interim Results from Study SRP-9001-103 (ENDEAVOR). *Annals of Neurology*, *94*(5), 955–968. https://doi.org/10.1002/ana.26755

Zhang, Y., Li, D., Zeng, Q., Feng, J., Fu, H., Luo, Z., Xiao, B., Yang, H., & Wu, M. (2021). LRRC4 functions as a neuron-protective role in experimental autoimmune encephalomyelitis. *Molecular Medicine*, *27*(1), 44. https://doi.org/10.1186/s10020-021-00304-4

Zhao, K., Shen, C., Lu, Y., Huang, Z., Li, L., Rand, C. D., Pan, J., Sun, X.-D., Tan, Z., Wang, H., Xing, G., Cao, Y., Hu, G., Zhou, J., Xiong, W.-C., & Mei, L. (2017). Muscle Yap Is a Regulator of Neuromuscular Junction Formation and Regeneration. *Journal of Neuroscience*, *37*(13), 3465–3477. https://doi.org/10.1523/JNEUROSCI.2934-16.2017

Zheng, G., Younsi, A., Scherer, M., Riemann, L., Walter, J., Skutella, T., Unterberg, A., & Zweckberger, K. (2021). The CatWalk XT® Gait Analysis Is Closely Correlated with Tissue Damage after Cervical Spinal Cord Injury in Rats. *Applied Sciences*, *11*(9), Article 9. https://doi.org/10.3390/app11094097

Zheng, Y., & He, J.-Q. (2022). Interleukin Receptor Associated Kinase 1 Signaling and Its Association with Cardiovascular Diseases. *Reviews in Cardiovascular Medicine*, *23*(3), 97. https://doi.org/10.31083/j.rcm2303097

Zhu, J., Huang, X., & Yang, Y. (2009). The TLR9-MyD88 pathway is critical for adaptive immune responses to adeno-associated virus gene therapy vectors in mice. *The Journal of Clinical Investigation*, *119*(8), 2388–2398. https://doi.org/10.1172/JCI37607

Zincarelli, C., Soltys, S., Rengo, G., & Rabinowitz, J. E. (2008). Analysis of AAV serotypes 1-9 mediated gene expression and tropism in mice after systemic injection. *Molecular Therapy*, *16*(6), 1073–1080. https://doi.org/10.1038/mt.2008.76

RÉSUMÉ

Les neurones somatosensoriels jouent un rôle essentiel dans les sensations et les réponses aux stimuli externes. Les neurones sensoriels se sont révélés sensibles aux toxicités induites par l'administration de fortes doses de virus adéno-associés (AAV) et de produits génétiques AAV dans le sang et le liquide céphalo-rachidien. La toxicité des ganglions de la racine dorsale (DRG) se caractérise généralement par une nécrose et une axonopathie dans les DRG, ainsi que par une dégénérescence axonale dans la moelle épinière et les nerfs périphériques. Ces résultats ont été rapportés chez des primates non humains, des lapins, des porcelets et des rongeurs. Comme l'utilisation des thérapies à base d'AAV continue de croître, le développement d'un modèle rapide et adaptable pour évaluer la toxicité du DRG est essentiel. Dans cette thèse, des souris C57BL/6J de type sauvage âgées de six semaines ont reçu par voie intrathécale une dose d'AAV-miR-SOD1, un vecteur connu pour causer une toxicité DRG. Les souris ont été soumises à des études transcriptomiques, physiologiques et comportementales visant à élucider les altérations moléculaires dans divers types de cellules et les conséquences fonctionnelles associées de la lésion des neurones sensoriels. Dans toutes les études, une augmentation des niveaux sériques de neurofilament léger (NfL) a indiqué une lésion du DRG, des résultats comparables à ceux d'études antérieures. Le séquençage de l'ARN d'un seul noyau a révélé une réduction de la population de neurones et de cellules de Schwann, une augmentation des fibroblastes et des cellules immunitaires, ainsi que l'émergence d'une population de cellules gliales satellites activées. L'analyse de l'enrichissement de l'ensemble des gènes a révélé des processus de développement et de neurogenèse dans la glie satellite activée et des signatures de gènes immunitaires innés et adaptatifs dans les cellules immunitaires, indiquant une inflammation. Sur le plan fonctionnel, les souris ont souffert d'une diminution de la force musculaire, de l'émergence d'une crispation des membres postérieurs, d'une diminution du poids corporel et d'une diminution du taux de survie. Cette thèse fournit de précieuses informations mécanistiques et fonctionnelles spécifiques aux cellules dans la réponse à la toxicité DRG induite par l'AAV chez les souris. Les souris se sont révélées être un modèle précieux et efficace pour étudier la toxicité du DRG. Ces résultats contribueront à la conception et au dépistage de futures thérapies géniques pour les maladies du SNC.

MOTS-CLÉS

Virus adéno-associé (AAV), Ganglions de la racine dorsale (DRG), Toxicité, Neurones sensoriels, Dégénérescence, Lumière des neurofilaments (NfL), Séquençage de l'ARN d'un seul noyau

ABSTRACT

Somatosensory neurons play a critical role in sensation and responses to external stimuli. Sensory neurons have been shown to be susceptible to toxicities induced by the administration of high doses of adeno-associated viruses (AAVs) and AAV gene products in the blood and the cerebrospinal fluid. Dorsal root ganglia (DRG) toxicity is generally characterized by necrosis and axonopathy in the DRG, along with axonal degeneration in the spinal cord and peripheral nerves. These findings have been reported in non-human primates, rabbits, piglets, and rodents. As the use of AAV-based therapeutics continues to grow, the development of a rapid and adaptable model to assess DRG toxicity is critical. In this dissertation, six-week-old C57BL/6J wild-type mice were intrathecally dosed with AAV-miR-SOD1, a vector known to cause DRG toxicity. Mice underwent transcriptomic, physiological, and behavioral studies focused to elucidate the molecular alterations in various cell types and the associated functional consequences of injury to sensory neurons. In all studies, a surge in serum neurofilament light (NfL) levels indicated DRG injury, findings comparable to previous studies. Single-nucleus RNA sequencing revealed a reduction in the population of neurons, Schwann cells, elevation of fibroblasts, immune cells, and emergence of an activated satellite glia population. Gene Set Enrichment analysis showed developmental and neurogenesis processes in activated satellite glia and innate and adaptive immune gene signatures in immune cells, indicative of inflammation. Functionally, mice suffered from a decline in muscle strength, emergence of hindlimb clasping, decreased body weight, and decreased survival. This thesis provides valuable cell specific mechanistic and functional insights in the response to AAV-induced DRG toxicity in mice. Mice were shown to be a valuable and efficient model to study DRG toxicity. These findings will aid in designing and screening future gene therapies for CNS diseases.

KEYWORDS

Adeno-associated virus (AAV), Dorsal root ganglia (DRG), Toxicity, Sensory neurons, Degeneration, Neurofilament light (NfL), Single-nucleus RNA sequencing